# Patient-specific dose calculation methods for high-dose-rate iridium-192 brachytherapy

*Emily S. Poon*

Department of Electrical and Computer Engineering
McGill University, Montréal

August 2009

---

*A thesis submitted to McGill University in partial fulfillment of the requirements of the degree of Doctor of Philosophy in Electrical Engineering.*

© Emily S. Poon 2009

*To the glory of God and*

*in loving memory of my grandmother,*

*Po Fong Sham, 1922-2008.*

Now to Him who is able to keep you from stumbling,
and to make you stand in the presence of His glory blameless with great joy,
to the only God our Savior, through Jesus Christ our Lord,
be glory, majesty, dominion and authority,
before all time and now and forever. Amen.

*Jude 24–25*

# Abstract

In high-dose-rate $^{192}$Ir brachytherapy, the radiation dose received by the patient is calculated according to the AAPM Task Group 43 (TG-43) formalism. This table-based dose superposition method uses dosimetry parameters derived with the radioactive $^{192}$Ir source centered in a water phantom. It neglects the dose perturbations caused by inhomogeneities, such as the patient anatomy, applicators, shielding, and radiographic contrast solution.

In this work, we evaluated the dosimetric characteristics of a shielded rectal applicator with an endocavitary balloon injected with contrast solution. The dose distributions around this applicator were calculated by the GEANT4 Monte Carlo (MC) code and measured by ionization chamber and GAFCHROMIC EBT film. A patient-specific dose calculation study was then carried out for 40 rectal treatment plans. The PTRAN_CT MC code was used to calculate the dose based on computed tomography (CT) images. This study involved the development of BrachyGUI, an integrated treatment planning tool that can process DICOM-RT data and create PTRAN_CT input initialization files. BrachyGUI also comes with dose calculation and evaluation capabilities.

We proposed a novel scatter correction method to account for the reduction in backscatter radiation near tissue-air interfaces. The first step requires calculating the doses contributed by primary and scattered photons separately, assuming a full scatter environment. The scatter dose in the patient is subsequently adjusted using a factor derived by MC calculations, which depends on the distances between the point of interest, the $^{192}$Ir source, and the body contour. The method was validated for multicatheter breast

brachytherapy, in which the target and skin doses for 18 patient plans agreed with PTRAN_CT calculations better than 1%.

Finally, we developed a CT-based analytical dose calculation method. It corrects for the photon attenuation and scatter based upon the radiological paths determined by ray tracing. The scatter dose is again adjusted using our scatter correction technique. The algorithm was tested using phantoms and actual patient plans for head-and-neck, esophagus, and MammoSite breast brachytherapy. Although the method fails to correct for the changes in lateral scatter introduced by inhomogeneities, it is a major improvement over TG-43 and is sufficiently fast for clinical use.

# Résumé

En curiethérapies à haut débit de dose, la dose aux patients est évaluée selon le protocole AAPM Task-Group 43 (TG43), qui utilise des paramètres dosimétriques obtenues avec une source dans l'eau. Cependant, le patient, l'applicateur et le contraste ont des propriétés radiologiques différentes de l'eau; ces inhomogénéités sont donc négligées dans TG43.

Dans ce travail, nous utilisons le programme Monte Carlo (MC) GEANT4 pour évaluer les propriétés dosimétriques d'un applicateur rectal muni d'un blindage radio-protecteur et d'un ballon intra-cavitaire. Ces résultats sont confirmés par des mesures d'une chambre d'ionisation et des films GAFCHROMIC EBT. Une étude des calculs de dose a été faite avec le programme PTRAN_CT avec l'aide des images scanner de 40 patients de cancer rectal. Ceci a conduit au développement de BrachyGUI, un programme de planification de curiethérapie, capable de traiter les données DICOM-RT des patients et générer les paramètres d'entrée pour PTRAN_CT. BrachyGUI dispose d'outils de calcul, d'extraction et d'analyse de dose.

Nous proposons une nouvelle méthode de calcul qui tient compte des effets de diffusion au voisinage des interfaces tissus-air. Cette méthode calcule séparément la dose due aux photons primaires et diffusés, ensuite la composante diffusée est ajustée par un paramètre extrait des calculs MC incluant les contours du patient, la source et sa position. Nos résultats s'accordent avec une incertitude inferieure à 1% avec les calculs de dose à la surface et dans la cible effectués avec PTRAN_CT pour 18 patients en curiethérapie du sein.

Enfin, nous avons conçu une méthode analytique de calcul de dose qui incorpore l'atténuation et la diffusion des photons, et qui est basée sur les chemins radiologiques déterminées par traçage des trajectoires. Cet algorithme est validé par l'utilisation de fantômes, des données de patients traités pour divers cancers (œsophage, tête et cou), et par la curiethérapie MammoSite du sein. Bien que cette méthode ne reproduise pas bien les diffusions latérales induites par les inhomogénéités, elle représente une amélioration majeure par-rapport-à TG43 et est rapide pour une implémentation clinique.

# Acknowledgements

First of all, I would like to thank Dr. Frank Verhaegen for supervising this work. He gave useful guidance and allowed me to explore new things independently. I also thank him for the opportunities to collaborate with fellow students and participate at international conferences.

My gratitude goes to all the members of the McGill Medical Physics Unit. In particular, Dr. Slobodan Devic shared with me his knowledge in radiochromic film dosimetry and rectal treatment planning. Dr. Wamied Abdel-Rahman helped me on computer-related issues. My initial development of BrachyGUI was inspired by Dr. Francois DeBlois, who gave me his REALbasic code for rectal dose superposition calculations. Brigitte Reniers gave me advice on brachytherapy dosimetry. Robin van Gils meticulously constructed the phantoms for my ionization chamber and radiochromic film experiments. I have appreciated Dr. Ervin Podgorsak, Dr. Jan Seuntjens, and Margery Knewstubb for their contributions to the academic program in so many ways.

I would like to thank Professor Jeffrey Williamson and Dr. Yi Le for providing me with the PTRAN_CT code and teaching me how to use it. I have great respect for their diligent efforts in developing this code. Thanks to Dr. Bruce Pike and Dr. Milica Popovich for being on my thesis committee, Dr. Té Vuong for her role in designing the rectal brachytherapy treatment technique, and Dr. Hani Al-Halabi for his contribution in a cervical brachytherapy patient study.

I would like to extend my thanks to the BrachyGUI user group: Andreea, Christophe, Daniel, Danielle, Gerard, Jason, Michel, and Yong. Their bug reports and

suggestions greatly improved the usability of BrachyGUI. Arman, Danielle, and Kristin proofread my papers. Magdalena taught me CT imaging. Jason took part in patient data collection. Gerard translated my abstract into French. Thanks to Thai Binh and Tatjana for their encouragement in my thesis writing. I am also grateful for the friendships of my colleagues: Andrew, Derek, Eunah, Keyvan, Li Heng, and Rong Ding.

I gratefully acknowledge funding and support from Nucletron BV and the Canadian Institutes of Health Research EIRR21 Research Training Program. Lastly, I am thankful for the continuous prayers of my family, my aunt, Mr. and Mrs. Duerksen, Kristin, Anne, and Gary.

# Contributions of Authors

This thesis consists of four manuscripts. As the main author, I was responsible for the experiments, algorithm designs, software development, dose calculations, data analyses, and writing. I am indebted to the co-authors and various individuals, whose contributions are acknowledged below.

The first paper presents a dosimetric study for an intracavitary endorectal applicator using Monte Carlo (MC) and experimental techniques. Slobodan Devic taught me radiochromic film dosimetry and reviewed the manuscript carefully. Té Vuong designed the rectal brachytherapy treatment protocol. Frank Verhaegen supervised the work and gave insightful comments. Brigitte Reniers gave me advice on MC absolute dose conversions. Robin Van Gils constructed the two phantoms for radiochromic film and ionization chamber experiments. Kristin Stewart proofread the manuscript.

In the second paper, the effects of applicator and tissue inhomogeneities for 40 rectal brachytherapy patients were investigated by patient-specific MC dose calculations. Jeffrey Williamson granted me permission to use the PTRAN_CT code and made constructive comments on the manuscript. The patient study was conducted retrospectively using the patient data due to Té Vuong. Frank Verhaegen provided guidance and valuable feedback. Yi Le, the main developer of PTRAN_CT, showed me how to run the code. (I later revised the code's input interface so as to compact the size of the input data and make it run more smoothly.) Slobodan Devic gave useful advice on endorectal brachytherapy quality assurance. Jason Yan transferred a part of the patient data from a treatment planning system. Danielle Fraser assisted in proofreading.

The third paper introduces a scatter correction technique and its application to HDR $^{192}$Ir multicatheter breast brachytherapy. Frank Verhaegen made helpful comments on the manuscript, which was also proofread by Danielle Fraser. The scatter correction method was benchmarked against PTRAN_CT calculations. The code was provided by Jeffrey Williamson and Yi Le.

The fourth paper presents a CT-based analytical dose calculation method for HDR $^{192}$Ir brachytherapy. It was reviewed by Frank Verhaegen and proofread by Arman Sarfehnia and Danielle Fraser. Again, we used the PTRAN_CT code of Jeffrey Williamson and Yi Le for benchmarking purposes.

# Table of Contents

# Chapter One

# Introduction



## 1.1. THE ROLE OF BRACHYTHERAPY IN CANCER TREATMENT

According to the Canadian Cancer Statistics 2009, the incidence of cancer in the aging population is rising. About 40% of Canadian women and 45% of men will develop cancer in their lifetime [1]. The expected number of new cancer diagnoses per year, excluding non-melanoma skin cancer, now stands at 171,000 [1]. Prostate, lung, breast, and colorectal cancers are most prevalent, accounting for over 55% of the new cases [1].

Cancer patients commonly receive a combination of treatments that may include surgery, chemotherapy, and radiotherapy. About half of the patients undergo radiotherapy whereby ionizing radiation is used to cure the disease or alleviate pain. The optimal therapeutic effect of radiotherapy is achieved when cancer cells are eradicated while normal tissue damage is kept to a minimum. The radiation source may be applied outside the body through external beam treatment or from the inside through brachytherapy.

In brachytherapy (from Greek *brachios*, meaning "short"), the patient is treated by placing radioactive sources close to or in contact with a well-defined target volume. The radiation dose in the near-source region is substantially higher than the prescribed dose at the target margin; and yet the dose falls off rapidly with distance, concomitantly reducing the risk of radiation injury to the surrounding normal tissues. To reduce normal tissue complications, the high dose heterogeneity should be well tolerated by the patient. This can be achieved by, for example, administering an appropriate dose-fractionation scheme and keeping the volume of overdosed normal tissues below 1 to 2 $cm^3$ [2].

External beam radiotherapy, in contrast, delivers a more uniform dose distribution from a distance, commonly via a linear accelerator. The International Commission on Radiation Units and Measurements (ICRU) Report No. 50 [3] recommends that the target should receive between 95% and 107% of the prescribed dose. Multiple treatment fractions are often used so as to allow time for the normal tissues irradiated along the treatment beams to repair. It is preferable to treat large tumors by external beam techniques because extreme hot spots in the dose distribution are more easily avoidable. Also, external beam radiotherapy is generally less invasive and less labour-intensive.

The superior dose conformity of brachytherapy makes it an ideal monotherapy for certain kinds of localized lesions, which can be superficial or deep-seated. As well, it is used to boost the target dose in conjunction with external beam radiotherapy. Sometimes brachytherapy is used preoperatively to shrink the tumor volume before surgery. It is also applied as a postoperative procedure to irradiate the remaining tumor bed.

Brachytherapy has played an important role in cancer therapy for over a century. Almost all kinds of lesions in the body have been treated by this technique with differing degrees of success. It is often used to cure cancers of the cervix and endometrium. Other

major treatment sites include the prostate, breast, lung, esophagus, and head and neck [4, 5]. It is also used to treat the rectum, bile duct, brain, skin, and soft tissue [6]. About 5% to 15% of radiotherapy patients are likely candidates for brachytherapy [7].

## 1.2. ACCURACY REQUIREMENTS FOR BRACHYTHERAPY DOSE DELIVERY

It is well established that the probabilities of tumor control and normal tissue damage both depend on the accuracy in radiation dose delivery [8]. The relative standard deviation $\sigma$ of the target mean dose should be within 3% if the absolute $\sigma$ in tumor control probability (TCP) is to be kept below 10% [9]. While ensuring adequate target coverage is important, excessive normal tissue damage should also be avoided. A 5% change in dose will lead to a 10–20% change in tumor control at a TCP of 50%, and a 20–30% change in normal tissue complications [10].

Accurate source localization is essential because of the steep dose falloff with distance characteristic of brachytherapy sources. The American Association of Physicists in Medicine (AAPM) Task Group Report No. 56 (TG-56) [11] suggested that a positioning accuracy of ±2 mm and a temporal accuracy of ±2% are reasonable. For computer-assisted dose calculations, an accuracy of ±2% consistent with the input data and computation algorithm is recommended [11].

## 1.3. ISSUES IN BRACHYTHERAPY TREATMENT PLANNING

Nowadays, most brachytherapy treatment planning systems support the AAPM Task Group No. 43 (TG-43) dosimetry protocol [12]. TG-43 provides a well-defined means of characterizing dose distributions around brachytherapy sources in a water phantom. The patient dose can be calculated by interpolating or extrapolating tabulated

TG-43 dosimetry parameters. This approach fails to account for the dosimetric effects of tissue inhomogeneities, high-density applicators and shielding, and radiographic contrast solution. It also cannot account for the reduced photon backscatter near the skin.

A few dose calculation techniques such as the collapsed cone superposition, discrete ordinates, and the Monte Carlo (MC) methods are able to account for the dose perturbations of such inhomogeneities. A major obstacle to their clinical utilization is the relatively long calculation time compared to the TG-43 formalism. The demand for high calculation efficiency is obvious for real-time treatment planning in which the dose is delivered soon after the brachytherapy catheters have been inserted into the patient.

## 1.4. THESIS HYPOTHESES AND OBJECTIVES

This thesis work focuses on dose calculation methods for high-dose-rate (HDR) $^{192}$Ir brachytherapy. We hypothesize that the water-based TG-43 formalism is not sufficiently accurate for certain treatment sites owing to inhomogeneity effects. The patient-specific analytical dose calculation method developed in this work will be of improved accuracy compared to TG-43, and it will be feasible for implementation in treatment planning systems. The objectives of this thesis are threefold:

1. *Develop a framework for fast patient-specific MC dose calculations*

This involves using the accelerated MC photon transport code PTRAN_CT [13] and modifying its input interface so as to improve the efficiency in loading patient data derived from computed tomography (CT) images. A software tool, BrachyGUI, will be developed to streamline the processing of PTRAN_CT input files using patient plans exported from a treatment planning system. The GEANT4 MC code [14] will also be used alongside PTRAN_CT for various aspects of this work as well as for comparison purposes.

*2. Evaluate the dosimetric effects of inhomogeneities for a variety of treatment sites*

CT-based PTRAN_CT dose calculations will be performed for treatment sites including the rectum, cervix, breast, head and neck, and esophagus. Applicator and tissue inhomogeneity effects will be evaluated using the dose analysis functions in BrachyGUI. The goal is to assess the adequacy of TG-43 for HDR $^{192}$Ir treatment planning. We will also use MC calculations and experimental techniques to characterize a silicone endorectal applicator with shielding and an inflatable balloon injected with iodine contrast solution. A cohort study with 40 rectal patients will be carried out to examine how inhomogeneities will affect the target coverage and normal tissue sparing.

*3. Develop a dose calculation algorithm feasible for patient-specific treatment planning*

We will develop a novel scatter correction technique to account for the reduced photon backscatter near tissue-air interfaces, as is commonly encountered in brachytherapy of the breast and other superficial lesions. This can be used in conjunction with a CT-based analytical dose calculation method to account for tissue and applicator inhomogeneities. The algorithms will be benchmarked against PTRAN_CT calculations and their efficiency will be evaluated.

## 1.5. PUBLISHED WORK

### 1.5.1. *Thesis-related publications*

This thesis includes the following four published manuscripts, which will be referred to as Papers I, II, III, and IV in the following chapters.

[I] Poon E, Reniers B, Devic S, Vuong T, Verhaegen F. Dosimetric characterization of a novel intracavitary mold applicator for $^{192}$Ir high dose rate endorectal brachytherapy treatment. Med Phys. 2006;33:4515-26.

[II] Poon E, Williamson JF, Vuong T, Verhaegen F. Patient-specific Monte Carlo dose calculations for high-dose-rate endorectal brachytherapy with shielded intracavitary applicator. Int J Radiat Oncol Biol Phys. 2008;72:1259-66.

[III] Poon E, Verhaegen F. Development of a scatter correction technique and its application to HDR $^{192}$Ir multicatheter breast brachytherapy. Med Phys. 2009;36:3703-13.

[IV] Poon E, Verhaegen F. A CT-based analytical dose calculation method for HDR $^{192}$Ir brachytherapy. Med Phys. 2009;36:3982-94.

### 1.5.2. *Other publications*

The following papers were published during the course of my study from 2005 to 2009. Papers V and VI describe the photon and electron transport algorithms in GEANT4, which was used in this work for characterizing brachytherapy sources and a shielded rectal applicator. The other papers describe various aspects of brachytherapy dosimetry, including treatment planning software development, image-guided HDR rectal brachytherapy dose delivery, comparsion of dose calculation algorithms, and dosimetric studies of low-dose-rate and electronic brachytherapy sources.

[V] Poon E, Seuntjens J, Verhaegen F. Consistency test of the electron transport algorithm in the GEANT4 Monte Carlo code. Phys Med Biol. 2005;50:681-94.

[VI] Poon E, Verhaegen F. Accuracy of the photon and electron physics in GEANT4 for radiotherapy applications. Med Phys. 2005;32:1696-711.

[VII] Devic S, Vuong T, Moftah B, Evans M, Podgorsak EB, Poon E, et al. Image-guided high dose rate endorectal brachytherapy. Med Phys. 2007;34:4451-8.

[VIII] Poon E, Le Y, Williamson JF, Verhaegen F. BrachyGUI: an adjunct to an accelerated Monte Carlo photon transport code for patient-specific brachytherapy dose calculations and analysis. J Phys Conf Ser. 2008;102:012018.

[IX] Furstoss C, Reniers B, Poon E, D'Amours M, Carrier JF, Beaulieu L, et al. Monte Carlo iodine brachytherapy dosimetry: study for a clinical application. J Phys Conf Ser. 2008;102:012011.

[X] Liu D, Poon E, Bazalova M, Reniers B, Evans M, Rusch T, et al. Spectroscopic characterization of a novel electronic brachytherapy system. Phys Med Biol. 2008;53:61-75.

[XI] Yan X, Poon E, Reniers B, Vuong T, Verhaegen F. Comparison of dose calculation algorithms for colorectal cancer brachytherapy treatment with a shielded applicator. Med Phys. 2008;35:4824-30.

[XII] Furstoss C, Reniers B, Bertrand MJ, Poon E, Carrier JF, Keller BM, et al. Monte Carlo study of LDR seed dosimetry with an application in a clinical brachytherapy breast implant. Med Phys. 2009;36:1848-58.

## 1.6. OUTLINE OF THE CHAPTERS

This thesis is organized as follows. Chapter 2 introduces the historical, physical, and clinical aspects of brachytherapy. Chapter 3 reviews the basics of HDR $^{192}$Ir dosimetry and various issues affecting the dose calculation accuracy in brachytherapy planning systems. It also provides an overview of brachytherapy dose calculation methods. In Chapter 4, the main features of BrachyGUI are described. Chapters 5 to 8 correspond to Papers I to IV. Chapter 5 reports the dosimetric characteristics of a shielded intracavitary applicator for endorectal brachytherapy. Chapter 6 presents a retrospective MC dose calculation study for 40 patients treated with the endorectal applicator. Chapter 7 introduces a novel scatter correction technique and its application to multicatheter breast brachytherapy. In Chapter 8, an analytical algorithm for CT-based dose calculations is presented. Finally, Chapter 9 gives a summary as well as the conclusions and a discussion of potential future work.

## 1.7. REFERENCES

1. Canadian Cancer Society's Steering Committee. Canadian Cancer Statistics 2009. Toronto, ON: Canadian Cancer Society; 2009.

2. Stewart AJ, Jones B. Radiobiologic concepts for brachytherapy. In: Devlin PM, editor. Brachytherapy: applications and techniques. Philadelphia: Lippincott Williams & Wilkins; 2007. p. 1-19.

3. International Commission on Radiation Units and Measurements. Prescribing, recording, and reporting photon beam therapy. Bethesda, MD: ICRU; 1993.

4. Nag S, Owen JB, Farnan N, Pajak TF, Martinez A, Porter A, et al. Survey of brachytherapy practice in the United States: a report of the Clinical Research Committee of the American Endocurietherapy Society. Int J Radiat Oncol Biol Phys. 1995;31:103-7.

5. Guedea F, Ellison T, Venselaar J, Borras JM, Hoskin P, Poetter R, et al. Overview of brachytherapy resources in Europe: a survey of patterns of care study for brachytherapy in Europe. Radiother Oncol. 2007;82:50-4.

6. Nag S, Scruggs GR. Clinical aspects and applications of high-dose-rate brachytherapy. In: Halperin EC, Perez CA, Brady LW, editors. Perez and Brady's principles and practice of radiation oncology. 5th ed. Philadelphia: Wolters Kluwer Health/Lippincott Williams & Wilkins; 2008. p. 560-82.

7. Glasgow GP. Brachytherapy. In: Van Dyk J, editor. The modern technology of radiation oncology: a compendium for medical physicists and radiation oncologists. Madison, WI: Medical Physics Pub.; 1999. p. 695-752.

8. Emami B, Lyman J, Brown A, Coia L, Goitein M, Munzenrider JE, et al. Tolerance of normal tissue to therapeutic irradiation. Int J Radiat Oncol Biol Phys. 1991;21:109-22.

9. Brahme A. Dosimetric precision requirements in radiation therapy. Acta Radiol Oncol. 1984;23:379-91.

10. Papanikolaou N, Battista JJ, Boyer AL, Kappas C, Klein E, Mackie TR, et al. Tissue inhomogeneity corrections for megavoltage photon beams. Madison, WI: American Association of Physicists in Medicine 2004. Report No.: 85.

11. Nath R, Anderson LL, Meli JA, Olch AJ, Stitt JA, Williamson JF. Code of practice for brachytherapy physics: report of the AAPM Radiation Therapy Committee Task Group No. 56. Med Phys. 1997;24:1557-98.

12. Rivard MJ, Coursey BM, DeWerd LA, Hanson WF, Huq MS, Ibbott GS, et al. Update of AAPM Task Group No. 43 Report: A revised AAPM protocol for brachytherapy dose calculations. Med Phys. 2004;31:633-74.

13. Le Y, Chibani O, Todor D, Siebers I, Williamson J. An integrated CT-based Monte Carlo dose-evaluation system for brachytherapy and its application to permanent prostate implant postprocedure dosimetric analysis. Med Phys. 2005;32:2068.

14. Agostinelli S, Allison J, Amako K, Apostolakis J, Araujo H, Arce P, et al. GEANT4-a simulation toolkit. Nucl Instrum Methods Phys Res A. 2003;506:250-303.

# Chapter Two

# Introduction to Brachytherapy



## 2.1. BASICS OF RADIOACTIVITY

*Radioactivity* describes a stochastic phenomenon in which an unstable nuclide spontaneously disintegrates by emitting particles so as to be transformed into a stable nuclide, possibly of different physical and chemical properties. *Radionuclides*, also referred to as radioisotopes, are atoms that undergo radioactive decay. They are used in radiotherapy, nuclear medicine, biochemistry, and various research and industrial applications.

### 2.1.1. *Activity, half-life, and specific activity*

The *activity* $\mathcal{A}$ of a radionuclide represents the number of disintegrations it undergoes per unit time. The SI derived unit of activity is the *becquerel* (Bq), where 1 Bq = 1 $s^{-1}$. Becquerel is related to the former unit curie (Ci) as follows:

$$1 \text{ Ci} = 3.7 \times 10^{10} \text{ Bq (exactly)} \qquad (2.1)$$

Radioactive atoms decay exponentially with time. The activity at time $t$ can be derived from the initial activity $\mathcal{A}_0$ and the decay constant $\lambda$:

$$\mathcal{A}(t) = \mathcal{A}_0 e^{-\lambda t} \tag{2.2}$$

The decay constant is a property specific to the radionuclide. It is inversely proportional to the *half-life* $T_{1/2}$, which is the time it takes for half of the existing atoms to disintegrate:

$$T_{1/2} = \frac{\ln 2}{\lambda} \approx \frac{0.693}{\lambda} \tag{2.3}$$

The *specific activity* $\alpha$ is defined as the activity per unit mass $m$:

$$\alpha = \frac{\mathcal{A}}{m} = \frac{N_A \lambda}{A} \tag{2.4}$$

$N_A$ is the Avogadro's number ($6.022 \times 10^{23}$ atoms/g-atom) and $A$ is the mass number. In practice, $\alpha$ is smaller when the radionuclides are mixed with stable isotopes.

### 2.1.2. *Particles emitted from brachytherapy sources*

Brachytherapy sources may emit alpha particles ($\alpha$), gamma rays ($\gamma$), x rays, beta particles ($\beta$), electrons ($e^-$), and/or neutrons. An $\alpha$ particle is identical to a helium nucleus, which consists of two protons and two neutrons and is positively charged. Gamma rays are photons and $\beta$ particles are electrons, both originating from radioactive nuclei. Characteristic x ray or an Auger electron is emitted when an orbital electron travels from an outer electron shell to an inner one to fill a vacancy.

### 2.1.3. *Radioactive transformations*

In a decay process, a radioactive parent $X$ of atomic number $Z$ and mass number $A$ is transformed into a daughter nuclide $Y$. In addition to ionizing radiation, neutrinos $v$ or antineutrinos $\bar{v}$ may be released. Successive transformations take place until a stable

state is reached. The modes of decay pertinent to radionuclides used in brachytherapy are described below.

*i.* *Alpha decay*

Alpha decay occurs when a heavy nucleus disintegrates and emits an $\alpha$ particle:

$$ {}^{A}_{Z}\mathrm{X} \rightarrow {}^{A-4}_{Z-2}\mathrm{Y} + \alpha \tag{2.5} $$

A notable example is the transformation of $^{226}$Ra into $^{222}$Rn and $\alpha$:

$$ {}^{226}_{88}\mathrm{Ra} \rightarrow {}^{222}_{86}\mathrm{Rn} + \alpha \tag{2.6} $$

*ii.* *Beta-minus decay*

The $\beta^-$ decay process converts a neutron into a proton, and ejects a negatively charged $\beta$ particle (a.k.a. negatron) and an antineutrino:

$$ {}^{A}_{Z}\mathrm{X} \rightarrow {}^{A}_{Z+1}\mathrm{Y} + \beta^- + \bar{\nu} \tag{2.7} $$

An example is the decay of $^{60}$Co into the excited state of $^{60}$Ni:

$$ {}^{60}_{27}\mathrm{Co} \rightarrow {}^{60}_{28}\mathrm{Ni}^{*} + \beta^- + \bar{\nu} \tag{2.8} $$

*iii.* *Electron capture*

An orbital electron can be captured by the nucleus and subsequently combined with a proton to form a neutron and a neutrino:

$$ {}^{A}_{Z}\mathrm{X} + e^- \rightarrow {}^{A}_{Z-1}\mathrm{Y} + \nu \tag{2.9} $$

The orbital electron is most probably from the K shell. It leaves behind a vacancy which may cause characteristic x rays and/or Auger electrons to emit. The transformation of $^{125}$I into the excited state of $^{125}$Te is an electron capture process:

$$ {}^{125}_{53}\mathrm{I} + e^- \rightarrow {}^{125}_{52}\mathrm{Te}^{*} + \nu \tag{2.10} $$

*iv.* *Gamma decay*

Gamma decay is the emission of $\gamma$ radiation as a daughter nucleus undergoes a transition from an excited energy state to the ground energy state:

$$ {}^{A}_{Z}\mathrm{X}^{*} \rightarrow {}^{A}_{Z}\mathrm{X} + \gamma \qquad (2.11) $$

For example, when $^{60}Ni^{*}$, a daughter product of $^{60}Co$ produced via $\beta^{-}$ decay, returns to the stable energy state, $\gamma$ rays of energies 1.173 and 1.332 MeV are emitted in cascade.

*v.* *Internal conversion*

Internal conversion occurs when an excited nucleus returns to the ground state and ejects an orbital electron (most likely from the K shell) with the excess energy:

$$ {}^{A}_{Z}\mathrm{X}^{*} \rightarrow {}^{A}_{Z}\mathrm{X} + e^{-}. \qquad (2.12) $$

Characteristic x rays and/or Auger electrons may be emitted through a series of orbital electron transitions to fill the inner shell vacancy. After the decay of $^{125}I$ into $^{125}Te^{*}$ through the electron capture process, there is a 93% probability for the emission of internal conversion electrons, and a 7% probability for the emission of 35 keV γ rays [1].

### 2.1.4. *Ionizing radiation and its related physical quantities*

Particles emitted by radionuclides cause ionizing radiation in matter and may produce secondary particles. The *ionization potential* is the minimum energy required to ionize an atom, i.e., to knock a bound electron out of orbit. It ranges from a few eV for alkali elements to 24.5 eV for helium, a noble gas (1 eV ≈ $1.602\times10^{-19}$ J) [1]. Uncharged particles may interact with atoms in the medium to set charged particles in motion. Damage to cancer cells as well as healthy tissues takes place along the tracks of charged particles, which ionize matter by Coulomb interactions with orbital electrons and cause DNA strand breaks as well as chromosomal aberrations.

The *absorbed dose D* is defined by the ICRU as the mean energy $d\bar{\varepsilon}$ imparted by ionizing radiation to a mass d$m$ of matter [2]:

$$D = \frac{\mathrm{d}\bar{\varepsilon}}{\mathrm{d}m} \tag{2.13}$$

The SI derived unit of absorbed dose is the gray (Gy), where 1 Gy = 1 J kg$^{-1}$.

X and γ radiation may be measured in terms of *exposure X*. The ICRU defines it as the quotient of d$Q$ by d$m$, where d$Q$ represents the absolute sum of the electrical charges of ions of one sign released in air when all the electrons and positrons released by photons in air of mass d$m$ are fully stopped in air [3]:

$$X = \frac{dQ}{dm} \tag{2.14}$$

$X$ is in units of roentgens (R). The SI unit is C kg$^{-1}$, where 1 R = 2.58 × 10$^{-4}$ C kg$^{-1}$.

## 2.2. TYPES OF BRACHYTHERAPY

### 2.2.1. *Implantation techniques*

Brachytherapy can be classified by implantation technique. Figure 2.1 shows an example for each category: *intracavitary*, *interstitial*, *intraluminal*, and *superficial* [4].

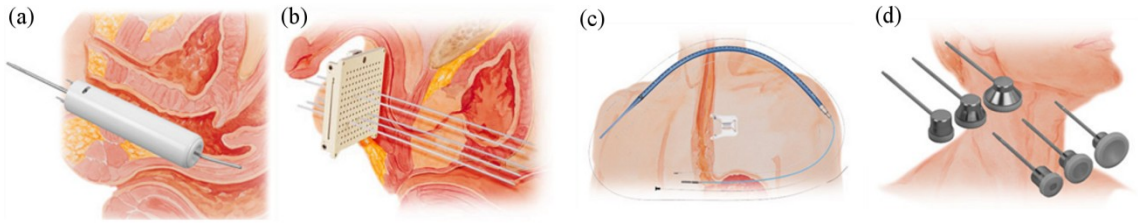


Figure 2.1. (a) Intracavitary brachytherapy with a vaginal applicator. (b) Interstitial brachytherapy with a prostate template and needles. (c) Intraluminal brachytherapy with an esophageal applicator. (d) Superficial brachytherapy with surface molds. (Nucletron BV, Veenendaal, the Netherlands.)

In intracavitary brachytherapy, radioactive sources are loaded into a body cavity through an applicator specific for the cancer site. It is widely used for treating gynaecological malignancies (e.g., cancers of the cervix, endometrium, and vagina), and less commonly, cancers of the nasopharynx and rectum. Interstitial brachytherapy involves the surgical placement of sources into the target volume. It is applicable for the treatments of head and neck, breast, and prostate cancers.

In intraluminal brachytherapy, sources are inserted into the lumen of an organ, which can be the bronchus, esophagus, bile duct, and blood vessels. Brachytherapy of the blood vessels is also described as *intravascular*. In superficial brachytherapy, a uniform dose, usually to a depth of a few millimetres, is delivered to the skin or mucosal surface. Molds and plaques containing radioactive sources are placed on top of the lesions.

A special technique known as *intraoperative brachytherapy* is performed during a surgical operation, immediately after the tumor has been resected in the operating room. A large radiation dose is delivered in one fraction to the exposed tumor bed while the surrounding normal tissue is displaced or shielded.

### 2.2.2. *Source loading techniques*

Brachytherapy can be delivered by *hot loading*, *manual afterloading*, or *remote afterloading* techniques. Hot loading refers to the manual placement of needles or an applicator, pre-loaded with radioactive sources, directly into the patient. To minimize the danger of radiation exposure to medical personnel, hot loading needs to be done precisely and efficiently. Safety concerns are reduced upon the introduction of afterloading technology, in which nonradioactive catheters are first inserted to the cancer site.

In manual afterloading, sources are loaded into pre-inserted catheters by hand with the aid of devices such as forceps, and are removed manually after the treatment. In remote afterloading, the loading and retraction of the source are controlled at a distance by a dedicated system. The source transfer between a dwell location and a shielded safe (where the source is stored) can be driven by a cable or by pneumatic pressure control. The patient is alone in a shielded vault while the radiation is being delivered.

### 2.2.3. *Implant durations*

The duration of the source implant can be either *temporary* or *permanent*. In a temporary treatment, the radioactive sources are removed after a prescribed dose has been delivered. In permanent brachytherapy, the implanted seeds remain inside the patient; the tumor cells are under continuous irradiation until the source strength has decreased to a negligible level.

### 2.2.4. *Dose rates*

The ICRU Report No. 38 (ICRU-38) [5] divides sources into three classes: *high dose rate* (HDR), *medium dose rate* (MDR), and *low dose rate* (LDR). An HDR treatment delivers over 12 Gy/h to a dose specification point. With an HDR $^{192}$Ir source whose dose rate can be up to 430 Gy/h [6], a treatment fraction lasts a few minutes. The MDR range is 2–12 Gy/h; it takes 1–5 h to deliver a fraction [7]. MDR brachytherapy is seldom used, as the biological effects do not compare favourably with other dose rates. The LDR range is 0.4–2 Gy/h; a temporary treatment at this classical LDR range takes 24–144 h [6]. Some interstitial sources (e.g. $^{103}$Pd and $^{125}$I seeds) are between 0.01 and 0.3 Gy/h [6]. This category is not defined in ICRU-38 and has been referred to as *ultra low dose rate* (ULDR), *very low dose rate*, or LDR (as opposed to classical LDR).

*Pulsed-dose-rate* (PDR) brachytherapy—or more correctly, *pulsed brachytherapy* [8, 9]—is a protracted form of HDR treatment. The tumor volume is irradiated by a series of short HDR pulses, lasting 10–30 min each, at hourly intervals over 1–2 days. This allows time for normal tissues to undergo repair during the course of treatment. The mechanism of dose delivery is the same as that for HDR remote afterloading, except the PDR source is shorter in length and one order of magnitude lower in activity.

## 2.3. BRACHYTHERAPY SOURCES

Brachytherapy sources are available in many shapes and sizes, and emit various types of radiation (see Figure 2.2). An ideal brachytherapy source should be of high specific activity so that it can be made small, and of low-to-intermediate energy to minimize shielding. It should be leakage-proof and not release $\alpha$ radiation. Although $\alpha$ particles have short ranges of 2–10 cm in air [10] and can easily be filtered, they are potentially lethal when ingested or inhaled. Once an implanted source ruptures, $\alpha$ particles ionize intensely and concentrate in the bones, causing serious health damage.

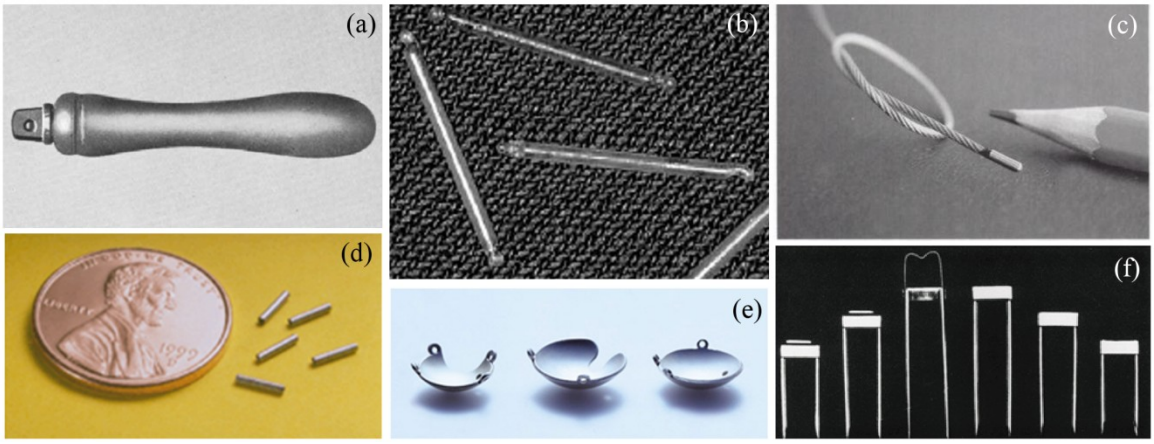


Figure 2.2. Brachytherapy sources. (a) An intracavitary applicator loaded with $^{226}$Ra [11]. (b) $^{222}$Rn in sealed glass capillary tubes [11]. (c) An HDR $^{192}$Ir source welded to a steel cable [12]. (d) $^{125}$I seeds [13]. (e) $^{106}$Ru eye plaques [13]. (e) Hairpins and an $^{192}$Ir wire on top of the third pin from the left [14].

### 2.3.1. *Photon-emitting sources*

Table 2.1 lists the physical properties of photon-emitting brachytherapy sources [6, 15]. $^{226}$Ra and $^{222}$Rn, now obsolete, are naturally occurring radionuclides. $^{103}$Pd can be produced by charged particle bombardment in a cyclotron, and $^{137}$Cs is a product of nuclear fission. The rest are created by bombarding neutrons with stable nuclides in a nuclear reactor. Among these radionuclides, $^{137}$Cs and $^{198}$Au are monoenergetic $\gamma$ emitters whereas the others emit polyenergetic photons.

The *half value layer* (HVL) is a measure of the beam quality. It represents the thickness of a given material that will attenuate the initial beam intensity by half. Sources with higher HVLs are more penetrating and thus require heavier shielding to reduce unintended exposure.

Radionuclides are divided into three energy categories based on the mean energy $\overline{E}$: *low* ($\overline{E} \leq 30$ keV), *intermediate* (30 keV < $\overline{E} \leq 300$ keV), and *high* ($\overline{E} > 300$ keV). Sources belonging to the same energy category have similar dosimetric characteristics in terms of attenuation and scatter in tissue, and therefore are used in similar applications. Nonetheless, each radionuclide has its individual properties and therapeutic effects.

Table 2.1. Physical characteristics of photon-emitting brachytherapy sources.

| Element | Radionuclide | Mean energy (MeV) | Half-life | Half value layer (mm lead) |
|---|---|---|---|---|
| Radium | $^{226}$Ra | 0.83 | 1600 yr | 12.0 |
| Radon | $^{222}$Rn | 0.83 | 3.83 d | 12.0 |
| Cobalt | $^{60}$Co | 1.25 | 5.26 yr | 11.0 |
| Cesium | $^{137}$Cs | 0.662 | 30.0 y | 5.5 |
| Gold | $^{198}$Au | 0.412 | 2.7 d | 2.5 |
| Iridium | $^{192}$Ir | 0.38 | 73.83 d | 2.5 |
| Ytterbium | $^{169}$Yb | 0.093 | 32 d | 0.48 |
| Americium | $^{241}$Am | 0.060 | 432 yr | 0.12 |
| Cesium | $^{131}$Cs | 0.030 | 9.69 d | 0.030 |
| Iodine | $^{125}$I | 0.028 | 59.4 d | 0.025 |
| Palladium | $^{103}$Pd | 0.021 | 17.0 d | 0.008 |

*i.* *Low-energy sources*

Low-energy sources are of shallow penetration in tissue and are used in interstitial brachytherapy to treat well-confined volumes. $^{125}$I has been extensively utilized for permanent prostate seed implants [16-18]. $^{103}$Pd, of high specific activity, is better at killing highly mitotic tumor cells because the sources are typically of higher dose rates compared with $^{125}$I [19, 20]. The $^{131}$Cs seeds recently marketed for prostate implants are higher in energy and can deliver a more uniform target dose [21]. A study based upon a linear quadratic model of cell survival indicated that a half-life in the range of 4–17 days produce more optimal biological effects [22]. Hence, $^{137}$Cs and $^{103}$Pd, with shorter half-lives of 9.69 and 17.0 days respectively, may offer better therapeutic outcome over $^{125}$I.

*ii.* *Intermediate-energy sources*

Intermediate-energy sources penetrate deeper in tissue and are suitable for slightly larger tumors. Given their short HVLs in lead, the dose to the surrounding critical organs can be easily attenuated by a small amount of high-*Z* material such as thin lead foils. $^{241}$Am sources are low in specific activity and therefore bulky, while $^{169}$Yb may be used for LDR interstitial implants or fabricated as miniaturized HDR sources. However, $^{169}$Yb has a short half-life; frequent source exchanges are a costly and inconvenient necessity.

*iii.* *High-energy sources*

$^{60}$Co has the highest mean energy among the brachytherapy sources in use today. $^{60}$Co can be fabricated as high-intensity sources similar in size to an HDR $^{192}$Ir source [23], and its half-life is 26 times longer than that of $^{192}$Ir. The cost of operating an HDR $^{60}$Co remote afterloading system is relatively low because it requires little maintenance and only one source exchange every ten years. However, the high-energy photons require heavy shielding, and $^{60}$Co is seldom used in more economically developed countries.

LDR $^{137}$Cs intracavitary cervical brachytherapy has been widely practiced over the years. Although the treatment is a clinical success, it is being phased out as the production of most $^{137}$Cs sources has been discontinued since 2002 [24]. $^{192}$Au seeds are used in permanent implants at the classical LDR regime, but its high energy causes radiation safety concerns. $^{192}$Ir is used in the forms of wires and ribbons for temporary LDR implants, and as a high-intensity miniaturized HDR source.

### 2.3.2. *Beta-emitting sources*

Table 2.2 lists the sealed $\beta$-emitting sources in common use [25]. $^{90}$Sr is in radioactive equilibrium with its daughter, $^{90}$Y, of 12 mm maximum range in tissue. $^{106}$Ru is highest in energy; its range in tissue is 18 mm. The short ranges of $\beta$-emitters make them appropriate for treating superficial lesions. For example, they are embedded in eye plaques for use in temporary treatment of intraocular melanoma. $^{32}$P is used in balloon angioplasty and intravascular brachytherapy.

Beta emitters are also used as unsealed sources for *targeted radionuclide therapy*, which uses a biologically targeted molecule specific for the treatment radionuclide to selectively deliver radiation dose to the tumor cells [26]. Although it is not a conventional form of radiotherapy, $^{131}$I has been successfully used for treating thyroid diseases, and $^{89}$Sr for relieving the pain of bone metastases [27]. On the other hand, $^{90}$Y-labeled microspheres are used to treat inoperable and metastatic liver tumors [28].

Table 2.2. Physical properties of sealed $\beta$-emitting brachytherapy sources.

| Element | Isotope | Maximum energy (MeV) | Half-life |
|---|---|---|---|
| Strontium | $^{90}$Sr | 0.54 | 29 yr |
| Yttrium | $^{90}$Y | 2.27 | 64 hr |
| Ruthenium | $^{106}$Ru | 3.54 | 368 d |
| Phosphorus | $^{32}$P | 1.71 | 14.3 d |

### 2.3.3. *Neutron-emitting sources*

$^{252}$Cf emits neutrons with an average energy of 2.1 MeV, as well as $\gamma$ rays. Low-intensity $^{252}$Cf sources had been used to treat cervical cancer patients in clinical trials [29]. In 1997, a high-activity source was developed for HDR neutron remote afterloading [30]. Despite the higher biological effectiveness of neutrons as well as promising patient outcome in the treatment of bulky and radioresistant tumors [29-31], neutron brachytherapy is rarely practiced outside of a few institutions.

### 2.3.4. *Miniature x-ray sources*

Radionuclide-free brachytherapy with a miniature kilovoltage x-ray tube was first introduced for clinical use in 1996 (Intrabeam photon radiosurgery system, Photoelectron Corporation; currently, Carl Zeiss Meditec, Jena, Germany). It is intended for single-fraction intraoperative radiosurgery of the brain and the breast [32-34]. In 2005, another x-ray tube model was launched (Axxent electronic brachytherapy system, Xoft Inc., Sunnyvale, CA). The accompanying applicator sets are used for fractionated breast and endometrial cancer treatments [35-39]. Both systems are shown in Figure 2.3 [35, 40-42]. Several research groups have invented other x-ray tube designs as well [32, 43-45].

The x-ray tubes emit photons of energies up to 50 keV. The depth dose characteristics are similar to those of low-energy sources [35]. The Axxent x-ray source can be programmed to stop at multiple dwell positions, similar to a stepping source remote afterloading unit. Since the dose rate is adjustable, the treatment can mimic contemporary LDR or HDR delivery. With current technology, the maximum dose rate is about that of a 7-Ci HDR $^{192}$Ir source [46].

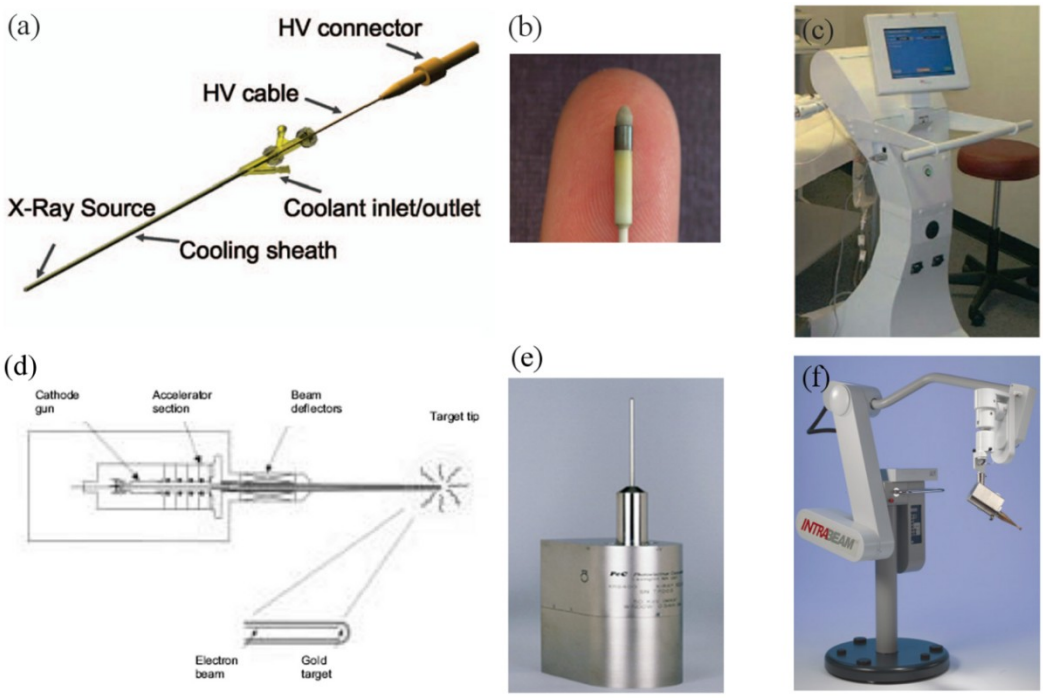


Figure 2.3. Electronic brachytherapy systems. The top panels show the Axxent system [35] and the bottom panels show the Intrabeam system [40-42]. The drawings and photographs of the x-ray tubes, and dose delivery units are shown from left to right.

It has been suggested that intensity-modulated electronic brachytherapy could one day be useful for the treatment of irregularly shaped tumors [47]. This will be achieved by optimizing the beam energies, source positions and dose rates, and using collimators to shield critical structures. There are still technical, dosimetric, and computational challenges to overcome before it can be realized clinically.

## 2.4. RADIATION QUALITY AND DOSE RATE EFFECTS

### 2.4.1. *Linear energy transfer*

In radiobiology, the effect of any given radiation quality can be described by the *linear energy transfer* (LET). It refers to the average energy imparted to the medium by a secondary charged particle per unit length of its track. The radiation quality is classified

as *low-LET* for all high-energy photon-emitting brachytherapy sources as well as kilovoltage x-rays above 50 kV [48]. For such radiation, the ionization density along the secondary electron tracks is relatively sparse. The LET increases with decreasing photon energy. Also, neutrons and heavy charged particles are of high LET. The higher the LET, the greater is the amount of cell kills per energy deposited.

### 2.4.2. *Oxygen enhancement ratio*

Oxygen increases the sensitivity of cells to ionizing radiation. The *oxygen enhancement ratio* (OER) is defined as the ratio of the dose delivered in hypoxia (i.e., deprived of oxygen) to the dose delivered in air to produce the same biological effect. The OER under HDR irradiation is approximately 3 for most cells, whereas it is 2 under LDR irradiation [49]. The OER is also lower when the absorbed dose is 3 Gy or less [50]. The lower the OER, the more effective it will be to kill hypoxic cells, which are more resistant to radiation damage.

### 2.4.3. *Relative biological effectiveness*

The *relative biological effectiveness* (RBE) for a given type of radiation is defined as the relative dose that gives the same biological effect as that induced by a reference radiation. This dimensionless quantity is also dependent on factors such as the dose, dose rate, fractionation schedule, and the kinetics of the tumor growth. The RBE increases with increasing LET up to a maximum value in the 3–8 range. Ling et al. [20] reported that, using $^{60}$Co as the reference radiation, the RBE is about 1.4 for $^{125}$I at a dose rate of 7 cGy/h, and about 1.9 for $^{103}$Pd at 7–14 cGy/h. Reniers et al. [51] calculated an RBE value of 1.4–1.5 relative to $^{60}$Co for the Axxent kilovoltage x-ray source. For high-energy photon emitters such as $^{137}$Cs and $^{192}$Ir, the RBE relative to $^{60}$Co can be regarded as unity.

### 2.4.4. *Typical dose rates of brachytherapy sources*

Biological effects tend to be dose-rate dependent when the dose rates are between 10 and 100 cGy/h [52]. The typical initial dose rates of $^{125}$I and $^{103}$Pd seeds for ULDR implants are 5–10 and 15–20 cGy/h, respectively [52]. LDR brachytherapy of $^{137}$Cs and $^{192}$Ir is delivered at 50–80 cGy/h, while HDR $^{192}$Ir and $^{60}$Co sources are in the 100–500 cGy/min range [52]. Brenner and Hall [53] found that PDR brachytherapy administered at intervals of 0.5–2.0 h yields biological effects similar to an LDR treatment.

The RBE generally increases with decreasing energy as well as decreasing dose rate. However, LDR treatments with initial dose rates that are too low may not be able to eradicate more highly proliferative tumors [54]. The therapeutic gain is optimal when the RBE for the tumor cells is high while the RBE for the surrounding tissue is kept low. Normal tissue complications may be more likely to arise for HDR brachytherapy because the treatment is usually delivered in a few minutes and there is insufficient time for the normal tissue to undergo repair. On the other hand, shorter treatment duration allows less time for the tumor cells to repopulate. It is therefore important to use a proper fractionation schedule and limit the critical organ dose for HDR brachytherapy.

## 2.5. HISTORICAL REVIEW OF BRACHYTHERAPY

Brachytherapy was first suggested by Pierre Curie in 1901 after several landmark discoveries in radiation physics, including x rays by Röntgen in 1895, radioactivity by Becquerel in 1896, and radium by the Curies in 1898. Ionizing radiation had been used with proven success in diagnostic radiology and x-ray therapy prior to the advent of brachytherapy. The early history of brachytherapy is well documented in the radiation physics and oncology literature [11, 55-60].

### 2.5.1. *Brachytherapy with $^{226}Ra$ and $^{222}Rn$*

During the first half of the 20th century, $^{226}$Ra and $^{222}$Rn were used exclusively in brachytherapy because artificial radionuclides were not yet available for clinical use. $^{226}$Ra was successfully applied for skin and gynaecological cancer therapy in 1903. Tubes, surface molds, and metal applicators containing $^{226}$Ra were placed on the skin or inserted into body cavities such as the vagina and the nasopharynx. Temporary interstitial implants with $^{226}$Ra needles were administered for prostate and head and neck cancers. Some large tumors were treated in combination with x-ray therapy [61]. LDR radiation was delivered over a set number of hours or days, sometimes spreading over several fractions. By the late 1910s, various body sites had been treated with established techniques [62, 63].

$^{222}$Rn, a gaseous daughter product of $^{226}$Ra, was known as *radium emanation* at the time. Radon seeds were produced by sealing $^{222}$Rn in thin capillary tubes made of gold or glass. Because of its short half-life of 3.83 days, radon seeds were suitable for both temporary and permanent interstitial brachytherapy [64].

$^{226}$Ra emits a complex spectrum of $\gamma$-rays, as well as $\beta$-particles of energies up to 3.26 MeV and $\alpha$-emitting radon gas. Because of its low specific activity ($3.656\times10^{10}$ Bq $g^{-1}$) and the heavy filtration needed to stop the unwanted $\beta$-particles, $^{226}$Ra sources were bulky and thus difficult to implant at times. The high cost of $^{226}$Ra extraction from uranium ore, radiation exposure to medical staff, potential hazards in the event of radon gas leakage, and stringent shielding requirements were among the reasons that diminished the use of brachytherapy in the 1950s and 1960s. In the same period, the popularity of external beam radiotherapy with megavoltage x rays and $^{60}$Co was on the rise.

### 2.5.2. *Radium substitutes and newer sources*

Advances in radionuclide production, remote afterloading techniques, quantitative dosimetry, and imaging technology contributed to major progress in brachytherapy from the 1950s to the present [24]. With the discovery of artificial radioactivity [65], a series of synthetic radionuclides have been created by bombarding particles with stable nuclides [66]. Among them are *radium substitutes* with mean photon energies above 300 keV: $^{60}$Co, $^{137}$Cs, $^{198}$Au, $^{182}$Ta, and $^{192}$Ir. The dosimetry of radium substitutes in tissue media is comparable to that of $^{226}$Ra, as the dose around a point source in water decreases approximately with the square of the distance. The maximum deviation from the inverse square law is 5% at distances up to 5 cm from the point source [6].

Many of the photon-emitting sources introduced after 1960 are either higher in intensity or lower in energy, hence not radium-equivalent [67]. For example, $^{192}$Ir fabricated with a high specific activity of $1.665\times10^{13}$ Bq g$^{-1}$ can be used for HDR brachytherapy. $^{125}$I and $^{103}$Pd are low-energy sources and less penetrating in tissue, allowing patients to be treated without prolonged isolation for radiation safety reasons.

The radium substitutes and the newer sources are preferable to $^{226}$Ra and $^{222}$Rn because of the lower production cost, absence of harmful $\alpha$ radiation, and better physical properties in terms of half-life, source energy and specific activity. However, the predominance of photoelectric effect at low energies makes the dose more strongly influenced by the source makeup and tissue inhomogeneities, complicating the dosimetry.

### 2.5.3. *Source loading technology*

The harmful effects of ionizing radiation, notably radiation dermatitis, were recognized soon after the discovery of x rays [68, 69]. An association between radiation

exposure and skin cancer had been established by 1902 [70]. Despite a relatively small level of risk to the brachytherapists, there were some anecdotal reports of finger injury due to routine hot loading of $^{226}$Ra sources over the years. The advancement in afterloading technology was primarily motivated by the desire to decrease occupational exposure, which was a matter of serious concern for health care professionals [71].

Strebel suggested the first manual afterloading method for interstitial brachytherapy of deep-seated tumors in 1903 [72]. Afterloading techniques became more widely used after artificial radionuclides were introduced [57]. LDR and MDR remote afterloaders with multiple $^{226}$Ra or $^{137}$Cs sources were built since the 1960s [73], pioneered by Walstam [74] and Henschke et al. [71, 75, 76]. In 1965, O'Connell et al. [77] designed an HDR remote afterloader containing up to nine $^{60}$Co sources (Cathetron, T. E. M. Instruments, Crawley, England). Typical $^{60}$Co source activities are 100–200 GBq [78], and fractionated treatment can be delivered in minutes on an outpatient basis [77]. HDR remote afterloading technology with a single $^{192}$Ir source of 370-GBq nominal activity phased in soon after its introduction by Gauwerky in 1977 [79]. It is the most common mode of HDR dose delivery at present.

### 2.5.4. *Classical dosimetry systems*

The early practice of brachytherapy was guided by clinical experience. Empirical studies of dose-response relationships laid the basis for various dosimetry systems. Such systems, consisting of well defined rules for source implantations and fractionation schedules, facilitate better adequacy and reproducibility of the dose delivery.

The *Paterson-Parker (Manchester)* [80-82] and the *Quimby* [83, 84] systems are classical dosimetry systems developed in the 1930s for $^{226}$Ra interstitial implants. In the

Paterson-Parker system, the source strength is concentrated around the target periphery so that a uniform dose within ±10% in a plane or volume can be achieved. This is in contrast to the Quimby system, in which the source strength is distributed uniformly within the target and hence the target center receives a higher dose. There are other source-specific implantation rules for radium substitutes. For instance, the Paris system [85] is used for implants with flexible $^{192}$Ir wires. In intracavitary cervical brachytherapy, Paris [86], Stockholm [87, 88], and Manchester [89, 90] systems have long-standing records of use.

### 2.5.5. *Classical treatment planning*

Before treatment planning became increasingly computerized in the 1960s [91-95], doses at specific points were calculated manually using dose rate tables and graphs derived from exposure rate distributions. The attenuation and scatter of photons in tissue as well as applicator and shielding effects were ignored. Source positions were localized using orthogonal or stereo radiographs. The dose for permanent implants was calculated by adding up dose contributions from all seeds, assuming each to be a point source. This is of reasonable accuracy as long as a large number of seeds oriented in random directions are used. The filtration effects of line sources, i.e., the lower regional dose due to self-attenuation of photons traveling along the radioactive core, were accounted for using the *Sievert integral* [96]. In this approach, the source was first partitioned into small segments. Corrections for source filtration and inverse square dependence were then made individually for each segment. Paterson-Parker tables, for example, were compiled using the numerical results of the Sievert integral to assist in hand calculations.

Historically, the total *milligram-hours* (mg-hrs) concept was used for dose prescription in intracavitary brachytherapy. The dosage was represented by the product of

the total source strength (in mg of radium) and the treatment duration (in hours). For radium substitutes, the source strength was quantified by the *milligram-radium-equivalent* (mgRaEq). It corresponds to the mass of radium, encapsulated by 0.5-mm thick platinum, which produces the same exposure rate at 1 m on the source transverse axis as the given source. For instance, 1 mgRaEq of a radium substitute yields an exposure rate of 0.825 $mR \cdot h^{-1}$ at 1 m. Dose tables for $^{226}Ra$ sources, relating the dose to mg-hrs, could thus be used directly for treatment planning with radium substitutes.

The Manchester system developed in 1938 [90] was the first dosimetry system that used a point-based dose prescription scheme rather than the mg-hrs for cervical brachytherapy [19]. This system evaluates dose values at four points: A, B, bladder, and rectum. The implant duration is determined by the dose to Point A, located at 2 cm superior to the lateral vaginal fornix and 2 cm lateral to the cervical canal. Although the dose to Point A and mg-hrs did not show appreciable correlations [97], both systems have been used for decades with successful curative outcome.

## 2.6. HDR IRIDIUM-192 BRACHYTHERAPY

Although the RBE of HDR brachytherapy is generally inferior to LDR implants, this technique offers some advantages. For instance, the use of a remote afterloading system reduces exposure to medical staff. There is also a higher degree of freedom in treatment planning; both the dwell positions and dwell times can be optimized to improve the therapeutic gain. Besides, the minimal movement of the applicator or the surrounding tissue during the few-minute treatment session reduces dose errors caused by geometrical shifts. As well, it is an outpatient procedure and requires little nursing care.

### 2.6.1. *Remote afterloading system*

Figure 2.4 shows the HDR $^{192}$Ir remote afterloaders in common use today: the 18-channel microSelectron v2 model (Nucletron, Veenendaal, the Netherlands), the 20-channel VariSource model (Varian Medical Systems, Palo Alto, CA), and the 24-channel GammaMed 12I model (Varian) [8]. An encapsulated $^{192}$Ir source, of approximately 1 mm in diameter and 4 mm in length, is attached to one end of a cable and housed inside a shielded safe. The nominal source activity is 370 GBq. Source exchanges are done quarterly to keep the dose delivery session well within half an hour.

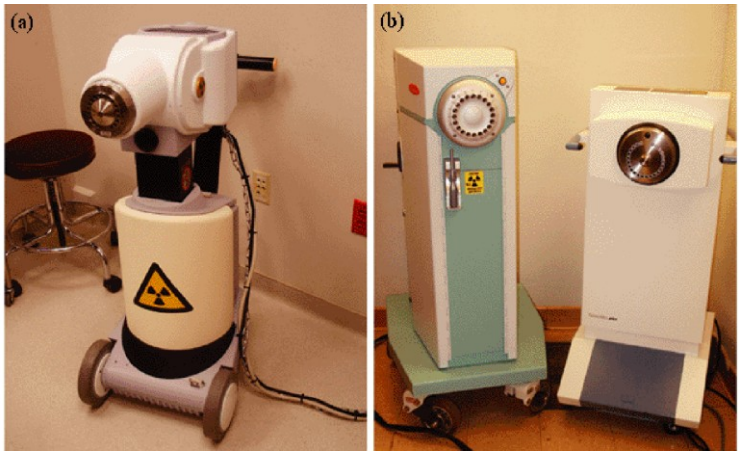


Figure 2.4. HDR $^{192}$Ir remote afterloaders [8]. (a) The Nucletron microSelectron v2 model. (b) The Varian VariSource (left) and GammaMed (right) models.

The afterloader is controlled by a computerized treatment control panel. Transfer tubes are connected between the implanted catheters and the afterloader. There is a check cable run prior to each dose delivery to ensure all transfer tube and catheter connections are secure and there is no obstruction during source transit. The source travels in incremental steps through the catheters one by one, stopping at each pre-programmed dwell position for a specific duration of time. During the treatment, the patient is alone in a shielded room and is monitored through an intercom system.

### 2.6.2. *Afterloading catheters, applicators and shielding*

#### *i.* *Interstitial brachytherapy*

Figure 2.5 shows the instruments used for HDR interstitial brachytherapy [98]. The flexible nylon catheters are of variable sizes (minimum circumference 4–6 mm, depending on the source model). They are threaded through the tumor volume with the aid of a metal trocar. Buttons are used to secure the catheters in place. A ruler and a crimper may be used during the insertion procedure. Radiopaque dummy sources with known spacing patterns help to identify the catheters on x-ray images.

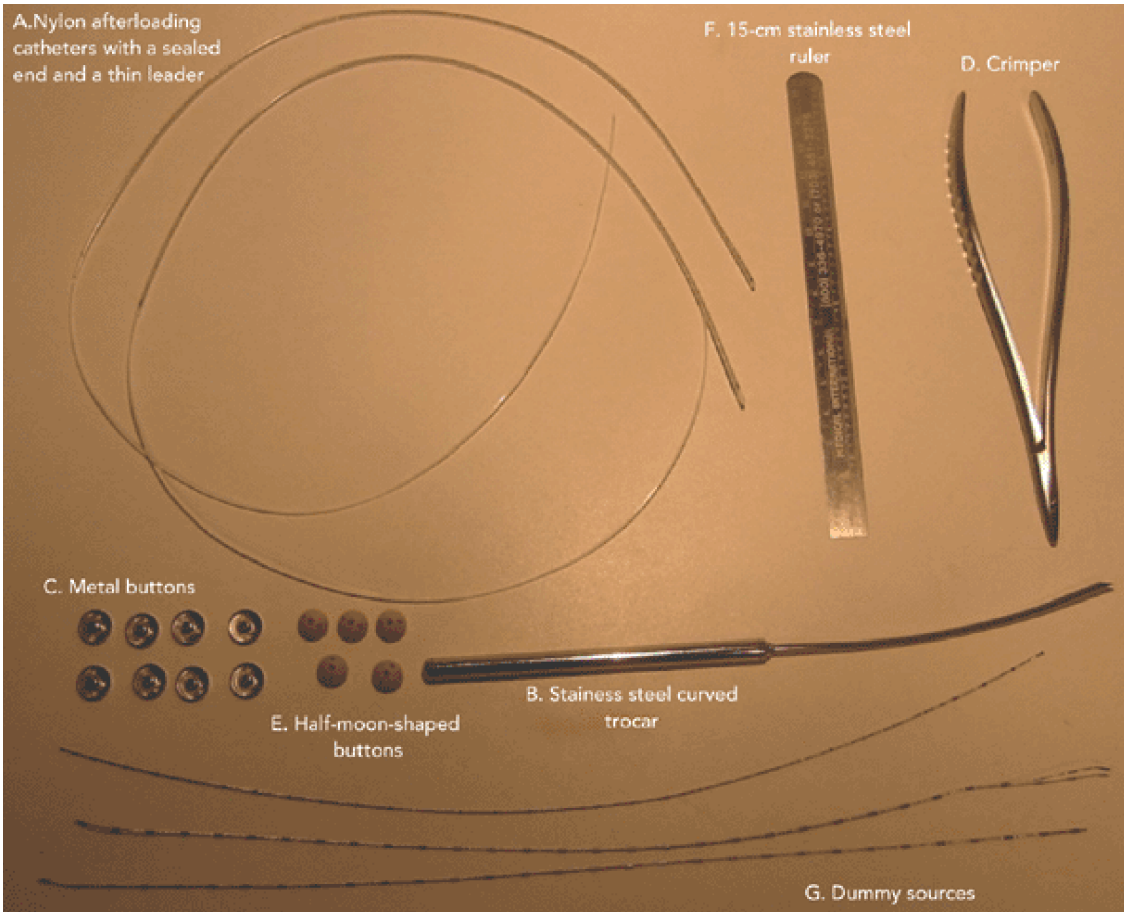


Figure 2.5. Instruments for interstitial HDR brachytherapy with flexible catheters [98].

*ii.* *Intracavitary brachytherapy*

HDR intracavitary brachytherapy applicators are designed for specific body sites. Stainless steel is a common applicator material because it can be sterilized and reused numerous times. The metallic components of applicators may cause artefacts on CT images and may be unusable for magnetic resonance imaging (MRI). Although plastic CT/MR-compatible applicators have been developed for these imaging modalities, they are less sturdy and cause more discomfort in patients because of the larger sizes.

Brachytherapy applicators are designed to optimize ease of use while enhancing dose conformity and reducing normal tissue damage. Some applicators provide room for shielding insertion, and some are liquid-inflatable. In the latter case, adjacent normal tissue can be pushed away from the source. Radiographic contrast solution is sometimes injected into the applicator to improve visualization on CT images. Figure 2.6 shows the tandem and ovoid applicator sets used for cervical brachytherapy, and the single-channel MammoSite applicators with balloons inflated with contrast solution for accelerated partial breast irradiation [99, 100].

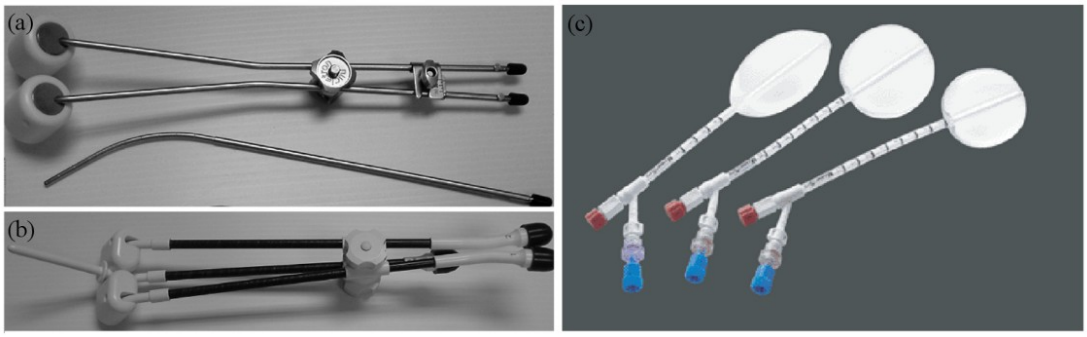


Figure 2.6. HDR intracavitary applicators. (a) Stainless steel tandem and ovoid applicator set [99]. (b) CT/MR-compatible tandem and ovoids [99]. (c) MammoSite balloon applicators [100].

### 2.6.3. *Catheter localization and imaging modalities for treatment planning*

In HDR brachytherapy, the source dwell positions are defined according to the locations of the catheters based on two-dimensional (2D) projection images or three-dimensional (3D) tomographic images. The major imaging modalities used for catheter localization and treatment planning include x-ray radiography, CT, cone-beam CT, and MRI. Dummy catheters, radiopaque markers and/or contrast solution may be used to improve their visibility. The catheter insertion process can be guided by radiography, fluoroscopy, or ultrasonography.

*i.* *Conventional radiographs*

Brachytherapy catheters can be reconstructed in 3D by manually matching radiographic films taken from two or more perspectives. This has been done routinely for treatment planning. It is sometimes challenging to locate common landmarks from images of different views because the catheters may be obscured by bones or contrast solution, or appear to overlap one another. Chang et al. [101] proposed a dual-energy technique which involves processing two image sets acquired with different x-ray energies to improve catheter localization.

*ii.* *CT*

CT is being increasingly used for treatment planning, as it allows for 3D dose-volume analysis and anatomy-based dose optimization. The catheters can be defined on a slice by slice basis, either manually or using auto-reconstruction techniques [102]. However, CT images do not show enough contrast for the tumor to be distinguishable from its surrounding tissue. Although it is adequate for organ at risk (OAR) delineations, target contouring based on CT images alone is not recommended [103].

In Monte Carlo (MC) dose calculations, CT Hounsfield Units (HU) are used to derive tissue material and density data. The HU for a given material is defined as:

$$\mathrm{HU} = 1000\,\frac{\mu - \mu_{\mathrm{wat}}}{\mu_{\mathrm{wat}}} \qquad (2.15)$$

The linear attenuation coefficients of the material and water are denoted by $\mu$ and $\mu_{\mathrm{wat}}$, respectively. The correspondence between HU values and mass (or electron) densities may be inferred by scanning a tissue characterization phantom containing inserts of tissue-equivalent media with known densities. The HU for water is 0, and it is around -1000 for air. Typical HU ranges are as follows: -600 < HU < -400 for lung, -100 < HU < -60 for adipose, 40 < HU < 80 for soft tissue, and 400 < HU < 3000 for bones [104].

HU values are dependent on the x-ray spectrum of the CT scanner. Kendall et al. [105] found that HU-to-density conversion errors caused by the neglect of tube potential variations have a minor impact on the dose for megavoltage photon beams. Incorrect tissue material assignments may cause errors in MC dose calculations, especially at energies where photoelectric effect or pair production is important [106, 107]. Such errors can be considerable for low-energy brachytherapy sources. Techniques have been developed to make tissue segmentation more accurate using dual-energy CT [108, 109].

Streaking artefacts around metallic objects (e.g. stainless steel applicators, shielding, and hip prostheses) may require corrections so as to reduce errors in organ delineations and MC dose calculations [110]. CT-compatible applicators made of plastic or aluminum instead of stainless steel may be used to avoid such artefacts [111]. Price et al. [112] recently designed a prototype cervical intracavitary applicator with shielding and CT/MR compatibilities. They also devised a novel step-and-shoot shield translation image acquisition method to eliminate metal streaking artefacts on CT images.

*iii.* *Cone-beam CT*

On-board cone-beam CT imaging systems [113] allow patients to be scanned in the same positions as they are treated, and come with capabilities for fluoroscopic and radiographic imaging. However, the scattered radiation reaching the flat-panel x-ray detector introduces noise in the reconstructed images, causing cupping artefacts as well as poorer image quality for low-contrast objects compared with CT images [114]. This compromises the accuracy of OAR delineations and MC dose calculations. Nonetheless, cone-beam CT provides excellent spatial resolution, also in the direction parallel to the scanner rotation axis, in contrast to fan beam CT. Besides, on-board imaging minimizes geometrical shifts of organs between the time of image acquisition and the time of treatment. It is an invaluable tool for image guidance in brachytherapy.

*iv.* *MRI*

MRI gives excellent tissue contrast, making it easy to identify tumor volumes in 3D. Optimized cervical brachytherapy treatment has been investigated using the guidance of MRI [115, 116]. However, the dummy catheters used for catheter localization with radiographs or CT images are not usable for MRI. The images also suffer from poor resolution and geometric distortions to some extent. Complementary data from CT images are therefore recommended when MRI is used for treatment planning [117].

### 2.6.4. *Treatment planning optimization*

The goal of optimization in HDR brachytherapy is to seek the optimal combination of dwell positions and dwell times that best fulfills the treatment objectives. This can be solved mathematically as a cost function minimization problem. The cost function is a measure of the quality of the dose distribution in reference to the objectives

specified by the physician. Multiple objectives can be formulated as a single cost function with each objective assigned a relative importance factor (or weight). There are also alternative algorithms that do not require the use of importance factors [118].

Optimization theory is a well-studied discipline in mathematics, control engineering, and radiotherapy. Algorithms that have been applied for HDR brachytherapy treatment planning include the least squares technique used in dose point optimization [119], geometric optimization [120], simulated annealing [121], and various deterministic methods (e.g., gradient-based, simplex, and linear programming [122-124]).

All modern HDR brachytherapy planning systems use the AAPM TG-43 dose calculation formalism [125]. TG-43 takes into account the effects of source filtration as well as the attenuation and scatter of photons in water, but neglects tissue and applicator inhomogeneities. Its high calculation efficiency is desirable since the optimization typically requires dose values at many points for every dwell position.

Dose-point optimization and geometric optimization are basic methods commonly available in HDR brachytherapy planning systems. Inverse planning simulated annealing (IPSA) is also gaining clinical acceptance and popularity in recent years [121].

*i.* *Dose-point optimization*

In dose point optimization, the prescribed dose or dose constraints are set to user-specified dose points. On radiographs, dose points are usually defined relative to the applicator according to well-defined rules. On CT or MR images, dose points may be defined along the periphery of the target to ensure its volume will receive at least the prescribed dose. Dose constraint points may also be set to limit the dose to OAR. To find the optimal combination of dwell times, the sum of the squares of the differences between the intended and the calculated dose values for all dose points needs to be minimized.

*ii.* *Geometric optimization*

In geometric optimization, the dwell time $t_i$ at a given position $i$ is given by [126]:

$$t_i = \left( \sum_{j=1, j \neq i}^{n} \frac{1}{d_{ij}^{\,2}} \right)^{-1} \tag{2.16}$$

where $n$ is the number of dwell positions and $d_{ij}$ is the distance to every other dwell position $j$. The relative dwell times for dwell positions near the periphery of the implant are usually the longest. This method improves the dose homogeneity within the target volume, especially when the dwell positions are distributed uniformly.

*iii.* *Anatomy-based inverse planning*

IPSA is an anatomy-based inverse planning method developed by Pouliot et al. [121]. The algorithm uses the simulated annealing approach to determine the optimal dwell times for all possible dwell positions that best satisfy the user-imposed dose constraints. Such constraints include the upper and lower dose limits as well as penalty factors for every target and critical structure. The cost function increases linearly in accordance with the penalty factor once a dose limit is exceeded.

## 2.7. REFERENCES


1. Podgoršak EB. Basic radiation physics. In: Podgoršak EB, editor. Radiation oncology physics : a handbook for teachers and students. Vienna: International Atomic Energy Agency; 2005. p. 1-43.

2. International Commission on Radiation Units and Measurements. Fundamental quantities and units for ionizing radiation. Bethesda, MD: ICRU; 1998.

3. International Commission on Radiation Units and Measurements. Radiation quantities and units. Washington, DC: ICRU; 1980.

4. Nucletron [homepage on the Internet]. Veenendaal, the Netherlands: Nucletron BV; 2005 [cited 2005 Oct 24]; Available from: http://www.nucletron.com/.

5. International Commission on Radiation Units and Measurements. Dose and volume specification for reporting intracavitary therapy in gynecology. Bethesda, MD: ICRU; 1985.

6. Williamson JF, Brenner DJ. Physics and biology of brachytherapy. In: Halperin EC, Perez CA, Brady LW, editors. Perez and Brady's principles and practice of radiation oncology. 5th ed. Philadelphia: Wolters Kluwer Health/Lippincott Williams & Wilkins; 2008. p. 423-75.

7. Dale RG, Deehan C. Brachytherapy. In: Dale RG, Jones B, editors. Radiobiological modelling in radiation oncology. London: British Institute of Radiology; 2007. p. 113-37.

8. Thomadsen B, Das R. The physics and dosimetry of high-dose-rate brachytherapy. In: Halperin EC, Perez CA, Brady LW, editors. Perez and Brady's principles and practice of radiation oncology. 5th ed. Philadelphia: Wolters Kluwer Health/Lippincott Williams & Wilkins; 2008. p. 540-59.

9. Dale RG. Radiobiology of brachytherapy. In: Mayles P, Nahum AE, Rosenwald J-C, editors. Handbook of radiotherapy physics: theory and practice. New York: Taylor & Francis; 2007. p. 1181-91.

10. Johns HE, Cunningham JR. The fundamentals of nuclear physics. The physics of radiology. 4th ed. Springfield, IL: Charles C. Thomas; 1983. p. 71-101.

11. Aronowitz JN. Buried emanation: the development of seeds for permanent implantation. Brachytherapy. 2002;1:167-78.

12. Baltas D, Sakelliou L, Zamboglou N. Production and construction of sealed sources. The physics of modern brachytherapy for oncology. Boca Raton: Taylor & Francis; 2007. p. 185-204.

13. BEBIG [homepage on the Internet]. Berlin, Germany: Eckert & Ziegler BEBIG GmbH; 2005 [cited 2005 Oct 24]; Available from: http://www.bebig.de/en/.

14. Montemaggi P, Guerrieri P, Federico M, Mortellaro G. Clinical applications of brachytherapy: low-dose-rate and pulse-dose-rate. In: Halperin EC, Perez CA, Brady LW, editors. Perez and Brady's principles and practice of radiation oncology. 5th ed. ed. Philadelphia: Wolters Kluwer Health/Lippincott Williams & Wilkins; 2008. p. 476-539.

15. Khan FM. Brachytherapy. The physics of radiation therapy. 3rd ed. Philadelphia; London: Lippincott Williams & Wilkins; 2003. p. 357-400.

16. Ragde H, Blasko JC, Grimm PD, Kenny GM, Sylvester JE, Hoak DC, et al. Interstitial iodine-125 radiation without adjuvant therapy in the treatment of clinically localized prostate carcinoma. Cancer. 1997;80:442-53.

17. Stock RG, Stone NN, Tabert A, Iannuzzi C, DeWyngaert JK. A dose-response study for I-125 prostate implants. Int J Radiat Oncol Biol Phys. 1998;41:101-8.

18. Zelefsky MJ, Kuban DA, Levy LB, Potters L, Beyer DC, Blasko JC, et al. Multi-institutional analysis of long-term outcome for stages T1-T2 prostate cancer treated with permanent seed implantation. Int J Radiat Oncol Biol Phys. 2007;67:327-33.

19. Perez CA, Purdy JA, Li Z, Hall EJ. Biologic and physical aspects of radiation oncology. In: Hoskins WJ, Perez CA, Young RC, Barakat RR, Markman M, Randall ME, editors. Principles and practice of gynecologic oncology. 4th ed. Philadelphia: Lippincott Williams & Wilkins; 2005. p. 375-459.

20. Ling CC. Permanent implants using Au-198, Pd-103 and I-125: radiobiological considerations based on the linear quadratic model. Int J Radiat Oncol Biol Phys. 1992;23:81-7.

21. Murphy MK, Piper RK, Greenwood LR, Mitch MG, Lamperti PJ, Seltzer SM, et al. Evaluation of the new cesium-131 seed for use in low-energy x-ray brachytherapy. Med Phys. 2004;31:1529-38.

22. Armpilia CI, Dale RG, Coles IP, Jones B, Antipas V. The determination of radiobiologically optimized half-lives for radionuclides used in permanent brachytherapy implants. Int J Radiat Oncol Biol Phys. 2003;55:378-85.

23. Granero D, Perez-Calatayud J, Ballester F. Technical note: Dosimetric study of a new Co-60 source used in brachytherapy. Med Phys. 2007;34:3485-8.

24. Williamson JF. Brachytherapy technology and physics practice since 1950: a half-century of progress. Phys Med Biol. 2006;51:R303-25.

25. Jones CH. Calibration and quality assurance of brachytherapy sources. In: Mayles P, Nahum AE, Rosenwald J-C, editors. Handbook of radiotherapy physics: theory and practice. New York: Taylor & Francis; 2007. p. 1101-15.

26. Mayles P, Rosenwald J-C. Therapy with unsealed sources. In: Mayles P, Nahum AE, Rosenwald J-C, editors. Handbook of radiotherapy physics: theory and practice. New York: Taylor & Francis; 2007. p. 1203.

27. Gaze MN. The current status of targeted radiotherapy in clinical practice. Phys Med Biol. 1996;41:1895-903.

28. Campbell JM, Wong CO, Muzik O, Marples B, Joiner M, Burmeister J. Early dose response to yttrium-90 microsphere treatment of metastatic liver cancer by a patient-specific method using single photon emission computed tomography and positron emission tomography. Int J Radiat Oncol Biol Phys. 2009;74:313-20.

29. Maruyama Y, van Nagell JR, Yoneda J, Donaldson ES, Gallion HH, Powell D, et al. A review of californium-252 neutron brachytherapy for cervical cancer. Cancer. 1991;68:1189-97.

30. Martin RC, Laxson RR, Miller JH, Wierzbicki JG, Rivard MJ, Marsh DL. Development of high-activity $^{252}$Cf sources for neutron brachytherapy. Appl Radiat Isot. 1997;48:1567-70.

31. Burmeister J, Kota C, Maughan RL. Measured microdosimetric spectra and therapeutic potential of boron neutron capture enhancement of $^{252}$Cf brachytherapy. Radiat Res. 2005;164:312-8.

32. Beatty J, Biggs PJ, Gall K, Okunieff P, Pardo FS, Harte KJ, et al. A new miniature x-ray device for interstitial radiosurgery: dosimetry. Med Phys. 1996;23:53-62.

33. Vaidya JS, Baum M, Tobias JS, D'Souza DP, Naidu SV, Morgan S, et al. Targeted intra-operative radiotherapy (Targit): an innovative method of treatment for early breast cancer. Ann Oncol. 2001;12:1075-80.

34. Douglas RM, Beatty J, Gall K, Valenzuela RF, Biggs P, Okunieff P, et al. Dosimetric results from a feasibility study of a novel radiosurgical source for irradiation of intracranial metastases. Int J Radiat Oncol Biol Phys. 1996;36:443-50.

35. Rivard MJ, Davis SD, DeWerd LA, Rusch TW, Axelrod S. Calculated and measured brachytherapy dosimetry parameters in water for the Xoft Axxent X-Ray Source: an electronic brachytherapy source. Med Phys. 2006;33:4020-32.

36. Dickler A, Kirk MC, Seif N, Griem K, Dowlatshahi K, Francescatti D, et al. A dosimetric comparison of MammoSite high-dose-rate brachytherapy and Xoft Axxent electronic brachytherapy. Brachytherapy. 2007;6:164-8.

37. Dickler A, Kirk MC, Coon A, Bernard D, Zusag T, Rotmensch J, et al. A dosimetric comparison of Xoft Axxent Electronic Brachytherapy and iridium-192 high-dose-rate brachytherapy in the treatment of endometrial cancer. Brachytherapy. 2008;7:351-4.

38. Dickler A. Xoft Axxent electronic brachytherapy: a new device for delivering brachytherapy to the breast. Nat Clin Pract Oncol. 2009;6:138-42.

39. Dickler A, Ivanov O, Francescatti D. Intraoperative radiation therapy in the treatment of early-stage breast cancer utilizing xoft axxent electronic brachytherapy. World J Surg Oncol. 2009;7:24.

40. Vaidya JS, Baum M, Tobias JS, Morgan S, D'Souza D. The novel technique of delivering targeted intraoperative radiotherapy (Targit) for early breast cancer. Eur J Surg Oncol. 2002;28:447-54.

41. Tobias JS, Vaidya JS, Keshtgar M, D'Souza DP, Baum M. Reducing radiotherapy dose in early breast cancer: the concept of conformal intraoperative brachytherapy. Br J Radiol. 2004;77:279-84.

42. Kraus-Tiefenbacher U, Steil V, Bauer L, Melchert F, Wenz F. A novel mobile device for intraoperative radiotherapy (IORT). Onkologie. 2003;26:596-8.

43. Gutman G, Sozontov E, Strumban E, Yin FF, Lee SW, Kim JH. A novel needle-based miniature x-ray generating system. Phys Med Biol. 2004;49:4677-88.

44. Gutman G, Strumban E, Sozontov E, Jenrow K. X-ray scalpel - a new device for targeted x-ray brachytherapy and stereotactic radiosurgery. Phys Med Biol. 2007;52:1757-70.

45. Dinsmore M, Harte KJ, Sliski AP, Smith DO, Nomikos PM, Dalterio MJ, et al. A new miniature x-ray source for interstitial radiosurgery: device description. Med Phys. 1996;23:45-52.

46. Holt RW, Thomadsen BR, Orton CG. Point/Counterpoint. Miniature x-ray tubes will ultimately displace Ir-192 as the radiation sources of choice for high dose rate brachytherapy. Med Phys. 2008;35:815-7.

47. Sternick EB, Todor DA, Orton CG. Point/Counterpoint. Intensity modulated electronic brachytherapy will soon become the brachytherapy treatment of choice for irregularly shaped tumor cavities or those closely bounded by critical structures. Med Phys. 2009;36:681-3.

48. Steel G. Radiobiology of tumors. In: Mayles P, Nahum AE, Rosenwald J-C, editors. Handbook of radiotherapy physics: theory and practice. New York: Taylor & Francis; 2007. p. 127-48.

49. Ling CC, Spiro IJ, Mitchell J, Stickler R. The variation of OER with dose rate. Int J Radiat Oncol Biol Phys. 1985;11:1367-73.

50. Palcic B, Skarsgard LD. Reduced oxygen enhancement ratio at low doses of ionizing radiation. Radiat Res. 1984;100:328-39.

51. Reniers B, Liu D, Rusch T, Verhaegen F. Calculation of relative biological effectiveness of a low-energy electronic brachytherapy source. Phys Med Biol. 2008;53:7125-35.

52. Nath R. Physical properties and clinical uses of brachytherapy radionuclides. In: Williamson JF, Thomadsen BR, Nath R, editors. Brachytherapy physics. Madison, WI: Medical Physics Pub.; 1995. p. 7-37.

53. Brenner DJ, Hall EJ. Conditions for the equivalence of continuous to pulsed low dose rate brachytherapy. Int J Radiat Oncol Biol Phys. 1991;20:181-90. In: Battermann JJ. Dose rates of the future. In: Mould RF, Battermann JJ, Martinez AA, Speiser BL, editors. Brachytherapy from radium to optimization. Veenendaal: Nucletron International; 1994. p. 385-91.

54. Arslan NC, Geard CR, Hall EJ. Low dose-rate effects of cesium-137 and iodine-125 on cell survival, cell progression, and chromosomal alterations. Am J Clin Oncol. 1986;9:521-6.

55. Baltas D, Sakelliou L, Zamboglou N. The early history of brachytherapy physics. The physics of modern brachytherapy for oncology. Boca Raton: Taylor & Francis; 2007. p. 1-14.

56. Dutreix J, Tubiana M, Pierquin B. The hazy dawn of brachytherapy. Radiother Oncol. 1998;49:223-32.

57. Ellis F. History of brachytherapy. In: Williamson JF, Thomadsen BR, Nath R, editors. Brachytherapy physics. Madison, WI: Medical Physics Pub.; 1995. p. 1-6.

58. Mould RF. A century of x-rays and radioactivity in medicine: with emphasis on photographic records of the early years. Bristol; Philadelphia: Institute of Physics Pub.; 1993.

59. Mould RF. Radium brachytherapy: historical review. In: Mould RF, Battermann JJ, Martinez AA, Speiser BL, editors. Brachytherapy from radium to optimization. Veenendaal: Nucletron International; 1994. p. 1-8.

60. Mould RF. Priority for radium therapy of benign conditions and cancer. Curr Oncol. 2007 Jun;14(3):118-22.

61. Samuel EC. Radium therapy. South Med J. 1917;10:490-4.

62. Janeway HH. Radium therapy in cancer at the Memorial Hospital, New York (First report: 1915-1916). New York: Paul B. Hoeber1917.

63. Duncan R. Radium: Its Local Application as a Therapeutic Agent-with Case Reports. Cal State J Med. 1917 Oct;15(10):406-12.

64. Stevenson WC. Preliminary clinical report on a new and economical method of radium therapy by means of emanation needles. Br Med J. 1914;2:9-10.

65. Joliot F, Curie I. Artificial production of a new kind of radio-element. Nature. 1934;133:201-2.

66. Brucer M. Brachytherapy. Am J Roentgenol Radium Ther Nucl Med. 1958;79:1080-90.

67. Aird E. Sources in brachytherapy. In: Joslin CAF, Flynn A, Hall EJ, editors. Principles and practice of brachytherapy: using afterloading systems. London: Arnold; 2001. p. 3-10.

68. Stevens LG. Injurious effects on the skin. Br Med J. 1896;1:998.

69. Gilchrist TC. A case of dermatitis due to the X rays. Bull Johns Hopkins Hosp. 1897;8:17-22. In: Mould RF. Priority for radium therapy of benign conditions and cancer. Curr Oncol. 2007 Jun;14(3):118-22.

70. Ron E. Ionizing radiation and cancer risk: evidence from epidemiology. Radiat Res. 1998;150:S30-41.

71. Henschke UK, Hilaris BS, Mahan GD. Intracavitary radiation therapy of cancer of the uterine cervix by remote afterloading with cycling sources. Am J Roentgenol Radium Ther Nucl Med. 1966;96:45-51.

72. Strebel H. Vorschläge zur Radiumtherapie [Proposals for radiumtherapy]. Dtsch Med Z. 1903;24:1145-6. In: Mould RF, Litten FS, Bruggmoser G, Aronowitz JN. Proposals for radium therapy in 1903. Nowotwory J Oncol. 2007;57:136e-8e.

73. Horwitz H, Kereiakes JG, Bahr GK, Cuxton SE, Barrett CM. An after-loading system utilizing Cesium 137 for the treatment of carcinoma of the cervix. Am J Roentgenol Radium Ther Nucl Med. 1964;91:176-91.

74. Walstam R. Remotely-controlled afterloading radiotherapy apparatus (a preliminary report). Phys Med Biol. 1962;7:225-8.

75. Henschke UK, Hilaris BS, Mahan GD. Afterloading in interstitial and intracavitary radiation therapy. Am J Roentgenol Radium Ther Nucl Med. 1963;90:386-95.

76. Henschke UK, Hilaris BS, Mahan GD. Remote afterloading with intracavitary applicators. Radiology. 1964;83:344-5.

77. O'Connell D, Howard N, Joslin CA, Ramsey NW, Liversage WE. A new remotely controlled unit for the treatment of uterine carcinoma. Lancet. 1965;2:570-1.

78. Bidmead M, Jones CH. Afterloading equipment for brachytherapy. In: Mayles P, Nahum AE, Rosenwald J-C, editors. Handbook of radiotherapy physics: theory and practice. New York: Taylor & Francis; 2007. p. 1117-29.

79. Gauwerky F. Short time afterloading curietherapy of gynecological carcinomas: technique and problems [in German]. Strahlentherapie. 1977;153:793-801. In: Williamson JF. Brachytherapy technology and physics practice since 1950: a half-century of progress. Phys Med Biol. 2006;51:R303-25.

80. Paterson R, Parker HM. A dosage system for gamma-ray therapy. Br J Radiol. 1934;7:592-632.

81. Paterson R, Parker HM. A dosage system for interstitial radium therapy. Br J Radiol. 1938;11:252-66, 313-40.

82. Meredith WJ, Paterson JRK. Radium dosage; the Manchester system. 2d ed. Edinburgh, London: Livingstone; 1967.

83. Quimby EH, Castro V. The calculation of dosage in interstitial radium therapy. Am J Roentgenol Radium Ther Nucl Med. 1953;70:739-49.

84. Goodwin PN, Quimby EH, Morgan RH. Dosage with radioactive materials. Physical foundations of radiology. 4th ed. ed. New York; London: Harper & Row; 1970. p. 241-84.

85. Pierquin B, Dutreix A, Paine CH, Chassagne D, Marinello G, Ash D. The Paris system in interstitial radiation therapy. Acta Radiol Oncol Radiat Phys Biol. 1978;17:33-48.

86. Regaud C. Radium therapy of cancer at the Radium Institute of Paris. Am J Roentgenol. 1929;21:1.

87. Heyman J. The so-called Stockholm method and the results of treatment of uterine cancer at the Radiumhemmet. Acta Radiol. 1935;16:129-48.

88. Heyman J. The technique in the treatment of cancer uteri at Radiumhemmet. Acta Radiol. 1929;10:49-64.

89. Tod M, Meredith WJ. Treatment of cancer of the cervix uteri, a revised Manchester method. Br J Radiol. 1953;26:252-7.

90. Tod MC, Meredith WJ. A dosage system for use in the treatment of cancer of the uterine cervix. Br J Radiol. 1938;11:809-24.

91. Shalek RJ, Stovall M. The M. D. Anderson method for the computation of isodose curves around interstitial and intracavitary radiation sources. I. Dose from linear sources. Am J Roentgenol Radium Ther Nucl Med. 1968;102:662-72.

92. Batten GW. The M. D. Anderson method for the computation of isodose curves around interstitial and intracavitary radiation sources. II. Mathematical and computational aspects. Am J Roentgenol Radium Ther Nucl Med. 1968;102:673-6.

93. Stovall M, Shalek RJ. The M. D. Anderson method for the computation of isodose curves around interstitial and intracavitary radiation sources. III. Roentgenograms for input data and relation of isodose calculations to the Paterson-Parker system. Am J Roentgenol Radium Ther Nucl Med. 1968;102:677-87.

94. Stovall M, Shalek RJ. A review of computer techniques for dosimetry of interstitial and intracavitary radiotherapy. Comput Programs Biomed. 1972;2:125-36.

95. Hope CS, Laurie J, Orr JS, Walters JH. The computation of dose distribution in cervix radium treatment. Phys Med Biol. 1964;16:344-57.

96. Sievert RM. Die intensitätsverteilung der primären γ-strahlung in der nähe medizinischer radiumpräparate. Acta Radiol. 1921;1:89-128.

97. Potish RA, Gerbi BJ. Role of point A in the era of computerized dosimetry. Radiology. 1986;158:827-31.

98. Han P, Hu KS, Shankar RA, Harrison LB. Head and neck brachytherapy. In: Hoskins WJ, Perez CA, Young RC, Barakat RR, Markman M, Randall ME, editors. Principles and practice of gynecologic oncology. 4th ed. Philadelphia: Lippincott Williams & Wilkins; 2005. p. 49-92.

99. Rownd J. Applicator design and dose distributions. In: Thomadsen B, Rivard MJ, Butler WM, editors. Brachytherapy physics. 2nd ed. Madison, WI.: Medical Physics Pub.; 2005. p. 797-804.

100. Kelley JR, Cuttino LW, Vicini FA, Arthur DW. Breast brachytherapy. In: Halperin EC, Perez CA, Brady LW, editors. Perez and Brady's principles and practice of radiation oncology. 5th ed. Philadelphia: Wolters Kluwer Health/Lippincott Williams & Wilkins; 2008. p. 115-35.

101. Chang JN, Suh TS, Park SY, Cho KH, Kim S. A dual-energy technique for enhanced localization accuracy in intracavitary brachytherapy. Med Phys. 2005;32:376-9.

102. Milickovic N, Giannouli S, Baltas D, Lahanas M, Kolotas C, Zamboglou N, et al. Catheter autoreconstruction in computed tomography based brachytherapy treatment planning. Med Phys. 2000;27:1047-57.

103. Viswanathan AN, Dimopoulos J, Kirisits C, Berger D, Potter R. Computed tomography versus magnetic resonance imaging-based contouring in cervical cancer brachytherapy: results of a prospective trial and preliminary guidelines for standardized contours. Int J Radiat Oncol Biol Phys. 2007;68:491-8.

104. Brant WE. Diagnostic imaging methods. In: Brant WE, Helms CA, editors. Fundamentals of diagnostic radiology. 3rd ed. Philadelphia: Lippincott, Williams & Wilkins; 2007. p. 3-26.

105. Kendall RL, Gifford KA, Kirsner SM. The impact of peak-kilovoltage settings on heterogeneity-corrected photon-beam treatment plans. Radiother Oncol. 2006;81:206-8.

106. Verhaegen F, Devic S. Sensitivity study for CT image use in Monte Carlo treatment planning. Phys Med Biol. 2005;50:937-46.

107. Vanderstraeten B, Chin PW, Fix M, Leal A, Mora G, Reynaert N, et al. Conversion of CT numbers into tissue parameters for Monte Carlo dose calculations: a multi-centre study. Phys Med Biol. 2007;52:539-62.

108. Bazalova M, Carrier JF, Beaulieu L, Verhaegen F. Tissue segmentation in Monte Carlo treatment planning: a simulation study using dual-energy CT images. Radiother Oncol. 2008;86:93-8.

109. Johnson TR, Krauss B, Sedlmair M, Grasruck M, Bruder H, Morhard D, et al. Material differentiation by dual energy CT: initial experience. Eur Radiol. 2007;17:1510-7.

110. Bazalova M, Beaulieu L, Palefsky S, Verhaegen F. Correction of CT artifacts and its influence on Monte Carlo dose calculations. Med Phys. 2007;34:2119-32.

111. Weeks KJ. Monte Carlo dose calculations for a new ovoid shield system for carcinoma of the uterine cervix. Med Phys. 1998;25:2288-92.

112. Price M. The imaging and dosimetric capabilities of a CT/MR-suitable, anatomically adaptive, shielded intracavitary brachytherapy applicator for the treatment of cervical cancer [dissertation]. Houston (TX): University of Texas; 2008.

113. Jaffray DA, Siewerdsen JH, Wong JW, Martinez AA. Flat-panel cone-beam computed tomography for image-guided radiation therapy. Int J Radiat Oncol Biol Phys. 2002;53:1337-49.

114. Endo M, Tsunoo T, Nakamori N, Yoshida K. Effect of scattered radiation on image noise in cone beam CT. Med Phys. 2001;28:469-74.

115. Haie-Meder C, Pötter R, Van Limbergen E, Briot E, De Brabandere M, Dimopoulos J, et al. Recommendations from Gynaecological (GYN) GEC-ESTRO Working

Group (I): concepts and terms in 3D image based 3D treatment planning in cervix cancer brachytherapy with emphasis on MRI assessment of GTV and CTV. Radiother Oncol. 2005 Mar;74:235-45.

116. Zwahlen D, Jezioranski J, Chan P, Haider MA, Cho YB, Yeung I, et al. Magnetic resonance imaging-guided intracavitary brachytherapy for cancer of the cervix. Int J Radiat Oncol Biol Phys. 2009;74:1157-64.

117. Krempien RC, Daeuber S, Hensley FW, Wannenmacher M, Harms W. Image fusion of CT and MRI data enables improved target volume definition in 3D-brachytherapy treatment planning. Brachytherapy. 2003;2:164-71.

118. Lahanas M, Baltas D, Zamboglou N. A hybrid evolutionary algorithm for multi-objective anatomy-based dose optimization in high-dose-rate brachytherapy. Phys Med Biol. 2003;48:399-415.

119. Anderson LL. Physical optimization of afterloading techniques. Strahlentherapie. 1985;161:264-9.

120. Edmundson GK. Volume optimisation: an American viewpoint. In: Mould RF, Battermann JJ, Martinez AA, Speiser BL, editors. Brachytherapy from radium to optimization. Veenendaal: Nucletron International; 1994. p. 314-8.

121. Lessard E, Pouliot J. Inverse planning anatomy-based dose optimization for HDR-brachytherapy of the prostate using fast simulated annealing algorithm and dedicated objective function. Med Phys. 2001;28:773-9.

122. Alterovitz R, Lessard E, Pouliot J, Hsu IC, O'Brien JF, Goldberg K. Optimization of HDR brachytherapy dose distributions using linear programming with penalty costs. Med Phys. 2006;33:4012-9.

123. Jozsef G, Streeter OE, Astrahan MA. The use of linear programming in optimization of HDR implant dose distributions. Med Phys. 2003;30:751-60.

124. Lahanas M, Baltas D, Giannouli S. Global convergence analysis of fast multiobjective gradient-based dose optimization algorithms for high-dose-rate brachytherapy. Phys Med Biol. 2003;48:599-617.

125. Rivard MJ, Coursey BM, DeWerd LA, Hanson WF, Huq MS, Ibbott GS, et al. Update of AAPM Task Group No. 43 Report: A revised AAPM protocol for brachytherapy dose calculations. Med Phys. 2004;31:633-74.

126. Ezzell GA, Luthmann RW. Clinical implementation of dwell time optimization techniques for single stepping-source remote applicators. In: Williamson JF, Thomadsen BR, Nath R, editors. Brachytherapy physics. Madison, WI: Medical Physics Pub.; 1995. p. 617-39.

# Chapter Three

# HDR Iridium-192 Brachytherapy Dosimetry



## 3.1. INTRODUCTION

Dosimetry is a subject concerning the measurement or calculation of energy deposition in a medium by ionizing radiation. The photons emitted from brachytherapy sources are a form of indirectly ionizing radiation in which energy is deposited in matter through a two-step process. First, photons undergo interactions and transfer energy to secondary electrons, liberating them from matter. Subsequently, these electrons lose kinetic energy along their tracks by collision interactions with atoms. The energy lost may cause cell damage or be dissipated as heat. In $^{192}$Ir brachytherapy dosimetry, only photon interactions are of interest. Because of the short ranges of secondary electrons in tissue, it can be assumed that the energy transferred to electrons is deposited on the spot.

The rapid falloff of dose with distance poses challenges in experimental brachytherapy dosimetry, and hence accurate dose computation techniques are highly valuable. This chapter will first introduce the basic concepts of photon interactions and $^{192}$Ir dosimetry. We will then describe the major issues affecting contemporary HDR $^{192}$Ir treatment planning, followed by an overview of dose calculations methods.

## 3.2. BASIC DOSIMETRIC QUANTITIES

The quantities defined below will be used throughout this chapter and Paper IV.

### 3.2.1. *Fluence and fluence rate*

The *photon fluence* ($\Phi$) is defined as the quotient of d$N$ by d$A$, where d$N$ is the number of photons impinging on an infinitesimal sphere of cross-sectional area dA:

$$\Phi = \frac{\mathrm{d}N}{\mathrm{d}A} \tag{3.1}$$

It is a scalar quantity in units of m$^{-2}$. For a polyenergetic photon beam, the fluence spectrum can be expressed as a differential distribution with respect to energy $E$, $\Phi_E$:

$$\Phi_E(E) = \frac{\mathrm{d}\Phi(E)}{\mathrm{d}E} \tag{3.2}$$

### 3.2.2. *Energy fluence and energy fluence rate*

The *photon energy fluence* $\Psi$ is defined as the quotient of d$E$ by d$A$, of units J m$^{-2}$, Here, d$E$ is the total energy of photons impinging on a sphere of cross-sectional area d$A$.

$$\Psi = \frac{\mathrm{d}E}{\mathrm{d}A} \tag{3.3}$$

$\Psi_E(E)$ is the differential distribution for the energy fluence of polyenergetic photons:

$$\Psi_E(E) = \frac{\mathrm{d}\Psi(E)}{\mathrm{d}E} = \Phi_E(E)\,E \tag{3.4}$$

The total energy fluence $\Psi$ is calculated as follows:

$$\Psi = \int_0^{E_{max}} \Psi_E(E)\,\mathrm{d}E \tag{3.5}$$

The *energy fluence rate*, or *intensity*, is the rate of energy fluence per unit time.

### 3.2.3. *Attenuation coefficients*

As a monogenetic and narrow photon beam with initial intensity $I_0$ travels along a medium of thickness $x$, its intensity $I$ is attenuated according to this equation:

$$I(x) = I_0 e^{-\mu x} \tag{3.6}$$

The *linear attenuation coefficient* $\mu$, typically expressed in units of $cm^{-1}$, is defined as:

$$\mu = \frac{1}{N}\frac{\mathrm{d}N}{\mathrm{d}l} \tag{3.7}$$

where $\mathrm{d}N/\mathrm{d}l$ represents the fraction of photons that undergo interactions as they travel a distance $\mathrm{d}l$ in the medium. The *mass attenuation coefficient* $\mu/\rho$ is density-independent. It is $\mu$ divided by the density $\rho$ of the attenuator, and its units are $cm^2\ g^{-1}$.

### 3.2.4. *Mass energy transfer and mass energy absorption coefficients*

The mass energy transfer coefficient $\mu_{tr}/\rho$ and the mass energy absorption coefficient $\mu_{en}/\rho$ are defined below:

$$\frac{\mu_{tr}}{\rho} = \frac{\mu}{\rho}\frac{\overline{E}_{tr}}{h\nu} \tag{3.8}$$

$$\frac{\mu_{en}}{\rho} = \frac{\mu}{\rho}\frac{\overline{E}_{en}}{h\nu} \tag{3.9}$$

$\overline{E}_{tr}$ is the mean energy transferred to secondary electrons (and positrons) per interaction in matter, whereas $\overline{E}_{en}$ refers to the mean energy deposited by electrons.

The effective mass energy absorption coefficient $\bar{\mu}_{\text{en}}/\rho$ is an $\Psi$-weighted mean quantity:

$$\frac{\bar{\mu}_{\text{en}}}{\rho} = \frac{1}{\Psi}\int_0^{E_{\max}} \Psi_E(E)\frac{\mu_{\text{en}}}{\rho}(E)\,\mathrm{d}E \tag{3.10}$$

$\bar{\mu}_{\text{tr}}/\rho$ is defined likewise. The two coefficients are related by the *radiative fraction* $\bar{g}$, which is the fraction of the energy of secondary electrons lost to bremsstrahlung photons:

$$\frac{\bar{\mu}_{\text{en}}}{\rho} = \frac{\bar{\mu}_{tr}}{\rho}\left(1-\bar{g}\right) \tag{3.11}$$

For energies up to 1 MeV, $\bar{g} \approx 0$ in tissue-equivalent media and so $\bar{\mu}_{tr}/\rho \approx \bar{\mu}_{\text{en}}/\rho$.

### 3.2.5. *Kerma and collision kerma*

*Kerma*, *K*, is an acronym for kinetic energy released per unit mass. It is defined as the mean energy ($\mathrm{d}\bar{E}_{tr}$) transferred from uncharged particles to secondary charged particles in a medium of mass d*m*:

$$K = \frac{\mathrm{d}\bar{E}_{tr}}{\mathrm{d}m} \tag{3.12}$$

Its units are J kg$^{-1}$, or Gy. The *collision kerma* $K_{\text{col}}$ excludes the radiative component:

$$K_{\text{col}} = \frac{\mathrm{d}\bar{E}_{\text{en}}}{\mathrm{d}m} = K\left(1-\bar{g}\right) \tag{3.13}$$

$K_{\text{col}} \approx K$ for $^{192}$Ir sources since $\bar{g} \approx 0$. It can be derived from $\Psi$ as follows:

$$K_{\text{col}} = \int_0^{E_{\max}} \Psi_E(E)\frac{\mu_{\text{en}}}{\rho}(E)\,\mathrm{d}E = \Psi\frac{\bar{\mu}_{\text{en}}}{\rho} \tag{3.14}$$

The relationship between $K_{\text{col}}$ in two media (denoted 1 and 2) is given by:

$$\frac{K_{\text{col},2}}{K_{\text{col},1}} = \frac{\Psi_2\left(\bar{\mu}_{\text{en}}/\rho\right)_2}{\Psi_1\left(\bar{\mu}_{\text{en}}/\rho\right)_1} = \left(\Psi\right)_1^2\left(\frac{\bar{\mu}_{\text{en}}}{\rho}\right)_1^2 \tag{3.15}$$

### 3.2.6. *Absorbed dose and collision kerma*

The absorbed dose is the same as $K_{col}$ when *charged particle equilibrium* (CPE) exists. CPE is realized in a volume $V$ provided that for every charged particle leaving $V$ there is another particle of the same type and energy entering it. In brachytherapy dosimetry, CPE is often assumed because the secondary electrons have short ranges not exceeding 1 mm in a wide range of media for photon energies up to 1 MeV [1]. Although it is mostly valid, CPE may break down near the source or interfaces of dissimilar media.

## 3.3. HDR IRIDIUM-192 SOURCES

The two HDR $^{192}$Ir source models investigated in this work are manufactured for use with the Nucletron microSelectron v1 and v2 remote afterloading systems (Veenendaal, the Netherlands). Figure 3.1 shows the schematic drawings of the v1 classic model (Part No. 080905) [2] and the v2 new model (Part No. 015.002) [3]. Each source consists of a pure iridium core of density 22.24 g/cm$^3$. The radioactivity of $^{192}$Ir is distributed uniformly within this core, which is encapsulated by stainless steel (AISI 316L) of density 8.02 g/cm$^3$. Its proximal end is welded to a steel cable of density 4.81 g/cm$^3$ [3].

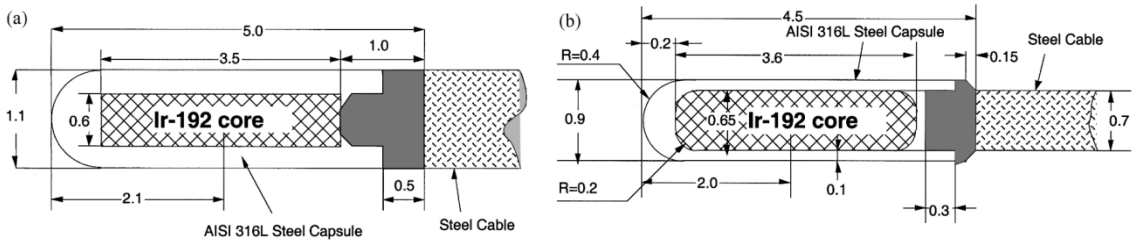


Figure 3.1. Schematic diagrams of the microSelectron HDR $^{192}$Ir sources [3]. (a) The v1 classic model. (b) The v2 new model. All dimensions are in mm.

### 3.3.1. *Photon spectrum*

$^{192}$Ir is produced through the neutron capture process by bombarding stable $^{191}$Ir with neutrons in a nuclear reactor. It disintegrates by $\beta^-$ decay to several excited states of $^{192}$Pt, and by electron capture to excited states of $^{192}$Os. An average of 2.363±0.3% photons are emitted per decay, including $\gamma$ rays and characteristic x-rays from the K and L orbital shells [4]. The photons are of discrete energies in the 8.9–1378.2 keV range, a negligible portion of which is above 885 keV [5].

Figure 3.2 shows the photon fluence spectrum emerging from the v2 HDR $^{192}$Ir source capsule. The mean energy is 360 keV, and it is 400 keV when weighted by the energy fluence. This spectrum is generated by our GEANT4 MC simulation (version 9.2, low-energy physics package) [6]. The photons are emitted in isotropic directions within the core and their initial energies are sampled from the Nudat 2.0 $^{192}$Ir photon spectrum [5]. Several other $^{192}$Ir spectra [7-11] have been used for MC dosimetric studies. Angelopoulos et al. [12] reported that the dosimetry in water is unaffected by fine details of the primary $^{192}$Ir spectrum.

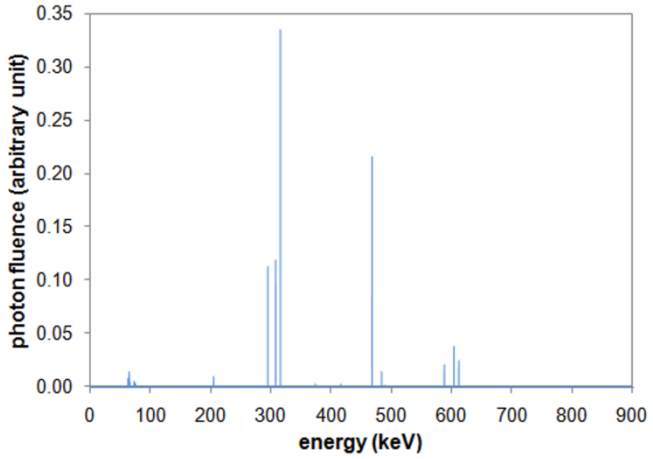


Figure 3.2. Fluence spectrum of photons emerging from the Nucletron microSelectron v2 HDR $^{192}$Ir source capsule.

### 3.3.2. *Beta spectrum*

$^{192}$Ir sources emit $\beta$ particles of mean energy 181 keV and maximum energy 672 keV [13], most of which are stopped within the iridium core and the stainless steel capsule. Baltas et al. [14] showed by MC calculations that only 0.002% and 0.08% of them remain unfiltered by the v1 and v2 sources, respectively. For the v2 source, $\beta$ particles increase the dose by 15% at a distance of 0.5 mm and 5% at 1 mm [14].

In MC simulations for $^{192}$Ir brachytherapy, the $\beta$ spectrum is often neglected. Also, secondary electrons are not transported and their kinetic energies are deposited on the spot. These simplifications, which help to reduce the MC calculation time, are valid for distances beyond 2 mm from an $^{192}$Ir source where $D \approx K_{\mathrm{col}}$ [13, 15].

### 3.3.3. *Decay correction*

Given the initial dose rate $\dot{D}_0$ and the half life $T_{1/2}$ of a radioactive source, the dose rate $\dot{D}$ at time $t$ can be calculated by accounting for the exponential decay:

$$\dot{D}(t) = \dot{D}_0 \exp\left(-\frac{t \ln 2}{T_{1/2}}\right) \tag{3.16}$$

The total dose $D$ delivered over a treatment duration $t_{\mathrm{d}}$ is given by:

$$D = \dot{D}_0 \int_0^{t_{\mathrm{d}}} \exp\left(-\frac{t \ln 2}{T_{1/2}}\right) \mathrm{d}t = \dot{D}_0 \frac{T_{1/2}}{\ln 2}\left[1 - \exp\left(-\frac{t_{\mathrm{d}} \ln 2}{T_{1/2}}\right)\right] \tag{3.17}$$

For an $^{192}$Ir source, $T_{1/2}$ = 73.83 d. Since a typical HDR treatment fraction lasts a few minutes, $t_{\mathrm{d}} \ll T_{1/2}$ and the exponential term is approximately equal to $1 + (t_{\mathrm{d}} \ln 2) T_{1/2}^{-1}$. Consequently, $D \approx \dot{D}_0 \, t_{\mathrm{d}}$ for HDR $^{192}$Ir brachytherapy.

## 3.4. PHOTONS INTERACTIONS

The photon interactions of relevance at $^{192}$Ir energies include photoelectric effect, Compton scattering, and Rayleigh scattering. The symbols for their linear attenuation coefficients are $\tau$, $\sigma_C$, and $\sigma_R$, respectively, and the corresponding absorption coefficients are denoted by the subscript *en*. The following equations are used to calculate $\mu$ and $\mu_{en}$:

$$\mu = \tau + \sigma_C + \sigma_R \tag{3.18}$$

$$\mu_{en} = \tau_{en} + \sigma_{C,en} \tag{3.19}$$

Pair production, of threshold energy 1.02 MeV, can be neglected for $^{192}$Ir sources.

### 3.4.1. *Photoelectric effect*

In the photoelectric interaction, a photon of energy $hv$ collides with an atom and ejects a bound electron from an orbital shell of binding energy $E_B$. The photon disappears while the ejected electron (known as a photoelectron) acquires a kinetic energy of $hv - E_B$. Since the photoelectron leaves behind a vacancy, characteristic x rays and/or Auger electrons are emitted as the atom returns from an excited state to the ground state. At $^{192}$Ir energies, all of the kinetic energy transferred may be assumed to be absorbed locally.

Photoelectric effect is most probable in high atomic number ($Z$) materials and at low photon energies. The dependence of $\tau/\rho$ on Z and energy $hv$ is approximately given by:

$$\frac{\tau}{\rho} \propto \frac{Z^3}{(hv)^3} \tag{3.20}$$

$\tau/\rho$ is increased at energies just above the binding energies of orbital shells, also known as the absorption edges.

### 3.4.2. *Compton scattering*

Compton scattering is also referred to as incoherent scattering. In this event, an incident photon of energy $h\nu$ is scattered at an angle $\theta$ as it transfers some of its energy to a recoil electron of binding energy $E_B$. The electron can be assumed free and stationary when $E_B \ll h\nu$. The Klein-Nishina equation [16] can be used to calculate the Compton attenuation coefficients and differential cross sections under the free electron assumption. Since this assumption breaks down at $h\nu < 100$ keV [17], it is recommended that MC-based brachytherapy dosimetry should account for electron binding effects [18].

The energy of the Compton scattered photon, $h\nu'$, is given by:

$$h\nu' = \frac{h\nu}{1+\varepsilon(1-\cos\theta)} \tag{3.21}$$

where $\varepsilon$ is a ratio of the initial photon energy to the electron rest mass, $m_0 c^2$:

$$\varepsilon = \frac{h\nu}{m_0 c^2} = \frac{h\nu}{0.511\,\mathrm{MeV}} \tag{3.22}$$

The energy of the recoil energy, $E = h\nu - h\nu'$, is deposited on the spot for incident $^{192}$Ir photons. When the free electron assumption is valid, $\sigma_C/\rho$ is independent of $Z$ and decreases with increasing photon energy.

### 3.4.3. *Rayleigh scattering*

Rayleigh scattering (or coherent scattering) is an elastic interaction between a photon and an atom. It does not involve any energy transfer. The photon is deflected slightly in the forward direction while the electrons of the atom are set into momentary oscillation. This interaction is more probable in high-Z media and at low photon energies:

$$\frac{\sigma_R}{\rho} \propto \frac{Z}{(h\nu)^2} \tag{3.23}$$

### 3.4.4. *Relative importance of interaction types*

Figure 3.3 shows $\mu/\rho$ along with $\tau/\rho$, $\sigma_C/\rho$, and $\sigma_R/\rho$ in the 1–1000 keV range for water and tungsten [19], representing low- and high-$Z$ materials respectively. The relative contribution of each interaction type to $\mu/\rho$ is shown in Figure 3.4. It is evident that photoelectric effect predominates at low photon energies (the energy range depends on the medium). Also, Compton scattering is an important interaction for $^{192}$Ir photons whereas Rayleigh scattering has minor dosimetric effects at all energies.

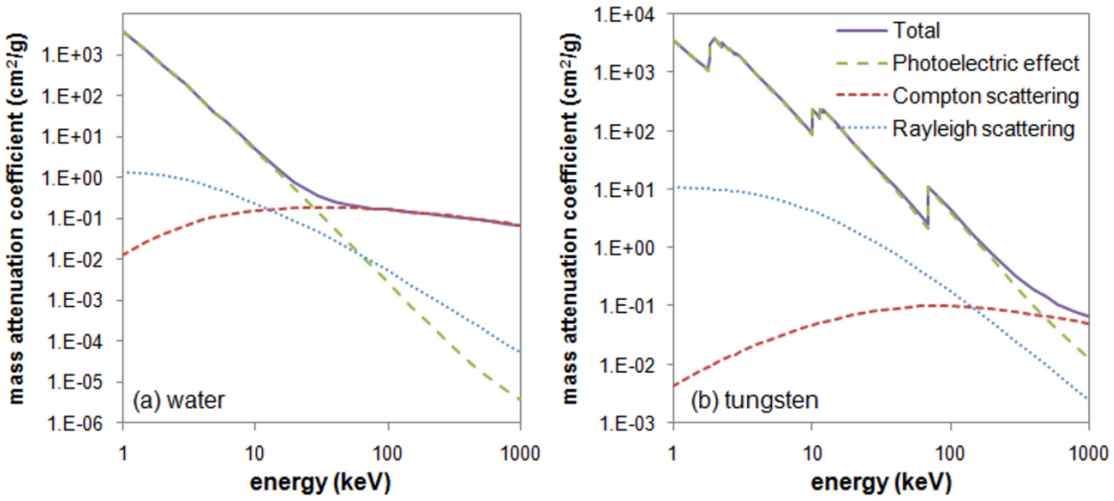


Figure 3.3. Mass attenuation coefficients for (a) water and (b) lead in the 1–1000 keV energy range. The contributions of individual effects are also shown.

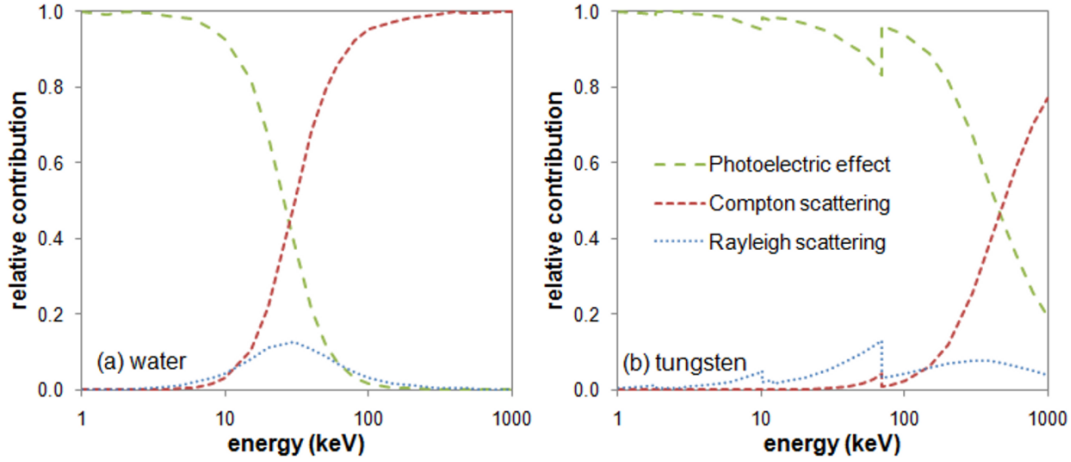


Figure 3.4. Relative contribution of each interaction effect to the total mass attenuation coefficient for (a) water and (b) tungsten in the 1–1000 keV range.

## 3.5. DEFINITIONS OF SOURCE STRENGTH

The mass of radium and the equivalent mass of radium, as described in Chapter 2, are historical measures of brachytherapy source strength. The quantities defined below are also source strength specifiers, among which the *reference air-kerma rate* and the *air-kerma strength* are currently recommended by the ICRU and the AAPM, respectively.

### 3.5.1. *Reference exposure rate*

The reference exposure rate is recommended by the National Council of Radiation Protection and Measurements [20]. It is the exposure rate at a reference distance along the transverse axis in air, with the attenuation and scatter in air corrected. The reference distance should be large (usually 1 m) so that the source can be assumed to be a point.

### 3.5.2. *Apparent activity*

The apparent activity $\mathcal{A}_{app}$ refers to the activity of a hypothetical point source, with an unfiltered emission spectrum, that gives the same exposure rate at 1 m in free space as a given source of the same radionuclide. The effects of filtration as well as the production of characteristic x rays within the real source are taken into account. $\mathcal{A}_{app}$ is in units of Bq.

### 3.5.3. *Reference air-kerma rate*

The reference air-kerma rate, defined in ICRU Reports 38 [21] and 60 [22], refers to the air-kerma rate in vacuum at a reference distance of 1 m along the source transverse plane. Its units are μGy $h^{-1}$.

### 3.5.4. *Air-kerma strength*

The air-kerma strength $S_K$ is defined in the AAPM Report 21 [23] and TG-43 [24]. Its unit is denoted by U, where 1 U = μGy $m^2$ $h^{-1}$. Below is the updated definition [18]:

$$S_K = \dot{K}_\delta(d)\,d^2 \tag{3.24}$$

$\dot{K}_\delta(d)$ is the reference air-kerma rate at distance $d$ along the transverse plane. Photons of energies below a cutoff $\delta$ are excluded in $\dot{K}(d)$, as they do not penetrate beyond 1 mm in tissue. $S_K$ is also the product of $\mathcal{A}_{\text{app}}$ and the *air kerma-rate constant* $(\Gamma_\delta)_k$, which is 111 μGy m$^2$ h$^{-1}$ GBq$^{-1}$ for $^{192}$Ir [7]. For an HDR $^{192}$Ir source of $\mathcal{A}_{\text{app}}$ = 370 GBq, $S_K$ = 41 100 U.

## 3.6. TG-43 DOSIMETRY PROTOCOL

Most, if not all, contemporary brachytherapy planning systems comply with the TG-43 dosimetry protocol for photon-emitting sources [18, 24]. The dose around an encapsulated source in water can be calculated using the TG-43 1D and 2D formalisms, which assume the radioactivity originates from a point and a line, respectively. The two approaches yield comparable dose distributions when there are multiple seeds in random orientations [25]. The 1D formalism is preferred for LDR applications such as prostate implants, as it is impractical to identify the orientations of all seeds with current imaging techniques. The 2D formalism, on the other hand, is almost exclusively used for HDR brachytherapy [26]. This is because the source orientations, which align with the implanted catheters, can be readily defined based on tomographic images.

### 3.6.1. *2D dose-calculation formalism*

Figure 3.5 shows the coordinate system used for 2D dose calculations around a cylindrically symmetric source of active length $L$ [18]. The point of interest (POI) is denoted by P($r$, $\theta$), where $r$ is the distance to the source center and $\theta$ is the polar angle relative to the longitudinal axis ($z$). The reference position is at $r_0$ = 1 cm and $\theta_0$ = 90°. The angle $\beta$, in radians, is subtended by the tips of the source core with respect to P($r$, $\theta$).

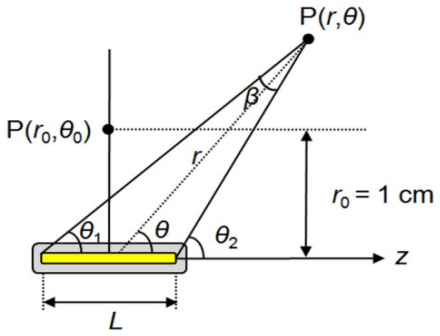


Figure 3.5. Coordinate system used for TG-43 2D dose calculations.

The 2D dose-rate equation using the line-source approximation is as follows [18]:

$$\dot{D}(r,\theta) = S_K \, \Lambda \, \frac{G_L(r,\theta)}{G_L(r_0,\theta_0)} \, g_L(r) \, F(r,\theta) \tag{3.25}$$

Here, $S_K$ denotes the air kerma strength as defined previously. The *dose rate constant* $\Lambda$ represents the dose rate in water at the reference position, $\dot{D}(r_0, \theta_0)$, divided by $S_K$. The *geometry function for a line source*, $G_L(r, \theta)$, accounts for the effects of the inverse square law and serves to improve the interpolation accuracy of tabulated dosimetry data [18]:

$$G_L(r,\theta) = \begin{cases} \dfrac{\beta}{L r \sin\theta} & \text{if } \theta \neq 0° \\ \dfrac{1}{r^2 - L^2/4} & \text{if } \theta = 0° \end{cases} \tag{3.26}$$

The *radial dose function* based on the line-source model, $g_L(r)$, is given by [18]:

$$g_L(r) = \frac{\dot{D}(r,\theta_0)}{\dot{D}(r_0,\theta_0)} \frac{\dot{G}_L(r_0,\theta_0)}{\dot{G}_L(r,\theta_0)} \tag{3.27}$$

It describes the dose variations with distance along the transverse plane due to photon interactions within the source and the surrounding water, excluding the inverse square dose fall-off. The 2D *anisotropy function* $F(r, \theta)$ describes the dose variations with $\theta$ [18]:

$$F(r,\theta) = \frac{\dot{D}(r,\theta)}{\dot{D}(r,\theta_0)} \frac{G_L(r,\theta_0)}{G_L(r,\theta)} \tag{3.28}$$

### 3.6.2. *Applications in treatment planning*

TG-43 allows for consistent source characterizations with well-defined dosimetry parameters. Although it was developed for LDR interstitial source dosimetry, TG-43 is also being used for HDR [27], intravascular [28], and electronic [29] brachytherapy applications. In treatment planning, the patient dose is calculated by adding up contributions from all dwell positions. This table-based single-source superposition method is fast enough for use in real-time intraoperative treatment planning, as well as anatomy-based inverse optimization in which efficient computations of doses to the target and organs at risk for all activated dwell positions are needed [30].

## 3.7. ISSUES IN DOSE CALCULATIONS

The main shortcomings of using the TG-43 formalism for treatment planning arise from the neglect of (1) applicator, shielding, and contrast solution perturbations, (2) scatter dose changes in the absence of a full scatter environment, and (3) tissue inhomogeneity effects. The related problems for low-energy sources have been examined in various studies, among which the effects of source-to-source shielding (a.k.a. interseed attenuation) and tissue calcifications are of particular interest [31-37]. The major issues pertinent to HDR $^{192}$Ir treatment planning will be discussed in this section.

The concept of primary and scatter dose separation [38-41] is useful for understanding the effects of inhomogeneities in a finite geometry. In this work, photons are classified as *primary* if they are created within the encapsulated source and have not interacted outside the source. All other photons are referred to as *scattered photons*. The *primary dose* $D_{\text{prim}}$ refers to $K_{\text{col}}$ resulting from the first interactions of primary photons, whereas the *scatter dose* $D_{\text{scat}}$ is the difference between the total dose and $D_{\text{prim}}$.

### 3.7.1. *Dose perturbations by applicators, shielding, and contrast solution*

#### *i. Effects of applicator materials*

Intracavitary brachytherapy applicators are commonly made of stainless steel because it is sturdy and durable for repeated use. Other usual applicator materials include aluminum alloy, plastic, and nylon. When applicators are used without extra shielding or contrast solution, their perturbation effects in regions of clinical interest tend to be well within a few percent [42]. Several studies of such effects are described in the following.

Russell and Ahnesjö [40] used EGS4 [43] MC simulations to quantify the dose reduction caused by applicators in the form of a hollow tube, 0.5 mm in wall thickness. Three applicator materials were tested: water, nylon, and stainless steel. They found the radial dose profiles along the transverse plane of an $^{192}$Ir source agreed closely for the water and nylon applicators. The profile for the stainless steel applicator, of 8.02 g/cm$^3$ density, was lower by 0.5% at 5 cm and 1% at larger distances.

Ye et al. [44] examined the effects of a stainless steel uterine applicator of 0.5 mm wall thickness, and a vaginal cylinder composed of the same stainless steel tube in addition to a polysulfone cylinder of 1 or 2 cm radius, 10 cm length, and 1.40 g/cm$^3$ density. They calculated $g_L(r)$ and $F(r, \theta)$ for an $^{192}$Ir source positioned within the applicator by MCNP [45] MC simulations, and verified the results by ionization chamber measurements in water. Compared to the calculations without the applicator for $r \leq 6$ cm, the maximum reductions in $g_L(r)$ were 1.4% for the stainless steel tube, 2.4% for the tube plus a 1 cm radius cylinder, and 3.6% for the tube plus a 2 cm radius cylinder [44]. On the other hand, $F(r, \theta)$ was reduced by up to 20% at oblique angles (within 5° of the source proximal side) due to a longer photon pathlength along the applicator [44].

Parsai et al. [46] performed a similar dosimetric study for the stainless steel Fletcher-Suit Delclos gynaecological applicator set. They used the MCNP MC code [45] and metal oxide semiconductor field effect transistor (MOSFET) point measurements in water. The applicator, of 0.72 mm wall thickness, caused the dose to the Manchester Point A [47] to decrease by 3% for a treatment plan with 18 dwell positions [46]. The contribution of each dwell position to Point A was reduced by 1.5–7.1% [46]. Oblique filtration caused larger differences of up to 16% for points along polar angles closer to the proximal and distal ends of the source [46].

Plastic applicators are sometimes used instead of metallic ones so as to avoid streaking artifacts on the CT planning images. Their dose attenuation effects were investigated by our MC simulations with the PTRAN code [48, 49] for 20 cervical treatment plans. These plans were delivered with the Nucletron Fletcher CT/MR applicator set with polysulfone ovoids of 2 or 2.5 cm diameters. In the MC simulations, the full applicator geometry was modeled while the patient body was replaced by a water phantom. The locations of the tandem and ovoids as well as various landmark dose points were determined from cone-beam CT images acquired prior to each treatment. These points include the Manchester Points A and B and the ICRU-38 bladder and rectal points [21]. As well, the bladder and rectum for each plan were contoured by a physician. Minimum doses to the hottest 0.1 $cm^3$ and 2 $cm^3$ of these organs ($D_{0.1cc}$ and $D_{2cc}$) were calculated. For comparison purposes, the same calculations were repeated with the Nucletron stainless-steel Fletcher-Williamson applicator with polysulfone ovoids (no shielding). Table 3.1 summarizes the doses relative to TG-43 calculations for both applicators. On average, the plastic applicator caused about 2–3% less dose attenuation compared to the stainless steel one.

Table 3.1. Dose ratio averages (MC/TG-43) of 20 cone-beam CT-based patient plans for two Fletcher-type applicator sets.

| | Dose ratio (MC/TG-43)±standard deviation | |
|---|---|---|
| | CT/MR-compatible polysulfone applicator | Fletcher-Williamson stainless-steel applicator |
| Point A | 0.993±0.002 | 0.974±0.002 |
| Point B | 0.994±0.001 | 0.978±0.001 |
| ICRU bladder point | 0.987±0.004 | 0.963±0.006 |
| ICRU rectal point | 0.981±0.003 | 0.956±0.003 |
| Bladder $D_{0.1cc}$ | 0.987±0.008 | 0.963±0.011 |
| Bladder $D_{2cc}$ | 0.985±0.004 | 0.962±0.008 |
| Rectum $D_{0.1cc}$ | 0.990±0.005 | 0.966±0.009 |
| Rectum $D_{2cc}$ | 0.988±0.005 | 0.960±0.007 |

*ii.* *Effects of shielding materials*

Metal shielding in the forms of disks or cylinders is sometimes used for sparing the organs at risk in gynaecological and rectal brachytherapy [42, 50-53]. Tungsten alloy, lead, and stainless steel have been used as shielding materials, among which tungsten alloy is the most attenuating, whereas stainless steel is the least effective [42, 54, 55].

Williamson et al. [56] found that the dose attenuation caused by shielding is highly dependent on its thickness and lateral dimensions, and its location with respect to the source and the POI. They used PTRAN to simulate cylindrical lead and stainless steel disks 1.5 cm away from an $^{192}$Ir source in water. The doses at points located 1–8 cm behind a lead disk (8.63 mm thick, 19.0 mm diameter) were reduced by 55–80%. The reduction range was 20–35% for a thinner disk (2.17 mm thick, 6.35 mm diameter). For stainless steel disks of thicknesses 14.88 mm and 2.17 mm, the reductions were 45–60% and 20–35%, respectively [56]. When the disk diameters were increased threefold, the doses were further attenuated by up to 20% for lead and 8% for stainless steel [56]. The results agreed with diode measurements within 6.5% (average, 0.9–2.7%) [56].

Waterman and Holcomb [50] showed that high-$Z$ media have limited dosimetric effects on the unshielded region for $^{192}$Ir. They performed ionization chamber measurements around a vaginal cylinder with 90°, 180°, and 270° tungsten shields. The applicator consisted of a cylindrical plastic shell of 25 mm outer diameter and 5 mm wall thickness, within which 8 mm-thick shielding was inserted. The doses within 1 cm of the cylinder on the unshielded side were at most 1–2% lower compared to measurements in homogeneous water [50]. The dose attenuations slowly increased to 3%, 5%, and 15% at 10 cm for the 90°, 180°, and 270° shields, respectively [50]. This was caused by a smaller backscatter contribution as primary photons got attenuated by photoelectric effect within the shield. The small dose decrease with distance may in fact be beneficial since the tissue beyond a few centimetres from the source is unlikely to be within the target. Besides, the 270° shield is rarely used for treatment.

Lymperopoulou et al. [42] compared the effects of tungsten and stainless steel shields with the same vaginal applicator model for a clinical treatment plan by MC simulations using MCNPX [57]. The outer diameter of the applicator they investigated was 3 cm. On the unshielded side of a 90° tungsten shield where the volume received at least 20% of the prescribed dose $D_{ref}$, there were negligible differences between the MC and TG-43 dose distributions. The MC dose was lower by up to 4% in the same volume for a 180° shield, whereas a 3% difference was noted at the 50% isodose level for a 270° shield [42]. However, the opposite effect occurred for stainless steel shields. At 2 cm from the source on the unshielded side, the MC doses were higher than those of TG-43 by 1%, 3%, and 6% for the 90°, 180°, and 270° shields, respectively [42]. This dose increase was due to a smaller photoelectric absorption for stainless steel compared with tungsten, and some photons were scattered at larger angles back to the unshielded side.

The small effects of shielding on the unshielded region make it unlikely that the target coverage is jeopardized for $^{192}$Ir brachytherapy (unless the target itself is partially shielded). This does not apply for lower-energy sources whose scatter-to-primary dose ratio (SPR) is higher and the angular distribution of scattered photons is more isotropic. For instance, thermoluminescent detector (TLD) measurements by Muench and Nath [58] indicated that lead-shielded vaginal applicators containing $^{241}$Am sources (60 keV-photon emitters) decreased the dose on the unshielded side by up to 20%. This dose decrease was distance-independent up to 10 cm. On the other hand, a higher dose is possible when the photons are at energies slightly above the absorption edges of the shielding material due to the increased production of characteristic x-rays. MC calculations by Carlsson Tedgren and Ahnesjö [59] showed that the dose at 1 cm from the unshielded side of a piece of 2.25×0.25×10 cm$^3$ lead was increased by 10% for a 100 keV source.

*iii.* *Effects of iodine contrast solution*

Radiographic contrast solution has a higher linear attenuation coefficients compared with tissue media, and thus can be visualized better on the planning CT images. Various researchers have investigated the effects of contrast media for breast brachytherapy with the MammoSite balloon applicator [60-65]. The effects are dependent on the elemental composition, concentration, and volume of the contrast solution. A dose enhancement can be expected within 1 mm of the balloon surface where CPE is absent [62]. Kassas et al. [64] found that if the concentration is kept below 10%, contrast solution will decrease $D_{ref}$ by at most 3%. According to Ye et al. [60], $D_{ref}$ can be decreased by 4–10% due to iodine contrast solution (5–10% concentration by volume) in addition to the reduced photon backscatter near the skin.

### 3.7.2. *Effects of variable scatter conditions*

It is well known that the scattering environment has an important influence on the dose. This is obvious in regions near a phantom boundary with air where photon backscatter is reduced [49, 66-72]. Williamson [49] compared TLD measurements in a finite solid water phantom with MC calculations in unbounded solid water. At points 5–15 cm away from an $^{192}$Ir seed, the measured dose was lower than the corresponding MC dose by 5%–20%. Such a notable discrepancy was observed despite a 10-cm distance between the source and the nearest phantom boundary in the experimental setup [73]. This is because $D_{scat}$ starts to dominate beyond 5 cm from the source where the total dose becomes more sensitive to phantom size variations.

*i.* *Influence of phantom size on TG-43 dosimetry parameters*

Although TG-43 recommends full scatter conditions for characterizing low-energy sources [18], there is not yet a specific guideline for $^{192}$Ir. Pérez-Calatayud et al. [67] reported that, based upon MC calculations with an $^{192}$Ir point source, a water sphere of 40 cm radius will provide full photon backscatter at radial distances up to 20 cm. In spite of this, the majority of the published $^{192}$Ir dosimetry data were derived by MC simulations using a water sphere of 15 cm radius [2, 3, 12, 74-77].

Pantelis et al. [78] compared TG-43 parameters for five HDR $^{192}$Ir sources centered in a water sphere of 15 cm radius. Using a Sievert integration calculation model, the values of $g_L(r)$ among the sources agree within 2% while those of $F(r, \theta)$ are strongly dependent on the active core length [78]. The results corroborate other studies [12, 76, 79] that the internal source makeup has a major influence on $F(r, \theta)$, but not $g(r)$[*].

[*] The notation $g(r)$, without the subscript $L$, is used here to denote the radial dose function calculated with either the point-source or the line-source approximation.

The aforementioned phenomenon is in contrast to the strong influence of the phantom size on $g(r)$, but not $F(r, \theta)$ [74, 80]. Figure 3.6 illustrates the variations of $g_L(r)$, including its primary and scatter components, with phantom size for an HDR $^{192}$Ir source. The data were derived by GEANT4 MC simulations in water spheres of radii 5, 10, 15, and 50 cm. The primary component, which only depends on the direct radiological path originating from the source, is unaffected by the phantom size. On the contrary, the scatter component is dependent on the phantom size and the proximity to the surface.

The scattering volume is of minor influence in the near-source region where $D_{prim}$ predominates. Its effects may become relevant from $r$ = 4 cm, where the SPR increases from 0.44 to 0.56 as the phantom radius increases from 5 to 50 cm. Compared to the unbounded case (radius = 50 cm), $g_L(r)$ for the phantoms of 5, 10, and 15 cm radii are smaller by 7.2%, 2.2%, and 0.7%, respectively at $r$ = 4 cm. The deviations are larger at longer distances, albeit for a diminishing dose. At $r$ = 9 cm, which is about one mean free path in water for $^{192}$Ir photons, 1.15 < SPR < 1.53 and $g_L(r)$ is smaller by 14.4% and 4.8% for the phantoms of 10 and 15 cm radii, respectively.

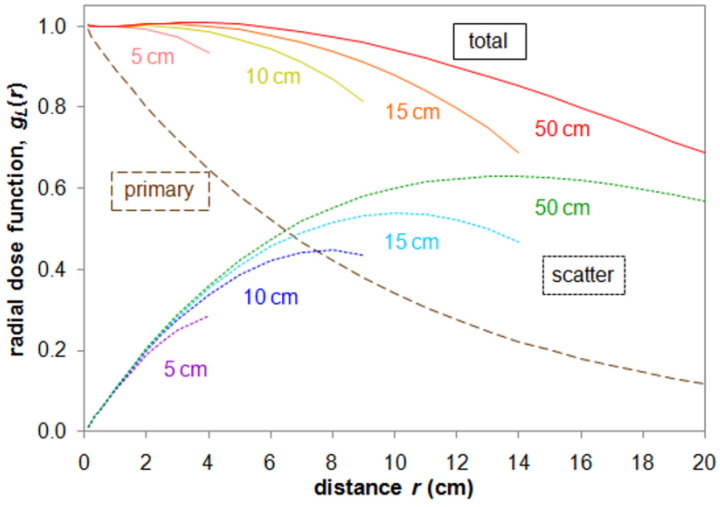


Figure 3.6. Total, primary, and scatter components of $g_L(r)$ for the microSelectron v2 HDR $^{192}$Ir source, calculated in water spheres of radii 5, 10, 15, and 50 cm.

Pérez-Calatayud et al. [67] analyzed $g(r)$ for $^{192}$Ir and $^{137}$Cs point sources in spherical phantoms of various sizes, from which mathematical relations were established for converting $g(r)$ for a given phantom radius to the corresponding one for an infinite phantom. Granero et al. [68] derived similar relations for spherical, cylindrical, and cubical water phantoms. These relations are helpful for compiling a database of $g(r)$ in unbounded geometry based on data derived from different phantom shapes and sizes.

*ii.* *Influence of body dimensions on patient dose*

The influence of the body dimensions on $D_{scat}$ is challenging to quantify. In multicatheter breast brachytherapy, the reduced scattering volume causes the skin dose to decrease by 5–15% [81, 82]. In intraoperative brachytherapy, the target dose may be reduced by 8–13% for prescription depths of 0.5–1.5 cm [83]. Anagnostopoulos et al. [84] suggested calculating $D_{scat}$ as the product of $D_{prim}$ and SPR at a given POI, where SPR is derived in a water sphere of a radius equal to the radiological distance between the POI and the nearest surface. However, this is not an ideal method for clinical situations since the body shape is irregular and the dwell positions are not centered in the body [81].

### 3.7.3. *Tissue inhomogeneity effects*

Since Compton scattering is predominant in low-$Z$ media for $^{192}$Ir photons, tissue composition variations have rather minor dosimetric effects [66, 85]. However, a comprehensive assessment of such effects for $^{192}$Ir brachytherapy is lacking [26]. Anagnostopoulos et al. [86] used MCNPX to simulate an esophagus treatment in a water phantom with bone, spinal cord, lung, and air inserts. The target dose was found to be unaffected by inhomogeneities, although the spinal cord and sternum bone doses differed by 13% and 15% respectively in the low-dose region (5–10% of $D_{ref}$) [86].

Tissue inhomogeneities alter the photon attenuation and energy absorption in the medium to the extent as indicated by the effective medium-to-water mass attenuation and mass energy absorption coefficient ratios, $(\bar{\mu}/\rho)_{\text{wat}}^{\text{med}}$ and $(\bar{\mu}_{\text{en}}/\rho)_{\text{wat}}^{\text{med}}$. The values as a function of energy for adipose, soft tissue, spongiosa, and cortical bone are plotted in Figure 3.7 [87]. According to ICRU-44, cortical bone is a hard bone of density 1.92 g/cm$^3$ and spongiosa is a soft bone of density 1.18 g/cm$^3$ [88].

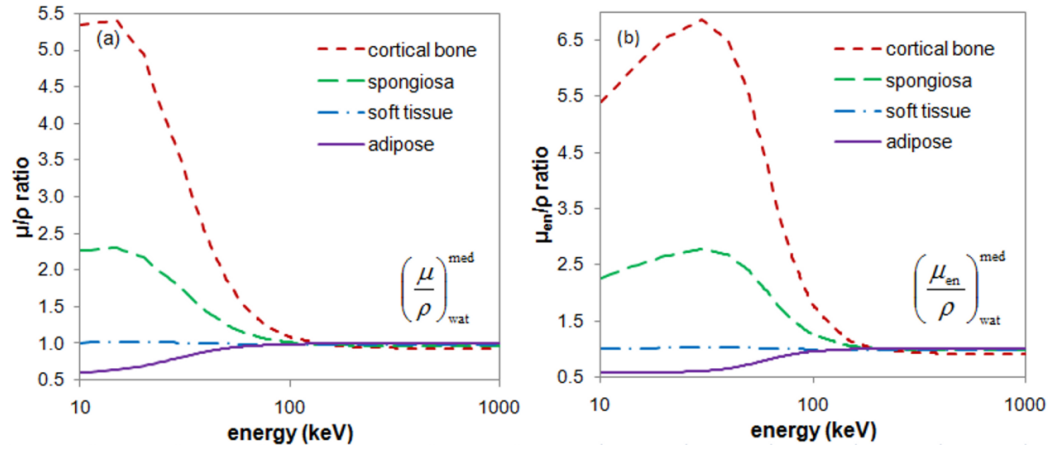


Figure 3.7. Effective $(\bar{\mu}/\rho)_{\text{wat}}^{\text{med}}$ and $(\bar{\mu}_{\text{en}}/\rho)_{\text{wat}}^{\text{med}}$ for four tissue media.

The degree of water equivalence for a given tissue type depends on the energy spectrum, which varies as the photons interact in the medium. Figure 3.7 shows that if the photon energies are mostly over 100 keV, then $(\bar{\mu}/\rho)_{\text{wat}}^{\text{med}}$ and $(\bar{\mu}_{\text{en}}/\rho)_{\text{wat}}^{\text{med}}$ are practically constant. Larger variations with energy can be expected below 50 keV. The values of $(\bar{\mu}_{\text{en}}/\rho)_{\text{wat}}^{\text{med}}$ for adipose and soft tissue are nearly constant at 1.00 and 0.99 respectively, while the values for bone depend on the $^{192}$Ir spectrum at the POI. The absorbed dose to medium $D_{\text{m}}$ and the absorbed dose to water $D_{\text{w}}$ may differ by up to 20–30% for bone. This is in contrast to $^{125}$I and $^{103}$Pd sources, for which $D_{\text{m}}$ may differ by 50% between soft tissue and adipose, and a factor of two between soft tissue and bone [26].

In Figure 3.8, the percentages of $^{192}$Ir photons below 50 and 100 keV versus distance in water and tissue phantoms are plotted. Our GEANT4 calculations show that only up to 4% of the primary photons are <100 keV, and very few are <50 keV. Hence, $D_{prim}$ is minimally affected by tissue composition variations. In contrast, the proportions of low-energy scattered photons increase with increasing distance. The increase is more gradual for higher-$Z$ media because of greater photoelectric absorption at low energies.

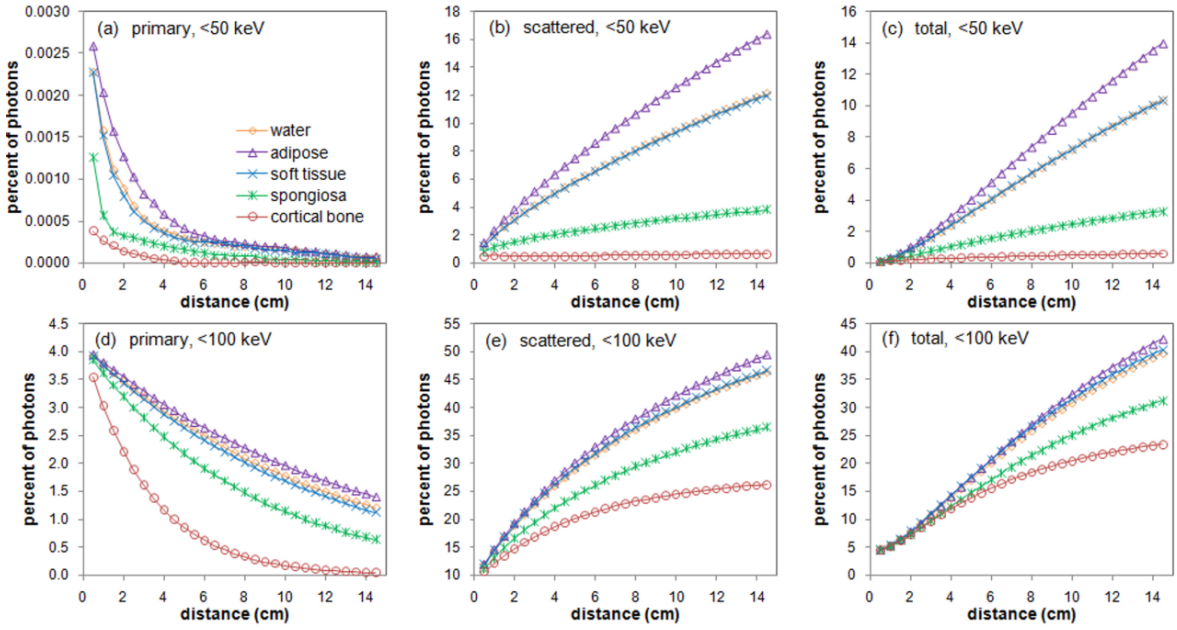


Figure 3.8. Percentages of primary, scattered, and all photons below 50 keV and 100 keV versus distance from an $^{192}$Ir source in various phantoms under full scatter conditions.

We also preformed GEANT4 simulations to examine spectral variations with distance for an $^{192}$Ir source in spherical phantoms of 5, 10, 15, and 50 cm radii. Figure 3.9 shows the mean energies of the primary, scattered, and all photons ( $\overline{E}_{prim}$, $\overline{E}_{scat}$, and $\overline{E}_{tot}$ ) versus distance in water. While $\overline{E}_{prim}$ increases slowly with increasing distance, the buildup of scattered photons leads to a gradual decrease in $\overline{E}_{scat}$ except near the surface where there is less photon backscatter.

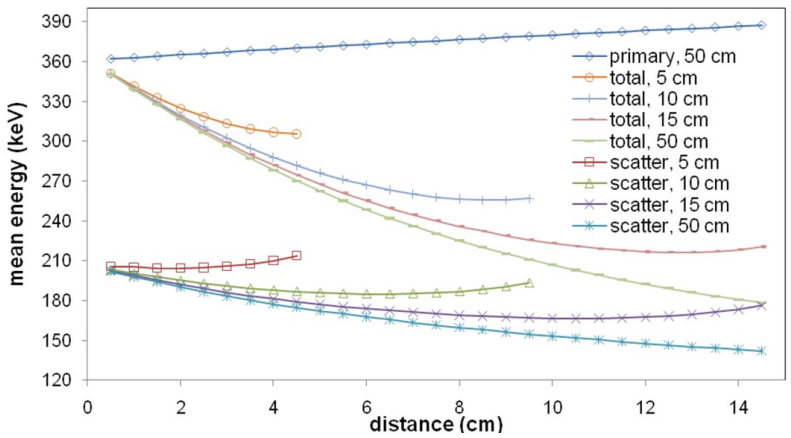


Figure 3.9. Mean energies of primary, scattered, and total photons versus distance from an HDR $^{192}$Ir source centered in water spheres of different radii.

Figure 3.10 shows similar trends of $\overline{E}$ variations with radiological distances in lung, adipose, soft tissue, spongiosa, and cortical bone phantoms under full scatter conditions. The higher $\overline{E}_{\text{scat}}$ for bone phantoms is a result of the greater importance of photoelectric effect, which causes more low-energy photons to be absorbed. And yet such deviations are unlikely in patient bodies because of the unrealistic thicknesses. Overall, the primary photons are only affected by the media between the source and the POI, while the scatter buildup depends also on the scattering volume. As the total $^{192}$Ir spectrum softens with distance, tissue inhomogeneity effects are greater at larger distances.

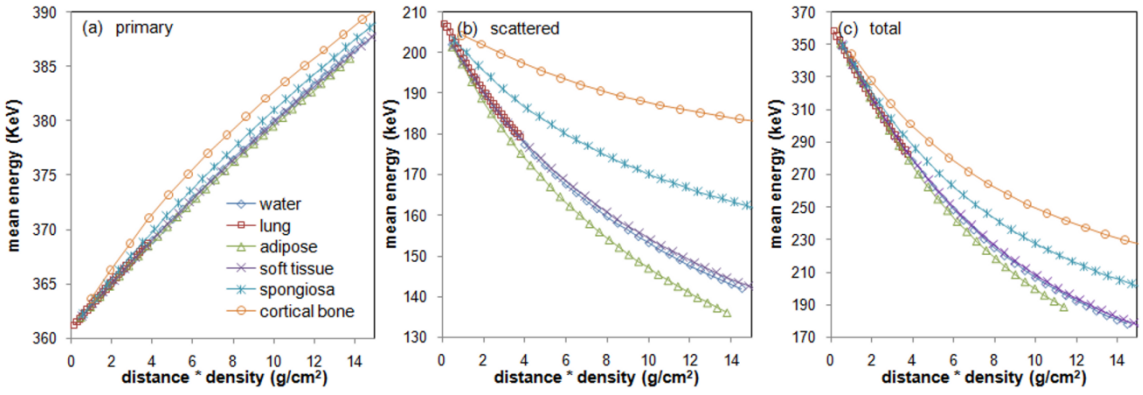


Figure 3.10. Mean energies of (a) primary, (b) scattered and (c) total photons versus radiological distance from an $^{192}$Ir source in tissue phantoms under full scatter conditions.

## 3.8. MONTE CARLO METHOD

The MC method is regarded as the most accurate approach for radiotherapy dose computation [89, 90]. It solves the radiation transport problem in terms of the Boltzmann transport equation by stochastic sampling of probability functions for a subset of particles interacting in a well-defined geometry [91, 92]. In the Boltzmann equation, the simulation geometry and the distribution of ionizing radiation in the system are characterized.

### 3.8.1. *Monte Carlo photon transport*

The MC method solves the Boltzmann transport equation stochastically by means of a random number generator using relevant cross section data. In $^{192}$Ir photon transport, the distance $d$ to the next interaction for a given photon depends on its linear attenuation coefficient $\mu$ and is determined by sampling a random number $r$ between 0 and 1:

$$d = -\frac{1}{\mu}\ln r \tag{3.29}$$

Another random number is sampled for determining the interaction type (photoelectric effect, Compton scattering, or Rayleigh scattering), which depends on the relative contribution of $\tau$, $\sigma_C$, and $\sigma_R$ to $\mu$. Differential cross sections are used to sample the energy and direction of the photon after an interaction. In a particle history, the trajectories of the photon and all secondary particles are tracked until they all exit the volume of interest, get absorbed in a photoelectric event, or possess energy below a cutoff. Quantities such as absorbed dose and particle fluence can be scored. A large number of histories must be tracked to reduce the statistical errors to an acceptable level. Provided the cross section data, the geometry modeling, and the interaction processes are correct, the MC method can be highly accurate regardless of the simulation complexity.

### 3.8.2. *Calculation efficiency and clinical applications*

The lengthy calculation time of the MC method is no longer a prohibitive factor for its clinical adaptation. In external beam radiotherapy, several MC codes are now being used in patient-specific treatment planning [93-96]. Variance reduction techniques [93] have been incorporated in these codes to improve the efficiency $\varepsilon$, defined as the inverse of the product of the calculation time $t$ and the variance estimate $\sigma^2$:

$$\varepsilon = \frac{1}{t\,\sigma^2} \tag{3.30}$$

Although MC codes are not yet available for clinical brachytherapy treatment planning, the MC method is often used to derive TG-43 parameters, study inhomogeneity effects, and benchmark against other dose calculation methods. It is also useful for verifying experimental results, since positioning shifts in the high dose-gradient region as well as energy and angular response issues may cause measurement errors. Conversely, experimental work is required to validate MC calculations since errors in the cross sections, geometry modeling, and other input parameters may not be easily detectable.

### 3.8.3. *Methods to calculate collision kerma*

In brachytherapy, $K_{\mathrm{col}}$ is often scored instead of the absorbed dose because $K_{\mathrm{col}}$ can be computed by more efficient means. Several kerma scoring methods have been investigated by Williamson [48]. The simplest approach is by *analog estimation*, which tallies energy transfers to uncharged particles directly as follows:

$$K_{\mathrm{col}} = \frac{1}{V\rho}\sum_j \left(w_{j-1}\,E_{j-1} - w_j\,E_j\right) \tag{3.31}$$

Here, $E_{\mathrm{j}}$ is the energy and $w_j$ is the weight of the photon at interaction $j$ that takes place within a scoring volume $V$ of density $\rho$.

Although analog scoring is straightforward to implement, more efficient kerma estimators are available. The *track-length estimation* (TLE) methods draw on the fact that the total photon pathlength per unit volume is equivalent to the photon fluence. Based upon Eq. (3.14), $K_{\mathrm{col}}$ can be calculated using the *linear TLE* method whereby the energy and weight of each photon traveling a distance $d_{\mathrm{j}}$ through the scoring voxel are tallied:

$$K_{\mathrm{col}} = \frac{1}{V}\sum_{j} w_j E_j d_j \frac{\mu_{\mathrm{en}}}{\rho}\left(E_j\right) \tag{3.32}$$

In a similar approach known as the *exponential TLE*, all photons whose trajectories in the forward direction intersect the scoring voxel contribute to $K_{\mathrm{col}}$. Ray tracing is required to compute straight-line distances of the trajectories. Details of the algorithm is described by Williamson [48].

Although the TLE methods require a longer CPU time per particle history than analog scoring, the efficiency can be improved by a factor of 2–50 [48, 97]. The efficiency gain depends on the simulation geometry and the photon spectrum. Both the TLE and the analog methods will converge to the expected results after sufficient particle histories have been simulated.

### 3.8.4. *Monte Carlo codes for brachytherapy applications*

The fast MC codes dedicated for external beam treatment planning are generally not useful for brachytherapy, since MC modeling of coupled photon-electron transport is unnecessary for photon-emitting sources except for $^{60}$Co and some $^{192}$Ir intravascular applications in which a correct dose in the near-source region is of interest. Besides, interactions important at low energies, such as bound Compton scattering and Rayleigh scattering, are not modeled in these codes.

The MC codes that have been identified as well benchmarked for brachytherapy dosimetry include the following [26]: EGS4 [43], BrachyDose [98], MCNP [45], MCNPX [57], PTRAN [48, 49], and GEANT4 [6]. This section will give a brief introduction to a few MC codes designed for brachytherapy applications.

*i.* *PTRAN*

PTRAN is an extensively validated MC photon transport code written by Williamson and his co-workers using FORTRAN [48, 49]. It can simulate photoelectric effect, characteristic x-ray production from the K and L shells, bound Compton scattering, Rayleigh scattering, and pair production followed by annihilation photon emission. The DLC-146 photon cross section library [99], considered up-to-date and the equivalent of XCOM [19] and EPDL97 [100], can be used. A variety of kerma scoring techniques are available [48]. $D_{prim}$ can be scored by analytical means via ray tracing.

Several variants of PTRAN are based on the PTRAN_CCG code. (CCG stands for complex combinatorial geometry.) PTRAN_CCG uses a geometric modelling system described by Li and Williamson [101]. It allows objects to be constructed by applying combinatorial operations (e.g. unions, intersections, and differences) on elemental volumes (e.g. elliptical cylinders, rectangular prisms, ellipsoids, cones, and angled planes). The volumes can be nested upon on another to any arbitrary depth.

PTRAN_CT is an extended version of PTRAN_CCG developed by Le et al. [102] for fast CT-based patient dose calculations. It allows applicators and sources to be defined independently of the patient geometry, represented by 3D matrices of material and density data derived from CT images. An integrated analytical and voxel ray tracing technique is used for efficient path length computation. A phase space source option is available for primary photon generation [35, 103]. $K_{col}$ is scored using an ETL estimator.

Hedtjärn et al. [97] modified PTRAN_CCG to allow for correlated sampling, a variance reduction technique described by Rief [104] and Lux and Koblinger [105]. In their method, photon histories are tracked in a homogeneous medium and dose differences caused by inhomogeneities are accounted for by means of weight correction factors. Considerable efficiency gain is achievable if the inhomogeneities only cause minor dose perturbations (<5%). This method does not work well when high-Z media are present, since it cannot model characteristic x-ray generation. The efficiency may in fact be compromised when the perturbations are in the order of 40–50% [97].

*ii. MCPI*

Chibani and Williamson [35] developed MCPI, a fast MC photon transport code for patient-specific prostate implant dosimetry. It is based on the general-purpose MC code GEPTS [106]. MCPI simulates photoelectric effect, bound Compton scattering, and Rayleigh scattering with relativistic atomic form factors. Characteristic x-ray emissions from K and L shells are modeled. The XCOM photon cross section data are used [19].

Similar to PTRAN_CT, MCPI allows brachytherapy seeds to be constructed independently of the patient geometry derived from CT images. There is a phase space source option for primary photon generation. $K_{col}$ is scored by the TLE method [48]. In a prostate implant calculation with 83 $^{103}$Pd seeds, a 2% uncertainty in the target required 59 s of CPU time for 2×2×2 mm$^3$ voxels using a single 2.4 GHz computer [35]. MCPI has not been tested for $^{192}$Ir applications, as more general algorithms for ray tracing along various applicator types are required. On the other hand, a longer CPU time will be needed for $^{192}$Ir dose calculations, since $^{192}$Ir photons lose energy in tissue mainly through Compton scattering [84] and the mean energy loss per interaction is less compared to that of low-energy sources.

*iii. BrachyDose*

BrachyDose is a user code of EGSnrc [107] designed for brachytherapy simulations by Yegin et al. [98]. EGSnrc can handle coupled photon-electron transport, which has been validated extensively and will be useful for modeling miniature x-ray sources. BrachyDose scores $K_{col}$ by the TLE method. Its accuracy has been verified by comparison with published TG-43 dosimetry parameters for various models of $^{125}$I, $^{103}$Pd, $^{169}$Yb, and $^{192}$Ir sources [80, 108]. Dose calculations for clinical prostate and eye plaque brachytherapy with low-energy seeds can be done in a few minutes using a single computer [98, 109].

*iv. Other MC codes*

Angelopoulos et al. [110] developed a MC code capable of coupled photon-electron transport. It was used to characterize the dose rate distributions around brachytherapy sources [12, 14, 70, 76], and to investigate the influence of $\beta$ particles in the near-source regions around $^{192}$Ir sources [14]. The code has been validated by TLD measurements [74].

Several researchers have modified existing MC codes for brachytherapy applications. Wang and Sloboda [111] modified EGS4 to handle bound Compton scattering and characteristic x-ray production so as to investigate $^{125}$I, $^{169}$Yb, and $^{192}$Ir source dosimetry. They later developed the DOSCGC user code to include a combinatorial geometry package for kerma calculations [112]. Chibani and Li [103] developed the IVBTMC code for intravascular brachytherapy based upon EGSnrc. Fragoso et al. [113] developed the EGSnrc user code GenUS, which also has a combinatorial geometry package useful for simulating complex brachytherapy source and applicator geometries.

## 3.9. OTHER DOSE CALCULATION METHODS

In addition to TG-43 and the MC method, various brachytherapy dose calculation techniques have been proposed. However, only a few correction-based methods have been adopted in the past for clinical use. The collapsed cone superposition and discrete ordinates techniques are promising alternatives to the MC method for patient-specific treatment planning for low-energy seed implant applications in the near future [26].

### 3.9.1. *Correction factors and lookup tables*

*i.* *Energy-absorption and tissue attenuation factors*

Before the introduction of the TG-43 protocol, brachytherapy dose distributions were traditionally derived from exposure assuming the source is a mathematical point in free space. The dose rate at a given distance was calculated using the apparent activity, the exposure rate constant, and an inverse square factor accounting for the dose falloff with distance. The theoretically based energy-absorption buildup factor proposed by Berger [114] or the experimentally derived tissue attenuation factor of Meisberger et al. [115] was used to account for the dose attenuation in water.

*ii.* *Extensions of TG-43 and 3D lookup tables*

The prevalent use of TG-43 has motivated its extension for dose calculations in inhomogeneous media. Rivard et al. [116] developed the Tufts technique in which TG-43 2D dosimetry parameters are derived by MC calculations considering the applicator together with the source configuration as a virtual source. This allows inhomogeneities to be accounted for using conventional TG-43-based treatment planning systems as long as the dose distributions exhibit cylindrical symmetry.

Watanabe et al. [51] generated 3D lookup tables by the MC method for dose calculations with the Henschke cervical applicator set. The tables included radial dose function $g(r)$ and anisotropy function $F(r, \theta, \varphi)$ to characterize the dose around each of the stainless-steel tandem and the tungsten-shielded ovoid. The extra dimension in $F(r, \theta, \varphi)$, which is the azimuth angle $\varphi$ in the spherical coordinate system, allows for dose distributions without cylindrical symmetry. However, this method cannot account for inter-applicator shielding effects.

*iii.* *Superposition of precalculated dose distributions*

Markman et al. [117] used an applicator-based dose superposition method for dose calculations around tandem and shielded ovoids. This method was also applied for a shielded endorectal applicator as described in Paper II. It requires a set of precalculated dose matrices around a single source for all possible dwell positions within an applicator in water. To calculate a patient plan, the appropriate dose matrix for each dwell position is scaled by a factor corresponding to the dwell time and the source strength. The final dose distribution is computed using the superposition principle with proper 3D coordinate transformations. This method fails to account for inter-applicator shielding effects.

### 3.9.2. *Attenuation and scatter correction methods*

*i.* *One-dimensional pathlength correction*

The *1D pathlength correction method* is a generalized form of the Sievert integral model [118] and is traditionally used to account for shielding attenuation in $^{137}$Cs brachytherapy [119-122]. In this method, the dose is scaled by an exponential attenuation factor which is a function of the pathlength along shielding and an effective transmission factor $\mu'$. The value of $\mu'$ can be derived from a *inhomogeneity correction factor*, defined

as the ratio of the dose at a point with shielding present to the dose at the same point in homogeneous water [50, 55]. This method gives an approximate dose since a constant $\mu'$ is used even though its value changes with the energy spectrum as photons interact in the medium. It is less accurate for $^{192}$Ir because of a larger perturbation of the SPR by shielding as well as a greater $D_{scat}$ contribution compared to $^{137}$Cs [39].

*ii.* *Scatter separation techniques*

Separate calculations of $D_{prim}$ and $D_{scat}$ have been suggested for brachytherapy source characterizations and dose calculations [39-41, 48, 123]. Williamson [38] introduced a scatter separation technique in which $D_{prim}$ is calculated by 1D pathlength correction whereas $D_{scat}$ is derived from MC-generated scatter dose ratio data tabulated as a function of distance. For shielded colpostats loaded with $^{137}$Cs or $^{226}$Ra sources, there is a ±20% variation in $D_{scat}$ compared to a factor-of-two variation with polar angle for $D_{prim}$ [38]. Since $D_{scat}$ ratios are relatively isotropic, their angular dependence is ignored in the tabulation. The method cannot account for the effects of the lateral dimensions of shielding. Also, it is less accurate for $^{192}$Ir sources because of the higher SPR [124].

A *1D scatter-subtraction method* was proposed by Williamson et al. [124] for dose calculations near 2D bounded density inhomogeneities. It is based on a scatter integration model introduced by Lulu and Bjärngard [125] for external $^{60}$Co beams. The method uses precalculated 2D SPR tables for collimated isotropic point sources. It accounts for the thickness and lateral dimensions of the inhomogeneity as well as its location relative to the POI. However, the inhomogeneities have to be of water-equivalent composition. Kirov and Williamson [126] later described a *2D scatter integration model* which is a generalized scatter subtraction method for 3D heterogeneities. Daskalov et al. [127] extended the method to account for high-Z inhomogeneities.

### 3.9.3. *Kernel superposition and convolution methods*

Point kernel superposition and convolution methods have been investigated for external beam radiotherapy [128-130] and brachytherapy applications [131, 132]. A point kernel describes the spatial distribution of dose around photon interaction sites and is often generated by the MC method. Kernel superposition is only needed to compute $D_{scat}$ since $D_{prim}$ can be derived analytically. The calculation involves a convolution of the total energy released per unit mass (terma) and the scatter point kernel over the irradiated volume. Kernel scaling and kernel tilting are CPU intensive operations used to account for inhomogeneities and to align the kernel along the primary beam direction [133]. The straightforward superposition method is considered too slow for clinical use [89].

Ahnesjö [134] developed the *collapsed-cone superposition method* to improve the efficiency for external photon beam calculations. As described by Carlsson Tedgren et al. [59, 132, 135, 136] who extended the method for brachytherapy applications, it requires [89]: (1) fitting the energy deposition kernels to exponential functions, (2) discretizing each kernel into a cone along which the transport is to take place, and (3) constructing a lattice of transport lines for the cone-axis directions to cover the calculation volume.

Kernel superposition methods are able to compute the first-scatter dose correctly, but not for the multiple-scatter dose. For instance, if the scatter point kernel is generated in a large phantom, $D_{scat}$ will be overestimated near the tissue-air interface when the multiple-scatter dose is significant [132]. In the *successive scattering superposition method*, doses contributed by once and multiply scattered photons are calculated sequentially [132]. It gives a more accurate multiple-scatter dose and reduces discrete-angle sampling artifacts in collapsed-cone superposition calculations [89].

The efficiency of the collapsed cone superposition algorithm has been optimized for low-energy sources by approximating the point kernels as isotropic [136]. However, this is not a valid approximation for $^{192}$Ir since the photon angular distribution is more forwardly directed [132]. The method is thus not yet feasible for $^{192}$Ir treatment planning.

### 3.9.4. *Discrete ordinates and analytical methods*

The radiation transport problem can be solved deterministically using the *discrete ordinates method*, in which the Boltzmann transport equation is discretized into a system of linear algebraic equations in the spatial, angular and energy domains [137-141]. Although deterministic codes are generally faster than the MC method, they have limited geometric modeling capabilities since a mesh-based approach is used in geometry construction. The discretization of the transport equation leads to artifacts such as ray effects. Gifford et al. [140] optimized the transport parameters for HDR $^{192}$Ir calculations and found an efficiency gain of 110 compared to MCNPX.

Anagnostopoulos et al. [84] developed an analytical dose calculation model for $^{192}$Ir brachytherapy. The dose rate per unit air kerma strength in a tissue medium ($\dot{D}_{\text{medium}}/S_{\text{K}}$) around an $^{192}$Ir point source is calculated as follows:

$$\frac{\dot{D}_{\text{medium}}}{S_K} = \left( \frac{\bar{\mu}_{\text{en}}}{\rho} \right)_{\text{air}}^{\text{medium}} \exp\left(-\bar{\mu}_{\text{medium}} r\right)\left[1 + SPR_{\text{water}}\left(\rho_{\text{medium}} r\right)\right]\frac{1}{r^2} \qquad (3.33)$$

$\left(\bar{\mu}_{\text{en}}/\rho\right)_{\text{air}}^{\text{medium}}$ and $\bar{\mu}_{\text{medium}}$ are energy fluence-weighted averages over the primary $^{192}$Ir spectrum. $SPR_{\text{water}}$ refers to the *SPR* derived in a water phantom, $\rho_{\text{medium}}$ is the density of the medium, and $r$ is the distance from the source. This technique has been generalized by Pantelis et al. [142] for encapsulated $^{192}$Ir sources. Its extension for patient-specific dose calculations is a subject of this thesis work and will be presented in Paper IV.

## 3.10. REFERENCES


1. Baltas D, Sakelliou L, Zamboglou N. Interaction properties of photons and electrons. The physics of modern brachytherapy for oncology. Boca Raton: Taylor & Francis; 2007. p. 87-140.

2. Williamson JF, Li Z. Monte Carlo aided dosimetry of the microselectron pulsed and high dose-rate $^{192}$Ir sources. Med Phys. 1995;22:809-19.

3. Daskalov GM, Loffler E, Williamson JF. Monte Carlo-aided dosimetry of a new high dose-rate brachytherapy source. Med Phys. 1998;25:2200-8.

4. Borg J, Rogers DW. Spectra and air-kerma strength for encapsulated $^{192}$Ir sources. Med Phys. 1999;26:2441-4.

5. Nuclear data from NuDat 2.0, a web-based database maintained by the National Nuclear Data Center [database on the Internet]. Brookhaven National Laboratory, Upton, NY 2004. Available from: http://www.nndc.bnl.gov/nudat2.

6. Agostinelli S, Allison J, Amako K, Apostolakis J, Araujo H, Arce P, et al. GEANT4-a simulation toolkit. Nucl Instrum Methods Phys Res A. 2003;506:250-303.

7. Glasgow GP, Dillman LT. Specific gamma-ray constant and exposure rate constant of $^{192}$Ir. Med Phys. 1979;6:49-52.

8. Kocher DC. Radioactive decay data tables: a handbook of decay data for application to radiation dosimetry and radiological assessments. Oak Ridge, TN: Technical Information Center, U.S. Dept. of Energy; 1981.

9. National Council on Radiation Protection and Measurements. A Handbook of radioactivity measurements procedures with nuclear data for some biomedically important radionuclides, reevaluated between August 1983 and April 1984. Bethesda, MD: National Council on Radiation Protection and Measurements; 1985. Available from: http://www.knovel.com/knovel2/Toc.jsp?BookID=1623.

10. Duchemin B, Coursol N. Reevaluation de '$^{192}$Ir, Technical Note LPRI/93/018. France: DAMRI, CEA; 1993. In: Borg J, Rogers DW. Spectra and air-kerma strength for encapsulated $^{192}$Ir sources. Med Phys. 1999;26:2441-4. .

11. Interstitial Collaborative Working Group. Interstitial brachytherapy: physical, biological, and clinical considerations. Anderson LL, Nath R, Weaver KA, editors. New York: Raven Press; 1990.

12. Angelopoulos A, Baras P, Sakelliou L, Karaiskos P, Sandilos P. Monte Carlo dosimetry of a new $^{192}$Ir high dose rate brachytherapy source. Med Phys. 2000;27:2521-7.

13. Wang R, Li XA. Dose characterization in the near-source region for two high dose rate brachytherapy sources. Med Phys. 2002;29:1678-86.

14. Baltas D, Karaiskos P, Papagiannis P, Sakelliou L, Loeffler E, Zamboglou N. Beta versus gamma dosimetry close to Ir-192 brachytherapy sources. Med Phys. 2001;28:1875-82.

15. Ballester F, Granero D, Pérez-Calatayud J, Melhus CS, Rivard MJ. Evaluation of high-energy brachytherapy source electronic disequilibrium and dose from emitted electrons. Med Phys. 2009;36:4250-6.

16. Klein O, Nishina Y. The scattering of light by free electrons according to Dirac's new relativistic dynamics. Nature. 1928;122:398-9.

17. Williamson JF, Deibel FC, Morin RL. The significance of electron binding corrections in Monte Carlo photon transport calculations. Phys Med Biol. 1984;29:1063-73.

18. Rivard MJ, Coursey BM, DeWerd LA, Hanson WF, Huq MS, Ibbott GS, et al. Update of AAPM Task Group No. 43 Report: A revised AAPM protocol for brachytherapy dose calculations. Med Phys. 2004;31:633-74.

19. XCOM: photon cross section database (version 1.4) [database on the Internet]. National Institute of Standards and Technology, Gaithersburg, MD. 2009 [cited Apr 28, 2009]. Available from: http://physics.nist.gov/PhysRefData/Xcom/Text/XCOM.html.

20. National Council on Radiation Protection and Measurements. Specification of gamma-ray brachytherapy sources. NCRP Report No. 41. Washington, DC: Government Printing Office; 1974.

21. International Commission on Radiation Units and Measurements. Dose and volume specification for reporting intracavitary therapy in gynecology. Bethesda, MD: ICRU; 1985.

22. International Commission on Radiation Units and Measurements. Fundamental quantities and units for ionizing radiation. Bethesda, MD: ICRU; 1998.

23. American Association of Physicists in Medicine. Specification of brachytherapy source strength. New York: American Institute of physics.1987. Report No.: 21.

24. Nath R, Anderson LL, Luxton G, Weaver KA, Williamson JF, Meigooni AS. Dosimetry of interstitial brachytherapy sources: recommendations of the AAPM Radiation Therapy Committee Task Group No. 43. American Association of Physicists in Medicine. Med Phys. 1995;22:209-34.

25. Williamson JF. The accuracy of the line and point source approximations in Ir-192 dosimetry. Int J Radiat Oncol Biol Phys. 1986;12:409-14.

26. Thomadsen BR, Williamson JF, Rivard MJ, Meigooni AS. Anniversary paper: past and current issues, and trends in brachytherapy physics. Med Phys. 2008;35:4708-23.

27. Li Z, Das RK, DeWerd LA, Ibbott GS, Meigooni AS, Pérez-Calatayud J, et al. Dosimetric prerequisites for routine clinical use of photon emitting brachytherapy sources with average energy higher than 50 keV. Med Phys. 2007;34:37-40.

28. Chiu-Tsao ST, Schaart DR, Soares CG, Nath R. Dose calculation formalisms and consensus dosimetry parameters for intravascular brachytherapy dosimetry: recommendations of the AAPM Therapy Physics Committee Task Group No. 149. Med Phys. 2007;34:4126-57.

29. Rivard MJ, Davis SD, DeWerd LA, Rusch TW, Axelrod S. Calculated and measured brachytherapy dosimetry parameters in water for the Xoft Axxent X-Ray Source: an electronic brachytherapy source. Med Phys. 2006;33:4020-32.

30. Lessard E, Pouliot J. Inverse planning anatomy-based dose optimization for HDR-brachytherapy of the prostate using fast simulated annealing algorithm and dedicated objective function. Med Phys. 2001;28:773-9.

31. Carrier JF, Beaulieu L, Therriault-Proulx F, Roy R. Impact of interseed attenuation and tissue composition for permanent prostate implants. Med Phys. 2006;33:595-604.

32. Carrier JF, D'Amours M, Verhaegen F, Reniers B, Martin AG, Vigneault E, et al. Postimplant dosimetry using a Monte Carlo dose calculation engine: a new clinical standard. Int J Radiat Oncol Biol Phys. 2007;68:1190-8.

33. Furstoss C, Reniers B, Bertrand MJ, Poon E, Carrier JF, Keller BM, et al. Monte Carlo study of LDR seed dosimetry with an application in a clinical brachytherapy breast implant. Med Phys. 2009;36:1848-58.

34. Afsharpour H, D'Amours M, Coté B, Carrier JF, Verhaegen F, Beaulieu L. A Monte Carlo study on the effect of seed design on the interseed attenuation in permanent prostate implants. Med Phys. 2008;35:3671-81.

35. Chibani O, Williamson JF. MCPI: a sub-minute Monte Carlo dose calculation engine for prostate implants. Med Phys. 2005;32:3688-98.

36. Chibani O, Williamson JF, Todor D. Dosimetric effects of seed anisotropy and interseed attenuation for $^{103}$Pd and $^{125}$I prostate implants. Med Phys. 2005;32:2557-66.

37. Meigooni AS, Meli JA, Nath R. Interseed effects on dose for $^{125}$I brachytherapy implants. Med Phys. 1992;19:385-90.

38. Williamson JF. Dose calculations about shielded gynecological colpostats. Int J Radiat Oncol Biol Phys. 1990;19:167-78.

39. Williamson JF. The Sievert integral revisited: evaluation and extension to $^{125}$I, $^{169}$Yb, and $^{192}$Ir brachytherapy sources. Int J Radiat Oncol Biol Phys. 1996;36:1239-50.

40. Russell KR, Ahnesjo A. Dose calculation in brachytherapy for a $^{192}$Ir source using a primary and scatter dose separation technique. Phys Med Biol. 1996;41:1007-24.

41. Russell KR, Carlsson Tedgren ÅK, Ahnesjö A. Brachytherapy source characterization for improved dose calculations using primary and scatter dose separation. Med Phys. 2005;32:2739-52.

42. Lymperopoulou G, Pantelis E, Papagiannis P, Rozaki-Mavrouli H, Sakelliou L, Baltas D, et al. A Monte Carlo dosimetry study of vaginal $^{192}$Ir brachytherapy applications with a shielded cylindrical applicator set. Med Phys. 2004;31:3080-6.

43. Nelson WR, Hirayama H, Rogers DWO. The EGS4 code system. Stanford: Stanford Linear Accelerator Center 1985. Report No.: SLAC-265.

44. Ye SJ, Brezovich IA, Shen S, Duan J, Popple RA, Pareek PN. Attenuation of intracavitary applicators in $^{192}$Ir-HDR brachytherapy. Med Phys. 2004;31:2097-106.

45. MCNP-a general Monte Carlo N-particle transport code. Version 4A. Briesmeister JF, editor. Los Alamos, NM: Los Alamos National Laboratory 1993.

46. Parsai EI, Zhang Z, Feldmeier JJ. A quantitative three-dimensional dose attenuation analysis around Fletcher-Suit-Delclos due to stainless steel tube for high-dose-rate brachytherapy by Monte Carlo calculations. Brachytherapy. 2009;8:318-23.

47. Tod M, Meredith WJ. Treatment of cancer of the cervix uteri, a revised Manchester method. Br J Radiol. 1953;26:252-7.

48. Williamson JF. Monte Carlo evaluation of kerma at a point for photon transport problems. Med Phys. 1987;14:567-76.

49. Williamson JF. Comparison of measured and calculated dose rates in water near I-125 and Ir-192 seeds. Med Phys. 1991;18:776-86.

50. Waterman FM, Holcomb DE. Dose distributions produced by a shielded vaginal cylinder using a high-activity iridium-192 source. Med Phys. 1994;21:101-6.

51. Watanabe Y, Roy JN, Harrington PJ, Anderson LL. Three-dimensional lookup tables for Henschke applicator cervix treatment by HDR $^{192}$IR remote afterloading. Int J Radiat Oncol Biol Phys. 1998;41:1201-7.

52. Vuong T, Devic S, Moftah B, Evans M, Podgorsak EB. High-dose-rate endorectal brachytherapy in the treatment of locally advanced rectal carcinoma: technical aspects. Brachytherapy. 2005;4:230-5.

53. Meigooni AS, Zhu Y, Williamson JF, Myerson RJ, Teague S, Loffler E, et al. Design and dosimetric characteristics of a high dose rate remotely afterloaded endocavitary applicator system. Int J Radiat Oncol Biol Phys. 1996;34:1153-63.

54. Kirov AS, Williamson JF, Meigooni AS, Zhu Y. Measurement and calculation of heterogeneity correction factors for an Ir-192 high dose-rate brachytherapy source behind tungsten alloy and steel shields. Med Phys. 1996;23:911-9.

55. Verellen D, De Neve W, Van den Heuvel F, Storme G, Coen V, Coghe M. On the determination of the effective transmission factor for stainless steel ovoid shielding segments and estimation of their shielding efficacy for the clinical situation. Med Phys. 1994;21:1677-84.

56. Williamson JF, Perera H, Li Z, Lutz WR. Comparison of calculated and measured heterogeneity correction factors for $^{125}$I, $^{137}$Cs, and $^{192}$Ir brachytherapy sources near localized heterogeneities. Med Phys. 1993;20:209-22.

57. Hendricks JS, McKinney GW, Waters LS, Hughes HG. MCNPX user's manual, version 2.4.0. Los Alamos, NM: Los Alamos National Laboratory 2002.

58. Muench PJ, Nath R. Dose distributions produced by shielded applicators using $^{241}$Am for intracavitary irradiation of tumors in the vagina. Med Phys. 1992;19:1299-306.

59. Carlsson Tedgren ÅK, Ahnesjö A. Accounting for high Z shields in brachytherapy using collapsed cone superposition for scatter dose calculation. Med Phys. 2003;30:2206-17.

60. Ye SJ, Brezovich IA, Shen S, Kim S. Dose errors due to inhomogeneities in balloon catheter brachytherapy for breast cancer. Int J Radiat Oncol Biol Phys. 2004;60:672-7.

61. Papagiannis P, Karaiskos P, Georgiou E, Baltas D, Lymperopoulou G, Pantelis E, et al. On the use of high dose rate $^{192}$Ir and $^{169}$Yb sources with the MammoSite radiation therapy system. Med Phys. 2007;34:3614-9.

62. Cheng CW, Mitra R, Li XA, Das IJ. Dose perturbations due to contrast medium and air in MammoSite treatment: an experimental and Monte Carlo study. Med Phys. 2005;32:2279-87.

63. Kirk MC, Hsi WC, Chu JC, Niu H, Hu Z, Bernard D, et al. Dose perturbation induced by radiographic contrast inside brachytherapy balloon applicators. Med Phys. 2004;31:1219-24.

64. Kassas B, Mourtada F, Horton JL, Lane RG. Contrast effects on dosimetry of a partial breast irradiation system. Med Phys. 2004;31:1976-9.

65. Oh S, Scott J, Shin DH, Suh TS, Kim S. Measurements of dose discrepancies due to inhomogeneities and radiographic contrast in balloon catheter brachytherapy. Med Phys. 2009;36:3945-54.

66. Melhus CS, Rivard MJ. Approaches to calculating AAPM TG-43 brachytherapy dosimetry parameters for $^{137}$Cs, $^{125}$I, $^{192}$Ir, $^{103}$Pd, and $^{169}$Yb sources. Med Phys. 2006;33:1729-37.

67. Pérez-Calatayud J, Granero D, Ballester F. Phantom size in brachytherapy source dosimetric studies. Med Phys. 2004;31:2075-81.

68. Granero D, Perez-Calatayud J, Pujades-Claumarchirant MC, Ballester F, Melhus CS, Rivard MJ. Equivalent phantom sizes and shapes for brachytherapy dosimetric studies of $^{192}$Ir and $^{137}$Cs. Med Phys. 2008;35:4872-7.

69. Mauceri T, Biggs P, Beatty J, Flynn D. Scatter and attenuation measurements at distances greater than 10 cm from an $^{192}$Ir source. Med Phys. 1999;26:97-9.

70. Sakelliou L, Sakellariou K, Sarigiannis K, Angelopoulos A, Perris A, Zarris G. Dose rate distributions around $^{60}$Co, $^{137}$Cs, $^{198}$Au, $^{192}$Ir, $^{241}$Am, $^{125}$I (models 6702 and 6711) brachytherapy sources and the nuclide $^{99}$Tcm. Phys Med Biol. 1992;37:1859-72.

71. Ellett WH. Specific absorbed fractions for photon point sources within a scattering medium. Phys Med Biol. 1969;14:615-26.

72. Melchert C, Kohr P, Schmidt R. Calculation of dose decrease in a finite phantom of a $^{192}$Ir point source. Med Phys. 2007;34:3943-50.

73. Nath R, Meigooni AS, Meli JA. Dosimetry on transverse axes of $^{125}$I and $^{192}$Ir interstitial brachytherapy sources. Med Phys. 1990;17:1032-40.

74. Karaiskos P, Angelopoulos A, Sakelliou L, Sandilos P, Antypas C, Vlachos L, et al. Monte Carlo and TLD dosimetry of an $^{192}$Ir high dose-rate brachytherapy source. Med Phys. 1998;25:1975-84.

75. Papagiannis P, Angelopoulos A, Pantelis E, Sakelliou L, Baltas D, Karaiskos P, et al. Dosimetry comparison of $^{192}$Ir sources. Med Phys. 2002;29:2239-46.

76. Karaiskos P, Angelopoulos A, Baras P, Sakelliou L, Sandilos P, Dardoufas K, et al. A Monte Carlo investigation of the dosimetric characteristics of the VariSource $^{192}$Ir high dose rate brachytherapy source. Med Phys. 1999;26:1498-502.

77. Karaiskos P, Papagiannis P, Angelopoulos A, Sakelliou L, Baltas D, Sandilos P, et al. Dosimetry of $^{192}$Ir wires for LDR interstitial brachytherapy following the AAPM TG-43 dosimetric formalism. Med Phys. 2001;28:156-66.

78. Pantelis E, Baltas D, Dardoufas K, Karaiskos P, Papagiannis P, Rosaki-Mavrouli H, et al. On the dosimetric accuracy of a Sievert integration model in the proximity of $^{192}$Ir HDR sources. Int J Radiat Oncol Biol Phys. 2002;53:1071-84.

79. Wang R, Sloboda RS. Influence of source geometry and materials on the transverse axis dosimetry of $^{192}$Ir brachytherapy sources. Phys Med Biol. 1998;43:37-48.

80. Taylor RPE, Rogers DWO. EGSnrc Monte Carlo calculated dosimetry parameters for $^{192}$Ir and $^{169}$Yb brachytherapy sources. Med Phys. 2008;35:4933-44.

81. Pantelis E, Papagiannis P, Karaiskos P, Angelopoulos A, Anagnostopoulos G, Baltas D, et al. The effect of finite patient dimensions and tissue inhomogeneities on dosimetry planning of $^{192}$Ir HDR breast brachytherapy: a Monte Carlo dose verification study. Int J Radiat Oncol Biol Phys. 2005;61:1596-602.

82. Mangold CA, Rijnders A, Georg D, Van Limbergen E, Pötter R, Huyskens D. Quality control in interstitial brachytherapy of the breast using pulsed dose rate: treatment planning and dose delivery with an Ir-192 afterloading system. Radiother Oncol. 2001;58:43-51.

83. Raina S, Avadhani JS, Oh M, Malhotra HK, Jaggernauth W, Kuettel MR, et al. Quantifying IOHDR brachytherapy underdosage resulting from an incomplete scatter environment. Int J Radiat Oncol Biol Phys. 2005;61:1582-6.

84. Anagnostopoulos G, Baltas D, Karaiskos P, Pantelis E, Papagiannis P, Sakelliou L. An analytical dosimetry model as a step towards accounting for inhomogeneities and bounded geometries in $^{192}$Ir brachytherapy treatment planning. Phys Med Biol. 2003;48:1625-47.

85. Meigooni AS, Nath R. Tissue inhomogeneity correction for brachytherapy sources in a heterogeneous phantom with cylindrical symmetry. Med Phys. 1992;19:401-7.

86. Anagnostopoulos G, Baltas D, Pantelis E, Papagiannis P, Sakelliou L. The effect of patient inhomogeneities in oesophageal $^{192}$Ir HDR brachytherapy: a Monte Carlo and analytical dosimetry study. Phys Med Biol. 2004;49:2675-85.

87. Hubbell JH, Seltzer SM. Tables of x-ray mass attenuation coefficients and mass energy-absorption coefficients 1 keV to 20 MeV for elements Z=1 to 92 and 48 additional substances of dosimetric interest. Gaithersburg, MD: National Institute of Standards and Technology 1995. Report No.: NISTIR 5632.

88. International Commission on Radiation Units and Measurements. Tissue substitutes in radiation dosimetry and measurement. Bethesda, MD: ICRU; 1989.

89. Carlsson Tedgren ÅK. Development of dose calculation methods for brachytherapy treatment planning [dissertation]. Stockholm: Stockholm University; 2003.

90. Chetty IJ, Curran B, Cygler JE, DeMarco JJ, Ezzell G, Faddegon BA, et al. Report of the AAPM Task Group No. 105: issues associated with clinical implementation of Monte Carlo-based photon and electron external beam treatment planning. Med Phys. 2007;34:4818-53.

91. Williamson JF. Radiation transport calculations in treatment planning. Comput Med Imaging Graph. 1989;13:251-68.

92. Rogers DWO, Bielajew AF. Monte Carlo techniques of electron and photon transport for radiation dosimetry. In: Kase KR, Bjärngard BE, Attix FH, editors. The dosimetry of ionizing radiation. New York: Academic; 1990. p. 427-539.

93. Kawrakow I, Fippel M. Investigation of variance reduction techniques for Monte Carlo photon dose calculation using XVMC. Phys Med Biol. 2000;45:2163-83.

94. Hartmann Siantar CL, Walling RS, Daly TP, Faddegon B, Albright N, Bergstrom P, et al. Description and dosimetric verification of the PEREGRINE Monte Carlo dose calculation system for photon beams incident on a water phantom. Med Phys. 2001;28:1322-37.

95. Sempau J, Wilderman SJ, Bielajew AF. DPM, a fast, accurate Monte Carlo code optimized for photon and electron radiotherapy treatment planning dose calculations. Phys Med Biol. 2000;45:2263-91.

96. Ma CM, Li JS, Pawlicki T, Jiang SB, Deng J, Lee MC, et al. A Monte Carlo dose calculation tool for radiotherapy treatment planning. Phys Med Biol. 2002;47:1671-89.

97. Hedtjärn H, Carlsson GA, Williamson JF. Accelerated Monte Carlo based dose calculations for brachytherapy planning using correlated sampling. Phys Med Biol. 2002;47:351-76.

98. Taylor RE, Yegin G, Rogers DW. Benchmarking BrachyBose: voxel based EGSnrc Monte Carlo calculations of TG-43 dosimetry parameters. Med Phys. 2007;34:445-57.

99. Radiation Safety Information Computational Center. HUGO-VI: Photon Interaction Data in ENDF/B-VI Format. Oak Ridge, TN Oak Ridge National Laboratory; 1989.

100. Cullen DE, Hubbell JH, Kissel L. EPDL97: The Evaluated Photon Data Library, '97 Version. Livermore, CA: Lawrence Livermore National Laboratory1997. Report No.: UCRL-50400, Rev. 5.

101. Li Z, Williamson JF. Volume-based geometric modeling for radiation transport calculations. Med Phys. 1992;19:667-77.

102. Le Y, Chibani O, Todor D, Siebers I, Williamson J. An integrated CT-based Monte Carlo dose-evaluation system for brachytherapy and its application to permanent prostate implant postprocedure dosimetric analysis. Med Phys. 2005;32:2068.

103. Chibani O, Li XA. IVBTMC, a Monte Carlo dose calculation tool for intravascular brachytherapy. Med Phys. 2003;30:44-51.

104. Rief H. Generalized Monte Carlo perturbation algorithms for correlated sampling and a second-order Taylor series approach. Ann Nucl Ener. 1984;11:455-76.

105. Lux I, Koblinger L. Monte Carlo particle transport methods: neutron and photon calculations. Boca Raton, FL: CRC Press; 1991.

106. Chibani O. Electron depth dose distributions in water, iron and lead: the GEPTS system. Nucl Instrum Methods Phys Res B. 1995;101:357-78.

107. Kawrakow I. Accurate condensed history Monte Carlo simulation of electron transport. I. EGSnrc, the new EGS4 version. Med Phys. 2000;27:485-98.

108. Taylor RE, Rogers DW. An EGSnrc Monte Carlo-calculated database of TG-43 parameters. Med Phys. 2008;35:4228-41.

109. Thomson RM, Taylor RE, Rogers DW. Monte Carlo dosimetry for $^{125}$I and $^{103}$Pd eye plaque brachytherapy. Med Phys. 2008;35:5530-43.

110. Angelopoulos A, Perris A, Sakellariou K, Sakelliou L, Sarigiannis K, Zarris G. Accurate Monte Carlo calculations of the combined attenuation and build-up factors, for energies (20-1500 keV) and distances (0-10 cm) relevant in brachytherapy. Phys Med Biol. 1991;36:763-78.

111. Wang R, Sloboda RS. EGS4 dosimetry calculations for cylindrically symmetric brachytherapy sources. Med Phys. 1996;23:1459-65.

112. Sloboda RS, Wang R. Combined experimental and Monte Carlo verification of $^{137}$Cs brachytherapy plans for vaginal applicators. Phys Med Biol. 1998;43:3495-507.

113. Fragoso M, Seco J, Nahum AE, Verhaegen F. Incorporation of a combinatorial geometry package and improved scoring capabilities in the EGSnrc Monte Carlo Code system. Med Phys. 2003;30:1076-85.

114. Berger MJ. Energy deposition in water by photons from point isotropic sources. J Nucl Med. 1968:Suppl 1:17-25.

115. Meisberger LL, Keller RJ, Shalek RJ. The effective attenuation in water of the gamma rays of gold 198, iridium 192, cesium 137, radium 226, and cobalt 60. Radiology. 1968;90:953-7.

116. Rivard MJ, Melhus CS, Granero D, Perez-Calatayud J, Ballester F. An approach to using conventional brachytherapy software for clinical treatment planning of complex, Monte Carlo-based brachytherapy dose distributions. Med Phys. 2009;36:1968-75.

117. Markman J, Williamson JF, Dempsey JF, Low DA. On the validity of the superposition principle in dose calculations for intracavitary implants with shielded vaginal colpostats. Med Phys. 2001;28:147-55.

118. Sievert RM. Die intensitätsverteilung der primären γ-strahlung in der nähe medizinischer radiumpräparate. Acta Radiol. 1921;1:89-128.

119. Prasad SC, Bassano DA, Kubsad SS. Buildup factors and dose around a $^{137}$Cs source in the presence of inhomogeneities. Med Phys. 1983;10:705-8.

120. Meertens H, van der Laarse R. Screens in ovoids of a Selectron cervix applicator. Radiother Oncol. 1985;3:69-80.

121. van der Laarse R, Meertens H. An algorithm for ovoid shielding of a cervix applicator. In: Cunningham JR, Ragan D, Van Dyk J, editors. 8th International Conference on the Use of Computers in Radiation Therapy; July 9-12, 1984; Toronto, Canada. Los Angeles, CA: IEEE Computer Society; 1984. p. 364-9.

122. Diffey BL, Klevenhagen SC. An experimental and calculated dose distribution in water around CDC K-type caesium-137 sources. Phys Med Biol. 1975;20:446-54.

123. Wang R, Sloboda RS. Brachytherapy scatter dose calculation in heterogeneous media: I. a microbeam ray-tracing method for the single-scatter contribution. Phys Med Biol. 2007;52:5619-36.

124. Williamson JF, Li Z, Wong JW. One-dimensional scatter-subtraction method for brachytherapy dose calculation near bounded heterogeneities. Med Phys. 1993;20:233-44.

125. Lulu BA, Bjärngard BE. Batho's correction factor combined with scatter summation. Med Phys. 1982;9:372-7.

126. Kirov AS, Williamson JF. Two-dimensional scatter integration method for brachytherapy dose calculations in 3D geometry. Phys Med Biol. 1997;42:2119-35.

127. Daskalov GM, Kirov AS, Williamson JF. Analytical approach to heterogeneity correction factor calculation for brachytherapy. Med Phys. 1998;25:722-35.

128. Ahnesjö A, Andreo P, Brahme A. Calculation and application of point spread functions for treatment planning with high energy photon beams. Acta Oncol. 1987;26:49-56.

129. Mackie TR, Scrimger JW, Battista JJ. A convolution method of calculating dose for 15-MV x rays. Med Phys. 1985;12:188-96.

130. Mohan R, Chui C, Lidofsky L. Differential pencil beam dose computation model for photons. Med Phys. 1986;13:64-73.

131. Williamson JF, Baker RS, Li ZF. A convolution algorithm for brachytherapy dose computations in heterogeneous geometries. Med Phys. 1991;18:1256-65.

132. Carlsson AK, Ahnesjo A. Point kernels and superposition methods for scatter dose calculations in brachytherapy. Phys Med Biol. 2000;45:357-82.

133. Sharpe MB, Battista JJ. Dose calculations using convolution and superposition principles: the orientation of dose spread kernels in divergent x-ray beams. Med Phys. 1993;20:1685-94.

134. Ahnesjö A. Collapsed cone convolution of radiant energy for photon dose calculation in heterogeneous media. Med Phys. 1989;16:577-92.

135. Carlsson ÅK, Ahnesjö A. The collapsed cone superposition algorithm applied to scatter dose calculations in brachytherapy. Med Phys. 2000;27:2320-32.

136. Carlsson Tedgren Å, Ahnesjö A. Optimization of the computational efficiency of a 3D, collapsed cone dose calculation algorithm for brachytherapy. Med Phys. 2008;35:1611-8.

137. Daskalov GM, Baker RS, Rogers DW, Williamson JF. Dosimetric modeling of the microselectron high-dose rate $^{192}$Ir source by the multigroup discrete ordinates method. Med Phys. 2000;27:2307-19.

138. Zhou C, Inanc F. Integral-transport-based deterministic brachytherapy dose calculations. Phys Med Biol. 2003;48:73-93.

139. Gifford KA, Horton JL, Wareing TA, Failla G, Mourtada F. Comparison of a finite-element multigroup discrete-ordinates code with Monte Carlo for radiotherapy calculations. Phys Med Biol. 2006;51:2253-65.

140. Gifford KA, Price MJ, Horton JL, Jr., Wareing TA, Mourtada F. Optimization of deterministic transport parameters for the calculation of the dose distribution around a high dose-rate $^{192}$Ir brachytherapy source. Med Phys. 2008;35:2279-85.

141. Vassiliev ON, Wareing TA, Davis IM, McGhee J, Barnett D, Horton JL, et al. Feasibility of a multigroup deterministic solution method for three-dimensional radiotherapy dose calculations. Int J Radiat Oncol Biol Phys. 2008;72:220-7.

142. Pantelis E, Papagiannis P, Anagnostopoulos G, Baltas D, Karaiskos P, Sandilos P, et al. Evaluation of a TG-43 compliant analytical dosimetry model in clinical $^{192}$Ir HDR brachytherapy treatment planning and assessment of the significance of

source position and catheter reconstruction uncertainties. Phys Med Biol. 2004;49:55-67.

# Chapter Four

# Development of an Integrated Brachytherapy Treatment Planning Tool



## 4.1. INTRODUCTION TO BRACHYGUI

An integral part of this thesis work has been the development of BrachyGUI, a treatment planning and dose evaluation tool. It is designed to streamline the process of patient-specific brachytherapy dose calculations with various calculation algorithms. To this end, BrachyGUI can process DICOM-RT* files exported from brachytherapy planning systems, and serves as a useful adjunct to MC codes. BrachyGUI also allows for 3D dose distribution comparison for both brachytherapy and external beam applications. Its capabilities are summarized in Table 4.1.

* DICOM-RT is an extension of the DICOM 3.0 standard which includes the radiotherapy modality.

Table 4.1.Capabilities of BrachyGUI.

| Category | Capabilities |
|---|---|
| Display options | - Single- and multi-panel displays<br>- Axial, coronal, and sagittal views<br>- Isodose lines and dose colorwash<br>- Thumbnail view for slice selection<br>- Fusion of registered images |
| Treatment planning | - Catheter construction<br>- Dwell position activation<br>- Dwell weight modification<br>- Reference dose point specification<br>- Structure contouring<br>- Rigid-body image registration<br>- 3D view of treatment plan<br>- Treatment plan optimization |
| Dose calculation | - Creation of 3D material and density matrices from CT images<br>- TG-43 1D and 2D formalisms<br>- Dose superposition method<br>- Scatter correction algorithm<br>- CT-based analytical dose calculation<br>- Interface to the PTRAN_CT MC code |
| Dose evaluation | - Dose transformation, summation, and normalization<br>- Cumulative, differential, and natural dose-volume histograms<br>- Dose-volume, plan-quality, and gamma index calculations<br>- Dose-difference, dose-ratio, and gamma map displays<br>- Profile plotting |

BrachyGUI is coded in MATLAB (versions 7.5.0 and 7.7.0, The Mathworks, Natick, MA), a numeric computing environment that comes with a variety of built-in functions for ease of data visualization, matrix arithmetic, image processing, and graphical user-interface development. Since the codes are interpreted at run time, MATLAB suffers from a slower speed compared with compiled languages such as C, FORTRAN, and REALbasic. To improve efficiency, the dose calculation algorithms in BrachyGUI are written in C and then compiled into MATLAB-executable functions.

The CERR [1] and DOSCTP [2] software packages, developed also in MATLAB, are available for research in radiotherapy treatment planning. However, a dedicated research environment for brachytherapy is lacking. Its importance is noted by Kirisits et al. [3], who found different brachytherapy planning systems gave discrepant dose volume histograms (DVHs) for the same patient plan. This is due to differences in structure volume determination and sampling points used for DVH analysis, and is more evident when the structure is small and the dose gradient within it is high. In this respect, BrachyGUI facilitates better consistency in calculation algorithm comparison studies.

## 4.2. INPUT AND OUTPUT FILES

### 4.2.1. *Conversion of DICOM-RT files*

Images of various modalities such as CT, cone-beam CT, MRI, and ultrasound can be displayed in BrachyGUI. Once the associated DICOM files have been imported, the user may create a composite image set by specifying the slices and region of interest, as well as voxel sizes if changes in resolution are desired. The 3D image set may then be saved as a binary file for faster loading in subsequent sessions. For patient-specific dose calculations, CT image data can be converted to 3D material and density matrices in the *egsphant* format [4]. Details of this conversion procedure will be described in Section 4.5.

BrachyGUI can read DICOM-RT structure, treatment plan, and dose distribution object files. The structure contour and treatment planning data (e.g. source strength, dwell positions, and dwell times) are processed by BrachyGUI and then converted to ASCII files. In this way, direct modifications to such data can be made without the need to save them as DICOM-RT objects. On the other hand, dose distribution data are converted to the *3ddose* format [4]. The dose grid resolution can be changed during the file conversion.

### 4.2.2. *DOSXYZnrc egsphant and 3ddose files*

The *egsphant* and *3ddose* files, described in the DOSXYZnrc user manual [4], are in ASCII format. BrachyGUI can convert these files between ASCII and binary formats. The binary format is preferred because it is faster to load and more compact in size, albeit unusable outside of BrachyGUI. All dose distributions generated by BrachyGUI are in the binary *3ddose* format unless the user specifies otherwise.

### 4.2.3. *XVMC dmx*, *d3d*, and *err files*

In the XVMC MC code [5] for external beam photon applications, the density, dose, and uncertainty data are stored as binary files with extension names *dmx*, *d3d* and *err*, respectively. These files, together with the associated header files that specify the 3D voxel grid, can be imported directly into BrachyGUI for dose evaluation without first converting to the corresponding *egsphant* and *3ddose* formats.

### 4.2.4. *PTRAN_CT input initialization files*

BrachyGUI facilitates CT-based patient dose calculations with PTRAN_CT [6], as described in an article by Poon et al. [7] entitled "*BrachyGUI: an adjunct to an accelerated Monte Carlo photon transport code for patient-specific brachytherapy dose calculations and analysis*." A portion of the article will be paraphrased in the following.

Table 4.2 lists the PTRAN_CT input files, among which the source-specific *phase space file* is precalculated using the MC method. The input interface of the PTRAN_CT source code has been modified so as to reduce the input file sizes and improve the MC initialization efficiency. The following files can be produced by BrachyGUI via an interactive window: (1) a *main input file* specifying the simulation geometry and input parameters, (2) a *patient-data file* in modified *egsphant* format that allows more than nine

simulation media (in contrast to the original format), (3) a *voxel data file* identifying voxels overlapped by a brachytherapy applicator and/or seeds, and (4) an *output preference file* defining the dose output format and data for absolute dose conversion. These files require manual editing when defining a new applicator or source geometry. There is a function to generate script files for running simulations on a computer cluster.

Table 4.2. A list of PTRAN_CT input files.

| File type | Description |
|---|---|
| Main input file | Specify simulation parameters: applicator/seed geometry, scoring options, source positions, orientations, and weights, etc. |
| Voxel data file | Identify each voxel occupied by the applicator/seed with a unique index; stores the region number of the associated overlapping structure, and the fraction of the volume intersected by it |
| Patient data file | Store the voxel grid, and material and density data in *egsphant* format |
| Output preference file | Store the output option and parameters for absolute dose conversion (air kerma strength, total treatment time, and dose conversion factor) |
| Phase space file | Record the energy, position, and direction of photons reaching the capsule surface from the source core |

## 4.3. GRAPHICAL USER INTERFACE

### 4.3.1. *Display options*

BrachyGUI can display greyscale images as well as density, material, dose, dose difference, dose ratio, and gamma maps. Axial, coronal, and sagittal image slices can be viewed in a single panel or multiple panels. The greyscale window width and level can be adjusted for optimal contrast. Structure contours, isodose lines and dose colorwash can be overlaid on the images. Zooming, profile plotting, and parallel display of two dose distributions can also be done. A thumbnail viewing panel can be used for quick slice selection. Figure 4.1 shows a screenshot of a BrachyGUI session comparing the isodose distributions for an HDR $^{192}$Ir treatment of a superficial arm lesion.

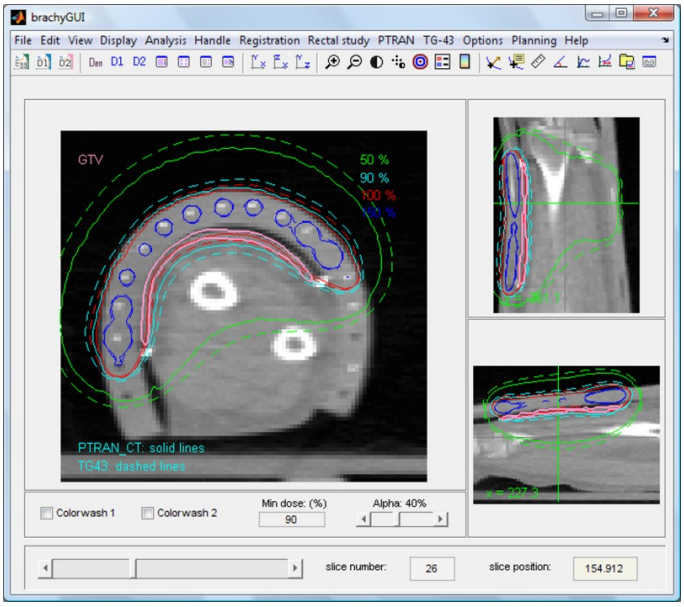


Figure 4.1. Screenshot of a BrachyGUI session. Isodose distributions calculated by PTRAN_CT and TG-43 along the axial, coronal, and sagittal views are compared.

Figure 4.2 displays the isodose distributions and profiles of the materials, density, dose, dose ratio, and dose difference between PTRAN_CT and TG-43 calculations for a breast patient plan. The endpoints of the profiles are specified interactively by the user.

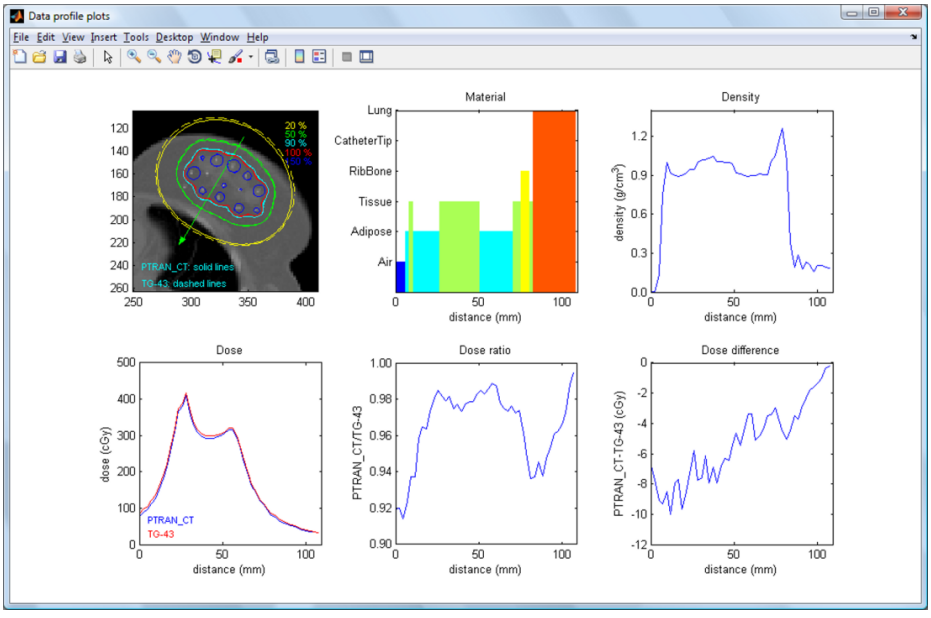


Figure 4.2. BrachyGUI screenshot showing the isodose distributions as well as material, density, dose, dose ratio, and dose difference profiles with user-defined endpoints.

### 4.3.2. *Image registration and fusion*

Two image registration techniques, known as the *point correspondence* [8] and the *chamfer matching* [9, 10] methods, have been implemented in BrachyGUI. These techniques are based on the rigid body assumption and are applicable for multi-modality image registration. The purpose of both methods is to obtain the transformation vector $T$, comprised of three translational and three rotational elements, which map the coordinate system of one 3D image to that of another.

*i.* *Point correspondence method*

The point correspondence method requires the user to specify at least three pairs of control points that match certain features of two image sets. These points can be determined via mouse clicks in a BrachyGUI window with the image sets displayed side by side. Denoting the points in one image set $P$ and those in the other $Q$, this can be formulated as a least squares problem for which the cost function $C$ is to be minimized:

$$C(T) = \|T(P) - Q\|^2 \tag{4.1}$$

This cost function can be solved in MATLAB using singular value decomposition.

*ii.* *Chamfer matching*

The chamfer matching method is a well-established technique for mapping brain and pelvic images [9-12]. It seeks to find the vector $T$ that maximizes the correlation of some features between two image sets. Its implementation in BrachyGUI follows the algorithm of van Herk and Kooy [10], for which the cost function is minimized by the downhill simplex method [13, 14]. Chamfer matching is fast, can tolerate substantial noise in one of the image sets, and requires little user interaction.

*iii.* *Clinical applications*

Rigid-body image registration methods may have limited usefulness in brachytherapy unless the time gap between the acquisitions of the two image sets is kept to a minimum. When the applicator needs to be re-inserted before acquiring the second image set, it may deform the surrounding organs differently. It will be of interest to investigate non-rigid registration methods [15] to account for organ deformations by brachytherapy applicators as well as geometric displacements of various organs [16].

*iv.* *Image fusion*

In BrachyGUI, registered images can be fused using one of several options with user-defined weights and greyscale windowing adjustments. Figure 4.3 shows a screenshot of BrachyGUI in checkerboard fusion display mode, in which CT and cone-beam CT images of the pelvic phantom RANDO (Radiology Support Devices, Long Beach, CA) are shown. These images have been pre-registered using chamfer matching.

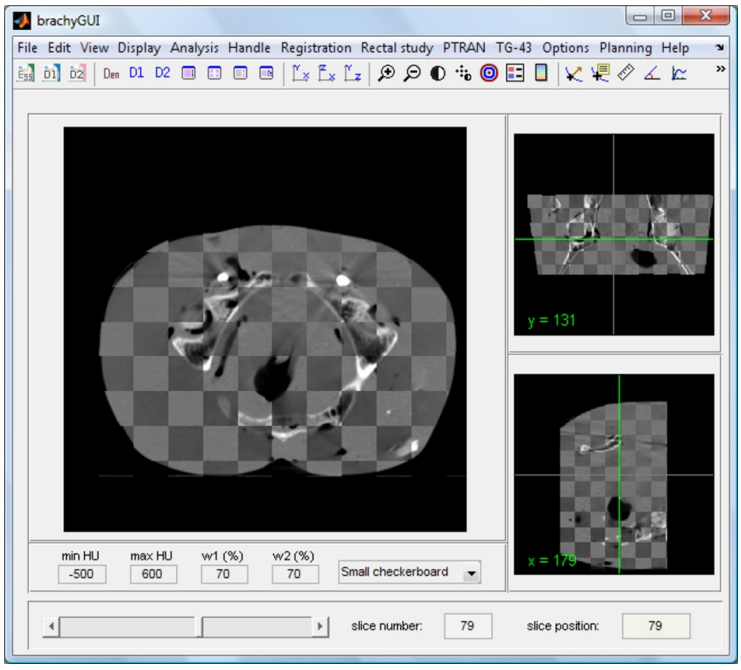


Figure 4.3. Screenshot of BrachyGUI showing the fusion of CT and CBCT images for a RANDO pelvic phantom that has been co-registered by the chamfer matching method.

## 4.4. BASIC BRACHYTHERAPY TREATMENT PLANNING

A basic treatment planning module has been developed, allowing the user to define catheters, activate dwell positions, modify dwell weights, specify reference dose points, and contour structures. The treatment plan can be visualized in 3D, as illustrated in Figure 4.4 for an HDR $^{192}$Ir multicatheter breast patient. Anatomy-based inverse treatment planning can be done for breast patients, as described in Paper III in Chapter 7.

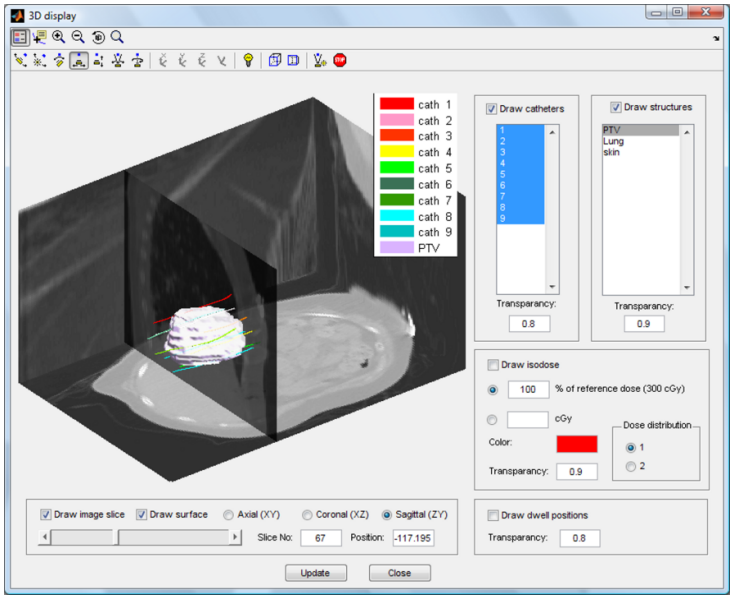


Figure 4.4. Screenshot of 3D display for an HDR $^{192}$Ir multicatheter breast treatment plan.

## 4.5. CT NUMBER TO MATERIAL AND DENSITY CONVERSION

Similar to the CTCREATE code distributed with DOSXYZnrc [4], BrachyGUI provides a function for converting CT numbers to material and mass density data. It uses a default conversion scheme with multiple linear ramp sections derived by a calibration phantom scan (RMI electron density CT phantom, Gammex, Middleton, MI). The user may import a new conversion scheme with any number of linear or discrete ramps, and specify a subset of the CT images and the voxel grid for the conversion.

BrachyGUI processes DICOM CT images and creates a file in the *egsphant* format or a modified version of it for patient-specific dose calculations. The modified *egsphant* format allows more than nine simulation media to be defined. It is used by PTRAN_CT and the analytical calculation algorithm described in Paper IV in Chapter 8, both of which require uniform voxel length along each dimension in the Cartesian coordinate system.

Once an *egsphant* file has been created, both the material and density data in selected regions can be changed based on a combination of user-defined criteria via an interactive window in BrachyGUI. This feature is useful for making manual corrections in several scenarios. For example, the wrong materials and densities may be assigned to voxels because of metal streaking artifacts. Also, dummy markers used in CT-based HDR treatment planning are removed during dose delivery and the associated voxels may be replaced by tissue for dose calculations. As well, voxels occupied by contrast solution tend to be incorrectly interpreted as high-density bony structures.

## 4.6. DOSE CALCULATION ALGORITHMS

The brachytherapy dose calculation algorithms implemented in BrachyGUI include (1) the TG-43 1D and 2D formalisms [17]; (2) an applicator-based dose superposition algorithm for calculations with a shielded rectal applicator (Paper II in Chapter 6); (3) a scatter correction algorithm accounting for the reduced photon backscatter near the skin (Paper III in Chapter 7); and (4) a CT-based analytical dose calculation algorithm for HDR $^{192}$Ir brachytherapy (Paper IV in Chapter 8).

## 4.7. DOSE EVALUATIONS

### 4.7.1. *Processing of dose distribution data*

BrachyGUI provides options for combining multiple 3D dose distributions of different weights. Rotational and translational shifts can be applied individually to each distribution. The dose may be scaled by a constant or normalized at any user-defined point. Also, the voxel dimensions and boundaries can be changed by tri-linear interpolation of dose data. This allows the same dose grid to be used when comparing dose distributions calculated by different algorithms, thereby minimizing discrepancy in DVH calculations due to volume averaging effects and inconsistent voxel boundaries.

### 4.7.2. *Dose evaluation and comparison*

In BrachyGUI, dose distributions can be evaluated by means of isodose visualization, dose profile plotting, and DVH and dose-volume index calculations. Cumulative, differential, and natural DVHs can be calculated. There is an option to exclude contributions by voxels assigned as non-tissue media such as metal, air, and contrast solution.

BrachyGUI can evaluate the coverage index, external volume index, relative dose homogeneity index, and overdose volume index, as defined by Meertens et al. [18]. As well, it can calculate the ICRU treated volume [19], the conformation number defined by van't Riet et al. [20], and the conformal index defined by Baltas et al. [21].

In a given BrachyGUI session, up to two dose distributions can be loaded for dose comparison. Dose difference, dose ratio, and gamma maps can be displayed slice by slice along the axial, coronal, or sagittal plane. The gamma evaluation algorithm is implemented according to Wendling et al. [22].

## 4.8. ROLES IN PATIENT DOSE-CALCULATION STUDY

The roles of BrachyGUI in a brachytherapy dose-calculation study are summarized in Figure 4.5. It reads DICOM files exported from a brachytherapy planning system, create treatment plans, convert files to the appropriate formats, calculate dose distributions, and generate PTRAN_CT initialization data files. For both brachytherapy and external beam applications, BrachyGUI can be used to create *egsphant* patient data files as well as analyze, compare, and display dose distributions in *3ddose* or *d3d* format.

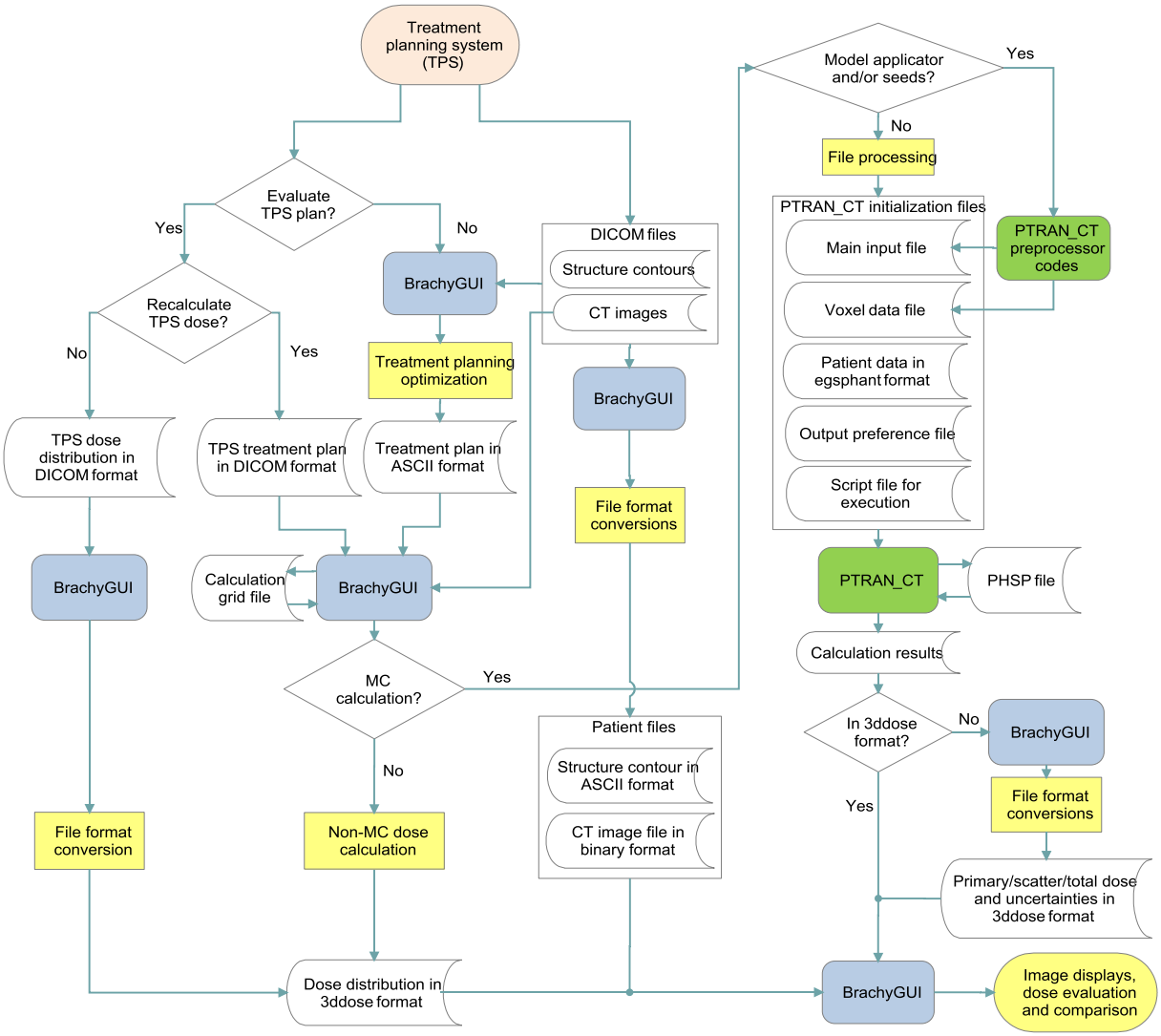


Figure 4.5. Roles of BrachyGUI in a brachytherapy patient dose-calculation study.

## 4.9. REFERENCES


1. Deasy JO, Blanco AI, Clark VH. CERR: a computational environment for radiotherapy research. Med Phys. 2003;30:979-85.

2. Chow JC, Leung MK. Treatment planning for a small animal using Monte Carlo simulation. Med Phys. 2007;34:4810-7.

3. Kirisits C, Siebert FA, Baltas D, De Brabandere M, Hellebust TP, Berger D, et al. Accuracy of volume and DVH parameters determined with different brachytherapy treatment planning systems. Radiother Oncol. 2007;84:290-7.

4. Walters B, Kawrakow I, Rogers DW. DOSXYZnrc Users Manual. Ottawa: National Research Council Canada 2009. Report No.: NRCC Report PIRS-794revB.

5. Kawrakow I, Fippel M. Investigation of variance reduction techniques for Monte Carlo photon dose calculation using XVMC. Phys Med Biol. 2000;45:2163-83.

6. Le Y, Chibani O, Todor D, Siebers I, Williamson J. An integrated CT-based Monte Carlo dose-evaluation system for brachytherapy and its application to permanent prostate implant postprocedure dosimetric analysis. Med Phys. 2005;32:2068.

7. Poon E, Le Y, Williamson JF, Verhaegen F. BrachyGUI: an adjunct to an accelerated Monte Carlo photon transport code for patient-specific brachytherapy dose calculations and analysis. J Phys Conf Ser. 2008;102:012018.

8. Hill DL, Hawkes DJ, Crossman JE, Gleeson MJ, Cox TC, Bracey EE, et al. Registration of MR and CT images for skull base surgery using point-like anatomical features. Br J Radiol. 1991;64:1030-5.

9. Barrow HG, Tenenbaum JM, Bolles RC, Wolf HC. Parametric correspondence and chamfer matching: Two new techniques for image matching. 5th International Joint Conference on Artificial Intelligence. Cambridge, MA: Cambridge University; 1977. p. 659-63.

10. van Herk M, Kooy HM. Automatic three-dimensional correlation of CT-CT, CT-MRI, and CT-SPECT using chamfer matching. Med Phys. 1994;21:1163-78.

11. Borgefors G. Hierarchical chamfer matching - a parametric edge matching algorithm. IEEE Transactions on Pattern Analysis and Machine Intelligence. 1988;10:849-65.

12. van Herk M, de Munck JC, Lebesque JV, Muller S, Rasch C, Touw A. Automatic registration of pelvic computed tomography data and magnetic resonance scans including a full circle method for quantitative accuracy evaluation. Med Phys. 1998(10):2054-67.

13. Nelder JA, Mead R. A simplex method for function minimization. Comp J. 1965;7:308-13.

14. Press WH, Flannery BP, Teukolsky SA, Vetterling WM. Numerical recipes in C : the art of scientific computing. Cambridge: Cambridge University Press; 1988.

15. Crum WR, Hartkens T, Hill DL. Non-rigid image registration: theory and practice. Br J Radiol. 2004;77 Spec No 2:S140-53.

16. Christensen GE, Carlson B, Chao KS, Yin P, Grigsby PW, Nguyen K, et al. Image-based dose planning of intracavitary brachytherapy: registration of serial-imaging studies using deformable anatomic templates. Int J Radiat Oncol Biol Phys. 2001;51:227-43.

17. Rivard MJ, Coursey BM, DeWerd LA, Hanson WF, Huq MS, Ibbott GS, et al. Update of AAPM Task Group No. 43 Report: A revised AAPM protocol for brachytherapy dose calculations. Med Phys. 2004;31:633-74.

18. Meertens H, Borger J, Steggerda M, Blom A. Evaluation and optimisation of interstitial brachytherapy dose distributions. In: Mould RF, Battermann JJ, Martinez AA, Speiser BL, editors. Brachytherapy from radium to optimization. Veenendaal: Nucletron International; 1994. p. 300-6.

19. International Commission on Radiation Units and Measurements. Prescribing, recording, and reporting photon beam therapy. Bethesda, MD: ICRU; 1993.

20. van't Riet A, Mak AC, Moerland MA, Elders LH, van der Zee W. A conformation number to quantify the degree of conformality in brachytherapy and external beam irradiation: application to the prostate. Int J Radiat Oncol Biol Phys. 1997;37:731-6.

21. Baltas D, Kolotas C, Geramani K, Mould RF, Ioannidis G, Kekchidi M, et al. A conformal index (COIN) to evaluate implant quality and dose specification in brachytherapy. Int J Radiat Oncol Biol Phys. 1998;40:515-24.

22. Wendling M, Zijp LJ, McDermott LN, Smit EJ, Sonke JJ, Mijnheer BJ, et al. A fast algorithm for gamma evaluation in 3D. Med Phys. 2007;34:1647-54.

# Chapter Five

# Paper I: Dosimetric Characterization of a Novel Intracavitary Mold Applicator for HDR $^{192}$Ir Endorectal Brachytherapy Treatment

Emily Poon, Brigitte Reniers, Slobodan Devic, Té Vuong, Frank Verhaegen
*Med Phys. 2006;33:4515-26*



At the McGill University Health Center, an eight-channel intracavitary silicone applicator is being used for HDR endorectal brachytherapy (HDR-EBT). It can be used with metal shielding and an endocavitary balloon injected with contrast medium. As presented in Chapter 3, shielding has limited effects on the dose in the unshielded regions. When the planning target volume is partially shielded, however, the target coverage may be compromised if shielding effects are not accounted for. In this paper, we examine the dosimetric properties of this applicator using the MC and experimental techniques. This investigation will be helpful for the development of a dose calculation method alternative to the TG-43 formalism for HDR-EBT treatment planning.

## ABSTRACT

The dosimetric properties of a novel intracavitary mold applicator for $^{192}$Ir high-dose-rate (HDR) endorectal cancer treatment have been investigated using Monte Carlo (MC) simulations and experimental methods. The 28 cm long applicator has a flexible structure made of silicone rubber for easy passage into cavities with deep-seated tumors. It consists of eight source catheters arranged around a central cavity for shielding insertion, and is compatible for use with an endocavitary balloon. A phase space model of the HDR source has been validated for dose calculations using the GEANT4 MC code. GAFCHROMIC™ EBT model film was used to measure dose distributions in water around shielded and unshielded applicators with two loading configurations, and to quantify the shielding effect of a balloon injected with an iodine solution (300 mg I/mL). The film calibration procedure was performed in water using an $^{192}$Ir HDR source. Ionization chamber measurements in a Lucite phantom show that placing a tungsten rod in the applicator attenuates the dose in the shielded region by up to 85%. Inserting the shielded applicator into a water-filled balloon pushes the neighboring tissues away from the radiation source, and the resulting geometric displacement reduces the dose by up to 53%; another 8% dose reduction can be achieved when the balloon is injected with an iodine solution. All experimental results agree with the GEANT4 calculations within measurement uncertainties.


## 5.1. INTRODUCTION

Patients with rectal cancer at an advanced stage are often treated by surgical excision of the tumor. Depending on the tumor location and volume, permanent colostomy may be required. External beam radiotherapy is sometimes given in high doses

as a palliative or neoadjuvant treatment. It is known that neoadjuvant radiotherapy improves tumor downsizing and results in better local tumor control [1-5], disease-free survival [4], and overall survival [4, 6]. Some studies also indicate that it increases sphincter preservation [3, 6]. However, significant toxicity to normal tissues becomes a concern when large volumes need to be irradiated. Although localized radiation treatment can be delivered by means of intracavitary brachytherapy, it is not a common modality for treating deep-seated, late-stage rectal tumors.

At the Montreal General Hospital, preoperative $^{192}$Ir high-dose-rate (HDR) brachytherapy for endorectal cancer treatment has been performed since 1998 using a Novi Sad applicator (Nucletron B. V., Veenendaal, The Netherlands) [7]. The aim of the procedure is to shrink the volume of an advanced rectal tumor before surgery. This inflatable, eight-channel applicator has high pliability, and it shows promising outcome for tumor downstaging and for facilitating sphincter preservation surgery [8]. Nucletron has recently developed an improved version of the applicator, which has a longer length and offers additional radiation protection advantages.

In this work, we examined the dosimetric characteristics of this intracavitary mold applicator using Monte Carlo (MC) simulations and experimental techniques. The applicator is shown in Figure 5.1. It is composed of silicone rubber (density = 1.14 g/cm$^3$), and is 28 cm in length and 2 cm in diameter. Its flexible structure permits deep penetration into the anal passage with tolerable patient discomfort. There are eight source catheters within its circumference, and the multichannel design enables better dose conformity [9]. Unlike the inflatable Novi Sad model, this applicator has a central cavity for insertion of shielding. When treating noncircumferential tumors, the healthy tissues contralateral to the target can be spared by placing an 8 mm diameter rod made of lead or

tungsten into the cavity, and additionally by inserting the applicator in an inflatable balloon (Civco Medical Solutions, Kalona, IA). As shown in Figure 5.2, the balloon can be expanded unilaterally by injecting a maximum of 30 mL of water or contrast medium. In this way, normal tissues can be pushed away from the $^{192}$Ir source by up to 1 cm. Compared to water, a contrast medium such as iodine solution provides additional radiation protection for the normal tissues and enables better visualization on computed tomography (CT) images.


Figure 5.1. (a) An intracavitary mold applicator developed by Nucletron B. V. for preoperative treatment of endorectal cancer. It is made of flexible silicone rubber, 28 cm long and 2 cm in diameter. It houses eight catheters within its circumference. (b) An 8 mm diameter rod made of tungsten or lead can be inserted into the central cavity of the applicator for shielding the surrounding normal tissues.

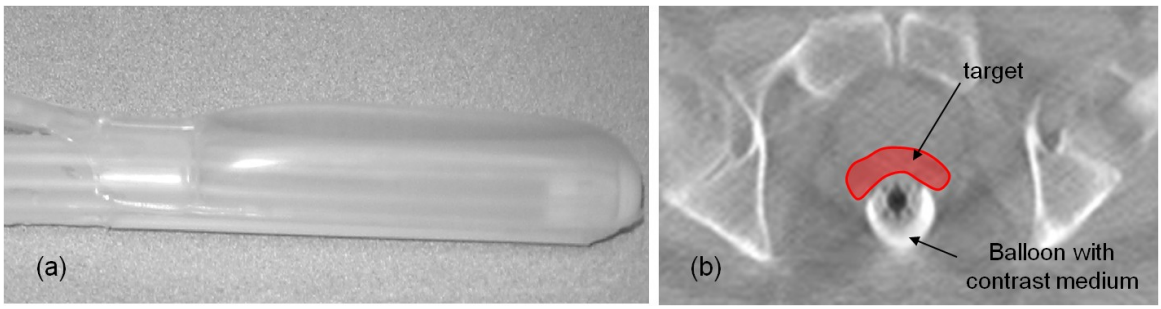


Figure 5.2. A photograph of the applicator inserted into an endocavitary balloon for additional radiation protection. (b) A CT slice showing the balloon filled with contrast medium. Note that the normal tissues are pushed away from the target.

Patients treated with this applicator at our institution are prescribed a total dose of 26 Gy to the target radial margin. Treatments are delivered over four daily fractions of 6.5 Gy on consecutive days. CT-based treatment plans are created using the Plato Brachytherapy Planning System (Nucletron B. V., Veenendaal, The Netherlands). This system assumes the entire simulation medium to be homogeneous water, in accordance with the TG-43 dose calculation formalism [10]. In this work, detailed MC simulations were performed to account for the presence of the applicator, balloon, and shielding. The Low-energy model (G4EMLOW2.3) of the GEANT4 particle simulation toolkit (version 7.0) [11] was used. The calculated dose distributions have been validated by radiochromic film and ionization chamber measurements. The applicability of a phase space (PHSP) concept for $^{192}$Ir simulations using GEANT4, as well as the validity of the GAFCHROMIC EBT$^{TM}$ model film for measurements with a HDR source in water have also been examined. A dosimetric evaluation of this applicator for clinical situations taking into account tissue-composition heterogeneities is beyond the scope of this article.

## 5.2. MATERIALS AND METHODS

### 5.2.1. *Modeling of the $^{192}$Ir HDR sources*

In our clinic, the intracavitary mold applicator is connected via transfer tubes to the Nucletron microSelectron HDR remote afterloader. Due to an upgrade of the afterloading unit during the course of this study, both the classic (part No. 080950) and the new (part No. 105002) $^{192}$Ir source designs were used in this work. Each design consists of a pure iridium core encapsulated by a stainless steel capsule that is welded to a steel cable. We modeled both designs in GEANT4 based on Ref. [12]. The capsule and the 1.85 mm long cable portion for the classic design were constructed as a unit comprised of

a cylinder and a half sphere of radius 0.55 mm at the distal end. The cylindrical iridium core was 0.6 mm in diameter and 3.5 mm in length. As for the new design, the capsule and the cable were modeled as a polyconical unit of total length 6.5 mm. The iridium core was 0.65 mm in diameter and 3.6 mm in length, and was constructed as a polyconical structure of six segments to account for the beveled ends. For both source designs, gamma particles were generated with random positions and directions from the active core. The gamma spectrum was obtained from the NuDat 2.0 database [13], and beta particles were not simulated because most of them will be absorbed in the steel capsule [14].

### 5.2.2. *Modeling of the intracavitary mold applicator*

Based on the blueprints provided by the manufacturer, we modeled the applicator in the GEANT4 code as a combinatorial unit of cylinders, tori, and polyconical structures. An 8 mm diameter and 25.4 cm long rod made of tungsten (Densimet 18.2, density = 18.0 g/cm$^3$) or lead (density = 11.35 g/cm$^3$) can be placed in the applicator central cavity of 8.3 mm diameter. The balloon geometry was modeled as a subtraction solid of an elliptical tube and a cylinder. The user code requires an input file to specify the source dwell positions and relative dwell times. For the results presented in Sec. 5.3 the catheters are numbered according to the convention shown in Figure 5.3.

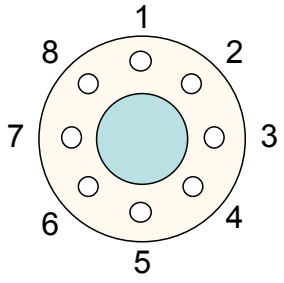


Figure 5.3. A cross-sectional view of the applicator from the proximal side. The catheter numbering convention used for this work is shown.

### 5.2.3. *GEANT4 dose calculations*

For better simulation efficiency, only photon transport was performed and dose was approximated by kerma. This was achieved by setting the electron production and tracking cutoffs to be sufficiently high. A kerma approximation is warranted for our study because beta particle and secondary electron generation mainly affects dose distributions up to 2 mm from the $^{192}$Ir source [15], which is within the confines of the applicator. Rayleigh scattering, bound Compton scattering, photoelectric effect, and its subsequent fluorescence emission were simulated in this work [16, 17]. The photon interaction and atomic relaxation data were obtained from the EPDL97 [18] and EADL [19] libraries, respectively. Track length estimation was used to calculate kerma, $K$,

$$K = \frac{l}{V} \cdot \frac{\mu_{en}}{\rho} \cdot E \,, \tag{5.1}$$

where $l$ is the distance traveled by a photon in a voxel of volume $V$ and $\mu_{en}/\rho$ is the mass energy absorption coefficient of the medium at energy $E$. The $\mu_{en}/\rho$ values for all materials were derived from National Institute of Standards and Technology elemental data [20]. We parameterized $\mu_{en}/\rho$ in two parts as a function of energy using sixth-order polynomial fittings. The fit curve agrees with the data to within 0.2%.

To validate the GEANT4 simulations of the $^{192}$Ir source, we calculated the radial dose function, $g(r)$, and the anisotropy function, $F(r, \theta)$, as defined in the TG-43 protocol. The $^{192}$Ir source was positioned in the center of a spherical water phantom of 15 cm radius. The voxels were constructed as segments of concentric spheres surrounding the source, and the dimensions were set such that volume averaging effects could be minimized [21]. For the calculation of $g(r)$, the thickness of the voxels, $\Delta r$, ranged from 0.1 mm at a radial distance $r$ of 1 mm, to 2 mm at $r$ = 14 cm. The polar angle $\theta$ spanned

from 82.5° to 97.5°, where 0° was defined at the distal end of the source. As for the calculation of $F(r, \theta)$, $\Delta r$ increases from 0.2 mm at $r$ = 2.5 mm to 2 mm at $r$ = 5 cm. The voxels were at 1° intervals near the longitudinal direction, and increased gradually to 15° along the transverse axis.

The calculated values of $g(r)$ and $F(r, \theta)$ for the classic design and the new design were compared with those of Williamson and Li [22] and Daskalov et al. [12], respectively. Their calculations were both performed using the PTRAN_CCG MC code, which utilizes either the bounded next-flight or the exponential track-length estimation technique for kerma calculation at a geometric point [23]. Since a similar trend of agreement was found between GEANT4 and PTRAN_CCG for both source designs, we will present only the results for the classic design in Sec. 5.3.1. The standard uncertainty on the mean kerma for the PTRAN_CCG calculations of Williamson and Li ranges from 0.5% near the $^{192}$Ir source to 2% at large distances from the source [22].

A PHSP model was used in the dose calculations around the applicator. In this approach, we first simulated the interactions of 40 million primary photons within the $^{192}$Ir source in vacuum. The energy, position, and direction of each photon reaching the surface of the source capsule were recorded in a PHSP file. In the second part of the calculation, the PHSP file was read to generate photons originating from the capsule surface in the simulation geometry. To allow the placement of the source in any given position, a transformation of the source coordinates with respect to the PHSP information was applied. This PHSP concept has been used in brachytherapy applications [24, 25] for higher simulation efficiency, since particle interactions within the source capsule are omitted in the second part of the calculation. Moreover, the PHSP file can be recycled multiple times.

This PHSP approach also permits the brachytherapy source to be absent in the simulation, although photons that are scattered back to the high density source region will not be properly accounted for. Such an approximation has been found acceptable for intravascular applications using beta and gamma sources ($^{32}$P, $^{90}$Sr/$^{90}$Y, and $^{192}$Ir) [25], where only a single source is present at a given time in the simulation. However, in cases such as prostate implants, the $^{125}$I or $^{103}$Pd seeds need to be present to account for interseed attenuation [26, 27]. To determine whether our application requires the $^{192}$Ir source to be present for accurate dose calculations, we computed the radial dose function and anisotropy function in a homogeneous water phantom with the photons generated from a PHSP file. The results were also compared to the full simulations of PTRAN_CCG [22].

The air kerma strength associated with the $^{192}$Ir PHSP source model, $S_K^{\mathrm{MC}}$, was used for converting the dose per particle history $D^{\mathrm{MC}}$ to absolute dose $D_{\mathrm{abs}}^{\mathrm{MC}}$. This quantity was obtained by generating $n$ photon histories from a PHSP file of the $^{192}$Ir source in vacuum. An annular scoring region of 2 mm width was specified at a distance $d$ of 5 cm from the source transverse axis. $S_K^{\mathrm{MC}}$ is given by

$$S_K^{\mathrm{MC}} = \sum_{i=1}^{n} \left( \frac{\mu_{\mathrm{en}}}{\rho}(E_i)_{\mathrm{air}} \cdot E_i \cdot \phi_i \right) \cdot \frac{d^2}{n}, \qquad (5.2)$$

and is in units of cGy cm$^2$/particle. The photon fluence per unit area of the scoring region is represented by $\phi_i$, and $E_i$ is the energy for a given photon $i$. Setting $n$ to be the number of photons scored in the PHSP file, the standard deviation of $S_K^{\mathrm{MC}}$ in our calculation was 0.3%. For comparison with experimental results, $D_{\mathrm{abs}}^{\mathrm{MC}}$ was calculated as follows:

$$D_{\text{abs}}^{\text{MC}} = \frac{D^{\text{MC}}}{\text{S}_K^{\text{MC}}} \cdot S_K^{\text{exp}} \cdot t \,. \qquad (5.3)$$

The air kerma strength of the actual source at the time of the experiment, $S_K^{\text{exp}}$, is in units of $U$ (1 $U$ = 1 cGy cm$^2$/h), and the source dwell time $t$ is in units of hours.

5.2.4. *Experimental validations*

We performed measurements using GAFCHROMIC$^{TM}$ EBT model film (International Specialty Products, Wayne, NJ) and the new design of the $^{192}$Ir source to obtain the dose distributions around the applicator in several source, shielding and balloon arrangements. The air kerma strength of the source was measured using a well-type ionization chamber (model HDR1000 Plus, Standard Imaging, Middleton, WI), which agreed with the value stated by the source manufacturer to within 0.4%. We also performed relative measurements using an Exradin A14P ionization chamber (Standard Imaging, Middleton, WI) and the classic design of the $^{192}$Ir source to quantify the amount of dose reduction due to tungsten shielding in a Lucite phantom.

*i.* *Radiochromic film dosimetry*

Dose distributions around the applicator in water were obtained using GAFCHROMIC$^{TM}$ EBT model film (lot No. 35322-0021), which has a high spatial resolution and is nearly tissue equivalent ($Z_{\text{eff}}$ = 6.98) [28]. Analysis was performed using an AGFA Arcus II flat-bed document scanner (AGFA, Mortsel, Belgium) based on the protocol described by Devic et al. [29]. Both the calibration and measurement films were scanned with a resolution of 127 pixels per inch in 48-bit RGB color mode, and the pixel values of the red channel were extracted. To minimize scanner artifacts due to light diffusion, the area of interest was restricted to a 10×10 cm$^2$ region in the central part of the

scanner bed. Each piece of film was scanned approximately 2 h before irradiation, and was scanned again 12 h after irradiation.

The film images were analyzed using an in-house MATLAB routine (The MathWorks, Natick, MA). An algorithm was written to correct for the scanner sensitivity as a function of the horizontal scanning position [30]. To remove sharp spikes in the dose distribution, each pixel that differed by more than 5% of the mean of its neighboring pixels was replaced by that mean value. A 5×5 Wiener filter was applied for smoothing the background noise. The net optical density (netOD) was calculated as follows [29]:

$$\text{netOD} = \log_{10} \frac{I_{\text{unexp}} - I_0}{I_{\text{exp}} - I_0}, \tag{5.4}$$

where $I_0$ represents the intensity value with zero light transmission, which we obtained by scanning a completely opaque piece of radiographic film. The averaged pixel values for the images before and after exposure are denoted $I_{\text{unexp}}$ and $I_{\text{exp}}$, respectively.

To monitor the effects of environmental conditions such as humidity and temperature on the film, four pieces of 3×3 $\text{cm}^2$ control film were used in each experiment. They were stored and scanned in the same manner as the exposed films, but were not irradiated. These control films were also placed in water for about 10 min, which was about the same amount of time that the exposed films were immersed in water. The mean netOD in the central 1×1 $\text{cm}^2$ region was found to be of the order of 0.002, which was considered insignificant. This value was subtracted from the netOD of the exposed films.

*a. Film calibration*

A procedure was developed for the film dosimetry system calibration in water using a HDR source. A custom-made Lucite frame was used for holding a 10 cm diameter circular film piece horizontally in the center of a 30×30×40 $cm^3$ water tank. Each calibration film had a central hole that allowed a 6-French endobronchial catheter to pass through. The source was delivered via an endobronchial catheter to a position where its transverse axis was in alignment with the film plane within ±0.5 mm. To arrive at a statistical uncertainty, the procedure was performed five times. One film piece was irradiated for 45 s when the source apparent activity, $A_{app}$, was 335.5 GBq. On another day when $A_{app}$ was 311.5 GBq, two pieces were exposed for 50 s each, and another two for 40 s each.

The pixel values for each calibration film were averaged over 3×3 adjacent pixels so that the distribution had a grid spacing of 0.6×0.6 $mm^2$. The netOD values were then calculated, and profiles along four radial directions 90° apart originating from the source center position were extracted. These profiles were averaged to obtain the netOD as a function of distance along the source transverse axis. The netOD values were mapped to the corresponding doses as calculated using the TG-43 formalism based on the data of Daskalov et al. [12].

For the five calibration films, the doses fell rapidly from a few hundred Gy near the source to about 0.2 Gy at 5 cm. In each case, a calibration curve was constructed according to the transverse axis netOD and the dose values in the distance range between 5.4 mm and 4.56 cm from the source. The dose range used for curve fitting was between 0.2 and 18 Gy for the five cases. The standard deviations of the four profiles of each

calibration film were within 1.5% for doses above 1 Gy, and were within 4% for doses between 0.25 and 1 Gy.

A calibration curve characterizing the dose as a function of netOD was obtained based on the average of the five calibration results. Since the relationship was nearly linear in the low dose region (netOD $\leq$ 0.4), and more quadratic for high doses (netOD > 0.4), two separate polynomial fittings were applied for the two segments of the calibration curve. The standard deviations were within 1.5% in the dose range between 0.5 and 7 Gy and were within 2.5% between 7 and 16 Gy.

*b. Measurements of dose distributions around the applicator*

The same Lucite frame used for calibration was also used for dose measurements around the intracavitary applicator. The frame held the two ends of the applicator so that it could be positioned vertically in a water tank. Each measurement film was cut to the shape of a 10 cm diameter circle with a hole in the center to allow the applicator to pass through. The film was placed horizontally around the middle part of the applicator, and the source was delivered to a position within ±1 mm of the film axial plane. To prevent water from entering into the central cavity, the applicator tip was covered by a thin latex sleeve. We measured the dose distributions with the source loaded in one channel and in three adjacent channels, with and without the presence of tungsten shielding. On the day of the experiment, the source activity was 358.4 GBq. The dwell times were set to 55 s for irradiations using one catheter position, and 18 s each for irradiations using three adjacent catheters.

*c. Measurements and simulations of dose reduction due to a balloon filled with iodine solution*

To examine the additional shielding effect of a contrast medium-filled balloon compared to water, measurements with EBT films in a water phantom were performed. We taped a 3×3 $cm^2$ film piece on a balloon injected with either iodine solution (300 mg I/mL) or water, and sent the source to a catheter on the side opposite the balloon with respect to the tungsten shielding. Because of the irregular shape of the balloon, the positioning uncertainty was estimated to be ±1.5 mm.

The experimental setup was simulated in GEANT4 according to the configuration shown in Figure 5.4. The source was positioned in catheters 3, 4, and 5 in separate simulations, and the dose deposited in a scoring voxel of 1.5 mm diameter and 0.5 mm depth at the distal side of the balloon was scored.

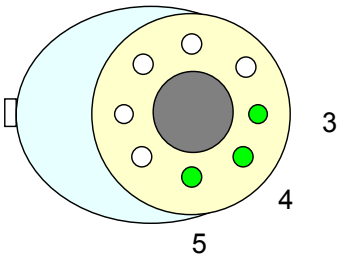


Figure 5.4. GEANT4 simulation setup for calculating dose reduction due to a balloon injected with iodine solution. The tungsten-shielded applicator is immersed in a water phantom. In separate simulations, the source is positioned in catheters 3, 4, and 5. The scoring voxel of 1.5 mm diameter and 0.5 mm depth is in contact with the balloon at the extreme left of the figure.

*ii.* *Ionization chamber measurements*

An Exradin A14P ionization chamber was used to measure the reduction in dose around the applicator due to the insertion of tungsten shielding. The small collection volume (0.002 $cm^3$) of the A14P chamber reduces volume averaging effects in regions of

high dose gradient, which makes it particularly suitable for brachytherapy applications. Figure 5.5 shows the experimental setup. We used Lucite as the phantom material because it is water equivalent for $^{192}$Ir dosimetry [31], and has a more uniform composition than solid water. The phantom is composed of three layers, and the total dimensions are 30×30×30 cm$^3$. The middle layer includes two slabs with custom-made holes for positioning the applicator and the ionization chamber. We inserted slabs of various thicknesses between the applicator and the ionization chamber holders, and loaded the source in different catheters to measure the dose distributions around the applicator. The uncertainty in the source-detector distance was about ±0.25 mm.

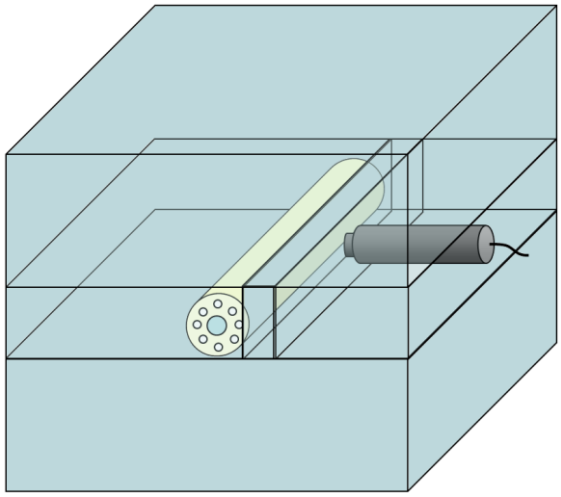

Figure 5.5. An Exradin A14P ionization chamber is placed in the middle layer of a 30×30×30 cm$^3$ Lucite phantom for measuring dose reduction at various points around the applicator due to tungsten shielding. The chamber has a 0.002 cm$^3$ sensitive volume at the distal end. Slabs of various thicknesses can be inserted between the chamber and the applicator, and the $^{192}$Ir source is sent to catheters 3–7 in separate measurements.

The $^{192}$Ir source was sent to the midpoint along the length of the applicator, in the same axial plane as the detector. To achieve a positioning accuracy of ±0.25 mm, we first sent the source in step intervals of 2.5 mm using five different 1 mm interval tip positions to determine the distance that gave the largest detector signal. For each measurement

position, the same irradiation time was used for the shielded and unshielded cases to eliminate inconsistency in source transit times. The source dwell times were determined based on the source activity and source-to-detector distance. Each signal obtained was an average of three repeated measurements, with the drift current subtracted. To account for the polarity effects that have been reported for the A14P ionization chamber [32], polarization voltages of +200 and −200 V were applied in separate experiments.

## 5.3. RESULTS

### 5.3.1. *TG-43 parameter calculations*

As shown in Table 5.1, the values of the radial dose function, $g(r)$, of the $^{192}$Ir source (classic design) calculated using GEANT4 agree with the PTRAN_CCG results [22] within 1%. Calculations with the PHSP model without the source present are in agreement with the full simulations, within a statistical uncertainty of 0.1%.

The anisotropy function, $F(r, \theta)$, computed with full simulation of the $^{192}$Ir source and a comparison with PTRAN_CCG are shown in Figure 5.6. The standard deviations of the GEANT4 calculations range from less than 0.1% near the transverse axis, to 2% along the longitudinal axis. The angle $\theta$ starts from 0° along the tip of the source and increases to 180° along the direction of the cable. For angles larger than 2° and 7° from the source longitudinal axis, agreement with PTRAN_CCG is within 2% and 1%, respectively. At $\theta$ = 1°, the GEANT4 calculations are lower and the deviations tend to increase with radial distance $r$. The discrepancy is 1.4% at $r$ = 0.25 cm, and 5.6% at $r$ = 5 cm. We attribute the disagreement to the finite voxel size of our code, since the technique used in PTRAN_CCG generates kerma at geometric points. Dose distributions in close proximity to the source longitudinal axis tend to be more sensitive to the voxel dimensions.

Table 5.1. Radial dose function of the $^{192}$Ir HDR classic model compared to PTRAN_CCG. The standard deviations of the GEANT4 results are less than 0.1%. The PHSP model without the source present is in agreement with the full simulation.

| Radial distance $r$ (cm) | $g(r)$ | | | GEANT4 full/ PTRAN_CCG | GEANT4 PHSP/ PTRAN_CCG |
|---|---|---|---|---|---|
| | GEANT4 full | GEANT4 PHSP | PTRAN_CCG [12] | | |
| 0.1 | 0.986 | 0.989 | 0.979 | 1.007 | 1.010 |
| 0.2 | 0.993 | 0.994 | 0.990 | 1.003 | 1.004 |
| 0.3 | 0.995 | 0.994 | 0.993 | 1.002 | 1.001 |
| 0.5 | 0.996 | 0.998 | 0.997 | 0.999 | 1.001 |
| 1 | 1.000 | 1.000 | 1.000 | 1.000 | 1.000 |
| 1.5 | 1.002 | 1.003 | 1.002 | 1.000 | 1.001 |
| 2 | 1.004 | 1.005 | 1.003 | 1.001 | 1.002 |
| 2.5 | 1.005 | 1.005 | 1.002 | 1.003 | 1.003 |
| 3 | 1.004 | 1.005 | 1.002 | 1.002 | 1.003 |
| 4 | 1.000 | 1.000 | 0.997 | 1.003 | 1.003 |
| 5 | 0.991 | 0.991 | 0.987 | 1.004 | 1.004 |
| 6 | 0.978 | 0.978 | 0.973 | 1.005 | 1.005 |
| 7 | 0.960 | 0.959 | 0.956 | 1.004 | 1.003 |
| 8 | 0.938 | 0.938 | 0.933 | 1.005 | 1.005 |
| 9 | 0.911 | 0.911 | 0.904 | 1.007 | 1.007 |
| 10 | 0.879 | 0.879 | 0.871 | 1.009 | 1.009 |
| 11 | 0.841 | 0.842 | 0.836 | 1.006 | 1.007 |
| 12 | 0.798 | 0.798 | 0.795 | 1.004 | 1.004 |
| 13 | 0.748 | 0.748 | 0.749 | 0.999 | 0.999 |
| 14 | 0.689 | 0.689 | 0.682 | 1.010 | 1.010 |

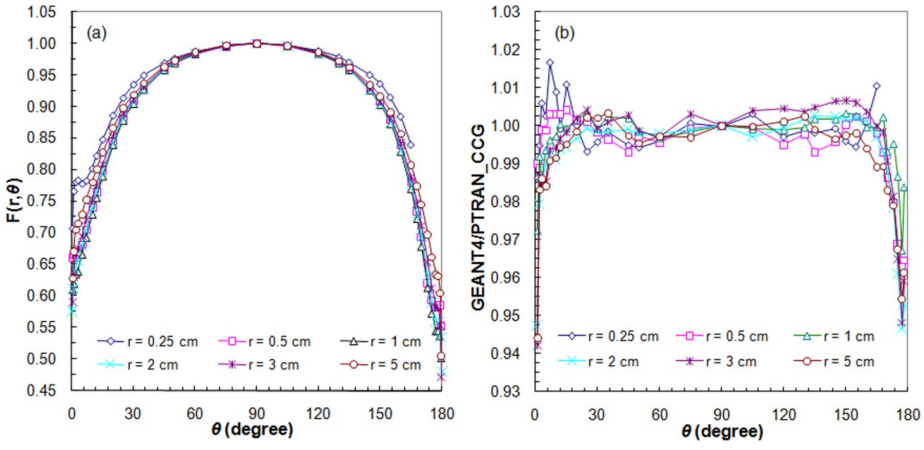


Figure 5.6. GEANT4 calculations of the anisotropy function of the Nucletron HDR classic model of the $^{192}$Ir source for six radial distances $r$ between 0.25 and 5 cm. (b) Comparison of GEANT4 with PTRAN_CCG results.

For the anisotropy function generated with the PHSP model in water without the $^{192}$Ir source present, there are slightly larger deviations from PTRAN_CCG compared to the full simulation. The agreement with PTRAN_CCG for angles larger than 5° and 15° from the longitudinal axis is within 2% and 1%, respectively. There are differences of up to 4% for $2° \leq \theta < 5°$, and up to 8% for $\theta = 1°$. This indicates that scattering and attenuation of photons that are backscattered into the source capsule lead to slight changes in dose distributions in regions close the source longitudinal axis. Nevertheless, the use of a PHSP file for particle generation is adequate for our work because photons scattered along the longitudinal axis tend to travel within the applicator. All MC results presented in the following sections were calculated using the PHSP model.

### 5.3.2. *Dose distributions in water*

Figure 5.7 shows an axial view of the isodose lines around the applicator in water. The contours are labeled in terms of absorbed dose in units of Gy. The MC voxel dimensions are 1×1×1 mm$^3$, whereas the pixel size of the EBT distributions is 1×1 mm$^2$. The standard deviations of the MC calculations increase from 0.1% for the voxels nearest the source to about 3% at 5 cm for the unshielded cases. In the tungsten-shielded region, the uncertainties increase to about 6%. For the EBT results, the distributions are rotated by up to 4° to match the MC isodose lines. Since the measurement films and the calibration films were handled and exposed under similar conditions, we expect that the measurement uncertainties are also within 1.5% and 2.5% for dose ranges of 0.5–7 Gy and 7–16 Gy, respectively.

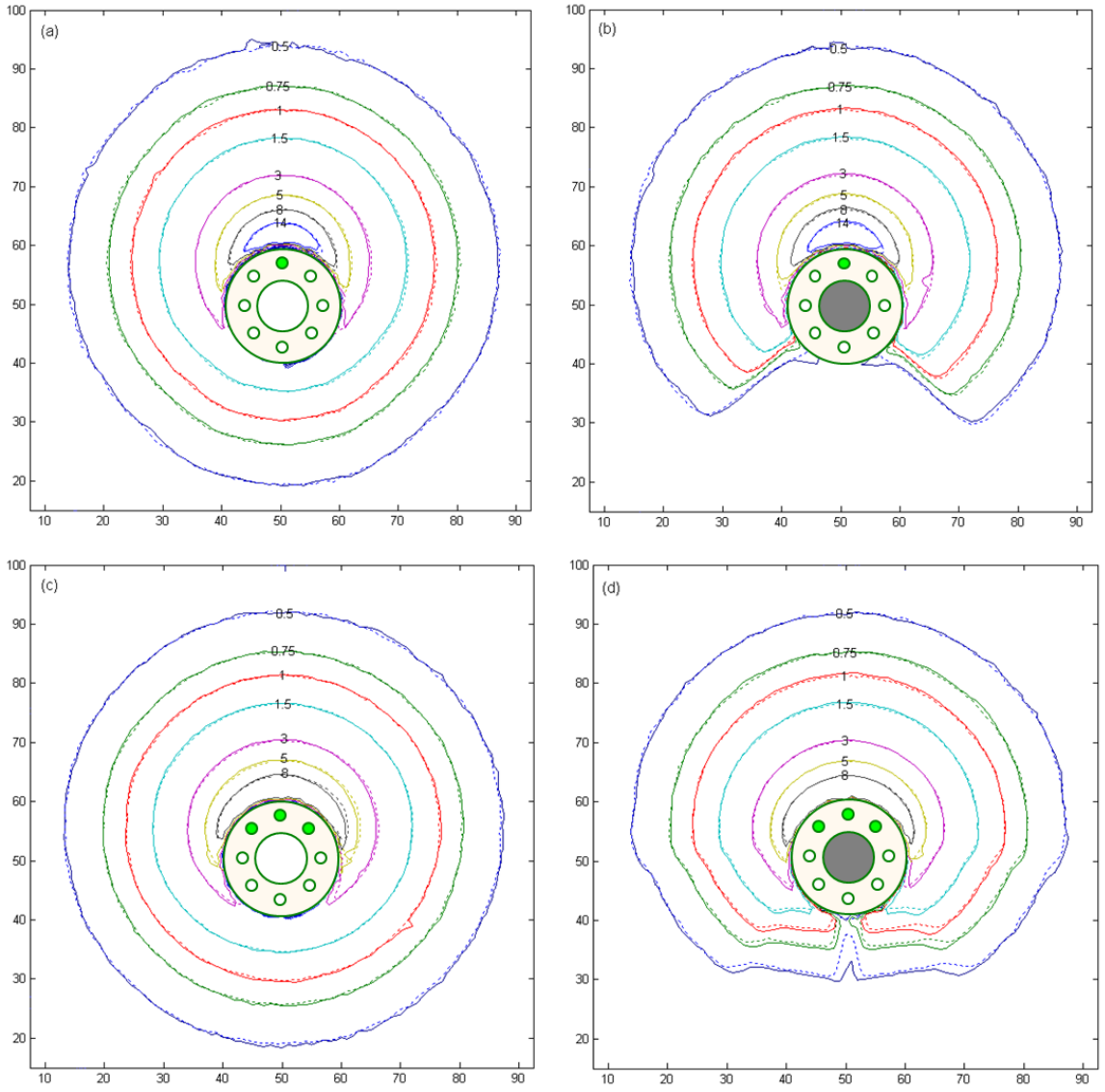


Figure 5.7. Absolute isodose distributions around the applicator with the source loaded in (a) catheter 1, without shielding, (b) catheter 1, with tungsten shielding, (c) catheters 1, 2, and 8, without shielding, and (d) catheters 1, 2, and 8, with tungsten shielding. EBT film measurements are represented by solid lines and GEANT4 results are represented by dotted lines. The contours are labeled in units of Gy.

The isodose distributions illustrate that when the tumor is confined to one side of the applicator, insertion of a tungsten rod allows significant sparing of normal tissues on the shielded side. This multichannel applicator provides a large degree of freedom in source positioning, which allows for better conformity of dose to the target volume.

### 5.3.3. *Dose reduction due to shielding*

The degree of tissue sparing due to high atomic number materials such as tungsten is sensitive to the shielding dimensions and the location of the point of interest relative to the source and the shielding [33]. We performed GEANT4 simulations to quantify the effect of shielding placement on the dose distributions around the applicator in a Lucite phantom. Figure 5.8 shows the reduction in dose due to lead or tungsten shielding, with the source positioned in catheter 7. Each abscissa represents the distance from the center of the applicator to a point on a line connecting the source and a given catheter in the radially outward direction lying on the same axial plane. In the shielded region, the dose is reduced by up to 85% for tungsten, and up to 80% for lead. On the unshielded side, the dose ratio decreases gradually from unity at the applicator surface to about 0.98 at 8 cm. A similar trend has been reported for a tungsten-shielded vaginal cylinder, and there it was attributed to a smaller amount of radiation scatter due to the shielding [34].

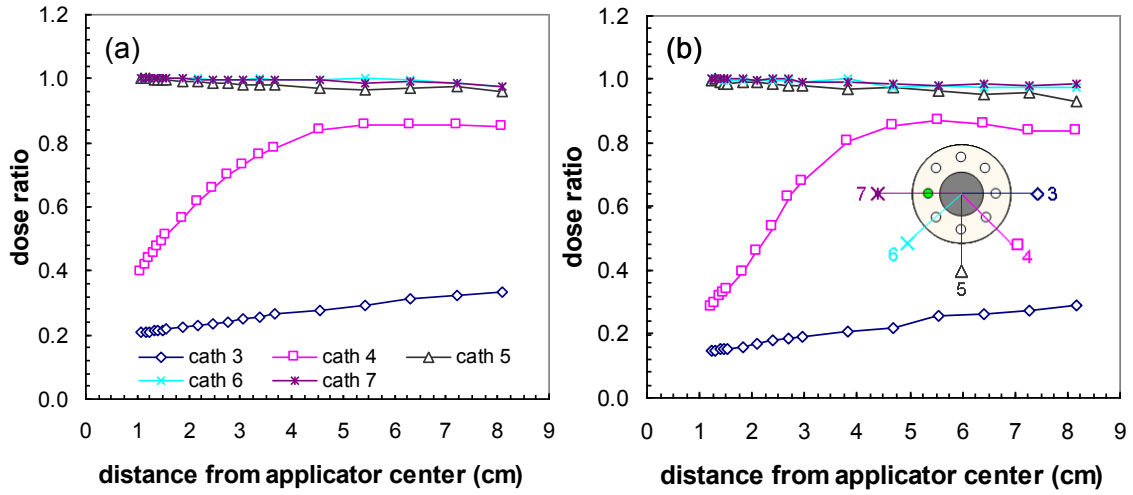


Figure 5.8. Ratios of dose with (a) lead and (b) tungsten shielding to dose without shielding as calculated using GEANT4. The source is positioned in catheter 7. The abscissa represents the distance between the applicator center and a point on a line through a given catheter.

In our work, the primary and scatter components of the dose distributions were analyzed to examine the cause of the slight dose decrease with distance on the unshielded side. Figure 5.9 compares the relative scatter dose contribution of an unshielded applicator with that of a tungsten-shielded one. In both cases, the scatter contribution increases with distance from the source position on the unshielded side. When the air cavity is replaced by a high-$Z$ absorber, many of the primary photons undergo photoelectric effect and are prevented from reaching the region behind the shielding. The reduced photon fluence leads to less photons being scattered back to the unshielded side. The effect becomes more observable with increasing distance because the primary dose dominates in regions close to the source. In addition, we found that characteristic x rays contribute to less than 0.1% of the dose in regions around the surface of the applicator, and the contribution decreases with distance from the source. Therefore, the increase in dose due to characteristic x rays originating from the tungsten rod is negligible.

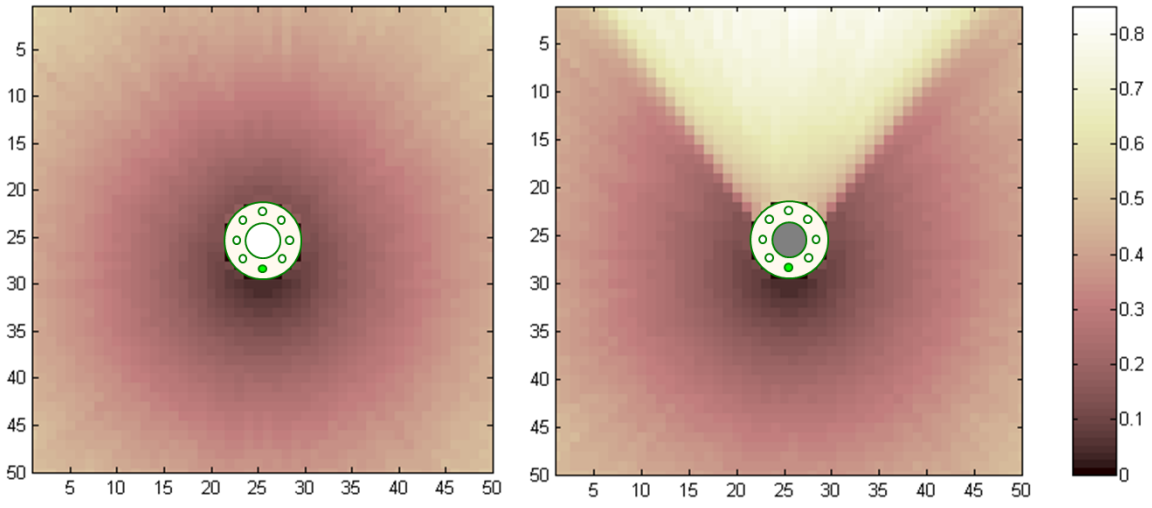


Figure 5.9. Distributions of the scatter to total dose ratios along the axial plane of (a) an unshielded and (b) a tungsten-shielded applicator with the source loaded at catheter 5. The voxel dimensions are $2\times2\times1$ mm$^3$.

We compared the simulation results with ionization chamber measurements. For higher simulation efficiency, the chamber geometry was not modeled in the MC calculations. We found that the photon energy spectra at various distances from the source are nearly unaffected by the presence of the shielding, except for the shielded region. On the tungsten-shielded side directly opposite from the source, GEANT4 calculations show that the average photon energy falls from 303 keV at a distance of 1.85 cm from the source position, to 179 keV at 5.15 cm. In the case of an unshielded applicator, the average energy drops from 318 to 255 keV. The variation in mass energy absorption coefficient ratios of Lucite to air for the photon energy range within this distance is within 0.2%. Furthermore, the small spectral variation is not expected to result in significant changes in perturbation due to the already small chamber volume. To verify our assumption, we compared simulation results with and without the air cavity modeled at distances of 1.7 and 5.2 cm from the source behind the shielded region. With the air cavity modeled, the ratios of doses with and without shielding at these two distances were 0.150±0.004 and 0.238±0.009, respectively. The dose ratios are slightly but insignificantly higher in this worst-case scenario compared to the ratios calculated without the air cavity present (0.148±0.004 and 0.222±0.008).

The doses at various points around the tungsten-shielded applicator in Lucite normalized to the cases without shielding are shown in Figure 5.10. The experimental uncertainties were calculated as the standard deviations of three measurements, which are less than 1% in front of the loaded catheter 7, and up to 44% in the low dose regions when the angle between the detector and the $^{192}$Ir source with respect to the applicator center is about 135°, i.e., in the shadow of the shielding. At other measurement positions, the uncertainties are within 5%.

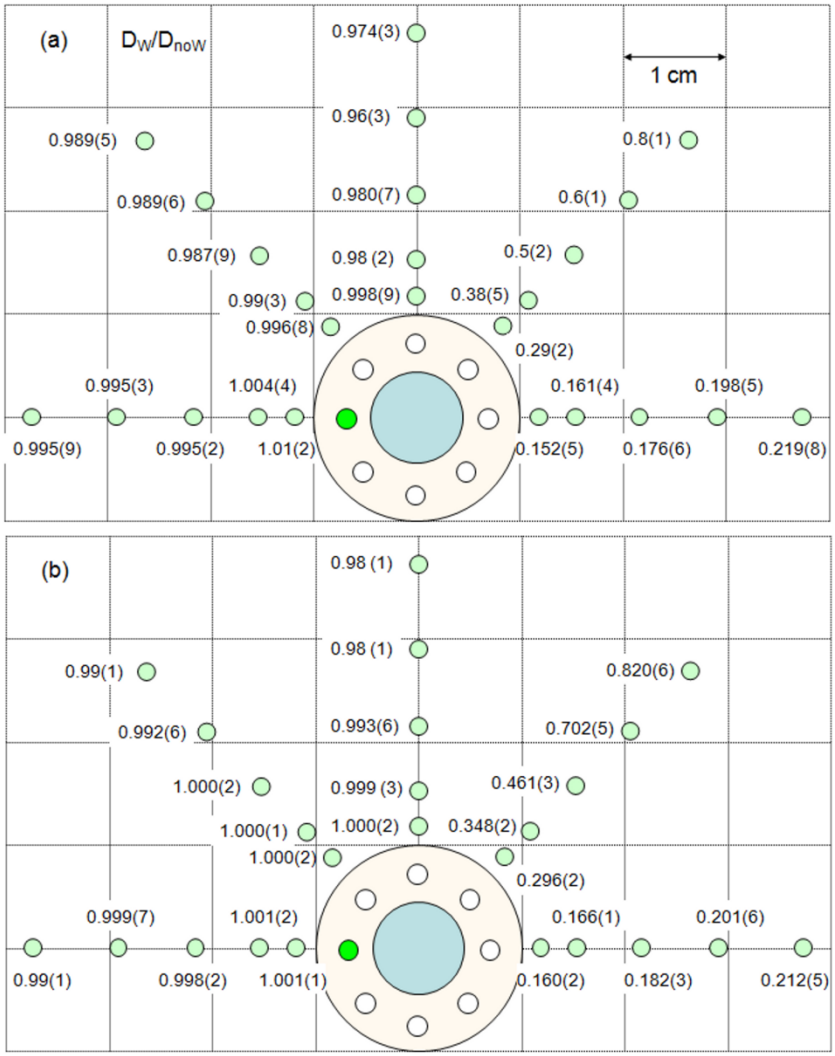


Figure 5.10. Ratios of dose around the applicator with tungsten shielding to dose without shielding as (a) measured using ion chamber, and (b) calculated using GEANT4. The source is positioned in catheter 7. Each number in brackets represents the uncertainty of the last digit.

We performed MC simulations in a Lucite phantom to investigate the changes in dose as a result of the applicator being rotated by 2°, 5°, 10°, 20°, and 30° while the detector position is fixed. In the unshielded regions, the dose variations are consistent with the inverse square law prediction. When shielding is inserted, drastic changes as shown in Figure 5.11 are seen in the regions partially shielded by the tungsten rod. The changes in

photon attenuation as the photons travel through the high density shielding cause the large experimental uncertainties in the case when the ionization chamber is in the shadow of the shielding. Taking into account the experimental uncertainties, the GEANT4 results are in agreement with the ionization chamber measurements.

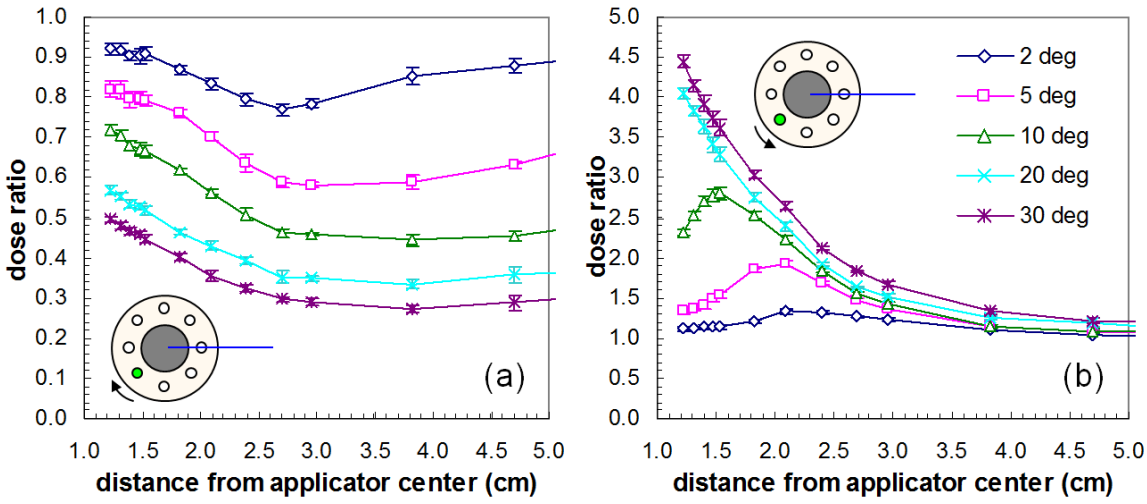


Figure 5.11. Dose along the direction as indicated by the line in the insert with the applicator rotated (a) clockwise and (b) counterclockwise by 2°, 5°, 10°, 20°, and 30° relative to the case without rotation. The source is in catheter 6 in both cases.

### 5.3.4. *Dose reduction due to liquid-filled balloon*

GEANT4 calculations show that there is a maximum of 8% additional dose reduction at a point in contact with the surface of a balloon injected with 30 mL of iodine solution (300 mg I/mL) compared to the case of a water-filled balloon. This maximum occurs when the source is loaded in catheter 3 of a tungsten-shielded applicator (see Figure 5.4). With the source positioned in catheters 4 and 5, the reductions are 5% and 4%, respectively. As the average distance traveled by photons inside the liquid is shorter, the extra radiation protection provided by the contrast medium is reduced slightly. The standard deviations in the calculations are within 1%.

EBT model film measurements were performed to verify the GEANT4 results. The source was sent to catheters 3 and 4 in separate experiments, which were on the opposite side of the shielding with respect to the balloon. With the region of interest set to a $3\times3$ mm$^2$ area, the extra dose reductions offered by the iodine solution were 7% and 4%, respectively, for the two loading locations. The agreement with MC calculations was considered good because the irregular shape of the balloon was not fully accounted for in GEANT4, and there was a rotational uncertainty of a few degrees in our experiments.

The results above indicate that a balloon injected with a contrast medium provides additional radiation protection of a few percent compared to water. Nonetheless, a water-filled balloon still offers significant sparing of the healthy tissues contralateral to the target because the balloon wall filled with liquid serves to push its neighboring tissues away from the $^{192}$Ir source. MC calculations show that with the source loaded in the catheter farthest away from the balloon, the dose at a point on the distal end of a water-filled balloon is lower by 53% compared to the dose without a balloon on the surface of the applicator in the tungsten-shielded region.

### 5.3.5. *Uncertainty analysis*

Table 5.2 summarizes the uncertainties for the EBT film measurements and Monte Carlo dose calculations, and the format is based on Table XII of the TG43 update [35]. The evaluation was performed for an $^{192}$Ir source loaded in one catheter position in an unshielded applicator in water, and all values are for 1-$\sigma$ uncertainties. Due to a lack of published work related to rigorous uncertainty assessments for high energy brachytherapy sources, we have made conservative estimates of the uncertainties.

Table 5.2. Uncertainty analysis for EBT film measurements and GEANT4 calculations along the transverse plane of the $^{192}$Ir source placed inside an unshielded intracavitary mold applicator in water. The distance $r$ is along the transverse axis originating from the source center. Types A and B uncertainties represent the 1-$\sigma$ statistical and systematic uncertainties, respectively.

| EBT film uncertainties | | | | |
|---|---|---|---|---|
| Component | $r$ = 1 cm | | $r$ = 4 cm | |
| | Type A | Type B | Type A | Type B |
| Repetitive measurements | 2.1% | | 2.5% | |
| Film calibration | | 1.2% | | 2.0% |
| Film readout | | 0.9% | | 0.9% |
| Source positioning | | 1.7% | | 0.8% |
| Quadrature sum | 2.1% | 2.3% | 2.5% | 2.3% |
| Total uncertainty | 3.1% | | 3.4% | |
| ADCL $S_K$ uncertainty | 1.3% | | | |
| Total combined uncertainty | 3.4% | | 3.7% | |

| Monte Carlo uncertainties | | |
|---|---|---|
| Component | $r$ = 1 cm | $r$ = 4 cm |
| Statistics | 0.4% | 2.2% |
| Photoionization cross sections | 2% | |
| Source geometry | 0.5% | |
| source energy spectrum | 0.1% | |
| Quadrature sum | 2.1% | 3.0% |

The EBT film experimental uncertainties based on three repeated measurements were estimated to be 2.1% and 2.5% at radial distances $r$ of 1 and 4 cm, respectively. The uncertainties for film calibration based on five repeated procedures were about 1.2% at $r$ = 1 cm and 2.0% at $r$ = 4 cm. Because the calibration and measurement procedures were both performed in water under similar conditions, a correction factor for the measurement medium can be eliminated. The uncertainty in film readout was based on the pixel values in three consecutive scans for a piece of uncut EBT film exposed to a uniform dose of 6 Gy using a 6 MV photon beam. Based on two profiles extracted along the longitudinal

and transverse directions in the central 10×10 $cm^2$ region for each of the three scans, the uncertainty was estimated to be 0.9%. For the source positioning, we assume an inverse square falloff of dose with distance, with an uncertainty of 1 mm in the source longitudinal direction and a rotational uncertainty of 5°. In this way, positioning uncertainties of 1.7% and 0.8% were calculated for $r$ = 1 and 4 cm, respectively. It should be noted that there are correlations between the uncertainties for the repetitive measurements and source positioning. According to the certification of calibration issued from the University of Wisconsin Accredited Dosimetry Calibration Laboratory (ADCL), the uncertainty for $S_K$ is 1.3%. Overall, the combined uncertainties are 3.4% for $r$ = 1 cm and 3.7% for $r$ = 4 cm.

For the Monte Carlo simulations, the statistical uncertainties are 0.4% and 2.2% for $r$ = 1 and 4 cm, respectively. The photoionization cross sections have uncertainties of up to 2% [18]. Assuming that the uncertainties are 0.5% for the source geometry [36] and 0.1% for the source energy spectrum, the total uncertainties are 2.1% for $r$ = 1 cm and 3.0% for $r$ = 4 cm.

## 5.4. SUMMARY AND CONCLUSIONS

The dosimetric properties of a novel intracavitary brachytherapy applicator have been investigated using the GEANT4 MC code and verified by GAFCHROMIC™ EBT film and ionization chamber measurements. The flexible structure and multichannel design of the applicator allow for conformal HDR brachytherapy treatment of deep-seated rectal tumors. Significant sparing of surrounding healthy tissues can be achieved because the applicator is compatible with shielding and balloon placement. An 8 mm diameter tungsten rod inserted into the applicator central cavity can reduce dose on the side

opposite the $^{192}$Ir source by up to 85%. A similar shielding effect can also be attained with a lead rod, for which the maximum dose reduction is 80%. The applicator can be inserted into a balloon filled with either water or contrast medium to push the healthy tissues away from the $^{192}$Ir source by up to 1 cm. Use of a contrast medium allows the balloon region to be visible on CT images and offers slightly better radiation protection.

The GEANT4 MC code has been validated for HDR intracavitary applications. The radial dose function and anisotropy function generated with full simulation of the $^{192}$Ir source agree with published data. We have established that the use of a PHSP model for HDR intracavitary applications does not require explicit placement of the source in the simulation medium. Although there is disagreement of up to 8% in the anisotropy function near the source longitudinal axis, photons emitted along the longitudinal ends of the source tend to travel within the applicator and will contribute little to patient dose.

Since there is a high dose gradient around the $^{192}$Ir source, ionization chamber measurements require accurate spatial positioning. The experimental uncertainty is highest when the detector is partially shielded by the tungsten rod. On the other hand, GAFCHROMIC$^{TM}$ EBT model film is found to be suitable for $^{192}$Ir brachytherapy dosimetry applications. Its high spatial resolution permits easy acquisition of two-dimensional dose distributions. We have shown that if carefully processed, it is safe to use this model film for in-water measurements. Using an $^{192}$Ir HDR source for film calibration in water and a flat bed document scanner for film scanning, we obtained good agreement between measurements and GEANT4 calculations.

## 5.5. REFERENCES


1. Swedish Rectal Cancer Trial. Improved survival with preoperative radiotherapy in resectable rectal cancer. N Engl J Med. 1997;336:980-7.

2. Kapiteijn E, Marijnen CA, Nagtegaal ID, Putter H, Steup WH, Wiggers T, et al. Preoperative radiotherapy combined with total mesorectal excision for resectable rectal cancer. N Engl J Med. 2001;345:638-46.

3. Sauer R, Becker H, Hohenberger W, Rodel C, Wittekind C, Fietkau R, et al. Preoperative versus postoperative chemoradiotherapy for rectal cancer. N Engl J Med. 2004;351:1731-40.

4. Cammà C, Giunta M, Fiorica F, Pagliaro L, Craxì A, Cottone M. Preoperative radiotherapy for resectable rectal cancer: A meta-analysis. JAMA. 2000;284:1008-15.

5. Colorectal Cancer Collaborative Group. Adjuvant radiotherapy for rectal cancer: a systematic overview of 8,507 patients from 22 randomised trials. Lancet. 2001;358:1291-304.

6. Gerard JP, Chapet O, Nemoz C, Hartweig J, Romestaing P, Coquard R, et al. Improved sphincter preservation in low rectal cancer with high-dose preoperative radiotherapy: the lyon R96-02 randomized trial. J Clin Oncol. 2004;22:2404-9.

7. Vuong T, Devic S, Moftah B, Evans M, Podgorsak EB. High-dose-rate endorectal brachytherapy in the treatment of locally advanced rectal carcinoma: technical aspects. Brachytherapy. 2005;4:230-5.

8. Vuong T, Belliveau PJ, Michel RP, Moftah BA, Parent J, Trudel JL, et al. Conformal preoperative endorectal brachytherapy treatment for locally advanced rectal cancer: early results of a phase I/II study. Dis Colon Rectum. 2002;45:1486-95.

9. Devic S, Vuong T, Moftah B. Advantages of inflatable multichannel endorectal applicator in the neo-adjuvant treatment of patients with locally advanced rectal cancer with HDR brachytherapy. J Appl Clin Med Phys. 2005 Spring;6(2):44-9.

10. Nath R, Anderson LL, Luxton G, Weaver KA, Williamson JF, Meigooni AS. Dosimetry of interstitial brachytherapy sources: recommendations of the AAPM Radiation Therapy Committee Task Group No. 43. American Association of Physicists in Medicine. Med Phys. 1995;22:209-34.

11. Agostinelli S, Allison J, Amako K, Apostolakis J, Araujo H, Arce P, et al. GEANT4-a simulation toolkit. Nucl Instrum Methods Phys Res A. 2003;506:250-303.

12. Daskalov GM, Loffler E, Williamson JF. Monte Carlo-aided dosimetry of a new high dose-rate brachytherapy source. Med Phys. 1998;25:2200-8.

13. Nuclear data from NuDat 2.0, a web-based database maintained by the National Nuclear Data Center [database on the Internet]. Brookhaven National Laboratory, Upton, NY 2004. Available from: http://www.nndc.bnl.gov/nudat2.

14. Baltas D, Karaiskos P, Papagiannis P, Sakelliou L, Loeffler E, Zamboglou N. Beta versus gamma dosimetry close to Ir-192 brachytherapy sources. Med Phys. 2001;28:1875-82.

15. Wang R, Li XA. Dose characterization in the near-source region for two high dose rate brachytherapy sources. Med Phys. 2002;29:1678-86.

16. GEANT4 Collaboration. Physics Reference Manual 2006. Available from: http://geant4.web.cern.ch/geant4/.

17. Poon E, Verhaegen F. Accuracy of the photon and electron physics in GEANT4 for radiotherapy applications. Med Phys. 2005;32:1696-711.

18. Cullen DE, Hubbell JH, Kissel L. EPDL97: The Evaluated Photon Data Library, '97 Version. Livermore, CA: Lawrence Livermore National Laboratory1997. Report No.: UCRL-50400, Rev. 5.

19. Perkins ST, Cullen DE, Chen MH, Hubbell JH, Rathkopf J, Scofield J. Tables and graphs of atomic subshell and relaxation data derived from the LLNL evaluated Atomic Data Library (EADL), Z=1–100. Livermore, CA: Lawrence Livermore National Laboratory 1991. Report No.: UCRL-50400.

20. Hubbell JH, Seltzer SM. Tables of x-ray mass attenuation coefficients and mass energy-absorption coefficients 1 keV to 20 MeV for elements Z=1 to 92 and 48 additional substances of dosimetric interest. Gaithersburg, MD: National Institute of Standards and Technology 1995. Report No.: NISTIR 5632.

21. Luxton G, Jozsef G. Radial dose distribution, dose to water and dose rate constant for monoenergetic photon point sources from 10 keV to 2 MeV:EGS4 Monte Carlo model calculation. Med Phys. 1999;26:2531-8.

22. Williamson JF, Li Z. Monte Carlo aided dosimetry of the microselectron pulsed and high dose-rate $^{192}$Ir sources. Med Phys. 1995;22:809-19.

23. Williamson JF. Monte Carlo evaluation of kerma at a point for photon transport problems. Med Phys. 1987;14:567-76.

24. Fragoso M, Seco J, Nahum AE, Verhaegen F. Incorporation of a combinatorial geometry package and improved scoring capabilities in the EGSnrc Monte Carlo Code system. Med Phys. 2003;30:1076-85.

25. Chibani O, Li XA. IVBTMC, a Monte Carlo dose calculation tool for intravascular brachytherapy. Med Phys. 2003;30:44-51.

26. Chibani O, Williamson JF. MCPI: a sub-minute Monte Carlo dose calculation engine for prostate implants. Med Phys. 2005;32:3688-98.

27. Carrier JF, Beaulieu L, Therriault-Proulx F, Roy R. Impact of interseed attenuation and tissue composition for permanent prostate implants. Med Phys. 2006;33:595-604.

28. Butson MJ, Cheung T, Yu PK. Weak energy dependence of EBT gafchromic film dose response in the 50 kVp-10 MVp X-ray range. Appl Radiat Isot. 2006;64:60-2.

29. Devic S, Seuntjens J, Sham E, Podgorsak EB, Schmidtlein CR, Kirov AS, et al. Precise radiochromic film dosimetry using a flat-bed document scanner. Med Phys. 2005;32:2245-53.

30. Wang Y, Lewis D, Poon E, Verhaegen F, Podgorsak E, Devic S. Sensitivity of document scanners used for radiochromic film dosimetry. Med Phys. 2006;33:2135.

31. Meli JA, Meigooni AS, Nath R. On the choice of phantom material for the dosimetry of $^{192}$Ir sources. Int J Radiat Oncol Biol Phys. 1988;14:587-94.

32. Lee HR, Pankuch M, Chu JC, Spokas JJ. Evaluation and characterization of parallel plate microchamber's functionalities in small beam dosimetry. Med Phys. 2002;29:2489-96.

33. Kirov AS, Williamson JF, Meigooni AS, Zhu Y. Measurement and calculation of heterogeneity correction factors for an Ir-192 high dose-rate brachytherapy source behind tungsten alloy and steel shields. Med Phys. 1996;23:911-9.

34. Waterman FM, Holcomb DE. Dose distributions produced by a shielded vaginal cylinder using a high-activity iridium-192 source. Med Phys. 1994;21:101-6.

35. Rivard MJ, Coursey BM, DeWerd LA, Hanson WF, Huq MS, Ibbott GS, et al. Update of AAPM Task Group No. 43 Report: A revised AAPM protocol for brachytherapy dose calculations. Med Phys. 2004;31:633-74.

36. Büermann L, Kramer HM, Schrader H, Selbach HJ. Activity determination of $^{192}$Ir solid sources by ionization chamber measurements using calculated corrections for self-absorption. Nucl Instrum Methods Phys Res A. 1994;339:369-76.

# Chapter Six

# Paper II: Patient-Specific Monte Carlo Dose Calculations for HDR $^{192}$Ir Endorectal Brachytherapy

Emily Poon, Jeffrey Williamson, Té Vuong, Frank Verhaegen

*Int J Radiat Oncol Biol Phys. 2008;72:1259-66*



In Chapter 5, we presented the dosimetric characteristics of a shielded endorectal applicator in homogeneous phantoms. In this chapter, we will focus on the effects of this applicator for cancer patients treated with HDR-EBT. A CT-based MC dose calculation approach for the retrospective evaluation of 40 HDR-EBT patient plans will be introduced. This study confirms our understanding (as discussed in Chapter 3) that tissue inhomogeneity effects are relatively minor for $^{192}$Ir brachytherapy. We are therefore able to use a more efficient dose superposition approach to account for effects of the shielded applicator for HDR-EBT treatment planning. The validation of this technique will be presented in this paper.

## ABSTRACT

Purpose: An integrated software platform was developed to perform a patient-specific dosimetric study on high-dose-rate $^{192}$Ir endorectal brachytherapy. Monte Carlo techniques were used to examine the perturbation effects of an eight-channel intracavitary applicator with shielding and a liquid-inflatable balloon. Such effects are ignored in conventional treatment planning systems that assume water-equivalent geometries.

Methods and Materials: A total of 40 Task Group 43-based rectal patient plans were calculated using the PTRAN_CT Monte Carlo photon transport code. The silicone applicator, tungsten or lead shielding, contrast solution-filled balloon, and patient anatomy were included in the simulations. The dose to water and dose to medium were scored separately. The effects of heterogeneities and uncertainties in source positioning were examined. A superposition calculation method using pre-generated Monte Carlo dose distributions about the shielded applicator in water was developed and validated for efficient treatment planning purposes.

Results: On average, metal shielding decreases the mean dose to the contralateral normal tissues by 24% and reduces the target volume covered by the prescribed dose from 97% to 94%. Tissue heterogeneities contribute to dose differences of <1% relative to the prescribed dose. The differences in the dose volume indices between dose to water and dose to medium-based calculations were <1% for soft tissues, <2% for bone marrow, and >20% for cortical bone. A longitudinal shift of ±2.5 mm and a rotational shift of ±15° in applicator insertion reduced the target volume receiving the prescribed dose by ≤4%.

Conclusion: The shielded applicator improved dose conformity and normal tissue sparing; however, Task Group 43-based treatment planning might compromise target coverage by not accounting for shielding.

## 6.1. INTRODUCTION

The Monte Carlo (MC) method is a valuable tool in brachytherapy dosimetry. It can be used to accurately characterize brachytherapy sources, applicators, and shielding. To date, most MC studies that have investigated tissue heterogeneity effects were based on simulations in mathematical phantoms [1, 2] rather than more realistic patient geometries derived from computed tomography (CT) images [3, 4]. The limitations of many MC codes in modeling complex brachytherapy simulation geometries make it difficult to perform clinical patient-specific dosimetric studies. In addition to the long calculation time, laborious preprocessing steps are needed to model the brachytherapy applicator and/or seed structures superimposed onto the three-dimensional patient geometry.

In this study, an integrated software platform that interfaces with a fast MC photon transport code was developed for brachytherapy dose calculations and analysis. It was used in a retrospective patient study to evaluate the effects of metal shielding and anatomic heterogeneities on high-dose-rate endorectal brachytherapy (HDR-EBT), practiced at the Montreal General Hospital as a preoperative treatment of locally advanced rectal cancer [5, 6].

## 6.2. METHODS AND MATERIALS

The McGill institutional review board provided ethical approval for this study (Study No. A03-M49-06B).

### 6.2.1. *Intracavitary applicator and HDR-EBT*

An eight-channel intracavitary applicator made of flexible silicone rubber (OncoSmart, Nucletron, Veenendaal, The Netherlands) was used in HDR-EBT (Figure 6.1). This 28-cm-long, 2-cm-diameter applicator can be inserted into a liquid-inflatable endocavitary balloon (Civco Medical Solutions, Kalona, IA) for a snug fit in the rectum. The applicator has a central lumen designed for the optional insertion of an 8-mm-diameter metal shielding rod, used for patients with noncircumferential lesions to protect the contralateral normal tissues [7].

Figure 6.1. Flexible, eight-channel intracavitary applicator for use in high-dose-rate $^{192}$Ir endorectal brachytherapy (Nucletron, Veenendaal, The Netherlands).

The PLATO brachytherapy planning system and the microSelectron HDR $^{192}$Ir remote afterloader (Nucletron) were used for treatment planning and delivery. The patient plans were created, assuming water-equivalent geometries in accordance with the American Association of Physicists in Medicine Task Group 43 (TG-43) protocol [8].

Most patients received four daily fractions of 6.5 Gy prescribed to the margin of the clinical target volume (CTV). The aim of the procedure is to downsize the tumor before surgery, which is performed a few weeks after brachytherapy. Some patients underwent three weekly fractions of 10 Gy as a boost to external beam radiotherapy without surgery. The dosimetric properties of the shielded applicator and technical aspects of HDR-EBT have been previously reported [7, 9, 10].

The treatment plans created between April 2005 and March 2006 were exported from PLATO for recalculation using MC techniques. Of these plans, 40 were delivered with shielding made of tungsten alloy (density, 18.0 g/cm$^3$, Densimet, Plansee SE, Austria) or lead (density, 11.35 g/cm$^3$). More recent patients treated with the same technique were excluded because of an upgrade of the afterloading system that involved a change in the $^{192}$Ir source design.

### 6.2.1. *Patient-specific calculations with PTRAN_CT*

The PTRAN_CT code developed by Le et al. [11] was used for MC calculations. PTRAN_CT is an extension of the well-benchmarked PTRAN photon transport code [12, 13] and is intended for patient-specific brachytherapy dose calculations. It allows the applicator and the source structures to be defined independently of the patient voxel geometry, which can be assigned continuous mass densities and material types. In this study, the DLC-146 cross-section library [14] and the mass energy absorption coefficients of Hubbell and Seltzer [15] were used. The absorbed dose was approximated by collision kerma and was scored using the exponential track length estimation method [12].

Each MC simulation requires a patient data file that contains the voxel boundaries and the anatomic information. Material and density matrices of 2×2×2 mm$^3$ voxel

resolution were derived from the CT data. Modifications were made to assign the proper media and densities for the contrast solution-filled balloon, endoscopic metal clips around the target, and bone marrow regions. A preprocessor code was used to identify the voxels occupied by the silicone applicator of 1.14 g/cm$^3$ density. In a separate input file, the geometry of the shielded applicator and the source positions were defined. The simulations included 12 media: air, adipose tissue, soft tissue, yellow marrow, spongiosa, femur bone, cortical bone, titanium, diluted iodine contrast solution (50 mg I/mL concentration), silicone, lead, and tungsten alloy.

Instead of modeling the Nucletron $^{192}$Ir classic source design explicitly, a phase space file of the source was used for photon generation. The primary photon spectrum was obtained from the NuDat, version 2.0, database [16]. This phase space source model was validated in a previous study [7]. In a simulation of the source in vacuum, the dose to a small mass of air at 5 cm along the source transverse axis was scored with 0.2% uncertainty. This was done to calculate the air kerma strength per primary photon history, which was needed to normalize the tissue dose distribution in terms of air kerma strength. Two CT-based simulations were performed for each patient to score the absorbed dose to water ($D_w$) and absorbed dose to medium ($D_m$) separately, using the mass energy absorption coefficients of the appropriate media. To examine the effects of tissue heterogeneities, water-based calculations ($D_{water\text{-}based}$) were performed in which the patient and balloon geometries outside the applicator were replaced by water of 1 g/cm$^3$ density. Of the 40 patient plans, 14 were calculated with tungsten shielding and 26 with lead. A total of 40 million histories were run to obtain mean 1−$\sigma$ statistical uncertainties of 0.5% in the CTV with a 29-cm$^3$ mean volume, and 1.8% averaged over the patient geometry of about 1 million voxels.

### 6.2.2. *Single-dwell superposition and TG-43 calculations*

A single-dwell superposition (SDS) algorithm was developed for efficient HDR-EBT dose calculations. The algorithm involves minimal preprocessing, apart from the one-time simulations of the $^{192}$Ir source inside a catheter at various points along the tungsten or lead-shielded applicator in water. Three-dimensional dose contribution matrices, $D_{ij}$, defined as the dose at voxel $i$ from a unit dwell weight at point $j$, were generated using version rev8 of PTRAN. Specific matrices for dwell positions within 4 cm of the catheter distal end were used to simulate the reduced perturbation of the shielding around its tip. All dwell positions were oriented in alignment with the applicator. Because the applicator is cylindrically symmetric, the dose contribution from a given position in any of the eight catheters can be calculated using the same $D_{ij}$ by applying a coordinate transformation. The statistical uncertainties of $D_{ij}$ were 1.2% at 10 cm from the source and 1.6% averaged over the 30×30×20-cm$^3$ volume of 2×2×2 mm$^3$ voxel dimensions.

All patient plans were calculated using TG-43 two-dimensional algorithm and the superposition method with both lead and tungsten shielding. The accuracy of the SDS algorithm and the differences between the two shielding materials were examined. A single dose grid was used for each patient so that dosimetric indices could be comparable, independent of the calculation algorithm used.

### 6.2.3. *Dose evaluation using BrachyGUI*

BrachyGUI, an in-house dose calculation and analysis tool developed using MATLAB, version 7.5.0 (MathWorks, Natick, MA), was used extensively for this study [17]. An interface allows BrachyGUI to process the treatment plans in DICOM format and to create the patient data and input files for the PTRAN_CT simulations. The SDS and

TG-43 algorithms were both implemented in BrachyGUI. Dose volume histograms and indices can also be calculated with BrachyGUI for plan quality evaluation.

The dose conformity was evaluated using the conformation number, CN [18]:

$$\mathrm{CN} = \frac{V_{\mathrm{T,ref}}^{2}}{V_{\mathrm{T}} V_{\mathrm{ref}}}, \tag{6.1}$$

where $V_{\mathrm{T}}$ is the target volume and $V_{\mathrm{T,ref}}$ is the target volume covered by the prescribed dose ($D_{\mathrm{ref}}$). The treated volume, $V_{\mathrm{ref}}$, refers to the total tissue volume covered by $D_{\mathrm{ref}}$. With a range of 0–1, a greater CN suggests a greater degree of conformity with better target coverage and normal tissue avoidance. The external volume index, EI, was calculated as follows [19]:

$$\mathrm{EI} = \frac{V_{\mathrm{tissue,ref}}}{V_{\mathrm{T}}}, \tag{6.2}$$

where $V_{\mathrm{tissue,ref}}$ is the normal tissue volume covered by $D_{\mathrm{ref}}$.

The dose and volume contributions from nontissue regions were excluded for the dosimetric evaluation. This was accomplished by using Boolean mask operations based on the material matrix in the patient data file. The exclusion allows for a better assessment of dose conformity, especially because the metal clips, applicator, and balloon are in close proximity to the CTV.

The percentage of the CTV covered by 100% and 150% of $D_{\mathrm{ref}}$ ($V_{100}$ and $V_{150}$), and the minimum dose received by 90% of the CTV ($D_{90}$) were calculated. The mean dose ($D_{\mathrm{mean}}$) to the contralateral normal tissues, comprising mainly the uninvolved rectal wall, was calculated to measure the effectiveness of the shielding. The volume was confined to within 5 mm of the perimeter of the balloon that did not extend beyond 1 cm of the superior and inferior margins of the target. It was defined systematically using

Boolean masks. For the 12 patients without a balloon on the CT images, the volume was confined to within 5 mm of the applicator. In addition, the minimum dose to the hottest 1, 2, and 5 $cm^3$ ($D_{1cc}$, $D_{2cc}$, and $D_{5cc}$) of the bladder and various bone types were calculated to examine anatomic heterogeneity effects. The doses are expressed as a percentage of $D_{ref}$.

### 6.2.4. *Applicator positioning sensitivity analysis*

The HDR-EBT patients received fractionated treatments according to the CT-based treatment plan created before the first fraction. A quality assurance procedure was devised to ensure correct dose delivery without having to acquire new CT images for every fraction [10]. The target, with its proximal and distal margins delineated by endoscopic metal clips, was located along the rectal wall and was in contact with the applicator. Because it would be difficult to reinsert the applicator reproducibly, the quality assurance procedure required daily image-guided longitudinal and rotational shift corrections. The shift in source loading was inferred from the relative locations of the clips on the CT-digitally reconstructed radiograph and on the radiograph acquired before treatment. Additionally, the applicator was rotated until a desired alignment pattern of the preloaded radiopaque markers was observed in fluoroscopic images.

The calculations in this study assumed the planning CT geometry. To estimate the errors associated with positioning uncertainties, TG-43 and superposition calculations were repeated for each patient with all dwell positions shifted longitudinally by ±2.5 mm and rotated by ±15°. These were the error margins estimated for the quality assurance procedure throughout the treatment course. The maximum and minimum CTV $V_{100}$ after

the shifts were compared with the original $V_{100}$ to quantify how the target coverage would be affected.

## 6.3. RESULTS

Throughout this section, comparisons have been made with MC results given as dose to water. Accordingly, the acronym MC refers to PTRAN_CT $D_w$-based calculations.

### 6.3.1. *Comparisons of isodose distributions*

Figures 6.2(a)–6.2(f) show the MC and TG-43 isodose distributions for three representative patients. The first patient plan [Figures 6.2(a)–6.2(b)] illustrates an ideal scenario in which the tungsten shielding decreased the dose to the contralateral normal tissues, leaving the target dose unaffected. The liquid-filled balloon further reduced the normal tissue dose owing to its volumetric expansion toward the shielded side. An undesirable situation is demonstrated in the second patient plan [Figures 6.2(c)–6.2(d)], in which the CTV was partially shielded by the lead and the cold spots cannot be predicted by TG-43. The third patient plan [Figures 6.2(e)–6.2(f)] shows that dose perturbations caused by the applicator, contrast solution, and anatomic heterogeneities were negligible. This last patient was treated without shielding and thus was excluded from the study cohort.

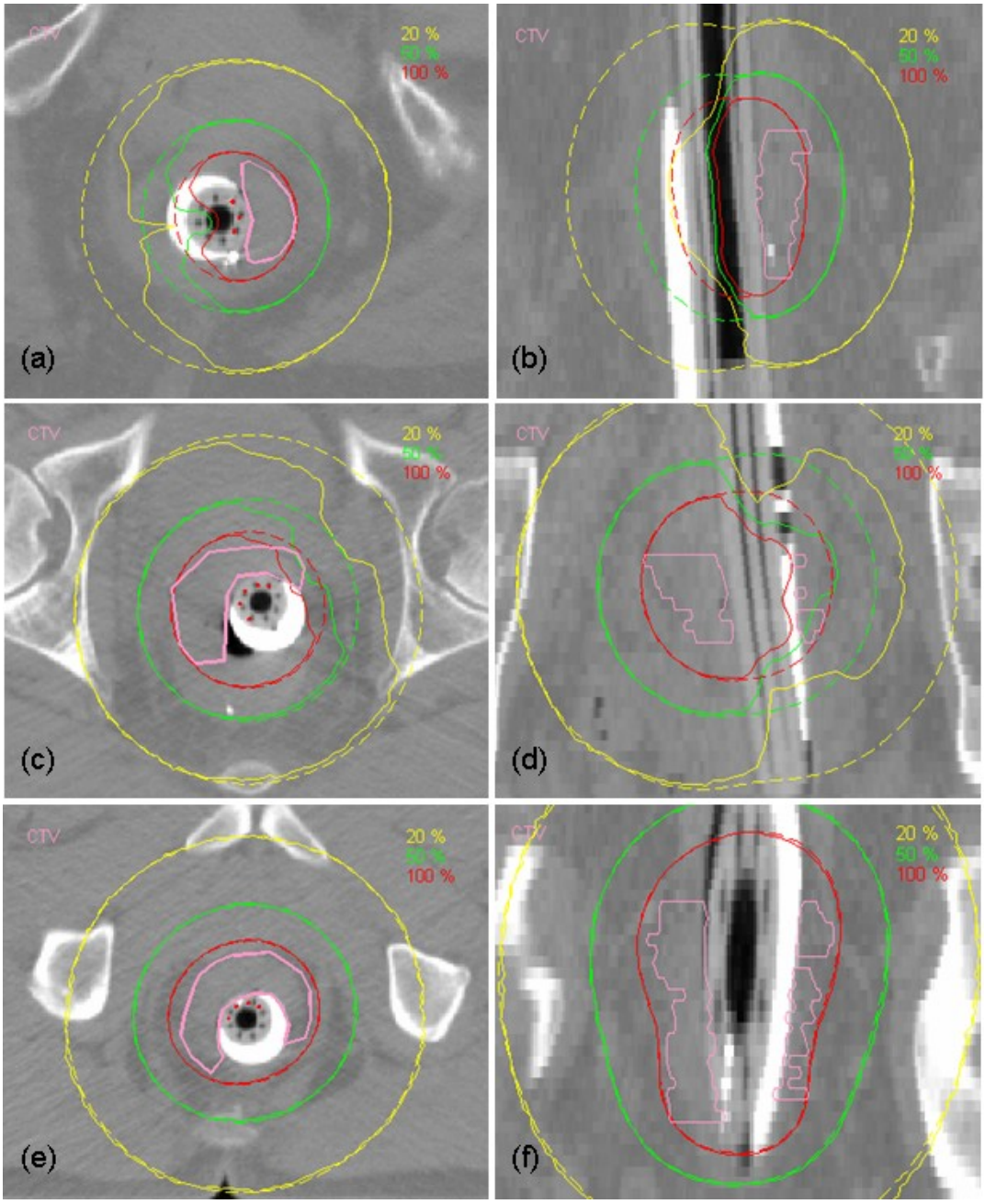


Figure 6.2. Axial and coronal views of Monte Carlo (solid lines) and Task Group 43 (dashed lines) isodose distributions for high-dose-rate $^{192}$Ir endorectal brachytherapy patients treated (a,b) with tungsten shielding, (c,d) with lead shielding, and (e,f) without shielding. The clinical target volume is outlined in pink, and the white structure around applicator is the endocavitary balloon injected with contrast solution.

### 6.3.2. *Comparisons of plan quality metrics*

Table 6.1 summarizes the CTV $V_{100}$, CTV $D_{90}$, CN, and EI for the MC and TG-43 calculations of the 40 patient plans. On average, TG-43 overestimated the $V_{100}$ by 3% (95% confidence interval [CI], 1.8–4.2%) and $D_{90}$ by 7% (95% CI, 4–9%). The CN was decreased by 12% (95% CI, 10–14%), and the EI was increased by 37% (95% CI, 31–43%) when shielding was not accounted for. In 9 cases, TG-43 overestimated the $V_{100}$ by ≥5% (mean, 9%; range, 5−14%), and cold spots were evident.

Table 6.1. Plan quality metrics for 40 patient plans based on MC and TG-43 calculations.

| | CTV $V_{100}$ (%) | | CTV $D_{90}$ (%) | | CN | | EI | |
|---|---|---|---|---|---|---|---|---|
| | MC | TG-43 | MC | TG-43 | MC | TG-43 | MC | TG-43 |
| Mean | 94 | 97 | 113 | 120 | 0.41 | 0.36 | 1.3 | 1.8 |
| Range | 81-100 | 85-100 | 86-138 | 97-140 | 0.20-0.54 | 0.19-0.50 | 0.6-2.8 | 1.0-3.7 |
| 95% CI | 93-96 | 96-98 | 109-117 | 117-124 | 0.38-0.43 | 0.33-0.38 | 1.1-1.5 | 1.6-2.0 |
| SD | 5 | 3 | 13 | 11 | 0.08 | 0.07 | 0.5 | 0.7 |

*Abbreviations:* MC = Monte Carlo; TG-43 = Task Group 43; CTV = clinical target volume; $D_{90}$ = minimum dose received by 90% of CTV; $V_{100}$ = volume receiving 100% of prescribed dose; CN = conformation number; EI = external volume index; CI = confidence interval; SD = standard deviation.

The contralateral normal tissue $D_{mean}$ using the MC calculations were 108% and 206% of $D_{ref}$ (95% CI, 92–123% and 157–255%, respectively) for patient plans with and without a balloon, respectively. The corresponding TG-43 $D_{mean}$ were 135% and 247% (95% CI, 116–155% and 189–306%). On average, shielding decreased the $D_{mean}$ by 24% ± 7%.

### 6.3.3. *Dose differences due to heterogeneities and $D_m$ reporting*

Table 6.2 lists the MC $D_w$-based dose volume indices ($D_x^{Dw}$) for various soft-tissue and bony structures. It also provides the percentage differences compared with TG-43 ($D_x^{TG43}$),PTRAN_CT water-based ($D_x^{water}$), and $D_m$-based ($D_x^{Dm}$) calculations. Local differences were expressed with respect to $D_x^{Dw}$ and relative differences with respect to $D_{ref}$. Box and whisker plots of the percentage differences to $D_{2cc}$ for the 40 patient plans are shown in Figure 6.3 to demonstrate the statistical distributions.

Compared with TG-43, which does not account for shielding, the mean local differences were ≥7%. Also, the standard deviations of the differences were the greatest because the shielding perturbed the doses differently in the different patient plans. In contrast, local agreement between $D_x^{Dw}$ and $D_x^{water}$ was ≤2%, except for the $D_{5cc}$ of the cortical bone, which was 5% on average. Moreover, all relative differences were well within 1%. However, the mean local differences between $D_x^{Dw}$ and $D_x^{Dm}$ were ≤2% for soft tissues and yellow marrow and ≤28% for other bony structures. The differences relative to $D_{ref}$ were ≤3% for all structures.

Table 6.2. Dose volume indices and standard deviations ($\sigma$) relative to prescribed dose ($D_{ref}$) for various structures based on PTRAN_CT calculations reporting dose to water $D_x^{Dw}$

| Structure | DVI | MC dose $D_x^{Dw} \pm \sigma$ (%) | Local difference $\frac{D - D_x^{Dw}}{D_x^{Dw}} \cdot 100\% \pm \sigma$ (%) | | | Relative difference $\frac{D - D_x^{Dw}}{D_{ref}} \cdot 100\% \pm \sigma$ (%) | | |
|---|---|---|---|---|---|---|---|---|
| | | | $D = D_x^{TG43}$ | $D = D_x^{water}$ | $D = D_x^{Dm}$ | $D = D_x^{TG43}$ | $D = D_x^{water}$ | $D = D_x^{Dm}$ |
| CTV | $D_{90}$ | 110±10 | 7±8 | 0.6±0.5 | -0.8±0.1 | 7±7 | 0.7±0.6 | -0.9±0.1 |
| Contralateral normal tissues | $D_{mean}$ | 140±70 | 24±7 | 0.9±0.3 | -0.7±0.1 | 30±20 | 1.1±0.4 | -1.0±0.5 |
| Bladder | $D_{1cc}$ | 50±30 | 26±30 | 1.2±0.7 | -0.7±0.1 | 10±10 | 0.5±0.3 | -0.3±0.2 |
| | $D_{2cc}$ | 40±30 | 30±30 | 1.2±0.7 | -0.7±0.1 | 10±10 | 0.4±0.3 | -0.3±0.2 |
| | $D_{5cc}$ | 40±20 | 30±40 | 1.3±0.7 | -0.7±0.1 | 9±10 | 0.4±0.2 | -0.3±0.2 |
| Yellow marrow | $D_{1cc}$ | 20±10 | 9±8 | 1.8±0.8 | -1.4±0.2 | 2±2 | 0.3±0.2 | -0.3±0.1 |
| | $D_{2cc}$ | 17±9 | 10±8 | 2.0±0.9 | -1.5±0.3 | 2±2 | 0.3±0.2 | -0.2±0.1 |
| | $D_{5cc}$ | 14±8 | 10±10 | 2±1 | -1.7±0.3 | 2±1 | 0.3±0.2 | -0.2±0.1 |
| Spongiosa | $D_{1cc}$ | 30±10 | 7±7 | 1.5±0.8 | 5±1 | 2±1 | 0.4±0.3 | 1.2±0.5 |
| | $D_{2cc}$ | 20±10 | 8±8 | 1.7±0.8 | 5±1 | 2±2 | 0.4±0.3 | 1.1±0.5 |
| | $D_{5cc}$ | 20±10 | 10±8 | 2.0±0.7 | 5±1 | 2±2 | 0.4±0.2 | 1.1±0.5 |
| Femur bone | $D_{1cc}$ | 40±20 | 7±8 | 1.0±0.9 | 6±2 | 2±3 | 0.4±0.4 | 2±1 |
| | $D_{2cc}$ | 40±20 | 7±6 | 1.0±0.8 | 7±2 | 2±2 | 0.3±0.4 | 2±1 |
| | $D_{5cc}$ | 30±10 | 7±6 | 1.1±0.6 | 8±2 | 2±2 | 0.3±0.3 | 2±1 |
| Cortical bone | $D_{1cc}$ | 16±8 | 14±9 | 3±1 | 21±6 | 2±1 | 0.4±0.2 | 3±1 |
| | $D_{2cc}$ | 14±8 | 20±10 | 3±1 | 23±5 | 2±1 | 0.4±0.2 | 3±1 |
| | $D_{5cc}$ | 10±6 | 20±10 | 5±2 | 28±7 | 2±1 | 0.4±0.2 | 3±1 |

*Abbreviations:* DVI = dose volume index; $D_{mean}$ = mean dose; $D_{1cc}$, $D_{2cc}$, $D_{5cc}$ = minimum dose to the hottest 1, 2, and 5 $cm^3$, respectively; other abbreviations as in Table 6.1. Data presented as local and relative percentage differences.

Symbols $D_x^{TG43}$, $D_x^{water}$, and $D_x^{Dm}$ refer to dose volume indices based on TG-43 calculations, PTRAN_CT calculations with patient anatomy replaced by water, and PTRAN_CT calculations reporting dose to medium, respectively.

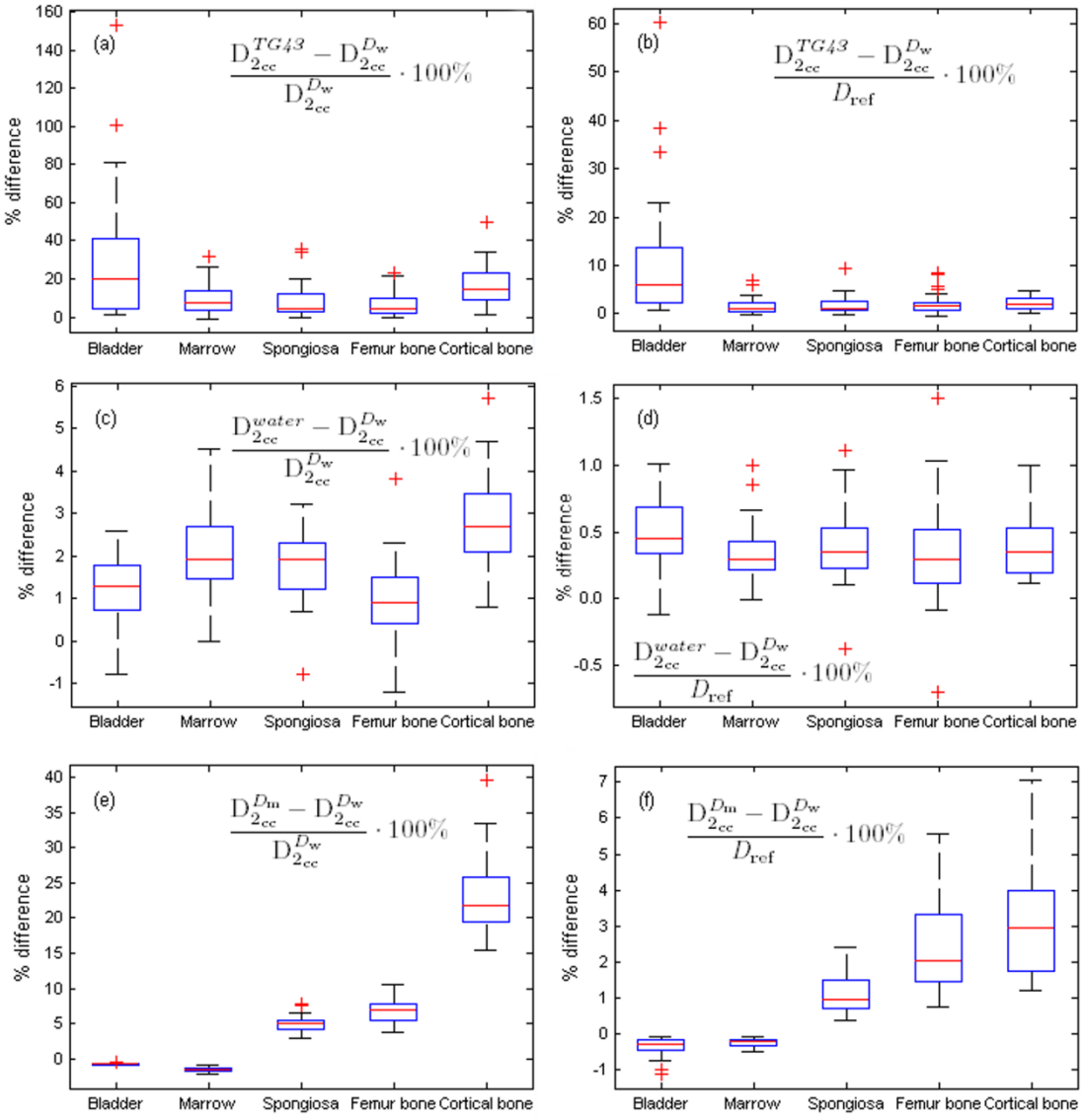


Figure 6.3. Box and whisker plots showing local and relative percentage differences in minimal dose to hottest 2 cm$^3$ for various structures. Superscripts $D_w$, $D_m$, and *water* represent PTRAN_CT calculations reporting dose to water, dose to medium, and with patient anatomy replaced by water, respectively. $D_{ref}$ represents prescribed dose.

### 6.3.4. *SDS calculation results*

The SDS dose distributions generally agreed with the $D_{water\text{-}based}$ calculations within statistical uncertainties. Although the isodose lines were indistinguishable, the ratio of the two distributions exhibited local fluctuations within ± 2% about unity. This

was because trilinear interpolation operations of the $D_{ij}$ matrices in superposition calculations introduced approximations. In a few patient plans, some discrepancy in the penumbra regions in the shadow of the shielding was observed because the catheters constructed in the PLATO treatment plan were not exactly equally spaced within the applicator. In contrast, the $^{192}$Ir source defined in $D_{ij}$ is at a fixed position with respect to the shielding. Nonetheless, the mean absolute difference in the CTV $D_{90}$, $V_{100}$, and $V_{150}$ were only 0.4% ± 0.4%, 0.2% ± 0.2%, and 0.5% ± 0.4%, respectively. Furthermore, the corresponding mean differences were all zero. The absolute differences in the $D_{mean}$ received by the CTV and the contralateral normal tissues were 0.6% ± 0.5% and 1.1% ± 0.9%, respectively.

### 6.3.5. *Tungsten vs. lead shielding*

The results of the SDS calculations indicated that the tungsten alloy reduces the contralateral normal tissue $D_{mean}$ by an additional 1.6% ± 0.4% compared with lead. The mean difference in the CTV $V_{100}$ between the two shielding media was 0.3% ± 0.4%.

### 6.3.6. *Sensitivity of dose to positioning uncertainties*

Figure 6.4 shows the box and whisker plots of the CTV $V_{100}$ according to the TG-43 and SDS calculations. The maximum and minimum $V_{100}$ after ±2.5 mm longitudinal displacement and ±15° rotation along the applicator were compared. Target coverage tended to decrease as a result of the shifts. Using the SDS calculations, the average maximum reduction in $V_{100}$ was 4% ± 2%. The TG-43 results indicated that without shielding, the average maximum reduction was 3% ± 2%.

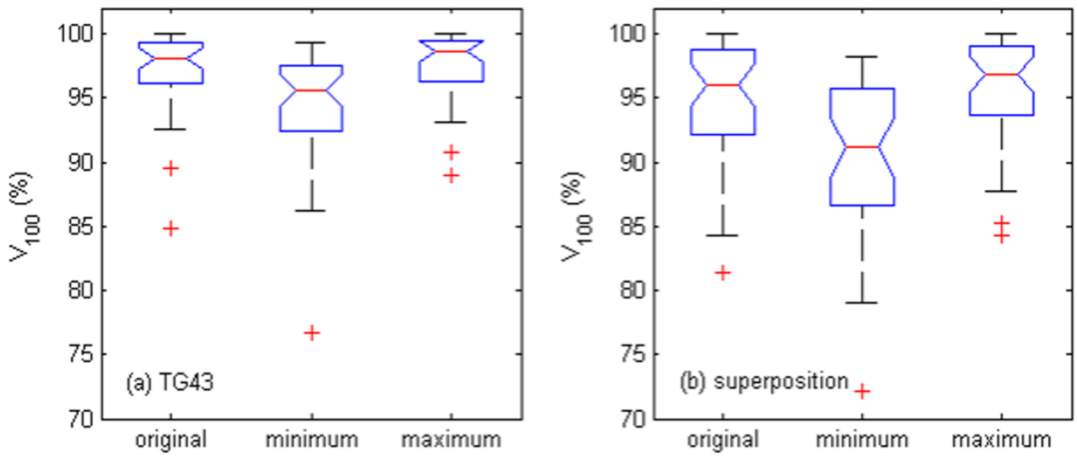


Figure 6.4. Box and whisker plots of target volume receiving 100% of prescribed dose ($V_{100}$) for 40 patient plans as calculated using (a) Task Group 43 and (b) single-dwell superposition algorithms. $V_{100}$ based on original treatment plans compared with minimum and maximum $V_{100}$ resulting from ±2.5 mm longitudinal and ±15° rotational shifts in source positions.

## 6.4. DISCUSSION

### 6.4.1. *HDR-EBT dosimetric evaluation*

Computed tomography-based MC calculations were performed to evaluate 40 HDR-EBT plans, which were delivered with a lead or tungsten-shielded intracavitary applicator. The results have indicated that metal shielding has the greatest influence on the dose, with minimal dose perturbations caused by the silicone applicator and diluted contrast solution. Anatomic heterogeneity effects were seen mostly in the low-dose regions around bony structures.

Improvements in treatment plan conformity and normal tissue avoidance due to metal shielding were indicated by the greater CN, lower EI, and lower $D_{mean}$ to the contralateral normal tissues. Geometric displacement by the inflated endocavitary balloon significantly improved normal tissue sparing owing to the inverse square falloff of dose

with distance. Conventional TG-43-based treatment planning might underdose the target by not accounting for the effect of internal shielding on the dose coverage.

The insensitivity of $^{192}$Ir photons to tissue heterogeneities was corroborated by the good agreement between the $D_w$ and $D_{water\text{-}based}$ results reported in Table 6.2. It is thus adequate to approximate the patient anatomy by water for HDR-EBT applications, although some discrepancy in the dose near the skin is expected owing to changes in the scattering conditions. The results have also validated the proposed SDS dose calculation technique, which assumes that the shielded applicator is in homogeneous water.

### 6.4.2. *SDS algorithm for HDR-EBT planning*

The excellent agreement between SDS and $D_{water\text{-}based}$ calculations suggest that it is adequate to use 2×2×2 mm$^3$ voxels for the $D_{ij}$ matrices. The efficiency of the SDS algorithm was proportional to the numbers of voxels and dwell positions, comparable to that of the TG-43 two-dimensional algorithm and two orders of magnitude faster than PTRAN_CT.

The applicator-based superposition principle has been applied by Markman et al. [20] to take into account shielded vaginal colpostats in the dose calculations. The mean errors of their results compared with full PTRAN simulations were 4.3% for low-dose-rate and 6.3% for HDR applications. The larger discrepancy was attributed to interapplicator shielding effects, which are not a problem for HDR-EBT.

In a few of the PLATO patient plans studied in this work, peripheral cold spots were observed because the normal tissue dose constraints could not be met without compromising target coverage. The constraints were imposed to avoid adversely affecting the outcome in sphincter-preserving surgery at a later stage. Because the superposition

algorithm can accurately take into account the dose reduction to the shielded regions, normal tissue dose constraints become easier to meet. Therefore, treatment planning using the SDS method will ensure better target coverage and dose conformity.

### 6.4.3. *MC method for patient-specific dose calculations*

The dose calculation and analysis platform developed in this work made it possible to perform patient-specific brachytherapy dose calculations within a reasonable time. It generally took <30 min to export a PLATO treatment plan to a personal computer and to prepare the PTRAN_CT patient data and input files [17]. PTRAN_CT uses highly efficient photon transport and dose scoring algorithms and is faster than most general purpose MC codes [4]. A few other fast MC codes have been developed for brachytherapy dose calculations [21, 22], but a patient cohort study using these codes has not been published.

The efficiency of PTRAN_CT has been discussed previously [17]. On average, each calculation in this study took 2.7 h to run on a single 64-bit, 2.67-GHz processor. To achieve a good level of precision for dose comparisons, many histories were run to reduce the statistical uncertainties over a large volume. If only the target dose is of interest, the calculation time can be reduced by an order of magnitude.

No consensus has yet been reached as to whether to report $D_w$ or $D_m$ for MC-based treatment planning [23, 24]. Our results have shown that large local dose differences can exist between $D_w$ and $D_m$-based calculations for bony structures. This resulted from the softening of the $^{192}$Ir photon spectrum within the patient's body. After a few centimeters from the source, dose contribution from photons at <100 keV becomes significant. Consequently, mass energy absorption coefficients for bones tend to be

noticeably greater at low doses. For soft tissues, the mass energy absorption coefficients are less sensitive to spectral changes; therefore, differences between $D_w$ and $D_m$ are generally <1%.

The dose volume indices for the nontarget structures listed in Table 6.2, as calculated using the planning CT images, were intended to demonstrate the perturbation effects of shielding and tissue heterogeneities. The actual doses delivered to deformable structures such as the bladder might not be the same. As reported in HDR gynecologic studies [25-27], changes in applicator position might cause significant differences in the dose to organs at risk in different fractions. Furthermore, the locations, shapes, and volumes of the organs are variable. Therefore, clinical applications of patient-specific MC calculations might be limited to postprocedure evaluations of patients with a CT examination taken around the time of the treatment.

## 6.5. REFERENCES


1. Pantelis E, Papagiannis P, Karaiskos P, Angelopoulos A, Anagnostopoulos G, Baltas D, et al. The effect of finite patient dimensions and tissue inhomogeneities on dosimetry planning of $^{192}$Ir HDR breast brachytherapy: a Monte Carlo dose verification study. Int J Radiat Oncol Biol Phys. 2005;61:1596-602.

2. Ye SJ, Brezovich IA, Shen S, Kim S. Dose errors due to inhomogeneities in balloon catheter brachytherapy for breast cancer. Int J Radiat Oncol Biol Phys. 2004;60:672-7.

3. DeMarco JJ, Smathers JB, Burnison CM, Ncube QK, Solberg TD. CT-based dosimetry calculations for $^{125}$I prostate implants. Int J Radiat Oncol Biol Phys. 1999;45:1347-53.

4. Carrier JF, D'Amours M, Verhaegen F, Reniers B, Martin AG, Vigneault E, et al. Postimplant dosimetry using a Monte Carlo dose calculation engine: a new clinical standard. Int J Radiat Oncol Biol Phys. 2007;68:1190-8.

5. Vuong T, Belliveau PJ, Michel RP, Moftah BA, Parent J, Trudel JL, et al. Conformal preoperative endorectal brachytherapy treatment for locally advanced rectal cancer: early results of a phase I/II study. Dis Colon Rectum. 2002;45:1486-95.

6. Vuong T, Devic S, Podgorsak E. High dose rate endorectal brachytherapy as a neoadjuvant treatment for patients with resectable rectal cancer. Clin Oncol. 2007;19:701-5.

7. Poon E, Reniers B, Devic S, Vuong T, Verhaegen F. Dosimetric characterization of a novel intracavitary mold applicator for $^{192}$Ir high dose rate endorectal brachytherapy treatment. Med Phys. 2006;33:4515-26.

8. Rivard MJ, Coursey BM, DeWerd LA, Hanson WF, Huq MS, Ibbott GS, et al. Update of AAPM Task Group No. 43 Report: A revised AAPM protocol for brachytherapy dose calculations. Med Phys. 2004;31:633-74.

9. Vuong T, Devic S, Moftah B, Evans M, Podgorsak EB. High-dose-rate endorectal brachytherapy in the treatment of locally advanced rectal carcinoma: technical aspects. Brachytherapy. 2005;4:230-5.

10. Devic S, Vuong T, Moftah B, Evans M, Podgorsak EB, Poon E, et al. Image-guided high dose rate endorectal brachytherapy. Med Phys. 2007;34:4451-8.

11. Le Y, Chibani O, Todor D, Siebers I, Williamson J. An integrated CT-based Monte Carlo dose-evaluation system for brachytherapy and its application to permanent prostate implant postprocedure dosimetric analysis. Med Phys. 2005;32:2068.

12. Williamson JF. Monte Carlo evaluation of kerma at a point for photon transport problems. Med Phys. 1987;14:567-76.

13. Williamson JF. Comparison of measured and calculated dose rates in water near I-125 and Ir-192 seeds. Med Phys. 1991;18:776-86.

14. Radiation Safety Information Computational Center. HUGO-VI: Photon Interaction Data in ENDF/B-VI Format. Oak Ridge, TN Oak Ridge National Laboratory; 1989.

15. Hubbell JH, Seltzer SM. Tables of x-ray mass attenuation coefficients and mass energy-absorption coefficients 1 keV to 20 MeV for elements Z=1 to 92 and 48 additional substances of dosimetric interest. Gaithersburg, MD: National Institute of Standards and Technology 1995. Report No.: NISTIR 5632.

16. Nuclear data from NuDat 2.0, a web-based database maintained by the National Nuclear Data Center [database on the Internet]. Brookhaven National Laboratory, Upton, NY 2004. Available from: http://www.nndc.bnl.gov/nudat2.

17. Poon E, Le Y, Williamson JF, Verhaegen F. BrachyGUI: an adjunct to an accelerated Monte Carlo photon transport code for patient-specific brachytherapy dose calculations and analysis. J Phys Conf Ser. 2008;102:012018.

18. van't Riet A, Mak AC, Moerland MA, Elders LH, van der Zee W. A conformation number to quantify the degree of conformality in brachytherapy and external beam irradiation: application to the prostate. Int J Radiat Oncol Biol Phys. 1997;37:731-6.

19. Meertens H, Borger J, Steggerda M, Blom A. Evaluation and optimisation of interstitial brachytherapy dose distributions. In: Mould RF, Battermann JJ, Martinez AA, Speiser BL, editors. Brachytherapy from radium to optimization. Veenendaal: Nucletron International; 1994. p. 300-6.

20. Markman J, Williamson JF, Dempsey JF, Low DA. On the validity of the superposition principle in dose calculations for intracavitary implants with shielded vaginal colpostats. Med Phys. 2001;28:147-55.

21. Chibani O, Williamson JF. MCPI: a sub-minute Monte Carlo dose calculation engine for prostate implants. Med Phys. 2005;32:3688-98.

22. Taylor RE, Yegin G, Rogers DW. Benchmarking BrachyBose: voxel based EGSnrc Monte Carlo calculations of TG-43 dosimetry parameters. Med Phys. 2007;34:445-57.

23. Liu HH, Keall P. $D_m$ rather than $D_w$ should be used in Monte Carlo treatment planning. Med Phys. 2002;29:922-3.

24. Chetty IJ, Curran B, Cygler JE, DeMarco JJ, Ezzell G, Faddegon BA, et al. Report of the AAPM Task Group No. 105: issues associated with clinical implementation

of Monte Carlo-based photon and electron external beam treatment planning. Med Phys. 2007;34:4818-53.

25. Datta NR, Kumar S, Das KJ, Pandey CM, Halder S, Ayyagari S. Variations of intracavitary applicator geometry during multiple HDR brachytherapy insertions in carcinoma cervix and its influence on reporting as per ICRU report 38. Radiother Oncol. 2001;60:15-24.

26. Hellebust TP, Dale E, Skjønsberg A, Olsen DR. Inter fraction variations in rectum and bladder volumes and dose distributions during high dose rate brachytherapy treatment of the uterine cervix investigated by repetitive CT-examinations. Radiother Oncol. 2001;60:273-80.

27. Bahena JH, Martinez A, Yan D, Mele E, Edmunson G, Brown D, et al. Spatial reproducibility of the ring and tandem high-dose rate cervix applicator. Int J Radiat Oncol Biol Phys. 1998;41:13-9.

# Chapter Seven

# Paper III: Development of a Scatter Correction Technique and its Application to HDR $^{192}$Ir Multicatheter Breast Brachytherapy

Emily Poon, Frank Verhaegen

*Med Phys. 2009;36:3703-13*



In Chapter 6, we discussed that CT-based MC dose calculations are better suited for post-treatment evaluation than for treatment planning, partly because of the lower computational efficiency compared to the case for low-energy seed implant applications. We have also shown that tissue inhomogeneity effects are small for $^{192}$Ir photons. In this paper, we will demonstrate that the influence of the scatter environment is more important than details of the patient anatomy for multicatheter breast brachytherapy. A novel water-based scatter correction technique that corrects for the scatter conditions based on the body contour will be presented. The technique will be useful for tumor sites near the skin.

## ABSTRACT

This article introduces a scatter correction (SC) technique for high-dose-rate (HDR) $^{192}$Ir brachytherapy dose calculations in the absence of a full scatter environment near the skin. The technique uses dosimetry data derived by Monte Carlo (MC) simulations for the Nucletron microSelectron v2 HDR $^{192}$Ir source. The data include the primary and scatter components of the radial dose function and the anisotropy function in addition to a SC table. The dose to a point of interest for each dwell position is estimated by first calculating the primary and scatter doses in an infinite water phantom. The scatter dose is then scaled by a SC factor that depends on the distances between the point of interest, the dwell position, and the body contour of the patient. SC calculations in water phantoms of three different shapes, as well as computed tomography-based geometries of 18 multicatheter breast patients, are compared with Task Group 43 (TG-43) and PTRAN_CT MC calculations. The SC calculations show improvement over TG-43 for all test cases while taking 50% longer to run. The target and skin doses for the breast patient plans are unaffected by tissue inhomogeneities, as indicated by an agreement better than 1% between the SC and MC results. On average, TG-43 overestimates the target coverage by 2% and the dose to the hottest 0.1 cm$^3$ ($D_{0.1\ cc}$) of the skin by 5%. The low-density lung causes the lung and heart $D_{0.1\ cc}$ to differ by up to 3% for the SC method and by 2%–5% for TG-43 compared with MC calculations. The SC technique is suitable for HDR $^{192}$Ir dose calculations near the skin provided that the dose is nearly unperturbed by internal inhomogeneities. It has been validated for multicatheter breast brachytherapy.

## 7.1. INTRODUCTION

The extent of the scattering medium has an important influence on the dose in brachytherapy. It is common practice to have full scatter conditions in the near-source region when characterizing a brachytherapy source in a water phantom. In treatment planning, however, the amount of scattered radiation at a given point depends on its distance from the skin and the dwell positions within the patient body. Conventional Task Group 43 (TG-43) dose calculations [1] tend to overestimate the scatter dose near the skin, as has been reported for breast, esophagus, and intraoperative brachytherapy [2-6].

The dependence of the dose on the phantom size has been studied extensively [7-11]. Mathematical relationships have been derived to compare radial dose functions calculated with different phantom shapes and sizes for $^{192}$Ir and $^{137}$Cs sources [11, 12]. Anagnostopoulos et al. [13] proposed that the dose in a finite phantom can be adjusted analytically using scatter-to-primary dose ratios. Such ratios are calculated in a water sphere of a radius that equals the shortest density-scaled distance between the source and the phantom surface. However, this method is not applicable for treatment planning scenarios in which the source positions are off center and the patient body is irregularly shaped [3].

The Monte Carlo (MC) method in photon transport is used in brachytherapy to study the interplay effects of patient dimensions, tissue composition and density variations, applicator, shielding, radiographic contrast solution, and interseed attenuation [14-17]. It is of special interest in low-dose-rate seed implant applications, since the dose is strongly influenced by atomic number variations at low energies. At present, most

planning systems use the water-based TG-43 formalism; MC codes are not yet used clinically.

This paper will present a scatter correction (SC) technique to take into account variations in photon backscatter near the skin for patient-specific $^{192}$Ir brachytherapy dose calculations. TG-43 dosimetry parameters are used to calculate the primary and scatter components of the dose in an infinite water phantom. Corrections to the scatter dose are then made using precalculated SC factors that take into consideration the dwell positions and the skin contour relative to the point of interest (POI). The patient body is assumed to be water equivalent. This technique was tested by means of water phantom and breast patient dose calculations with a high-dose-rate (HDR) $^{192}$Ir source. MC calculations were done for benchmarking purposes.

## 7.2. MATERIALS AND METHODS

### 7.2.1. *Software implementations and Monte Carlo codes*

The SC algorithm was coded in C and incorporated into BrachyGUI, a brachytherapy planning tool developed using MATLAB (version 7.7.0, MathWorks, Natick, MA) [15, 18]. BrachyGUI was also used to optimize the breast patient plans, create input files for MC simulations, and evaluate dose calculation results.

TG-43 dosimetry parameters for an $^{192}$Ir source, broken down into primary and scatter components, were calculated using version 9.2 of the GEANT4 MC code [19]. Photoelectric effect, Compton scattering, and Rayleigh scattering processes from the low-energy electromagnetic physics package were simulated. The calculations used the NUDAT 2.0 $^{192}$Ir photon spectrum [20], the EPDL97 photon cross section library [21], and the mass energy absorption coefficients of Hubbell and Seltzer [22]. The absorbed dose,

approximated by collision kerma, was scored using a linear track length estimator. This approximation is valid at distances >2 mm from the source where charged particle equilibrium conditions exist [23].

SC factors were derived by PTRAN (PTRAN_CCG version 8_00) [8, 24] MC photon transport calculations using the same photon spectrum and mass energy absorption coefficients as GEANT4. The cross section data came from the DLC-146 library [25]. Collision kerma was scored using an exponential track length estimator [24].

The SC and TG-43 calculations were benchmarked against those of PTRAN_CT [26], an extended version of PTRAN. It provides a phase space source option and is intended for computed tomography (CT)-based simulations with embedded brachytherapy sources and applicators. The absorbed dose to water, as approximated by water collision kerma, was reported.

*i.* *Dosimetry data*

Our SC method handles the primary and scatter doses separately, as put forward by Williamson [27, 28] and Russell and Ahnesjö [29, 30]. A photon is classified as primary until it undergoes an interaction outside the source encapsulation. *Scatter dose* is defined as the dose deposited by secondary electrons that originate from scattered photons.

*ii.* *TG-43 parameters for primary and scatter dose calculation*

TG-43 parameters were calculated for the microSelectron v2 HDR $^{192}$Ir source (Nucletron, Veenendaal, the Netherlands). The parameters included the dose rate constant $\Lambda$, as well as the primary and scatter components of the radial dose function $g_L(r)$ and anisotropy function $F(r, \theta)$. The symbols $r$ and $\theta$ denote the radial distance and the angle relative to the distal side of the source longitudinal axis, respectively. The source

geometry is described in Ref. [31]. MC simulations were done with the source centered in a liquid water sphere of 50 cm radius, providing full photon backscatter for $r$ <= 20 cm. In accordance with the reference conditions specified in TG-43 [1], the water density was set to 0.998 g/cm$^3$. The scoring voxels for $g_L(r)$ were in the forms of annular rings whose differences in the outer and inner radii were between 0.1 and 2 mm. The spherical scoring voxels for $F(r, \theta)$ were of radii ranging from 0.02 to 1.5 mm. To establish consistency with published data, we compared our $\Lambda$, $g_L(r)$, and $F(r, \theta)$ with BRACHYDOSE calculations [32]. The same calculations were done in a water sphere of 15 cm radius for comparison with PTRAN results [31].

The following equations define the primary and scatter components of $g_L(r)$:

$$g_{L,prim}(r) = \frac{\dot{D}_{prim}(r,\theta_0)}{\dot{D}(r_0,\theta_0)} \cdot \frac{G_L(r_0,\theta_0)}{G_L(r,\theta_0)} \tag{7.1}$$

$$g_{L,scat}(r) = \frac{\dot{D}_{scat}(r,\theta_0)}{\dot{D}(r_0,\theta_0)} \cdot \frac{G_L(r_0,\theta_0)}{G_L(r,\theta_0)} \tag{7.2}$$

The geometry function $G_L(r, \theta)$ uses the TG-43 line source approximation [1]. All parameters were normalized to the total dose rate $\dot{D}$ at the reference distance $r_0$ of 1 cm and the reference angle $\theta_0$ of 90°. Both $g_{L,\text{prim}}(r)$ and $g_{L,\text{scat}}(r)$ were fitted using fourth order polynomial functions for dose calculations.

The primary and scatter components of $F(r, \theta)$ are defined below:

$$F_{prim}(r,\theta) = \frac{\dot{D}_{prim}(r,\theta)}{\dot{D}_{prim}(r,\theta_0)} \cdot \frac{G_L(r,\theta_0)}{G_L(r,\theta)} \tag{7.3}$$

$$F_{scat}(r,\theta) = \frac{\dot{D}_{scat}(r,\theta)}{\dot{D}_{scat}(r,\theta_0)} \cdot \frac{G_L(r,\theta_0)}{G_L(r,\theta)} \tag{7.4}$$

After replacing $g_L(r)$ and $F(r, \theta)$ by the respective primary and scatter parameters, the primary and scatter doses in unbounded water can be calculated using the TG-43 two-dimensional (2D) formalism.

*iii.* *Generation of scatter correction factors*

We used PTRAN to calculate the scatter dose around the $^{192}$Ir source located at 1 of 37 points in a 15 cm radius water sphere surrounded by air. The same scatter dose distributions were calculated in unbounded water using TG-43. The voxels were $2\times2\times2$ mm$^3$. Ratios of the scatter doses in bounded water to unbounded water were evaluated.

From the scatter dose ratios, a 3D lookup table of SC factors $f_{scat}$ was created. As depicted in Figure 7.1, $f_{scat}$ is a function of three distance variables. (1) The closest distance between the source and the phantom surface, $d_1$, ranges from 0 to 15 cm; the spacing is 1 mm near the surface and increases gradually to 1 cm near the sphere center. (2) The closest distance between the POI and the phantom surface, $d_2$, ranges from −15 to 15 cm at intervals of 2 mm; negative values correspond to distances outside the phantom. (3) The distance between the POI and the source, $d_3$, ranges from 0 to 40 cm at 2 mm intervals. The source orientation dependence of $f_{scat}$ is neglected.

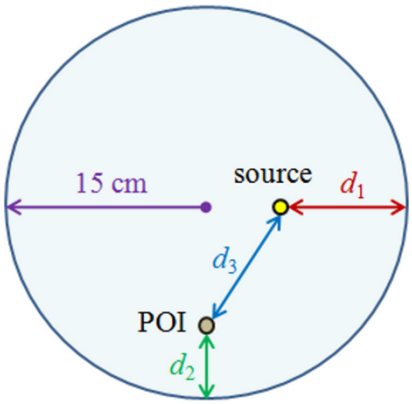


Figure 7.1. SC factors are derived from Monte Carlo simulations of an HDR $^{192}$Ir source positioned at various distances $d_1$ from the surface of a 15 cm radius water sphere. For a given POI, its distances to the phantom surface and the brachytherapy source are denoted by $d_2$ and $d_3$, respectively.

### 7.2.2. *Scatter correction technique*

#### *i.* *Identification of external contours and distance transform*

The SC method entails a few patient-specific preprocessing steps, which can be done in 1–2 min with minimal user input using MATLAB routines. First, we need to specify a dose grid $G$ that defines the resolution, boundaries, and coordinate system of the dose matrix. Next, a matrix of Hounsfield units (HUs) is generated by trilinearly interpolating the CT image data onto $G$. From the HU matrix, a binary map identifying the skin contour according to a HU threshold is created. Then, the nearest distances to the skin for all points in $G$ is calculated by applying a 3D Euclidean distance transform* on the binary map; distances for points outside the patient body are multiplied by −1 for identification purposes. A distance map $T$ is stored for later use.

* Y. Mishchenko, 2007, "3D Euclidean distance transform for variable data aspect ratio," MATLAB Central File Exchange, The MathWorks (Natick, MA), http://www.mathworks.com/matlabcentral/fileexchange.

*ii.* *Scatter correction algorithm*

In the first step of the SC algorithm, we use TG-43 to calculate the primary and scatter dose rates in unbounded water. Then, we scale the scatter dose rate contributed from a dwell position at a given point, $\dot{D}_{\text{TG-43,scat}}$, by $f_{\text{scat}}$ to correct for the scatter conditions in a bounded geometry. The primary component $\dot{D}_{\text{TG-43,prim}}$ is unaffected by the scattering medium. The total dose rate $\dot{D}$ is given by:

$$\dot{D} = \dot{D}_{TG43,prim} + \dot{D}_{TG43,scat} \cdot f_{scat} \qquad (7.5)$$

We find the indices for table lookup of $f_{\text{scat}}$ from three distances ($d_{m1}$, $d_{m2}$, $d_{m3}$) by taking the nearest neighbors. For each dwell position $m$, we get the closest distance $d_{m1}$ to the skin from the distance map $T$. For each point in the dose grid $G$, $T$ provides the closest distance $d_{m2}$ to the skin, whereas $d_{m3}$ is between the dose point and the dwell position.

### 7.2.3. *Algorithm validation*

In view of the loss in source orientation dependence during the tabulation of $f_{\text{scat}}$, we compared the SC and TG-43 2D dose distributions around the $^{192}$Ir source centered in a water sphere of 15 cm radius. To ensure consistency in the comparison, this TG-43 calculation was done using our GEANT4 parameters. The other TG-43 results presented in this paper used published dosimetry parameters [31].

We benchmarked the SC calculations against PTRAN_CT calculations in phantom and patient geometries. Since modeling the source at every position is impractical, we used a phase space file containing the energies, positions, and directions of photons exiting the source encapsulation in vacuum. Coordinate transformations were applied to get the initial positions and directions of the primary photons. The conversion from dose per particle history to dose per unit air kerma strength is described in Ref. [15].

*i.* *Dose calculations in phantoms*

We calculated the dose in spherical, cylindrical, and trapezoidal water phantoms as shown in Figure 7.2. The dwell positions were at 5 mm step intervals and were weighted equally. In the first phantom, nine dwell positions were aligned along $\{x = 0, y = -9 \text{ cm}\}$ from $z = -2$ to 2 cm. The voxels were $2\times2\times2$ mm$^3$. The second setup mimicked the treatment of extremity soft tissue sarcoma. Five lines of dwell positions were arranged 22.5° apart semi-circumferentially, 3.5 cm away from the central axis. Twenty-one dwell positions were along each line from $z = -5$ to 5 cm. The voxels were $1\times1\times3$ mm$^3$. In the third phantom, ten dwell positions going from $y = -4$ cm to 5 mm were positioned along $\{x = 0, z = 0\}$. The voxels were $2\times2\times2$ mm$^3$.

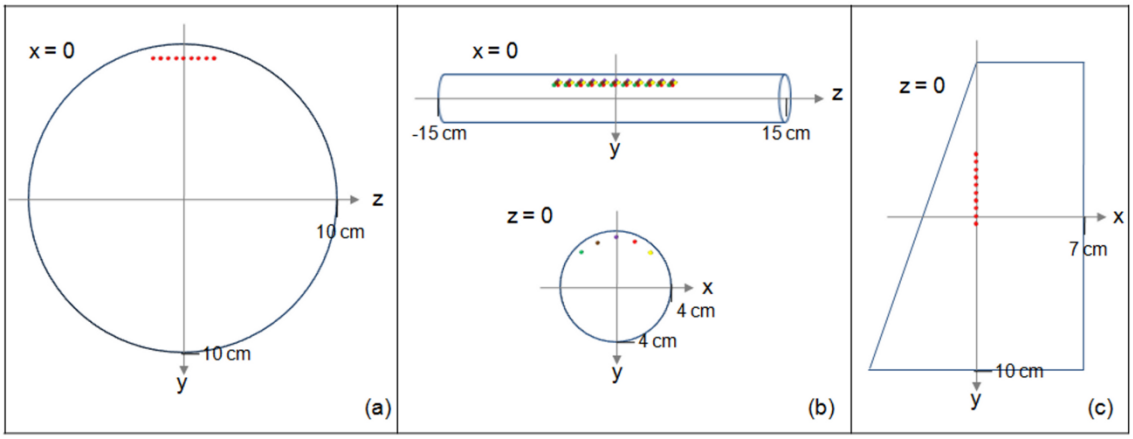


Figure 7.2. Water phantoms in the forms of (a) a sphere of 10 cm radius, (b) a cylinder of 4 cm radius and 30 cm height, and (c) a trapezoidal prism of 20 cm length along the $y$ axis and 8 cm along $z$; the parallel sides along $x$ are 7 and 14 cm wide. The dots represent the dwell positions.

*ii.* *Dose calculations and treatment planning for breast patients*

We calculated 18 multicatheter breast treatment plans. The average number of catheters was 13±4 (range of 6–18), and the target volume was 104±56 cm$^3$ (range of 44–256 cm$^3$). Dose-volume indices were used to measure differences between the dose

calculation methods. The minimum doses received by 90% and 100% of the PTV ($D_{90}$ and $D_{100}$) are given as a percentage of the prescribed dose $D_{ref.}$ $V_n$ represents the percentage of the PTV volume receiving at least $n$% of $D_{ref.}$ The minimum doses to the hottest $n$ $cm^3$ ($D_{n\,cc}$) of the skin, ipsilateral lung, and heart (for the 11 patients with left-sided lesions) are expressed as a percentage of $D_{ref.}$ $V_{n\,Gy}$ refers to the volume of the lung or heart receiving a minimum of $n$ Gy during the whole course of treatment. The dose homogeneity index (DHI) evaluates the uniformity of the PTV dose. It is defined as follows [33]:

$$\mathrm{DHI} = 1 - \frac{\mathrm{V}_{150}}{\mathrm{V}_{100}} \tag{7.6}$$

To make the dosimetry consistent for all patients in this hypothetical study, the treatment plans were optimized retrospectively. We did TG-43-based inverse planning to maximize the target coverage and dose homogeneity while limiting the skin dose. The optimization made use of the pattern search algorithm in MATLAB. We set up the cost function to keep the skin $D_{0.1\,cc} < 100\%$ and DHI > 0.75, maximize the PTV $V_{100}$, and penalize excessive normal tissue dose.

In the MC calculations, the density data were converted from CT images using a continuous HU scale with multiple linear segments, which we derived by a calibration phantom scan. Four anatomic materials were used: lung, adipose, soft tissue, and rib bone; the elemental compositions were taken from the International Commission on Radiation Units and Measurements Reports 44 and 46 [34, 35]. We corrected for some CT artifacts around the metallic buttons and replaced the catheters by soft tissues. To examine whether tissue inhomogeneity effects could be ignored, MC calculations were repeated with the

patient body changed to water of 1 g/cm$^3$ density; the results will be referred to as $MC_{water}$. The dose grid resolution was 2×2×2 mm$^3$.

## 7.3. RESULTS

### 7.3.1. *TG-43 parameters*

The dose rate constant of the microSelectron v2 HDR $^{192}$Ir source is 1.109(±0.1%) cGy h$^{-1}$ U$^{-1}$. It agrees with the literature: 1.108(±0.13%) cGy h$^{-1}$ U$^{-1}$ for PTRAN [31] and 1.109(±0.2%) cGy h$^{-1}$ U$^{-1}$ for BRACHYDOSE [32]. The $g_L(r)$ and $F(r, \theta)$ calculated in a water sphere of 15 cm radius agree within the standard errors of the mean ($\sigma_M$) of PTRAN: 0.5% near the source and 1.2% far from it [31]. The only exceptions are for $F(r, \theta)$ at $r$ = 2.5 mm and $\theta \leq 10°$ where our results are higher by 0.9%–1.5%.

Table 7.1 lists the values of $g_L(r)$, $g_{L,\text{prim}}(r)$, and $g_{L,\text{scat}}(r)$ calculated in full scatter conditions. The maximum $\sigma_M$ is 0.12%, and the agreement with BRACHYDOSE [32] for $g_L(r)$ is within 0.4%. The values $F(r, \theta)$, $F_{\text{prim}}(r, \theta)$, and $F_{\text{scat}}(r, \theta)$ are listed separately in Tables 7.2–7.4. The $\sigma_M$ are between 0.06% and 0.35%. The agreement of $F(r, \theta)$ with BRACHYDOSE [32] is within 1% except for $r$ = 2.5 mm. At this distance, the BRACHYDOSE data are unavailable for $\theta \leq 10°$, and are higher by up to 3% for $\theta > 10°$. Compared with PTRAN, the $F(r, \theta)$ of BRACHYDOSE are higher by 5% for $r$ = 2.5 mm and $\theta \leq 10°$ [32]. Such differences could be due to a discrepancy in the source geometry modeling.

Table 7.1. Radial dose function $g_L(r)$ of the Nucletron microSelectron v2 HDR $^{192}$Ir source calculated in a 50 cm radius water sphere. The primary and scatter components are denoted by the subscripts prim and scat, respectively.

| Distance, $r$ (cm) | $g_L(r)$ | $g_{L,prim}(r)$ | $g_{L,scat}(r)$ |
|---|---|---|---|
| 0.1 | 1.001 | 0.991 | 0.010 |
| 0.2 | 0.999 | 0.978 | 0.021 |
| 0.3 | 0.998 | 0.966 | 0.032 |
| 0.5 | 0.998 | 0.944 | 0.054 |
| 1 | 1.000 | 0.893 | 0.107 |
| 1.5 | 1.003 | 0.846 | 0.157 |
| 2 | 1.005 | 0.802 | 0.204 |
| 2.5 | 1.007 | 0.760 | 0.248 |
| 3 | 1.008 | 0.720 | 0.288 |
| 4 | 1.008 | 0.647 | 0.361 |
| 5 | 1.004 | 0.581 | 0.423 |
| 6 | 0.998 | 0.522 | 0.476 |
| 7 | 0.987 | 0.469 | 0.518 |
| 8 | 0.975 | 0.421 | 0.553 |
| 9 | 0.959 | 0.379 | 0.580 |
| 10 | 0.942 | 0.340 | 0.601 |
| 11 | 0.921 | 0.306 | 0.615 |
| 12 | 0.900 | 0.275 | 0.625 |
| 13 | 0.877 | 0.248 | 0.629 |
| 14 | 0.852 | 0.223 | 0.629 |
| 15 | 0.827 | 0.201 | 0.626 |
| 16 | 0.800 | 0.181 | 0.619 |
| 17 | 0.772 | 0.163 | 0.609 |
| 18 | 0.744 | 0.146 | 0.598 |
| 19 | 0.715 | 0.132 | 0.584 |
| 20 | 0.687 | 0.119 | 0.568 |

Table 7.2. Anisotropy function $F(r, \theta)$ of the Nucletron microSelectron v2 HDR $^{192}$Ir source calculated in a 50 cm radius water phantom.

| Angle, | Distance, $r$ (cm) | | | | | | | | | | |
|---|---|---|---|---|---|---|---|---|---|---|---|
| $\theta$ (°) | 0.25 | 5 | 1 | 2 | 3 | 5 | 7.5 | 10 | 12.5 | 15 | 20 |
| 0 | 0.739 | 0.661 | 0.633 | 0.641 | 0.661 | 0.700 | 0.746 | 0.778 | 0.802 | 0.822 | 0.851 |
| 1 | 0.738 | 0.662 | 0.633 | 0.642 | 0.663 | 0.703 | 0.750 | 0.781 | 0.805 | 0.825 | 0.851 |
| 2 | 0.739 | 0.662 | 0.631 | 0.649 | 0.672 | 0.711 | 0.756 | 0.786 | 0.809 | 0.829 | 0.854 |
| 3 | 0.739 | 0.663 | 0.641 | 0.659 | 0.681 | 0.719 | 0.761 | 0.791 | 0.813 | 0.832 | 0.856 |
| 4 | 0.739 | 0.665 | 0.652 | 0.669 | 0.691 | 0.727 | 0.769 | 0.797 | 0.818 | 0.836 | 0.859 |
| 5 | 0.740 | 0.672 | 0.662 | 0.681 | 0.701 | 0.736 | 0.777 | 0.803 | 0.824 | 0.841 | 0.863 |
| 6 | 0.741 | 0.682 | 0.675 | 0.693 | 0.714 | 0.747 | 0.784 | 0.809 | 0.829 | 0.845 | 0.867 |
| 7 | 0.742 | 0.692 | 0.687 | 0.705 | 0.724 | 0.756 | 0.792 | 0.815 | 0.835 | 0.851 | 0.869 |
| 8 | 0.747 | 0.704 | 0.700 | 0.718 | 0.737 | 0.766 | 0.800 | 0.821 | 0.841 | 0.855 | 0.874 |
| 10 | 0.762 | 0.729 | 0.727 | 0.743 | 0.759 | 0.785 | 0.817 | 0.836 | 0.852 | 0.865 | 0.881 |
| 12 | 0.783 | 0.754 | 0.753 | 0.767 | 0.782 | 0.805 | 0.832 | 0.849 | 0.863 | 0.875 | 0.891 |
| 14 | 0.804 | 0.778 | 0.777 | 0.790 | 0.803 | 0.822 | 0.846 | 0.862 | 0.874 | 0.884 | 0.898 |
| 16 | 0.825 | 0.800 | 0.800 | 0.810 | 0.821 | 0.839 | 0.861 | 0.874 | 0.884 | 0.893 | 0.905 |
| 20 | 0.861 | 0.838 | 0.837 | 0.847 | 0.855 | 0.867 | 0.885 | 0.895 | 0.903 | 0.911 | 0.919 |
| 24 | 0.888 | 0.868 | 0.869 | 0.875 | 0.881 | 0.891 | 0.904 | 0.911 | 0.918 | 0.924 | 0.931 |
| 30 | 0.919 | 0.903 | 0.903 | 0.908 | 0.911 | 0.918 | 0.927 | 0.932 | 0.937 | 0.941 | 0.946 |
| 36 | 0.941 | 0.928 | 0.929 | 0.931 | 0.935 | 0.939 | 0.946 | 0.949 | 0.953 | 0.955 | 0.958 |
| 42 | 0.958 | 0.947 | 0.948 | 0.952 | 0.953 | 0.956 | 0.960 | 0.963 | 0.964 | 0.966 | 0.968 |
| 48 | 0.970 | 0.962 | 0.963 | 0.964 | 0.966 | 0.967 | 0.971 | 0.972 | 0.973 | 0.975 | 0.976 |
| 58 | 0.985 | 0.979 | 0.982 | 0.981 | 0.982 | 0.983 | 0.984 | 0.985 | 0.986 | 0.987 | 0.986 |
| 73 | 0.996 | 0.995 | 0.996 | 0.996 | 0.995 | 0.995 | 0.997 | 0.996 | 0.995 | 0.997 | 0.997 |
| 88 | 1.000 | 1.000 | 1.000 | 1.001 | 1.001 | 1.000 | 1.001 | 1.000 | 1.000 | 1.001 | 1.001 |
| 90 | 1.000 | 1.000 | 1.000 | 1.000 | 1.000 | 1.000 | 1.000 | 1.000 | 1.000 | 1.000 | 1.000 |
| 103 | 0.997 | 0.997 | 0.997 | 0.998 | 0.999 | 0.998 | 0.998 | 0.998 | 0.998 | 0.998 | 0.998 |
| 118 | 0.989 | 0.985 | 0.986 | 0.987 | 0.987 | 0.988 | 0.989 | 0.989 | 0.988 | 0.989 | 0.990 |
| 128 | 0.976 | 0.970 | 0.971 | 0.973 | 0.974 | 0.974 | 0.976 | 0.977 | 0.979 | 0.980 | 0.981 |
| 133 | 0.967 | 0.960 | 0.961 | 0.962 | 0.965 | 0.966 | 0.970 | 0.970 | 0.971 | 0.973 | 0.975 |
| 138 | 0.958 | 0.948 | 0.948 | 0.950 | 0.952 | 0.954 | 0.960 | 0.961 | 0.963 | 0.965 | 0.966 |
| 143 | 0.946 | 0.932 | 0.932 | 0.935 | 0.937 | 0.940 | 0.947 | 0.951 | 0.953 | 0.956 | 0.959 |
| 148 | 0.929 | 0.911 | 0.912 | 0.915 | 0.920 | 0.926 | 0.932 | 0.937 | 0.940 | 0.944 | 0.947 |
| 153 | 0.907 | 0.885 | 0.884 | 0.889 | 0.894 | 0.902 | 0.913 | 0.921 | 0.925 | 0.931 | 0.937 |
| 158 | 0.876 | 0.850 | 0.850 | 0.856 | 0.864 | 0.876 | 0.890 | 0.899 | 0.908 | 0.914 | 0.922 |
| 165 | 0.811 | 0.781 | 0.780 | 0.791 | 0.804 | 0.824 | 0.846 | 0.862 | 0.873 | 0.884 | 0.896 |
| 169 | | 0.726 | 0.725 | 0.741 | 0.757 | 0.785 | 0.814 | 0.834 | 0.849 | 0.863 | 0.880 |
| 170 | | 0.710 | 0.708 | 0.726 | 0.743 | 0.772 | 0.805 | 0.826 | 0.843 | 0.857 | 0.875 |
| 172 | | 0.679 | 0.676 | 0.696 | 0.715 | 0.749 | 0.784 | 0.809 | 0.828 | 0.844 | 0.867 |
| 173 | | 0.663 | 0.658 | 0.680 | 0.701 | 0.737 | 0.775 | 0.801 | 0.822 | 0.838 | 0.860 |
| 174 | | 0.646 | 0.640 | 0.663 | 0.686 | 0.724 | 0.764 | 0.793 | 0.814 | 0.831 | 0.855 |
| 175 | | 0.626 | 0.622 | 0.647 | 0.672 | 0.712 | 0.756 | 0.785 | 0.807 | 0.827 | 0.850 |
| 176 | | 0.610 | 0.607 | 0.633 | 0.658 | 0.700 | 0.746 | 0.777 | 0.802 | 0.821 | 0.848 |
| 177 | | 0.610 | 0.593 | 0.618 | 0.645 | 0.689 | 0.737 | 0.770 | 0.795 | 0.815 | 0.843 |
| 178 | | 0.609 | 0.582 | 0.606 | 0.633 | 0.679 | 0.728 | 0.763 | 0.789 | 0.811 | 0.840 |
| 179 | | 0.609 | 0.582 | 0.597 | 0.623 | 0.669 | 0.722 | 0.758 | 0.785 | 0.807 | 0.837 |
| 180 | | 0.608 | 0.582 | 0.596 | 0.621 | 0.665 | 0.718 | 0.754 | 0.784 | 0.806 | 0.834 |

Table 7.3. Primary components of the anisotropy function $F_{prim}(r, \theta)$.

| Angle, | Distance, $r$ (cm) | | | | | | | | | | |
|---|---|---|---|---|---|---|---|---|---|---|---|
| $\theta$ (°) | 0.25 | 5 | 1 | 2 | 3 | 5 | 7.5 | 10 | 12.5 | 15 | 20 |
| 0 | 0.748 | 0.656 | 0.608 | 0.584 | 0.579 | 0.575 | 0.577 | 0.578 | 0.580 | 0.584 | 0.593 |
| 1 | 0.747 | 0.657 | 0.608 | 0.586 | 0.582 | 0.581 | 0.584 | 0.587 | 0.590 | 0.594 | 0.603 |
| 2 | 0.748 | 0.657 | 0.606 | 0.595 | 0.593 | 0.593 | 0.598 | 0.599 | 0.602 | 0.605 | 0.613 |
| 3 | 0.748 | 0.658 | 0.618 | 0.607 | 0.606 | 0.607 | 0.610 | 0.612 | 0.614 | 0.616 | 0.622 |
| 4 | 0.748 | 0.660 | 0.630 | 0.620 | 0.619 | 0.619 | 0.623 | 0.625 | 0.627 | 0.630 | 0.638 |
| 5 | 0.749 | 0.668 | 0.641 | 0.633 | 0.632 | 0.633 | 0.639 | 0.642 | 0.644 | 0.647 | 0.654 |
| 6 | 0.750 | 0.677 | 0.655 | 0.650 | 0.650 | 0.651 | 0.653 | 0.655 | 0.657 | 0.660 | 0.668 |
| 7 | 0.751 | 0.688 | 0.668 | 0.663 | 0.664 | 0.666 | 0.669 | 0.670 | 0.672 | 0.676 | 0.684 |
| 8 | 0.755 | 0.701 | 0.683 | 0.679 | 0.680 | 0.681 | 0.683 | 0.684 | 0.687 | 0.691 | 0.698 |
| 10 | 0.771 | 0.727 | 0.712 | 0.709 | 0.709 | 0.709 | 0.715 | 0.716 | 0.719 | 0.721 | 0.727 |
| 12 | 0.792 | 0.753 | 0.740 | 0.738 | 0.738 | 0.739 | 0.742 | 0.744 | 0.745 | 0.749 | 0.756 |
| 14 | 0.813 | 0.778 | 0.767 | 0.764 | 0.765 | 0.766 | 0.768 | 0.770 | 0.771 | 0.774 | 0.781 |
| 16 | 0.834 | 0.801 | 0.791 | 0.789 | 0.789 | 0.790 | 0.794 | 0.794 | 0.795 | 0.797 | 0.805 |
| 20 | 0.870 | 0.840 | 0.832 | 0.832 | 0.831 | 0.831 | 0.836 | 0.837 | 0.839 | 0.841 | 0.846 |
| 24 | 0.896 | 0.871 | 0.865 | 0.864 | 0.864 | 0.864 | 0.866 | 0.865 | 0.867 | 0.870 | 0.876 |
| 30 | 0.927 | 0.906 | 0.902 | 0.902 | 0.901 | 0.900 | 0.904 | 0.902 | 0.902 | 0.905 | 0.908 |
| 36 | 0.947 | 0.931 | 0.928 | 0.927 | 0.928 | 0.928 | 0.929 | 0.929 | 0.929 | 0.930 | 0.934 |
| 42 | 0.963 | 0.950 | 0.949 | 0.949 | 0.949 | 0.949 | 0.951 | 0.950 | 0.951 | 0.951 | 0.953 |
| 48 | 0.974 | 0.964 | 0.964 | 0.963 | 0.963 | 0.963 | 0.964 | 0.963 | 0.961 | 0.962 | 0.966 |
| 58 | 0.987 | 0.980 | 0.982 | 0.981 | 0.981 | 0.982 | 0.982 | 0.981 | 0.981 | 0.980 | 0.979 |
| 73 | 0.997 | 0.996 | 0.996 | 0.996 | 0.996 | 0.995 | 0.996 | 0.994 | 0.993 | 0.992 | 0.994 |
| 88 | 1.000 | 1.000 | 1.000 | 1.001 | 1.002 | 1.001 | 1.002 | 1.000 | 0.999 | 0.999 | 1.001 |
| 90 | 1.000 | 1.000 | 1.000 | 1.000 | 1.000 | 1.000 | 1.000 | 1.000 | 1.000 | 1.000 | 1.000 |
| 103 | 0.998 | 0.997 | 0.997 | 0.999 | 0.999 | 0.999 | 0.998 | 0.995 | 0.995 | 0.995 | 0.995 |
| 118 | 0.990 | 0.987 | 0.987 | 0.988 | 0.987 | 0.987 | 0.988 | 0.985 | 0.984 | 0.983 | 0.986 |
| 128 | 0.979 | 0.973 | 0.972 | 0.973 | 0.973 | 0.971 | 0.972 | 0.970 | 0.970 | 0.970 | 0.971 |
| 133 | 0.971 | 0.963 | 0.961 | 0.961 | 0.962 | 0.963 | 0.962 | 0.961 | 0.960 | 0.960 | 0.961 |
| 138 | 0.963 | 0.951 | 0.949 | 0.948 | 0.948 | 0.948 | 0.949 | 0.948 | 0.948 | 0.947 | 0.951 |
| 143 | 0.952 | 0.935 | 0.932 | 0.932 | 0.931 | 0.931 | 0.934 | 0.932 | 0.932 | 0.933 | 0.936 |
| 148 | 0.936 | 0.914 | 0.911 | 0.910 | 0.912 | 0.912 | 0.912 | 0.911 | 0.912 | 0.913 | 0.916 |
| 153 | 0.915 | 0.888 | 0.882 | 0.881 | 0.880 | 0.881 | 0.884 | 0.885 | 0.886 | 0.890 | 0.892 |
| 158 | 0.885 | 0.853 | 0.846 | 0.844 | 0.845 | 0.845 | 0.846 | 0.847 | 0.849 | 0.852 | 0.857 |
| 165 | 0.821 | 0.782 | 0.771 | 0.767 | 0.768 | 0.771 | 0.771 | 0.772 | 0.774 | 0.776 | 0.781 |
| 169 | | 0.726 | 0.711 | 0.708 | 0.708 | 0.711 | 0.712 | 0.714 | 0.716 | 0.719 | 0.726 |
| 170 | | 0.709 | 0.693 | 0.690 | 0.690 | 0.691 | 0.697 | 0.698 | 0.700 | 0.703 | 0.710 |
| 172 | | 0.676 | 0.657 | 0.654 | 0.654 | 0.655 | 0.658 | 0.660 | 0.662 | 0.664 | 0.672 |
| 173 | | 0.661 | 0.638 | 0.635 | 0.635 | 0.637 | 0.640 | 0.642 | 0.644 | 0.647 | 0.654 |
| 174 | | 0.643 | 0.618 | 0.613 | 0.615 | 0.617 | 0.620 | 0.620 | 0.622 | 0.625 | 0.632 |
| 175 | | 0.622 | 0.599 | 0.595 | 0.596 | 0.599 | 0.602 | 0.604 | 0.606 | 0.609 | 0.616 |
| 176 | | 0.605 | 0.581 | 0.577 | 0.577 | 0.579 | 0.583 | 0.585 | 0.588 | 0.591 | 0.599 |
| 177 | | 0.605 | 0.566 | 0.559 | 0.560 | 0.563 | 0.565 | 0.569 | 0.571 | 0.574 | 0.583 |
| 178 | | 0.604 | 0.553 | 0.545 | 0.544 | 0.545 | 0.547 | 0.550 | 0.552 | 0.555 | 0.562 |
| 179 | | 0.604 | 0.554 | 0.534 | 0.530 | 0.530 | 0.534 | 0.537 | 0.541 | 0.545 | 0.554 |
| 180 | | 0.604 | 0.554 | 0.532 | 0.527 | 0.524 | 0.526 | 0.530 | 0.532 | 0.536 | 0.543 |

Table 7.4. Scatter components of the anisotropy function $F_{scat}(r, \theta)$.

| Angle, | Distance, $r$ (cm) | | | | | | | | | | |
|---|---|---|---|---|---|---|---|---|---|---|---|
| $\theta$ (°) | 0.25 | 5 | 1 | 2 | 3 | 5 | 7.5 | 10 | 12.5 | 15 | 20 |
| 0 | 0.396 | 0.751 | 0.840 | 0.863 | 0.867 | 0.874 | 0.885 | 0.891 | 0.895 | 0.898 | 0.904 |
| 1 | 0.396 | 0.749 | 0.838 | 0.862 | 0.868 | 0.875 | 0.887 | 0.891 | 0.895 | 0.899 | 0.903 |
| 2 | 0.398 | 0.750 | 0.840 | 0.862 | 0.869 | 0.876 | 0.887 | 0.891 | 0.895 | 0.901 | 0.904 |
| 3 | 0.398 | 0.751 | 0.837 | 0.863 | 0.871 | 0.877 | 0.886 | 0.892 | 0.896 | 0.901 | 0.905 |
| 4 | 0.404 | 0.752 | 0.839 | 0.865 | 0.872 | 0.878 | 0.889 | 0.894 | 0.897 | 0.903 | 0.905 |
| 5 | 0.408 | 0.752 | 0.840 | 0.868 | 0.875 | 0.880 | 0.890 | 0.895 | 0.899 | 0.904 | 0.906 |
| 6 | 0.413 | 0.757 | 0.842 | 0.865 | 0.876 | 0.882 | 0.892 | 0.897 | 0.900 | 0.904 | 0.909 |
| 7 | 0.419 | 0.758 | 0.843 | 0.870 | 0.878 | 0.883 | 0.894 | 0.898 | 0.903 | 0.907 | 0.908 |
| 8 | 0.425 | 0.762 | 0.846 | 0.874 | 0.881 | 0.887 | 0.896 | 0.899 | 0.905 | 0.908 | 0.911 |
| 10 | 0.439 | 0.767 | 0.855 | 0.880 | 0.885 | 0.891 | 0.901 | 0.905 | 0.908 | 0.911 | 0.913 |
| 12 | 0.459 | 0.776 | 0.861 | 0.884 | 0.890 | 0.897 | 0.905 | 0.909 | 0.912 | 0.915 | 0.919 |
| 14 | 0.479 | 0.781 | 0.865 | 0.890 | 0.897 | 0.902 | 0.911 | 0.914 | 0.917 | 0.920 | 0.922 |
| 16 | 0.499 | 0.790 | 0.874 | 0.895 | 0.902 | 0.908 | 0.917 | 0.919 | 0.921 | 0.924 | 0.926 |
| 20 | 0.544 | 0.809 | 0.885 | 0.908 | 0.914 | 0.918 | 0.926 | 0.929 | 0.930 | 0.933 | 0.934 |
| 24 | 0.593 | 0.823 | 0.900 | 0.920 | 0.924 | 0.928 | 0.935 | 0.936 | 0.939 | 0.941 | 0.942 |
| 30 | 0.660 | 0.849 | 0.915 | 0.934 | 0.938 | 0.943 | 0.947 | 0.950 | 0.951 | 0.953 | 0.954 |
| 36 | 0.726 | 0.876 | 0.934 | 0.947 | 0.952 | 0.954 | 0.960 | 0.961 | 0.962 | 0.963 | 0.963 |
| 42 | 0.784 | 0.900 | 0.947 | 0.961 | 0.963 | 0.965 | 0.968 | 0.970 | 0.970 | 0.971 | 0.971 |
| 48 | 0.833 | 0.919 | 0.958 | 0.969 | 0.972 | 0.973 | 0.976 | 0.978 | 0.979 | 0.979 | 0.978 |
| 58 | 0.904 | 0.954 | 0.978 | 0.983 | 0.984 | 0.985 | 0.986 | 0.987 | 0.989 | 0.989 | 0.988 |
| 73 | 0.979 | 0.986 | 0.995 | 0.995 | 0.995 | 0.995 | 0.998 | 0.997 | 0.996 | 0.999 | 0.998 |
| 88 | 1.003 | 1.000 | 1.000 | 1.000 | 1.001 | 0.999 | 1.001 | 1.000 | 1.000 | 1.002 | 1.001 |
| 90 | 1.000 | 1.000 | 1.000 | 1.000 | 1.000 | 1.000 | 1.000 | 1.000 | 1.000 | 1.000 | 1.000 |
| 103 | 0.986 | 0.995 | 0.996 | 0.996 | 0.999 | 0.997 | 0.998 | 0.999 | 0.999 | 0.998 | 0.999 |
| 118 | 0.927 | 0.962 | 0.980 | 0.984 | 0.987 | 0.988 | 0.991 | 0.991 | 0.990 | 0.991 | 0.990 |
| 128 | 0.863 | 0.933 | 0.966 | 0.974 | 0.978 | 0.979 | 0.980 | 0.981 | 0.982 | 0.983 | 0.983 |
| 133 | 0.824 | 0.916 | 0.955 | 0.966 | 0.970 | 0.971 | 0.975 | 0.976 | 0.976 | 0.977 | 0.977 |
| 138 | 0.777 | 0.898 | 0.940 | 0.959 | 0.961 | 0.962 | 0.968 | 0.968 | 0.970 | 0.970 | 0.970 |
| 143 | 0.725 | 0.875 | 0.931 | 0.949 | 0.951 | 0.954 | 0.958 | 0.961 | 0.961 | 0.963 | 0.963 |
| 148 | 0.676 | 0.850 | 0.917 | 0.937 | 0.942 | 0.945 | 0.949 | 0.951 | 0.952 | 0.954 | 0.953 |
| 153 | 0.618 | 0.827 | 0.901 | 0.924 | 0.928 | 0.932 | 0.938 | 0.942 | 0.942 | 0.944 | 0.946 |
| 158 | 0.550 | 0.802 | 0.885 | 0.906 | 0.914 | 0.920 | 0.926 | 0.929 | 0.932 | 0.934 | 0.935 |
| 165 | 0.450 | 0.763 | 0.859 | 0.883 | 0.893 | 0.898 | 0.908 | 0.913 | 0.915 | 0.918 | 0.919 |
| 169 | | 0.739 | 0.845 | 0.872 | 0.881 | 0.888 | 0.897 | 0.902 | 0.905 | 0.909 | 0.912 |
| 170 | | 0.733 | 0.839 | 0.868 | 0.878 | 0.884 | 0.895 | 0.899 | 0.903 | 0.906 | 0.909 |
| 172 | | 0.722 | 0.833 | 0.864 | 0.871 | 0.879 | 0.889 | 0.894 | 0.898 | 0.901 | 0.907 |
| 173 | | 0.714 | 0.829 | 0.858 | 0.869 | 0.876 | 0.888 | 0.892 | 0.895 | 0.899 | 0.903 |
| 174 | | 0.712 | 0.827 | 0.859 | 0.865 | 0.873 | 0.883 | 0.890 | 0.894 | 0.897 | 0.901 |
| 175 | | 0.707 | 0.822 | 0.854 | 0.864 | 0.870 | 0.884 | 0.888 | 0.891 | 0.897 | 0.899 |
| 176 | | 0.699 | 0.822 | 0.853 | 0.860 | 0.869 | 0.881 | 0.885 | 0.892 | 0.894 | 0.900 |
| 177 | | 0.695 | 0.821 | 0.850 | 0.859 | 0.867 | 0.879 | 0.885 | 0.889 | 0.892 | 0.897 |
| 178 | | 0.691 | 0.819 | 0.850 | 0.859 | 0.865 | 0.878 | 0.884 | 0.888 | 0.893 | 0.897 |
| 179 | | 0.691 | 0.818 | 0.850 | 0.856 | 0.863 | 0.877 | 0.883 | 0.887 | 0.892 | 0.896 |
| 180 | | 0.687 | 0.818 | 0.848 | 0.856 | 0.863 | 0.877 | 0.881 | 0.889 | 0.893 | 0.895 |

### 7.3.2. *Scatter correction factors*

Figure 7.3 shows a portion of the SC table for the $^{192}$Ir source, presented as 2D images for $d_1$ = 0.2, 1, 2, and 5 cm. There are gradual changes in $f_{scat}$ with the distances $d_1$, $d_2$, and $d_3$. The combined statistical and interpolation errors in $f_{scat}$ are <3%. A comparison of SC and TG-43 calculations shows that neglecting the directional dependence of $f_{scat}$ leads to a maximum error of ±1.2% within 10 cm from the source.

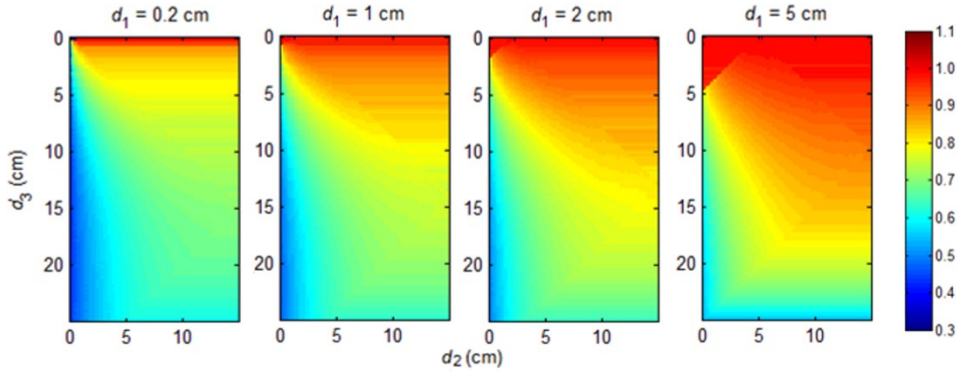


Figure 7.3. Part of the SC lookup table for an HDR $^{192}$Ir source. It is a function of three distances: $d_1$, $d_2$, and $d_3$. Out-of-range points are extrapolated by a nearest neighbor search of $d_2$. Values of $f_{scat}$ for POIs in air are not shown.

### 7.3.3. *Phantom calculations*

Figure 7.4 compares the MC, SC, and TG-43 isodose in the three water phantoms. TG-43 overestimates the dose particularly in the regions near the phantom surfaces.

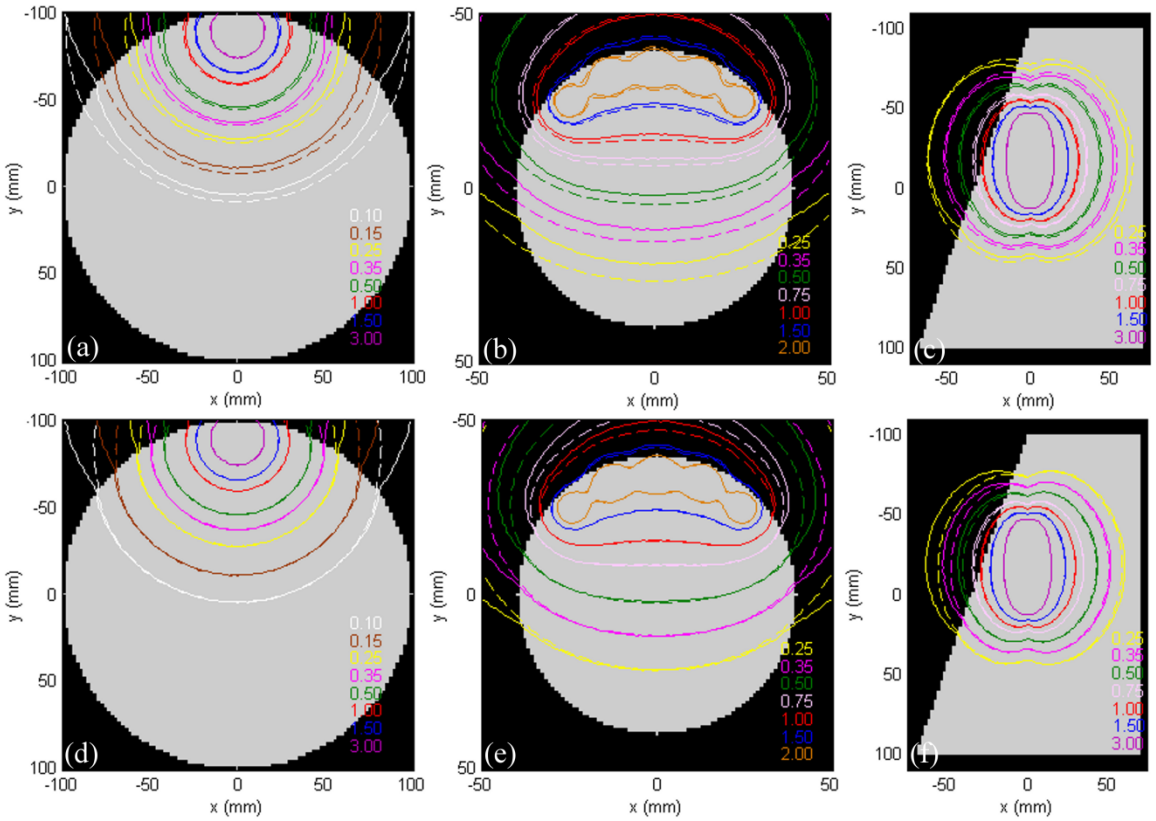


Figure 7.4. Isodose distributions along the plane at $z = 0$ in spherical, cylindrical, and trapezoidal prism water phantoms are displayed in separate columns from left to right. MC calculations, in solid lines, are shown in all panels. TG-43 2D calculations, in dashed lines, are in upper panels (a)–(c). SC calculations, also in dashed lines, are in lower panels (d)–(f). The dose per total dwell time is in units of mGy $U^{-1}$ $h^{-1}$.

### 7.3.4. *Breast patient calculations*

Table 7.5 lists the dose-volume statistics for the breast cohort. The isodose and dose-volume histograms for a patient are shown in Figure 7.5. A similar comparison of the MC and TG-43 isodoses has been demonstrated by Pantelis et al. [3], who used MCNPX to calculate a breast patient plan in a mathematical phantom. The breast dimensions and the nearby lung have only a minor influence on the target dose, because the scatter-to-primary dose ratio near the source is low (from about 3% at 3 mm to about 12% at 1 cm).

Table 7.5. Dose-volume index statistics for 18 multicatheter breast patient plans.

| Structure | Dose-volume index | MC | | ratio | | | | |
|---|---|---|---|---|---|---|---|---|
| | | Mean±σ | Range | $\frac{MC_{water}}{MC}$ | $\frac{SC}{MC}$ | $\frac{TG43}{MC}$ | $\frac{SC}{MC_{water}}$ | $\frac{TG43}{MC_{water}}$ |
| PTV | $D_{90}$ (%) | 103.1±2.8 | 96.9–107.2 | 1.002±0.006 | 1.000±0.007 | 1.026±0.006 | 0.998±0.002 | 1.024±0.005 |
| | $D_{100}$ (%) | 68.8±10.3 | 47.8–89.9 | 1.001±0.009 | 1.001±0.010 | 1.025±0.040 | 1.000±0.009 | 1.024±0.040 |
| | $V_{90}$ (%) | 98.0±1.7 | 94.2–100.0 | 1.001±0.001 | 1.000±0.001 | 1.006±0.003 | 1.000±0.001 | 1.005±0.003 |
| | $V_{100}$ (%) | 93.4±2.7 | 87.5–96.9 | 0.999±0.015 | 0.996±0.022 | 1.020±0.006 | 0.997±0.008 | 1.022±0.019 |
| | DHI | 0.771±0.051 | 0.643–0.882 | 0.997±0.003 | 1.002±0.004 | 0.991±0.005 | 1.005±0.004 | 0.994±0.005 |
| Skin | $D_{0.1cc}$ (%) | 86.4±11.2 | 51.6–97.7 | 0.999±0.006 | 0.989±0.010 | 1.047±0.012 | 0.990±0.007 | 1.048±0.012 |
| | $D_{1cc}$ (%) | 71.5±9.2 | 45.5–85.1 | 0.999±0.004 | 0.987±0.008 | 1.060±0.007 | 0.989±0.007 | 1.061±0.009 |
| | $D_{10cc}$ (%) | 44.1±11.4 | 28.0–72.1 | 0.996±0.005 | 0.987±0.010 | 1.089±0.011 | 0.992±0.007 | 1.094±0.012 |
| Lung | $D_{0.1cc}$ (%) | 53.3±20.9 | 6.9–83.2 | 1.026±0.009 | 1.025±0.009 | 1.053±0.009 | 0.999±0.005 | 1.026±0.008 |
| | $V_{5Gy}$ ($cm^3$) | 144.3±110.5 | 0–481.1 | 0.941±0.043 | 0.929±0.045 | 1.034±0.074 | 0.987±0.012 | 1.098±0.039 |
| | $V_{10Gy}$ ($cm^3$) | 29.7±29.2 | 0–88.2 | 1.124±0.208 | 1.119±0.213 | 1.461±0.686 | 0.995±0.026 | 1.257±0.319 |
| Heart | $D_{0.1cc}$ (%) | 25.5±12.6 | 7.1–50.7 | 0.980±0.045 | 0.974±0.048 | 1.021±0.037 | 0.994±0.007 | 1.043±0.014 |
| | $V_{5Gy}$ ($cm^3$) | 30.6±41.8 | 0–129.7 | 0.841±0.249 | 0.823±0.262 | 1.140±0.198 | 0.957±0.092 | 1.555±0.769 |

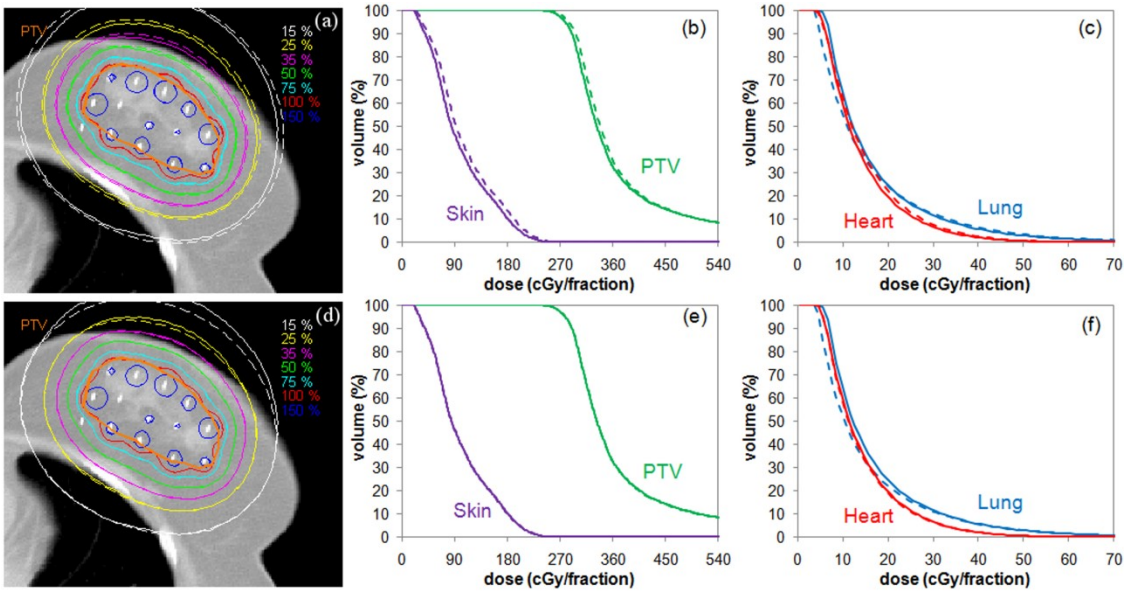


Figure 7.5. Isodose and dose-volume histogram comparisons for a multicatheter breast brachytherapy patient. MC results (solid lines, all panels) are compared with TG-43 results [dashed lines, upper panels (a)–(c)] and SC results [dashed lines, lower panels (d)–(f)]. The isodose distributions are normalized to the prescribed dose of 270 cGy per fraction over 12 fractions.

The MC and $MC_{water}$ calculations of the PTV and skin dose agree within 0.5%. The differences for the lung and heart $D_{0.1\ cc}$ are up to 2.6%. The heart $V_{5\ Gy}$ shows the highest deviation because of a smaller backscatter contribution near the skin and the lung as well as less photon attenuation along the lung.

The SC and $MC_{water}$ results agree within 1% except for the heart $V_{5\ Gy}$. The lung and heart $D_{0.1\ cc}$ deviate from MC calculations by ±2.5%. Differences in $V_{5\ Gy}$ for the lung and heart are greater because of tissue inhomogeneity effects.

TG-43 and $MC_{water}$ agree within 2.4% for the PTV dose-volume indices. The TG-43 skin, lung, and heart $D_{0.1\ cc}$ are higher by 5%, 3%, and 4%, respectively, compared with $MC_{water}$. There are larger variations for the lung and heart $V_{5\ Gy}$.

### 7.3.5. *Calculation efficiency*

The efficiency of both the SC and TG-43 algorithms is inversely proportional to the product of the number of dwell positions and the number of dose points. Based upon the calculation times for the 18 breast patients, the SC algorithm runs 50% longer than TG-43 on a 32 bit Windows operating system.

## 7.4. DISCUSSION AND CONCLUSIONS

### 7.4.1. *Algorithm limitations*

The SC method assumes that the patient body consists of water. It is intended for the commonly used $^{192}$Ir radionuclide and for treatment sites with minimal internal dose perturbations. As Compton scattering is the dominant interaction in tissue, $^{192}$Ir dosimetry is not sensitive to tissue composition variations. The accuracy may be compromised around shielding, high-concentration radiographic contrast solution, air cavities, and bones. The method is not intended for low-energy sources, as tissue inhomogeneities are generally not water equivalent owing to the dominance of photoelectric effect.

From Figures 7.4 and 7.5, it is obvious that the SC and MC dose distributions in air disagree. The primary dose is incorrect because of the smaller photon attenuation in air. We included $f_{scat}$ for exterior points in the SC table to ensure a smooth dose gradient across the skin-air interface. Since the dose to air is not of clinical importance, the calculation efficiency can be improved by setting the dose in air to zero.

We made $f_{scat}$ independent of the source orientation so as to reduce the size of the SC table, which is justified by earlier investigations that the scatter dose is nearly isotropic [27, 28, 36]. Besides, $f_{scat}$ is a ratio of two scatter dose values at the same distance and angle and hence its value has an even smaller angular dependence. This

simplification causes an estimated 1.2% maximum dose difference within 10 cm of the HDR source. However, there could be larger errors for sources with longer active lengths.

### 7.4.2. *Algorithm applications*

The overestimate of the TG-43 dose near the skin can be regarded as a conservative measure to reduce normal tissue damage. On the other hand, our technique will be useful for patient plans with challenging dosimetric constraints. In our multicatheter breast inverse planning, for instance, a DHI > 0.75 was unattainable for 3 out of 18 patients because of either a dose coverage constraint or a skin dose limit. By using the SC method for treatment planning, the skin dose constraint is effectively relaxed and a better optimization becomes feasible.

When the target spreads over a large area near the skin, the dose to a region in the target contributed by a dwell position far from it will be overestimated by TG-43. Although the dose can be adjusted by correction factors derived by empirical means [37], the SC technique is more robust because $f_{scat}$ corrects for the scattered radiation according to the distances between the skin, the source, and the POI. It is potentially useful for the treatment planning of superficial lesions and intraoperative brachytherapy.

Our technique serves as an efficient alternative to the MC method for $^{192}$Ir brachytherapy. Compared with low-energy seed implant calculations, effects of tissue composition variations at $^{192}$Ir energies are less severe and MC-based HDR treatment planning may be unwarranted unless highly attenuating materials such as shielding are present. Besides, the technique only requires locating the body contour. It can be used for dose calculations based on cone-beam CT or magnetic resonance images.

### 7.4.3. *Summary and conclusions*

The proposed SC technique, of calculation efficiency comparable to TG-43, is intended for fast HDR $^{192}$Ir brachytherapy dose calculations in the absence of full scatter conditions. The method works well as long as internal inhomogeneity effects are small. It can be implemented in treatment planning systems after a few modifications to the software. These include adding capabilities to (1) allow the importation of the primary and scatter components of TG-43 parameters and tables of SC factors, (2) perform 3D distance transform on a binary map of the skin contour, and (3) calculate the primary and scatter doses separately and then scale the scatter dose by a SC factor according to the distances between the point of interest, the dwell position, and the skin. The technique has been validated for multicatheter breast brachytherapy, in which the target and skin doses for 18 patients agree with MC calculations better than 1%.

## 7.5. REFERENCES


1. Rivard MJ, Coursey BM, DeWerd LA, Hanson WF, Huq MS, Ibbott GS, et al. Update of AAPM Task Group No. 43 Report: A revised AAPM protocol for brachytherapy dose calculations. Med Phys. 2004;31:633-74.

2. Mangold CA, Rijnders A, Georg D, Van Limbergen E, Pötter R, Huyskens D. Quality control in interstitial brachytherapy of the breast using pulsed dose rate: treatment planning and dose delivery with an Ir-192 afterloading system. Radiother Oncol. 2001;58:43-51.

3. Pantelis E, Papagiannis P, Karaiskos P, Angelopoulos A, Anagnostopoulos G, Baltas D, et al. The effect of finite patient dimensions and tissue inhomogeneities on dosimetry planning of $^{192}$Ir HDR breast brachytherapy: a Monte Carlo dose verification study. Int J Radiat Oncol Biol Phys. 2005;61:1596-602.

4. Lymperopoulou G, Papagiannis P, Angelopoulos A, Karaiskos P, Georgiou E, Baltas D. A dosimetric comparison of $^{169}$Yb and $^{192}$Ir for HDR brachytherapy of the breast, accounting for the effect of finite patient dimensions and tissue inhomogeneities. Med Phys. 2006;33:4583-9.

5. Anagnostopoulos G, Baltas D, Pantelis E, Papagiannis P, Sakelliou L. The effect of patient inhomogeneities in oesophageal $^{192}$Ir HDR brachytherapy: a Monte Carlo and analytical dosimetry study. Phys Med Biol. 2004;49:2675-85.

6. Raina S, Avadhani JS, Oh M, Malhotra HK, Jaggernauth W, Kuettel MR, et al. Quantifying IOHDR brachytherapy underdosage resulting from an incomplete scatter environment. Int J Radiat Oncol Biol Phys. 2005;61:1582-6.

7. Angelopoulos A, Perris A, Sakellariou K, Sakelliou L, Sarigiannis K, Zarris G. Accurate Monte Carlo calculations of the combined attenuation and build-up factors, for energies (20-1500 keV) and distances (0-10 cm) relevant in brachytherapy. Phys Med Biol. 1991;36:763-78.

8. Williamson JF. Comparison of measured and calculated dose rates in water near I-125 and Ir-192 seeds. Med Phys. 1991;18:776-86.

9. Serago CF, Houdek PV, Pisciotta V, Schwade JG, Abitbol AA, Lewin AA, et al. Scattering effects on the dosimetry of iridium-192. Med Phys. 1991;18:1266-70.

10. Melhus CS, Rivard MJ. Approaches to calculating AAPM TG-43 brachytherapy dosimetry parameters for $^{137}$Cs, $^{125}$I, $^{192}$Ir, $^{103}$Pd, and $^{169}$Yb sources. Med Phys. 2006;33:1729-37.

11. Pérez-Calatayud J, Granero D, Ballester F. Phantom size in brachytherapy source dosimetric studies. Med Phys. 2004;31:2075-81.

12. Granero D, Perez-Calatayud J, Pujades-Claumarchirant MC, Ballester F, Melhus CS, Rivard MJ. Equivalent phantom sizes and shapes for brachytherapy dosimetric studies of $^{192}$Ir and $^{137}$Cs. Med Phys. 2008;35:4872-7.

13. Anagnostopoulos G, Baltas D, Karaiskos P, Pantelis E, Papagiannis P, Sakelliou L. An analytical dosimetry model as a step towards accounting for inhomogeneities and bounded geometries in $^{192}$Ir brachytherapy treatment planning. Phys Med Biol. 2003;48:1625-47.

14. Carrier JF, D'Amours M, Verhaegen F, Reniers B, Martin AG, Vigneault E, et al. Postimplant dosimetry using a Monte Carlo dose calculation engine: a new clinical standard. Int J Radiat Oncol Biol Phys. 2007;68:1190-8.

15. Poon E, Williamson JF, Vuong T, Verhaegen F. Patient-specific Monte Carlo dose calculations for high-dose-rate endorectal brachytherapy with shielded intracavitary applicator. Int J Radiat Oncol Biol Phys. 2008;72:1259-66.

16. Afsharpour H, D'Amours M, Coté B, Carrier JF, Verhaegen F, Beaulieu L. A Monte Carlo study on the effect of seed design on the interseed attenuation in permanent prostate implants. Med Phys. 2008;35:3671-81.

17. Furstoss C, Reniers B, Bertrand MJ, Poon E, Carrier JF, Keller BM, et al. Monte Carlo study of LDR seed dosimetry with an application in a clinical brachytherapy breast implant. Med Phys. 2009;36:1848-58.

18. Poon E, Le Y, Williamson JF, Verhaegen F. BrachyGUI: an adjunct to an accelerated Monte Carlo photon transport code for patient-specific brachytherapy dose calculations and analysis. J Phys Conf Ser. 2008;102:012018.

19. Agostinelli S, Allison J, Amako K, Apostolakis J, Araujo H, Arce P, et al. GEANT4-a simulation toolkit. Nucl Instrum Methods Phys Res A. 2003;506:250-303.

20. Nuclear data from NuDat 2.0, a web-based database maintained by the National Nuclear Data Center [database on the Internet]. Brookhaven National Laboratory, Upton, NY 2004. Available from: http://www.nndc.bnl.gov/nudat2.

21. Cullen DE, Hubbell JH, Kissel L. EPDL97: The Evaluated Photon Data Library, '97 Version. Livermore, CA: Lawrence Livermore National Laboratory1997. Report No.: UCRL-50400, Rev. 5.

22. Hubbell JH, Seltzer SM. Tables of x-ray mass attenuation coefficients and mass energy-absorption coefficients 1 keV to 20 MeV for elements Z=1 to 92 and 48 additional substances of dosimetric interest. Gaithersburg, MD: National Institute of Standards and Technology 1995. Report No.: NISTIR 5632.

23. Wang R, Li XA. Dose characterization in the near-source region for two high dose rate brachytherapy sources. Med Phys. 2002;29:1678-86.

24. Williamson JF. Monte Carlo evaluation of kerma at a point for photon transport problems. Med Phys. 1987;14:567-76.

25. Radiation Safety Information Computational Center. HUGO-VI: Photon Interaction Data in ENDF/B-VI Format. Oak Ridge, TN Oak Ridge National Laboratory; 1989.

26. Le Y, Chibani O, Todor D, Siebers I, Williamson J. An integrated CT-based Monte Carlo dose-evaluation system for brachytherapy and its application to permanent prostate implant postprocedure dosimetric analysis. Med Phys. 2005;32:2068.

27. Williamson JF. Dose calculations about shielded gynecological colpostats. Int J Radiat Oncol Biol Phys. 1990;19:167-78.

28. Williamson JF. The Sievert integral revisited: evaluation and extension to $^{125}$I, $^{169}$Yb, and $^{192}$Ir brachytherapy sources. Int J Radiat Oncol Biol Phys. 1996;36:1239-50.

29. Russell KR, Ahnesjo A. Dose calculation in brachytherapy for a $^{192}$Ir source using a primary and scatter dose separation technique. Phys Med Biol. 1996;41:1007-24.

30. Russell KR, Carlsson Tedgren ÅK, Ahnesjö A. Brachytherapy source characterization for improved dose calculations using primary and scatter dose separation. Med Phys. 2005;32:2739-52.

31. Daskalov GM, Loffler E, Williamson JF. Monte Carlo-aided dosimetry of a new high dose-rate brachytherapy source. Med Phys. 1998;25:2200-8.

32. Taylor RPE, Rogers DWO. EGSnrc Monte Carlo calculated dosimetry parameters for $^{192}$Ir and $^{169}$Yb brachytherapy sources. Med Phys. 2008;35:4933-44.

33. Wu A, Ulin K, Sternick ES. A dose homogeneity index for evaluating $^{192}$Ir interstitial breast implants. Med Phys. 1988;15:104-7.

34. International Commission on Radiation Units and Measurements. Tissue substitutes in radiation dosimetry and measurement. Bethesda, MD: ICRU; 1989.

35. International Commission on Radiation Units and Measurements. Photon, electron, proton and neutron interaction data for body tissues. Bethesda, MD: ICRU; 1992.

36. Karaiskos P, Angelopoulos A, Baras P, Rozaki-Mavrouli H, Sandilos P, Vlachos L, et al. Dose rate calculations around $^{192}$Ir brachytherapy sources using a Sievert integration model. Phys Med Biol. 2000 Feb;45:383-98.

37. Oh M, Wang Z, Malhotra HK, Jaggernauth W, Podgorsak MB. Impact of surface curvature on dose delivery in intraoperative high-dose-rate brachytherapy. Med Dosim. 2009;34:63-74.

# Chapter Eight

# Paper IV: A CT-based Analytical Dose Calculation Method for HDR $^{192}$Ir Brachytherapy

Emily Poon, Frank Verhaegen

*Med Phys. 2009;36:3982-94*



In this chapter, we will present a CT-based analytical dose calculation method for HDR $^{192}$Ir brachytherapy. It is partly based upon the work of Anagnostopoulos et al. [1], and is able to account for the perturbation effects of applicators, shielding, contrast solution, and tissue inhomogeneities. The algorithm also incorporates the scatter correction technique introduced in Chapter 7. It is a viable alternative to the sophisticated and less efficient CT-based MC method, which we presented in Chapter 6. We will also evaluate the adequacy of TG-43 for HDR $^{192}$Ir treatment planning, based on the calculations for head-and-neck, esophagus, and MammoSite brachytherapy patient plans.

## ABSTRACT

Purpose: This article presents an analytical dose calculation method for high-dose-rate $^{192}$Ir brachytherapy, taking into account the effects of inhomogeneities and reduced photon backscatter near the skin. The adequacy of the Task Group 43 (TG-43) two-dimensional formalism for treatment planning is also assessed.

Methods: The proposed method uses material composition and density data derived from computed tomography images. The primary and scatter dose distributions for each dwell position are calculated first as if the patient is an infinite water phantom. This is done using either TG-43 or a database of Monte Carlo (MC) dose distributions. The latter can be used to account for the effects of shielding in water. Subsequently, corrections for photon attenuation, scatter, and spectral variations along medium- or low-$Z$ inhomogeneities are made according to the radiological paths determined by ray tracing. The scatter dose is then scaled by a correction factor that depends on the distances between the point of interest, the body contour, and the source position. Dose calculations are done for phantoms with tissue and lead inserts, as well as patient plans for head-and-neck, esophagus, and MammoSite balloon breast brachytherapy treatments. Gamma indices are evaluated using a dose-difference criterion of 3% and a distance-to-agreement criterion of 2 mm. PTRAN_CT MC calculations are used as the reference dose distributions.

Results: For the phantom with tissue and lead inserts, the percentages of the voxels of interest passing the gamma criteria ($P_{\gamma\geq1}$) are 100% for the analytical calculation and 91% for TG-43. For the breast patient plan, TG-43 overestimates the target volume receiving the prescribed dose by 4% and the dose to the hottest 0.1 cm$^3$ of the skin by 9%, whereas

the analytical and MC results agree within 0.4%. $P_{\gamma\geq1}$ are 100% and 48% for the analytical and TG-43 calculations, respectively. For the head-and-neck and esophagus patient plans, $P_{\gamma\geq1}$ are ≥99% for both calculation methods.

Conclusions: A correction-based dose calculation method has been validated for HDR $^{192}$Ir brachytherapy. Its high calculation efficiency makes it feasible for use in treatment planning. Because tissue inhomogeneity effects are small and primary dose predominates in the near-source region, TG-43 is adequate for target dose estimation provided shielding and contrast solution are not used.

## 8.1. INTRODUCTION

$^{192}$Ir is the most commonly used radionuclide in high-dose-rate (HDR) brachytherapy. At $^{192}$Ir photon energies, Compton scattering is the predominant interaction in tissue, and the attenuation of primary photons is nearly offset by the buildup of scattered radiation within the first 4–5 cm from the source [1]. The dose is thus largely characterized by an inverse square falloff with distance [2], while the effects of tissue composition variations play a secondary role in $^{192}$Ir dosimetry.

All modern HDR brachytherapy planning systems comply with the water-based Task Group 43 (TG-43) dose calculation formalism [3]. Although computed tomography (CT) is increasingly being used for three-dimensional (3D) image-based treatment planning, the tissue composition and density information derived from CT images is not yet used clinically for brachytherapy dose calculations [4].

The objectives of this paper are twofold. Firstly, we will introduce an efficient CT-based analytical dose calculation method for HDR $^{192}$Ir brachytherapy. Secondly, we will assess the adequacy of TG-43 for treatment planning. Monte Carlo (MC) dose

calculations are used as a benchmark. Given that tissue inhomogeneity effects of $^{192}$Ir are small compared to those of lower energy sources [5, 6], we will focus on cancer sites near the lungs, air cavities, bones, and radiographic contrast solution. In light of some simplifications made in this method, we will point out its limitations and intended clinical applications. Advantages over alternative dose calculation methods will be discussed.

## 8.2. MATERIALS AND METHODS

### 8.2.1. *Algorithm overview*

This correction-based dose calculation method uses a primary and scatter dose separation approach proposed by Williamson [7, 8] and Russell et al. [9, 10]. The basic idea is to first calculate the primary and scatter doses for each dwell position as if the source is in an infinite water phantom. Then, the radiological path between a given point of interest (POI) and the source, determined by ray tracing, is used to correct for photon attenuation and scatter along tissue inhomogeneities. Lastly, the scatter dose is scaled by a scatter correction (SC) factor to account for the lack of a full scatter environment near the skin. This factor depends on the distances between the source, the POI, and the body contour, as was demonstrated in our previous study [11]. The SC method is useful for clinical cases where the dwell positions are off center and the nearby skin boundary has an irregularly smooth curvature. To report the absorbed dose to medium $D_m$, the dose is multiplied by an effective medium-to-water mass energy absorption coefficient ratio.

The photon energies of $^{192}$Ir correspond to secondary electron ranges that are short enough for the absorbed dose to be equal to collision kerma [12]. In this paper, primary photons refer to photons created inside the encapsulated source and have not undergone interactions outside the source. Primary dose represents the collision kerma resulting from

the interactions of primary photons, and scatter dose results from all other photon interactions.

### 8.2.2. *Algorithm implementation and preprocessing*

The analytical algorithm is incorporated into BrachyGUI [13], an in-house brachytherapy planning system developed in MATLAB (version 7.7, MathWorks, Natick, MA). The microSelectron v2 HDR $^{192}$Ir source model (Nucletron, Veenendaal, The Netherlands) [14] and the NuDat 2.0 $^{192}$Ir photon spectrum [15] are used.

We import the CT images of the patient into BrachyGUI to create 3D material and density matrices for tissue inhomogeneity corrections. The elemental tissue compositions are taken from the International Commission on Radiation Units and Measurements (ICRU) Reports 44 and 46 [16, 17]. The mass densities are derived from the CT Hounsfield units. We create a 3D distance map for looking up the closest distance between a given voxel and the skin, which will be needed for the SC method. The distance map is created by a preprocessing routine [11], which delineates the body contour and performs a 3D Euclidean distance transform of the contour.*

### 8.2.3. *Dose calculations in an infinite water phantom*

In the first step of the algorithm, the primary and scatter doses in an infinite water phantom ($D_{\text{prim,wat}}$ and $D_{\text{scat,wat}}$) are calculated. This can be done using the TG-43 two-dimensional (2D) formalism [3] with the radial dose function and anisotropy function broken down into primary and scatter components [11]. When high-atomic-number (high-$Z$) materials such as shielding are present, we use a database of 3D primary and scatter

* Y. Mishchenko, 2007, "3D Euclidean distance transform for variable data aspect ratio," MATLAB Central File Exchange, The MathWorks, Natick, MA, http://www.mathworks.com/matlabcentral/fileexchange.

dose data [18, 19] instead to account for their dosimetric effects in water. To generate this database, all possible arrangements of single dwell positions with respect to each shielding type are to be simulated by the MC method. Coordinate transformations are applied to the appropriate 3D dose data in accordance with the source orientation and the patient coordinate system to calculate $D_{\text{prim,wat}}$ and $D_{\text{scat,wat}}$.

8.2.4. *Correcting for tissue inhomogeneities and finite patient dimensions*

*i.* *Primary dose calculation*

The primary dose $D_{\text{prim,med}}$ at a POI in the medium *med* is calculated as follows:

$$D_{\text{prim,med}} = D_{\text{prim,wat}} \exp\left\{\sum_i \left[-\left(\frac{\bar{\mu}}{\rho}\right)_{\text{prim,med}_i} \rho_i + \bar{\mu}_{\text{prim,wat}}\right] r_i\right\} \left(\frac{\bar{\mu}_{\text{en}}}{\rho}_{\text{prim}}\right)_{\text{wat}}^{\text{med}} . \quad (8.1)$$

The exponential term will be referred to as the attenuation correction factor. It corrects for the difference in photon attenuation caused by inhomogeneities along the radiological path $d$ between the source and the POI. We ray trace through the patient's density matrix to determine $d$, which comprises multiple segments $i$ of density $\rho_i$ and length $r_i$,

$$d = \sum_i \rho_i r_i . \quad (8.2)$$

The ray tracing procedure will be described in Sec. 8.2.4.iv.

The effective mass attenuation coefficient of the medium $\left(\bar{\mu}/\rho\right)_{\text{med}}$, the effective linear attenuation coefficient for water $\bar{\mu}_{\text{wat}}$, and the effective medium-to-water mass energy absorption coefficient ratio $\left(\bar{\mu}_{\text{en}}/\rho\right)_{\text{wat}}^{\text{med}}$ are given the subscript *prim*. Each quantity is averaged over the primary $^{192}$Ir photon energy fluence spectrum. We use $\left(\bar{\mu}_{\text{en}}/\rho\right)_{\text{wat}}^{\text{med}}$ to convert from absorbed dose to water $D_{\text{w}}$ to $D_{\text{m}}$. For nontissue media (e.g. air, radiographic

contrast solution, and shielding), we set $\left(\bar{\mu}_{\text{en}}/\rho\right)_{\text{wat}}^{\text{med}}$ to unity because they are not of clinical interest.

*ii.* *Scatter dose calculation*

The scatter dose $D_{\text{scat,med}}$ is calculated as follows:

$$D_{\text{scat,med}} = D_{\text{scat,wat}} \exp\left( \sum_i \left\{ -\left[ \frac{\bar{\mu}}{\rho}(d_4, d_3) \right]_{\text{scat,med}_i} \rho_i + \left[ \bar{\mu}(d_4, d_3) \right]_{\text{scat,wat}} \right\} r_i \right) \times \left[ \frac{\bar{\mu}_{\text{en}}}{\rho}_{\text{scat}} (d_4, d_3) \right]_{\text{wat}}^{\text{med}} f_{\text{scat}}(d_1, d_2, d_3) \frac{SPR_{\text{wat}}(d_4, d)}{SPR_{\text{wat}}(d_4, d_3\, \rho_{\text{wat}})} \quad (8.3)$$

Five distance variables are used here: $d$ represents the radiological path between the source and the POI; $d_1$ refers to the distance between the source and the patient's skin; $d_2$ is the distance between the POI and the skin; $d_3$ is the distance between the POI and the source; and $d_4=d_2+d_3$, which is the distance from the source to the skin through the POI. Both $d_1$ and $d_2$ are determined from a 3D distance map.

The subscript *scat* in $\left(\bar{\mu}/\rho\right)_{\text{scat,med}}$, $\bar{\mu}_{\text{scat,wat}}$, and $\left(\bar{\mu}_{\text{en}}/\rho\right)_{\text{wat}}^{\text{med}}$ denotes their association with the scattered photons. They are functions of the distances $d_4$ and $d_3$, whose effects on the spectral energy variations in tissues have been quantified systematically using the approach described in Sec. 8.2.4.iii.

The SC factor $f_{\text{scat}}$ at a given point is a ratio of the scatter dose in bounded water to the scatter dose in unbounded water [11]. Its value is retrieved from a SC table derived by MC calculations. The indices for table lookup come from the distances $d_1$, $d_2$, and $d_3$. In general, $f_{\text{scat}}$ decreases with decreasing $d_1$ and $d_2$, and increasing $d_3$. The minimum value of $f_{\text{scat}}$ for the $^{192}$Ir source is 0.177.

According to Anagnostopoulos et al. [1], the scatter to primary dose ratio (SPR) at a distance $d_3$ and radiological distance $d$ from an $^{192}$Ir point source in tissue materials under full scatter conditions can be approximated by $SPR_{wat}(d)$, which is the SPR at radiological distance $d$ in an infinite water phantom of density $\rho_{wat}$=1 g/cm$^3$. We apply their finding to correct for the scatter dose altered by inhomogeneities. Given that $SPR_{wat}$ is different in a finite volume, we include the extra variable $d_4$ in Eq. (8.3) to indicate that $SPR_{wat}$ is calculated in a water sphere of radius $d_4$. The dose correction thus entails taking the SPR ratio, which is $SPR_{wat}(d_4,d)$ divided by $SPR_{wat}(d_4,d_3\,\rho_{wat})$.

We calculated $SPR_{wat}$ at various distances from an HDR $^{192}$Ir source in spherical water phantoms with radii of 5, 7.5, 10, 12.5, 15, and 50 cm using the GEANT4 MC code (version 9.1) [20]. The *low-energy* electromagnetic physics package [20], the EPDL97 photon cross section library [21], and the mass energy absorption coefficients of Hubbell and Seltzer [22] were used. We scored the primary and scatter dose using a linear track length estimator [23]. The $SPR_{wat}$ corresponding to each phantom radius was fitted as a quadratic function of radiological distance. To determine the SPR ratio for a POI, we look up the $SPR_{wat}$ function according to the associated $d_4$ value by a nearest neighbor search.

*iii.* *Derivations of $\bar{\mu}/\rho$ and $\bar{\mu}_{en}/\rho$ ratios*

GEANT4 was used to simulate the $^{192}$Ir source in the center of spherical water phantoms with radii of 5, 7.5, 10, 15, and 50 cm. The primary and scatter energy fluences were tallied at 5 mm radial distance intervals. The primary components of $\bar{\mu}/\rho$ and $\left(\bar{\mu}_{en}/\rho\right)_{wat}^{med}$ are derived from the primary energy fluence of the largest phantom. Since the values vary slowly with distance in tissue, they are set as constants for dose calculations. The scatter components were fitted using quadratic functions for the five phantoms of

different radii. The functions related to the phantom radius closest to $d_4$ are used to find $(\bar{\mu}/\rho)_{\text{scat,med}}$, $\bar{\mu}_{\text{scat,wat}}$, and $(\bar{\mu}_{\text{en}}/\rho_{\text{scat}})_{\text{wat}}^{\text{med}}$ at a POI.

*iv.* *Ray tracing in 3D patient body*

We ray trace through the patient body in the spherical coordinate system. For each dwell position, 271 paths at 2° separation are traced along the azimuth and zenith directions in 2 mm steps, i.e., $\Delta\theta = \Delta\varphi = 2°$, for $0° \le \theta \le 358°$, $0° \le \varphi \le 180°$, and $\Delta r =$ 2 mm. Let the term inside the exponential function of Eq. (8.1) or Eq. (8.3) be called $t$. We calculate each attenuation correction factor for a POI in a Cartesian dose grid by taking the exponential of the mean of the eight nearest $t$ values determined by ray tracing. There may be fewer than eight $t$ values if the POI is near the grid boundary. The SPR ratio and $f_{\text{scat}}$ are calculated similarly. We take the mean rather than using an eight-point interpolation method [24] to reduce the CPU time. To evaluate the robustness and efficiency gain of this method, a comparison was made with a calculation that ray traced in the 3D Cartesian grid using an improved version [25] of Siddon's algorithm [26].

On the other hand, $D_{\text{prim,wat}}$ and $D_{\text{scat,wat}}$ include already the effects of shielding, if they are present. A separate ray tracing through shielding is then not needed, and the voxels occupied by shielding are replaced by water with a density of 1 g/cm$^3$.

8.2.5. *MC vs analytical and TG-43 calculations*

The analytical and TG-43 calculations in phantom and CT-based geometries were compared to PTRAN_CT [27] calculations. PTRAN_CT is an extended version of the PTRAN MC photon transport code [23, 28]. We used a phase space file to generate the primary photons [13, 19] and an exponential track length estimator to score the dose [23]. The DLC-146 photon cross section library [29] and the mass energy absorption coefficients of

Hubbell and Seltzer [22] were used. The dose per particle history was converted to dose per unit air kerma strength [19]. Above 10% of the prescribed dose $D_{ref}$, the maximum 1-$\sigma$ statistical uncertainties are 0.6% for the phantom calculations and 1.5% for the patient calculations.

Dose differences were quantified by the 3D gamma evaluation method of Wendling et al. [30], using PTRAN_CT calculations as the reference dose distributions. We set the dose-difference criterion to 3% of $D_{ref}$, the distance-to-agreement criterion to 2 mm, the sample step size to 0.5 mm, and the maximum search distance to 6.67 mm. The maximum intensity projections of the gamma indices ($\gamma_{MIP}$) along the axial plane were generated for the patient plans. We reported the mean gamma ($\gamma_{mean}$), the 99th percentile ($\gamma_{1\%}$), and the percentage of points with gamma indices below unity ($P_{\gamma\leq1}$). These three quantities were evaluated for regions receiving >20% of $D_{ref}$ as calculated by the MC method, excluding voxels assigned as air, contrast solution, or lead.

*i.* *Phantom calculations*

Figures 8.1(a)–8.1(b) show the two phantom calculation setups. In both cases, the $^{192}$Ir source was centered in a phantom consisting of 2×2×2 mm$^3$ voxels. We set the air kerma strength to 40 000 U (1 U=1 $\mu$Gy m$^2$ h$^{-1}$), the dwell time to 100 s, and $D_{ref}$ to 3 Gy.

The first setup was used to study tissue inhomogeneity effects in an environment lacking full photon backscatter. The soft tissue phantom contained lung, adipose, spongiosa, and cortical bone inserts. Cortical bone represents one of the densest and least water-equivalent tissue media. Spongiosa is composed of cortical bone, red marrow, and yellow marrow in equal proportion by mass. We also did a calculation using the SC method alone [11].

The second setup was designed to study tissue inhomogeneity effects near shielding. The water phantom contained eight tissue inserts and one lead insert. The MC dose in this phantom with only a lead insert was also calculated. Moreover, we examined if ray tracing along the lead insert could be done to account for its effects on photon attenuation and scatter.

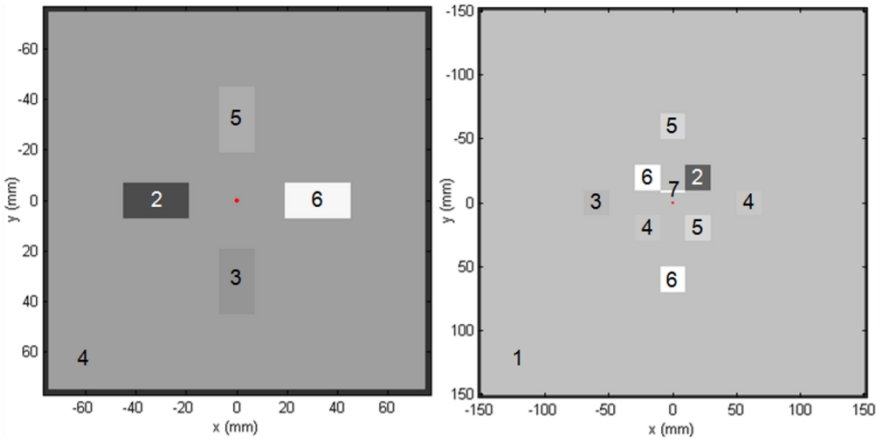


| No. | Material | Density (g/cm³) |
|---|---|---|
| 1 | Water | 1.00 |
| 2 | Lung | 0.26 |
| 3 | Adipose | 0.95 |
| 4 | Soft tissue | 1.06 |
| 5 | Spongiosa | 1.18 |
| 6 | Cortical bone | 1.92 |
| 7 | Lead | 11.36 |

Figure 8.1. (a) A 15×15×10 $cm^3$ soft tissue phantom without shielding. Four 3×1.5×1.5 $cm^3$ tissue inserts are placed inside. (b) A 30×30×25 $cm^3$ water phantom with lead shielding. It contains eight 2×2×2 $cm^3$ tissue inserts. The center of mass of a 2×0.2×2 $cm^3$ lead insert is 0.8 cm away from the phantom's center. The numbers correspond to the listed materials and densities. The HDR $^{192}$Ir source is placed in the center (marked by a dot).

*ii.* *Patient calculations*

Three clinical treatment plans were calculated. The first one was for a head-and-neck cancer patient undergoing nasopharyngeal brachytherapy. Two catheters and 52 dwell positions were used to deliver 6 Gy/fraction to the target. The voxel dimensions were 1.05×1.05×3 $mm^3$.

The second plan was for an esophageal cancer patient. A film-based treatment plan was created to deliver 5 Gy/fraction at 1 cm from the catheter. Seventeen dwell

positions at 5 mm step intervals were used. The same plan was then done retrospectively using CT images. The voxels were 1.8×1.8×5 $mm^3$.

The last plan was for a breast cancer patient treated with a MammoSite balloon applicator (Cytyc Corporation, Marlborough, MA) [31]. The $D_{ref}$ was 3.4 Gy/fraction prescribed at 1 cm from the balloon's surface. After the injection of diluted iodine contrast solution (Omnipaque, GE Healthcare, UK), the balloon diameter expanded to around 43 mm. One dwell position was used. The voxels were 2×2×2 $mm^3$. The contrast solution was assigned, according to the proportion of water mixed with the contrast solution, a concentration of 50 mg I/ml and a density of 1.056 $g/cm^3$. Two additional calculations, regarding the patient body to be composed of water, were done using the SC method and the MC method taking only density variations into account. The results for the latter will be denoted as $MC_{den}$.

The following were calculated for the breast patient plan: The target volumes receiving at least 90%, 100%, 150%, and 200% of $D_{ref}$ ($V_{90}$, $V_{100}$, $V_{150}$, and $V_{200}$); the minimum doses to 90% and 100% of the target ($D_{90}$ and $D_{100}$); and the minimum doses to the hottest 0.1, 1, and 10 $cm^3$ of the skin, lung, and chest wall ($D_{0.1\ cc}$, $D_{1\ cc}$, and $D_{10\ cc}$).

## 8.3. RESULTS AND DISCUSSION

### 8.3.1. $\bar{\mu}/\rho$, $(\bar{\mu}_{en}/\rho)_{wat}^{med}$, *and SPR*

Figures 8.2(a)–8.2(d) show $\bar{\mu}/\rho$ versus distance from the $^{192}$Ir source for water and six tissue materials derived from the primary and scattered photon spectra in water phantoms of different sizes. In Figures 8.3(a)–8.3(d), $(\bar{\mu}_{en}/\rho)_{wat}^{med}$ for six tissue materials are shown. The primary components of both quantities exhibit a slow decrease with

increasing distance because of beam hardening. The scatter components are affected more by spectral changes, especially for bones in the larger phantoms.

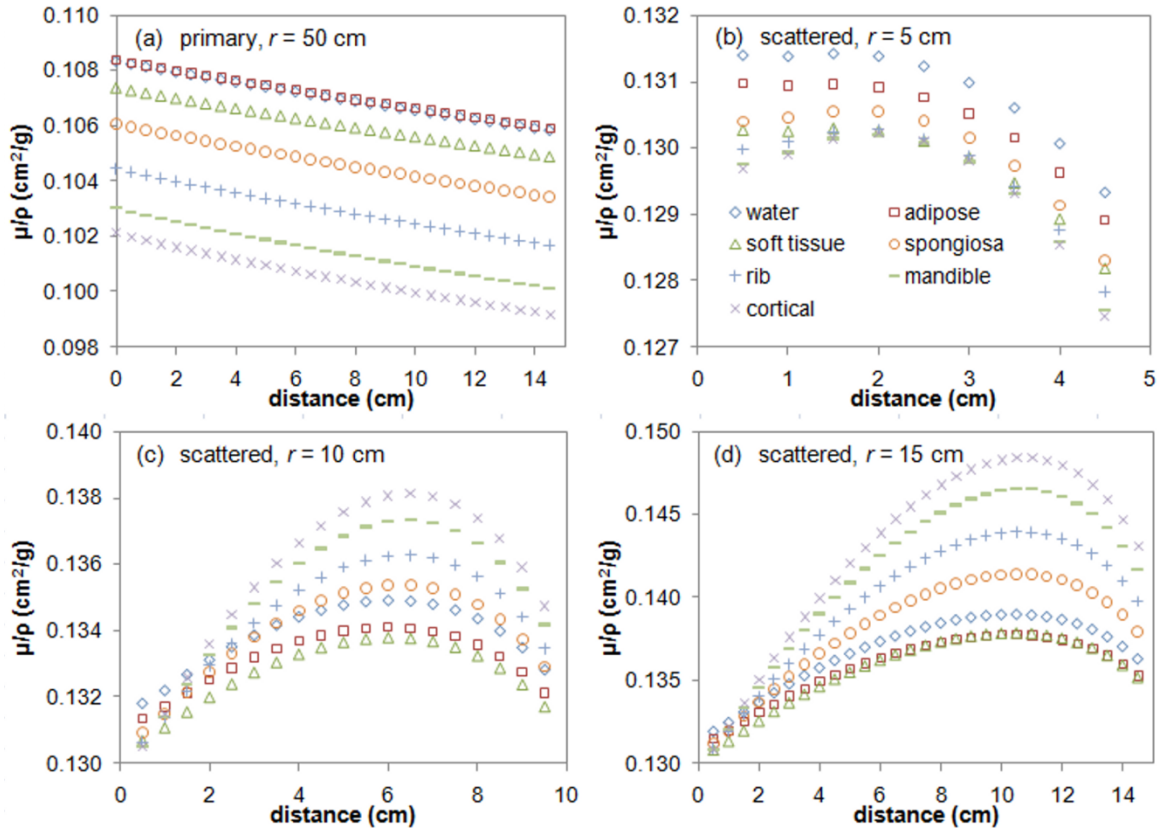


Figure 8.2. Primary and scatter components of the effective mass attenuation coefficients of water and six different tissue materials versus distance from the HDR $^{192}$Ir source. The values are calculated according to the photon spectra at various radial distances in spherical water phantoms of radii *r*.

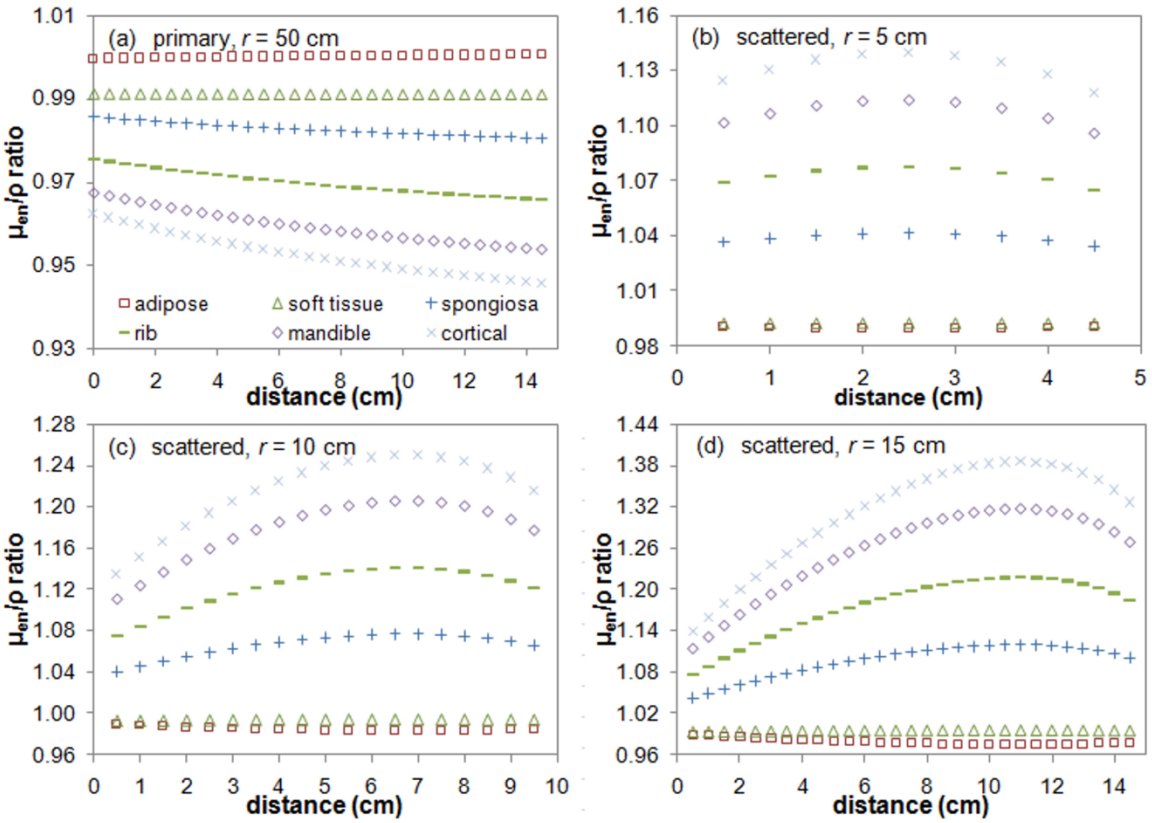


Figure 8.3. Primary and scatter components of the effective medium-to-water mass energy absorption coefficient ratios versus distance for six different tissue media. The values are calculated according to the photon spectra at various radial distances in spherical water phantoms of radii *r*.

Figure 8.4 shows the $SPR_{wat}$ for the $^{192}Ir$ source calculated in water spheres of six different radii. For the phantoms of radii $\leq$ 7.5 cm, $SPR_{wat}$ is always below unity and the primary dose at any POI is always higher than the scatter dose. In the larger phantoms, the primary and scatter dose contributions become nearly the same at 7 cm.

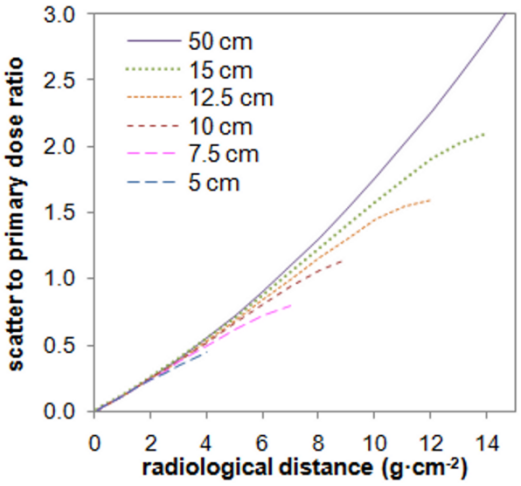


Figure 8.4. Scatter to primary dose ratio as a function of radiological distance from the HDR $^{192}$Ir source calculated in water spheres of different radii (50, 15, 12.5, 10, 7.5, and 5 cm).

### 8.3.2. *3D gamma evaluation*

The statistics of the gamma indices for the phantom and patient calculations are summarized in Table 8.1. The values of $\gamma_{mean}$ for the analytical calculations are consistently lower compared to TG-43, indicating a better general agreement with MC calculations.

Table 8.1. 3D gamma statistics for the analytical and TG-43 calculations in phantom and patient geometries. The reference dose distributions are calculated using PTRAN_CT. Voxels assigned as air or contrast solution are excluded in the statistics.

| Calculation | $\gamma_{mean}$ | | $\gamma_{1\%}$ | | $P_{\gamma\leq1}$ (%) | |
|---|---|---|---|---|---|---|
| | Analytical | TG-43 | Analytical | TG-43 | Analytical | TG-43 |
| Phantom with tissue inserts | 0.08 | 0.42 | 0.35 | 0.85 | 99.9 | 99.6 |
| Phantom with tissue and lead inserts | 0.05 | 0.51 | 0.50 | 6.25 | 100.0 | 90.7 |
| Head-and-neck patient | 0.17 | 0.30 | 0.70 | 1.03 | 99.7 | 98.9 |
| Esophagus patient | 0.13 | 0.24 | 0.52 | 0.51 | 99.6 | 99.7 |
| Breast patient | 0.18 | 1.06 | 0.63 | 2.11 | 100.0 | 48.3 |

### 8.3.3. *Phantom studies*

*i.* *Phantom with tissue material inserts*

Figures 8.5(a)–8.5(c) show the first phantom calculation results. The TG-43 dose is higher and the overestimate becomes increasingly obvious near the phantom surface. A better agreement is seen after applying the SC method despite the higher density (1.06 g/cm$^3$) of this soft tissue phantom. The dose is nearly unperturbed by the adipose and spongiosa inserts. Below the 30% isodose level, the SC dose is lower by up to 15% behind the lung insert and higher by up to 17% behind the cortical bone. The analytical method underestimates the dose behind the lung insert by up to 7%, but is otherwise in agreement with the MC calculation within 3%.

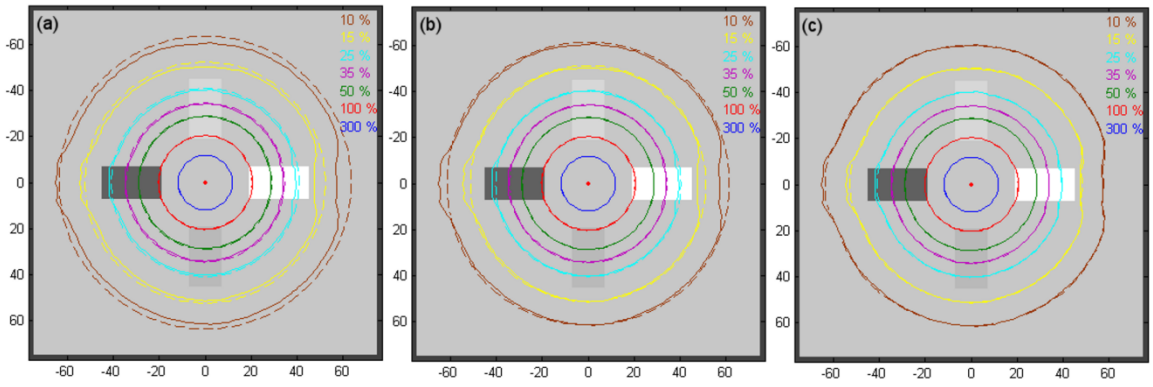


Figure 8.5. Isodose distributions around an HDR $^{192}$Ir source in a soft tissue phantom with four tissue inserts. The MC isodose is shown in all panels in solid lines. The dashed isodose distributions are calculated using (a) TG-43, (b) scatter correction method, and (c) analytical method.

The primary and scatter dose distributions calculated by the analytical method are compared to the corresponding MC distributions in Figures 8.6(a)–8.6(b). The primary dose distributions agree better than 2%. However, the analytical method underestimates the scatter dose behind the lung insert by up to 20% and slightly overestimates the dose around it. The reverse happens on a smaller scale around the cortical bone, and the

maximum scatter dose error is 7%. The differences demonstrate that the analytical method cannot account for the lateral scatter near regions of markedly lower or higher densities. Nonetheless, the total dose error is smaller and $P_{\gamma\leq1}$=99.9% because the primary dose predominates.

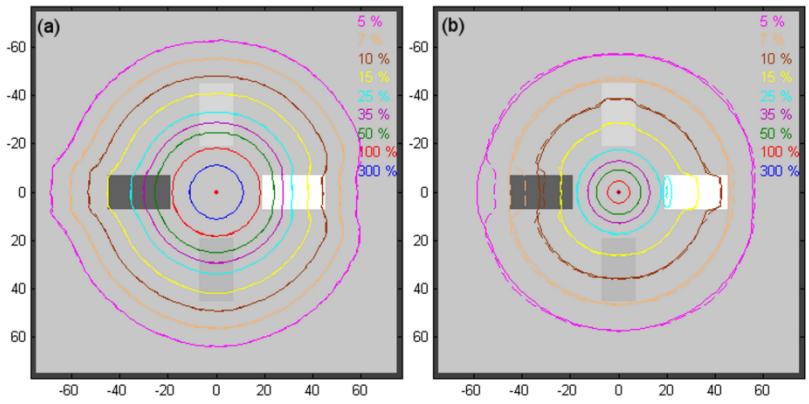


Figure 8.6. (a) Primary and (b) scatter components of the isodose distributions around an HDR $^{192}$Ir source in a soft tissue phantom with four tissue inserts. In both panels, the solid isodose lines are MC calculations, and the dashed lines are analytical calculations.

*ii.* *Phantoms with tissue and shielding inserts*

Figure 8.7(a) illustrates tissue inhomogeneity effects near lead shielding. The analytical method, which uses precalculated 3D dose data to account for shielding perturbations, is able to partially correct for such effects [see Figure 8.7(b)]. As it neglects the lateral scatter altered by the tissue inserts, there are small local differences of up to 5% and 10% behind the lung and cortical bone regions on the shielded side, respectively. The differences occur in the low-dose region and $P_{\gamma\leq1}$=100.0%.

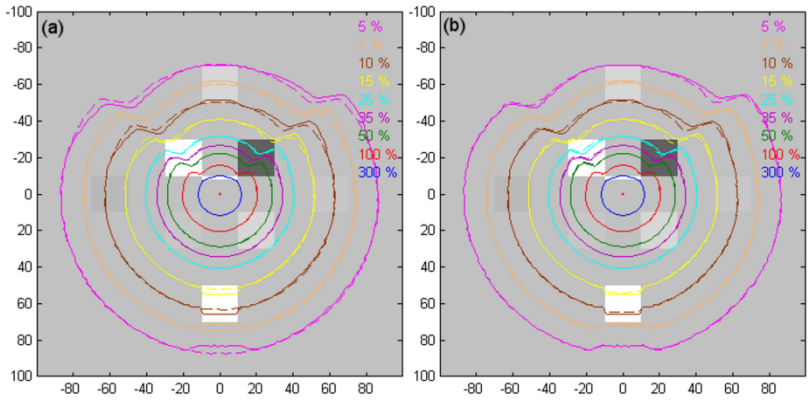


Figure 8.7. Isodose distributions around an HDR $^{192}$Ir source in a water phantom with lead and tissue inserts. The MC isodose is in solid lines in both panels. The dashed lines in (a) represent the MC isodose which only includes shielding effects. The dashed lines in (b) represent the isodose calculated by the analytical method.

The total, primary, and scatter dose components of the MC calculations are compared to the analytical results in Figures 8.8(a)–8.8(c). In this particular analytical calculation, we corrected for both shielding and tissue inhomogeneity effects via ray tracing. Since lead absorbs more of the lower energy photons and yet a constant value is used for $\bar{\mu}/\rho_{\text{prim}}$, the primary dose is underestimated by up to 18%. The method also fails to predict the increase in the SPR behind the lead, because the increased importance of photoelectric effect invalidates the determination of the SPR ratio based on $\text{SPR}_{\text{wat}}$ and density scaling [1]. The values of $\gamma_{\text{mean}}$, $\gamma_{1\%}$, and $P_{\gamma\leq 1}$ are 0.36, 3.70, and 90.9%, respectively. The improved Siddon algorithm was used here because the phantom contains a lead insert, and our ray tracing method will cause discretization artifacts [see Figure 8.8(d)]. Nonetheless, the isodose lines for both ray tracing methods are indistinguishable on the unshielded side because the $^{192}$Ir spectrum, $f_{\text{scat}}$, and SPR ratios vary slowly over the sampling interval for lower-$Z$ media. The efficiency gain over the improved Siddon method is sevenfold when calculating the dose in 153×153×128 voxels.

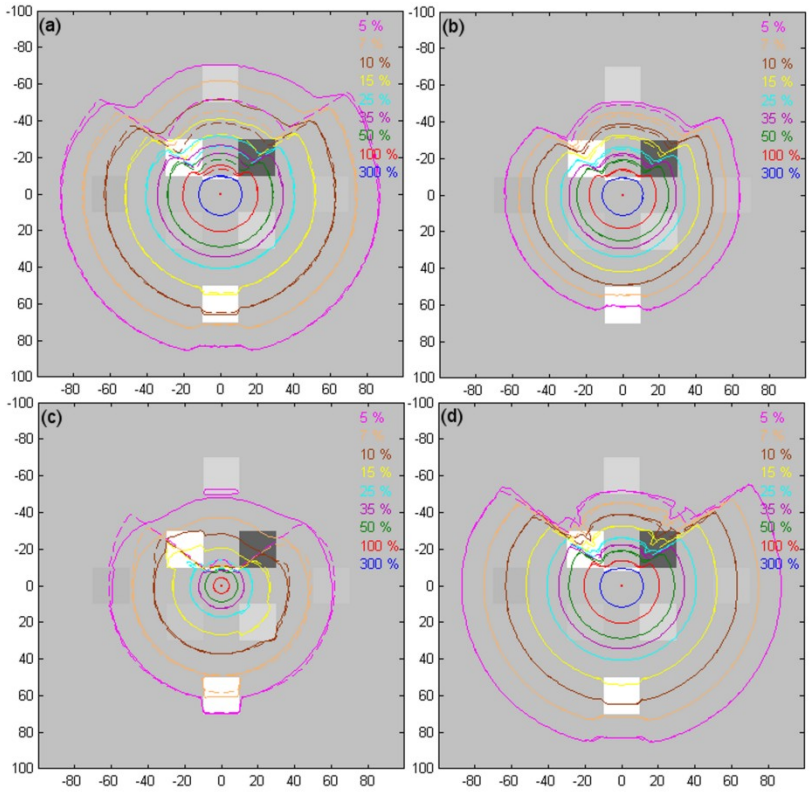


Figure 8.8. Isodose distributions around an HDR $^{192}$Ir source in a water phantom with lead and tissue inserts. The (a) total, (b) primary, and (c) scatter components of the dose calculated by the MC method (solid lines) are compared to the analytical results. In this analytical calculation, the improved Siddon algorithm is used to correct for both shielding and tissue inhomogeneity effects. In (d), the analytical calculation using our proposed ray tracing method (solid lines) is compared to the calculation using the improved Siddon method (dashed lines).

### 8.3.4. *Patient studies*

#### *i.* *Head-and-neck cancer patient*

The isodose, axial $\gamma_{MIP}$ image, and dose-volume histogram (DVH) comparisons for the head-and-neck patient calculations are shown in Figures 8.9(a)–8.9(f). The isodose lines above 50% of $D_{ref}$ for all calculations are practically the same because the inverse square law has a greater dosimetric impact than tissue inhomogeneity effects in the near-source region. The gamma indices for voxels of <2 mm from the dwell positions apply to

a steep dose-gradient region and their values are above unity, but such differences may not be clinically important. As the primary dose predominates, the target coverage is immune to the influence of scatter despite its proximity to the skin, nasal cavities, and bones. The TG-43 dose is higher near the skin, while the analytical and MC results are in better agreement. TG-43 also slightly overestimates the dose to the brain stem, which is lightly screened by bones. The DVHs show that the three methods are comparable in predicting the dose to organs at risk (OARs).

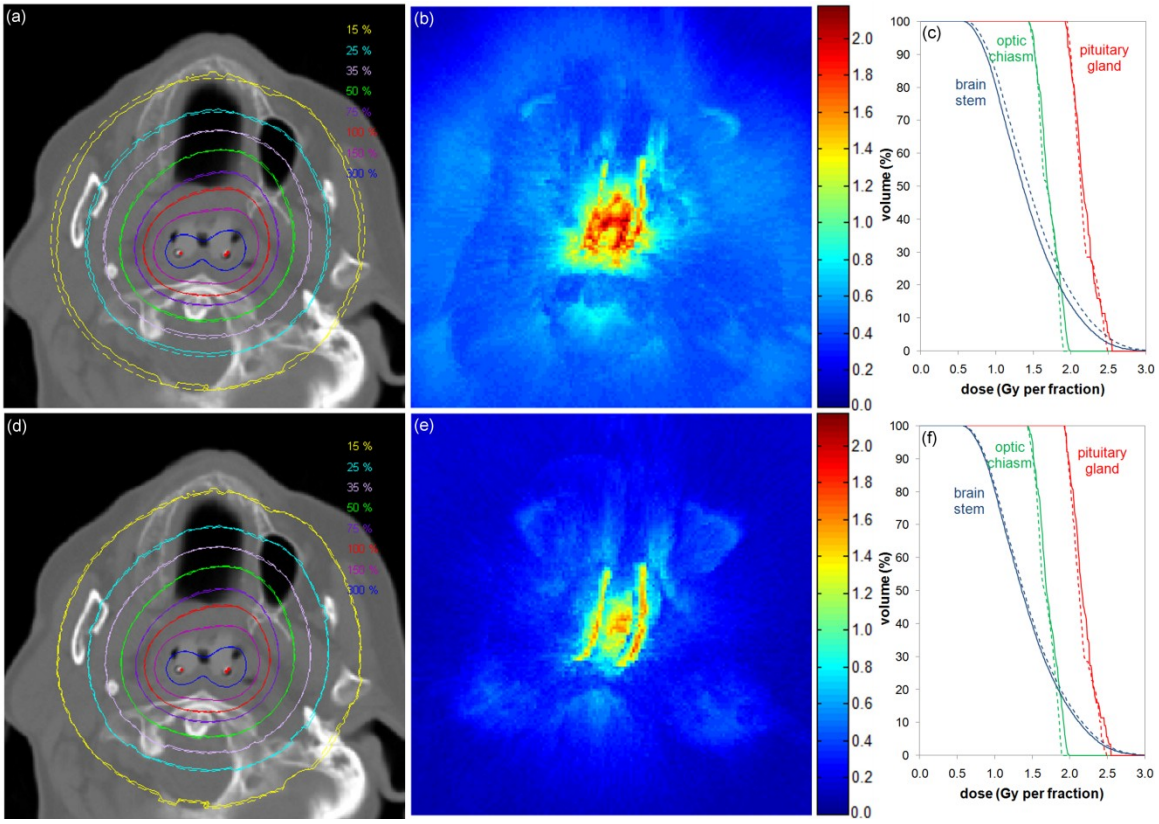


Figure 8.9. Isodose distributions, axial $\gamma_{MIP}$, and OAR DVHs for a head-and-neck patient plan. The isodose distributions are normalized to the $D_{ref}$ of 6 Gy/fraction. In the upper panels, MC (solid lines) and TG-43 (dashed lines) calculations are compared. The lower panels compare the MC (solid lines) and analytical (dashed lines) calculations.

*ii.* *Esophagus cancer patient*

Figures 8.10(a)–8.10(f) show the calculation results for the esophageal patient plan. Changes in the scatter conditions caused by the lung and spinal cord are somewhat localized. Even though the slight discrepancy around the lung cannot be resolved by analytical means, there is close agreement in the OAR DVHs. Our results are similar to those of Anagnostopoulos et al. [32] who developed their own analytical algorithm [1, 33]. They used MC and analytical methods to calculate an esophagus treatment plan with a phantom that mimics the upper thorax.

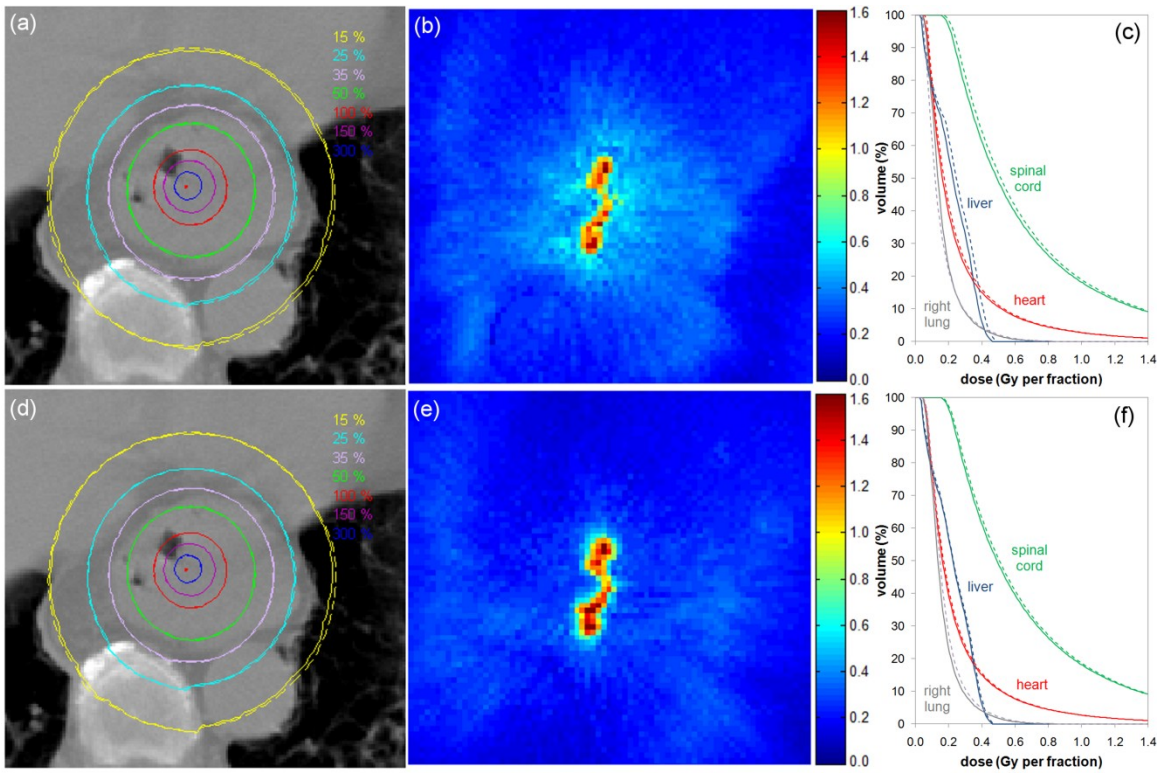


Figure 8.10. Isodose distributions, axial $\gamma_{MIP}$, and OAR DVHs for an esophageal patient plan. The isodose distributions are normalized to the $D_{ref}$ of 5 Gy/fraction. In the upper panels, MC (solid lines) and TG-43 (dashed lines) calculations are compared. The lower panels compare MC (solid lines) and analytical (dashed lines) calculations.

*iii.* *Breast cancer patient*

The MammoSite patient calculations in Figures 8.11(a)–8.11(f) show a larger discrepancy between the TG-43 and MC calculations. Since the target is >2 cm away from the $^{192}$Ir source, the scatter dose contribution is more important compared to the other two patient cases. Also, the balloon applicator pushes the target closer to the skin where the photon backscatter is reduced. Furthermore, the contrast solution causes more photon attenuation.

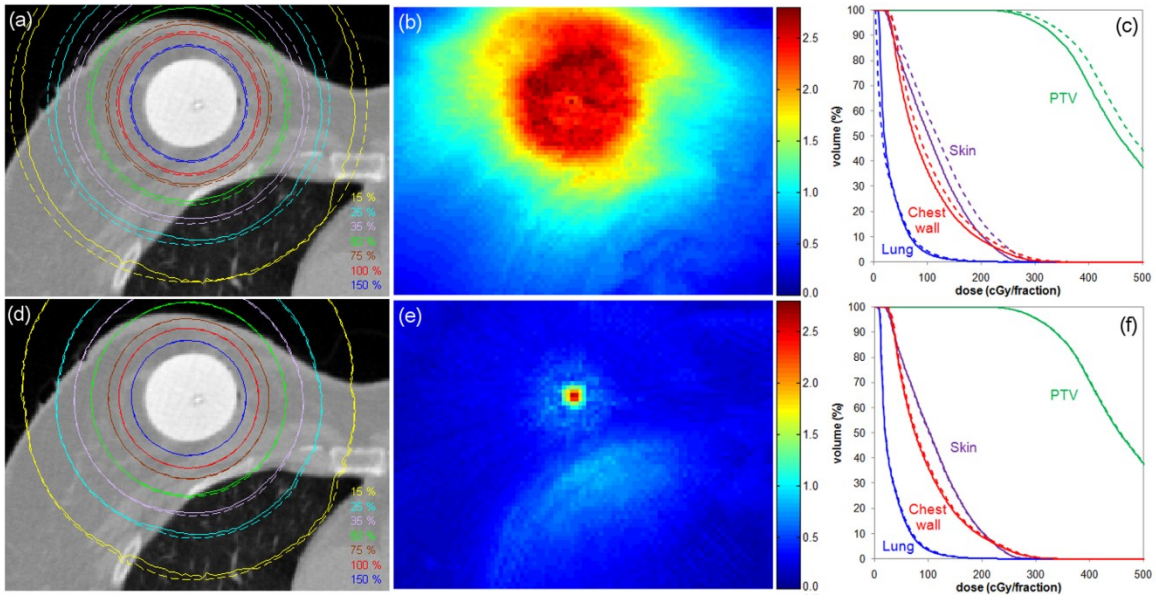


Figure 8.11. Isodose distributions, axial $\gamma_{MIP}$, and DVHs for a MammoSite breast patient plan. The isodose distributions are normalized to the $D_{ref}$ of 3.4 Gy/fraction. In the upper panels, MC (solid lines) and TG-43 (dashed lines) calculations are compared. The lower panels compare MC (solid lines) and analytical (dashed lines) calculations.

Table 8.2 shows the dose-volume indices for the target, skin, ipsilateral lung, and chest wall. TG-43 overestimates the dose to all structures by ≥5%. The errors are reduced by the SC method. The analytical method further improves the accuracy, although small differences are seen around the lung. For the $MC_{den}$ calculation, the scatter dose is overestimated while the primary beam hardening has minimal effects. The high-dose

volumes (target $V_{150}$ and $V_{200}$) are larger, and the dose to OAR is higher by 2%. Previous MC studies [34-36] corroborate our finding that making adjustments for density variations alone is not enough to correct for the attenuation effects of contrast solution. A phantom study by Ye et al.[34] shows that contrast solution may reduce the dose by 1.0%–4.8%, depending on its concentration. The total dose error ranges from 4% to 10% when the smaller backscatter near the skin is also neglected [34].

Table 8.2. Dose-volume indices for MammoSite breast patient calculations.

| Structure | Dose-volume index | MC | ratio | | | |
|---|---|---|---|---|---|---|
| | | | TG-43 / MC | SC / MC | analytic / MC | $MC_{den}$ / MC |
| Target | $D_{90}$ (%) | 97.9 | 1.06 | 1.03 | 1.00 | 1.02 |
| | $D_{100}$ (%) | 59.8 | 1.05 | 1.02 | 1.01 | 1.01 |
| | $V_{90}$ (%) | 94.3 | 1.02 | 1.01 | 1.00 | 1.01 |
| | $V_{100}$ (%) | 88.6 | 1.04 | 1.02 | 1.00 | 1.02 |
| | $V_{150}$ ($cm^3$) | 31.5 | 1.20 | 1.11 | 1.01 | 1.08 |
| | $V_{200}$ ($cm^3$) | 7.0 | 1.40 | 1.25 | 1.02 | 1.18 |
| Skin | $D_{0.1\ cc}$ (%) | 81.1 | 1.09 | 1.03 | 1.00 | 1.02 |
| | $D_{1\ cc}$ (%) | 73.3 | 1.10 | 1.02 | 1.00 | 1.02 |
| | $D_{10\ cc}$ (%) | 52.0 | 1.12 | 1.02 | 1.00 | 1.02 |
| Lung | $D_{0.1\ cc}$ (%) | 68.0 | 1.09 | 1.06 | 1.03 | 1.02 |
| | $D_{1\ cc}$ (%) | 59.9 | 1.09 | 1.07 | 1.04 | 1.02 |
| | $D_{10\ cc}$ (%) | 44.5 | 1.09 | 1.06 | 1.04 | 1.02 |
| Chest wall | $D_{0.1\ cc}$ (%) | 94.3 | 1.06 | 1.04 | 1.02 | 1.01 |
| | $D_{1\ cc}$ (%) | 82.7 | 1.07 | 1.04 | 1.02 | 1.02 |
| | $D_{10\ cc}$ (%) | 53.9 | 1.08 | 1.05 | 1.03 | 1.02 |

### 8.3.5. *Calculation efficiency*

The codes for the TG-43 and analytical algorithms were compiled into MATLAB callable C executables using the LCC-WIN32 compiler. We did all calculations on a 2.0 GHz processor running a 32-bit Windows operating system. On average, the analytical method took 3.6 times longer to run than TG-43. Its efficiency depends on the dose grid and is inversely proportional to the number of dwell positions. Typical CPU times range

from 1 s for a MammoSite patient plan to a few minutes for a multicatheter breast patient plan with >200 dwell positions. This is different than the MC method, whose efficiency depends on the scattering volume and is less influenced by the number of dwell positions. Also, the MC CPU time is related to the statistical uncertainties. It could be one to three orders of magnitude slower than the analytical method.

8.3.6. *Algorithm assumptions and limitations*

The analytical algorithm is partly based on the work of Anagnostopoulos et al.[1]. They found that by using $\bar{\mu}/\rho$ and $\left(\bar{\mu}_{\text{en}}/\rho\right)_{\text{wat}}^{\text{med}}$ weighted over the $^{192}$Ir spectrum, one can collectively account for the contributions from every emission line of the polyenergetic source (cf. Ref. [37]) with better than 2% accuracy [1, 33]. In tissue media under full scatter conditions, the approach of Anagnostopoulos et al. to find the SPR by using $\text{SPR}_{\text{wat}}$ and density scaling gives a maximum error of 2% in the total dose [1].

As the makeup of a human body is complex, approximations are used to make dose calculations efficient and applicable for various treatment sites. We make two suppositions in determining $\left(\bar{\mu}/\rho\right)_{\text{scat}}$ and $\left(\bar{\mu}_{\text{en}}/\rho_{\text{scat}}\right)_{\text{wat}}^{\text{med}}$: (1) The scattered photon spectrum at the POI has not been greatly altered by inhomogeneities and (2) the scatter conditions are nearly equivalent to having the POI positioned in a water sphere of radius $d_4$. The latter also applies to the determination of the SPR ratio. Provided shielding is not present, the errors arising from the breakdown of these conditions are small because changes in the $^{192}$Ir spectrum do not strongly influence the dose in tissue materials [6]. Furthermore, the attenuation correction factor depends on the difference between $\bar{\mu}_{\text{scat,med}}$ and $\bar{\mu}_{\text{scat,wat}}$,

which is less error prone than their respective values. Similarly, an error in estimating the scattering medium does not influence the SPR ratio as much as the individual SPR values.

The inability to account for lateral and backscatter radiation near inhomogeneities is a limitation of this analytical method. It manifests itself mainly in scatter dose errors around low density regions such as large air cavities and the lungs. The errors around bones in realistic patient geometries are small. As shown in the patient calculations, this limitation is unlikely to affect the target coverage because the near-source region is dominated by primary dose.

The phantom calculations show that, in principle, using precalculated MC dose data improves the dosimetric accuracy near high-$Z$ materials. We have not demonstrated the technique for patient dose calculations with shielding. Proper material and density segmentations may require corrections of CT metal streaking artifacts [38] as well as dual energy CT imaging [39].

### 8.3.7. *Other dose calculation methods*

The MC method in radiation transport is a well-established approach for accurate dose calculations. Several MC codes [27, 40, 41] allow for efficient simulations of complex brachytherapy seeds together with the patient body derived from CT data. The target dose in low-energy seed implants applications can be calculated in less than 1 min [41]. A longer CPU time is needed for $^{192}$Ir brachytherapy owing to a more gradual energy loss primarily by Compton scattering compared to sources in the low-energy range where the photon mean free paths are shorter [4]. In fact, the CPU time to calculate the dose to the OARs by the MC method could be considerable when low statistical uncertainties are desired. This is particularly so when the organs are a few centimeters away from the

treatment site where the scatter dose becomes important. On the contrary, the efficiency of the analytical method is independent of the scattering volume. The CPU time could be further reduced by only calculating the dose to selected organs. The analytical method is hence more suitable for anatomy-based inverse treatment planning.

The collapsed cone superposition technique is a promising dose calculation method, but the long CPU time for $^{192}$Ir brachytherapy is still an unresolved issue [42-44]. Techniques have also been proposed for tissue inhomogeneity corrections in phantoms of cylindrical symmetry [5] and for scatter dose calculations around inhomogeneities of known dimensions [45-47], but they are not adaptable for CT-based geometries. For brachytherapy of superficial skin lesions that extend over a large region, the SC method alone is faster and can adequately correct for the reduced photon backscatter near the skin [11].

The one-dimensional path length correction method [8, 48] was designed for $^{137}$Cs brachytherapy with a shielded applicator. Since $^{137}$Cs photons are higher in energy, the dose is contributed mostly by primary photon interactions and is unaffected by spectral energy variations. This method is less accurate for $^{192}$Ir applications and therefore we did not use ray tracing to account for shielding effects. As shown in this work and elsewhere [49, 50], dose errors are mainly on the shielded side.

Deterministic approaches of solving the 3D Boltzmann transport equation such as the discrete ordinates method have been investigated for brachytherapy applications [51-53]. Since all geometries are modeled as composites of meshes, ray effects originating from brachytherapy sources and applicators will be noticeable unless small meshes are used. Gifford et al. [53] showed that deterministic transport parameters can be optimized

for a faster calculation speed, but the method has not been applied for CT-based dose calculations yet.

## 8.4. CONCLUSIONS

A correction-based analytical dose calculation algorithm has been developed for HDR $^{192}$Ir brachytherapy to account for the effects of tissue inhomogeneities, shielding, and the reduced photon backscatter near the skin. Although the method neglects the lateral and backscatter around inhomogeneities, it is a major improvement over the TG-43 formalism. It is of interest especially for brachytherapy with a shielded applicator, or breast brachytherapy with a balloon applicator injected with contrast solution.

This work also shows that TG-43 is adequate for $^{192}$Ir treatment planning when shielding and contrast solution are not used. It gives the correct target dose even for treatment sites near the lungs, air cavities, and bones. This is because of the small tissue inhomogeneity effects and the predominance of primary dose in the near-source region.

## 8.5. REFERENCES


1. Anagnostopoulos G, Baltas D, Karaiskos P, Pantelis E, Papagiannis P, Sakelliou L. An analytical dosimetry model as a step towards accounting for inhomogeneities and bounded geometries in $^{192}$Ir brachytherapy treatment planning. Phys Med Biol. 2003;48:1625-47.

2. Williamson JF, Brenner DJ. Physics and biology of brachytherapy. In: Halperin EC, Perez CA, Brady LW, editors. Perez and Brady's principles and practice of radiation oncology. 5th ed. Philadelphia: Wolters Kluwer Health/Lippincott Williams & Wilkins; 2008. p. 423-75.

3. Rivard MJ, Coursey BM, DeWerd LA, Hanson WF, Huq MS, Ibbott GS, et al. Update of AAPM Task Group No. 43 Report: A revised AAPM protocol for brachytherapy dose calculations. Med Phys. 2004;31:633-74.

4. Rivard MJ, Venselaar JLM, Beaulieu L. The evolution of brachytherapy treatment planning. Med Phys. 2009;36:2136-53.

5. Meigooni AS, Nath R. Tissue inhomogeneity correction for brachytherapy sources in a heterogeneous phantom with cylindrical symmetry. Med Phys. 1992;19:401-7.

6. Melhus CS, Rivard MJ. Approaches to calculating AAPM TG-43 brachytherapy dosimetry parameters for $^{137}$Cs, $^{125}$I, $^{192}$Ir, $^{103}$Pd, and $^{169}$Yb sources. Med Phys. 2006;33:1729-37.

7. Williamson JF. Dose calculations about shielded gynecological colpostats. Int J Radiat Oncol Biol Phys. 1990;19:167-78.

8. Williamson JF. The Sievert integral revisited: evaluation and extension to $^{125}$I, $^{169}$Yb, and $^{192}$Ir brachytherapy sources. Int J Radiat Oncol Biol Phys. 1996;36:1239-50.

9. Russell KR, Ahnesjo A. Dose calculation in brachytherapy for a $^{192}$Ir source using a primary and scatter dose separation technique. Phys Med Biol. 1996;41:1007-24.

10. Russell KR, Carlsson Tedgren ÅK, Ahnesjö A. Brachytherapy source characterization for improved dose calculations using primary and scatter dose separation. Med Phys. 2005;32:2739-52.

11. Poon E, Verhaegen F. Development of a scatter correction technique and its application to HDR $^{192}$Ir multicatheter breast brachytherapy. Med Phys. 2009;36:3703-13.

12. Wang R, Li XA. Dose characterization in the near-source region for two high dose rate brachytherapy sources. Med Phys. 2002;29:1678-86.

13. Poon E, Le Y, Williamson JF, Verhaegen F. BrachyGUI: an adjunct to an accelerated Monte Carlo photon transport code for patient-specific brachytherapy dose calculations and analysis. J Phys Conf Ser. 2008;102:012018.

14. Daskalov GM, Loffler E, Williamson JF. Monte Carlo-aided dosimetry of a new high dose-rate brachytherapy source. Med Phys. 1998;25:2200-8.

15. Nuclear data from NuDat 2.0, a web-based database maintained by the National Nuclear Data Center [database on the Internet]. Brookhaven National Laboratory, Upton, NY 2004. Available from: http://www.nndc.bnl.gov/nudat2.

16. International Commission on Radiation Units and Measurements. Tissue substitutes in radiation dosimetry and measurement. Bethesda, MD: ICRU; 1989.

17. International Commission on Radiation Units and Measurements. Photon, electron, proton and neutron interaction data for body tissues. Bethesda, MD: ICRU; 1992.

18. Markman J, Williamson JF, Dempsey JF, Low DA. On the validity of the superposition principle in dose calculations for intracavitary implants with shielded vaginal colpostats. Med Phys. 2001;28:147-55.

19. Poon E, Williamson JF, Vuong T, Verhaegen F. Patient-specific Monte Carlo dose calculations for high-dose-rate endorectal brachytherapy with shielded intracavitary applicator. Int J Radiat Oncol Biol Phys. 2008;72:1259-66.

20. Agostinelli S, Allison J, Amako K, Apostolakis J, Araujo H, Arce P, et al. GEANT4-a simulation toolkit. Nucl Instrum Methods Phys Res A. 2003;506:250-303.

21. Cullen DE, Hubbell JH, Kissel L. EPDL97: The Evaluated Photon Data Library, '97 Version. Livermore, CA: Lawrence Livermore National Laboratory1997. Report No.: UCRL-50400, Rev. 5.

22. Hubbell JH, Seltzer SM. Tables of x-ray mass attenuation coefficients and mass energy-absorption coefficients 1 keV to 20 MeV for elements Z=1 to 92 and 48 additional substances of dosimetric interest. Gaithersburg, MD: National Institute of Standards and Technology 1995. Report No.: NISTIR 5632.

23. Williamson JF. Monte Carlo evaluation of kerma at a point for photon transport problems. Med Phys. 1987;14:567-76.

24. Altschuler MD, Sontag MR, Bloch P. Rapid three-dimensional treatment planning: I. ray-tracing approach to primary component dose calculations. Phys Med Biol. 1987;32:543-56.

25. Jacobs F, Sundermann E, De Sutter B, Christiaens M, Lemahieu I. A fast algorithm to calculate the exact radiological path through a pixel or voxel space. J Comp Inf Technol. 1998;6:89-94.

26. Siddon RL. Fast calculation of the exact radiological path for a three-dimensional CT array. Med Phys. 1985;12:252-5.

27. Le Y, Chibani O, Todor D, Siebers I, Williamson J. An integrated CT-based Monte Carlo dose-evaluation system for brachytherapy and its application to permanent prostate implant postprocedure dosimetric analysis. Med Phys. 2005;32:2068.

28. Williamson JF. Comparison of measured and calculated dose rates in water near I-125 and Ir-192 seeds. Med Phys. 1991;18:776-86.

29. Radiation Safety Information Computational Center. HUGO-VI: Photon Interaction Data in ENDF/B-VI Format. Oak Ridge, TN Oak Ridge National Laboratory; 1989.

30. Wendling M, Zijp LJ, McDermott LN, Smit EJ, Sonke JJ, Mijnheer BJ, et al. A fast algorithm for gamma evaluation in 3D. Med Phys. 2007;34:1647-54.

31. Edmundson GK, Vicini FA, Chen PY, Mitchell C, Martinez AA. Dosimetric characteristics of the MammoSite RTS, a new breast brachytherapy applicator. Int J Radiat Oncol Biol Phys. 2002;52:1132-9.

32. Anagnostopoulos G, Baltas D, Pantelis E, Papagiannis P, Sakelliou L. The effect of patient inhomogeneities in oesophageal $^{192}$Ir HDR brachytherapy: a Monte Carlo and analytical dosimetry study. Phys Med Biol. 2004;49:2675-85.

33. Pantelis E, Papagiannis P, Anagnostopoulos G, Baltas D, Karaiskos P, Sandilos P, et al. Evaluation of a TG-43 compliant analytical dosimetry model in clinical $^{192}$Ir HDR brachytherapy treatment planning and assessment of the significance of source position and catheter reconstruction uncertainties. Phys Med Biol. 2004;49:55-67.

34. Ye SJ, Brezovich IA, Shen S, Kim S. Dose errors due to inhomogeneities in balloon catheter brachytherapy for breast cancer. Int J Radiat Oncol Biol Phys. 2004;60:672-7.

35. Kirk MC, Hsi WC, Chu JC, Niu H, Hu Z, Bernard D, et al. Dose perturbation induced by radiographic contrast inside brachytherapy balloon applicators. Med Phys. 2004;31:1219-24.

36. Papagiannis P, Karaiskos P, Georgiou E, Baltas D, Lymperopoulou G, Pantelis E, et al. On the use of high dose rate $^{192}$Ir and $^{169}$Yb sources with the MammoSite radiation therapy system. Med Phys. 2007;34:3614-9.

37. Daskalov GM, Kirov AS, Williamson JF. Analytical approach to heterogeneity correction factor calculation for brachytherapy. Med Phys. 1998;25:722-35.

38. Bazalova M, Beaulieu L, Palefsky S, Verhaegen F. Correction of CT artifacts and its influence on Monte Carlo dose calculations. Med Phys. 2007;34:2119-32.

39. Bazalova M, Carrier JF, Beaulieu L, Verhaegen F. Tissue segmentation in Monte Carlo treatment planning: a simulation study using dual-energy CT images. Radiother Oncol. 2008;86:93-8.

40. Taylor RE, Yegin G, Rogers DW. Benchmarking BrachyBose: voxel based EGSnrc Monte Carlo calculations of TG-43 dosimetry parameters. Med Phys. 2007;34:445-57.

41. Chibani O, Williamson JF. MCPI: a sub-minute Monte Carlo dose calculation engine for prostate implants. Med Phys. 2005;32:3688-98.

42. Carlsson ÅK, Ahnesjö A. The collapsed cone superposition algorithm applied to scatter dose calculations in brachytherapy. Med Phys. 2000;27:2320-32.

43. Carlsson Tedgren ÅK, Ahnesjö A. Accounting for high Z shields in brachytherapy using collapsed cone superposition for scatter dose calculation. Med Phys. 2003;30:2206-17.

44. Carlsson Tedgren Å, Ahnesjö A. Optimization of the computational efficiency of a 3D, collapsed cone dose calculation algorithm for brachytherapy. Med Phys. 2008;35:1611-8.

45. Kirov AS, Williamson JF. Two-dimensional scatter integration method for brachytherapy dose calculations in 3D geometry. Phys Med Biol. 1997;42:2119-35.

46. Wang R, Sloboda RS. Brachytherapy scatter dose calculation in heterogeneous media: I. a microbeam ray-tracing method for the single-scatter contribution. Phys Med Biol. 2007;52:5619-36.

47. Wang R, Sloboda RS. Brachytherapy scatter dose calculation in heterogeneous media: II. empirical formulation for the multiple-scatter contribution. Phys Med Biol. 2007;52:5637-54.

48. Meertens H, van der Laarse R. Screens in ovoids of a Selectron cervix applicator. Radiother Oncol. 1985;3:69-80.

49. Kirov AS, Williamson JF, Meigooni AS, Zhu Y. Measurement and calculation of heterogeneity correction factors for an Ir-192 high dose-rate brachytherapy source behind tungsten alloy and steel shields. Med Phys. 1996;23:911-9.

50. Lymperopoulou G, Pantelis E, Papagiannis P, Rozaki-Mavrouli H, Sakelliou L, Baltas D, et al. A Monte Carlo dosimetry study of vaginal $^{192}$Ir brachytherapy applications with a shielded cylindrical applicator set. Med Phys. 2004;31:3080-6.

51. Daskalov GM, Baker RS, Rogers DW, Williamson JF. Dosimetric modeling of the microselectron high-dose rate $^{192}$Ir source by the multigroup discrete ordinates method. Med Phys. 2000;27:2307-19.

52. Gifford KA, Horton JL, Wareing TA, Failla G, Mourtada F. Comparison of a finite-element multigroup discrete-ordinates code with Monte Carlo for radiotherapy calculations. Phys Med Biol. 2006;51:2253-65.

53. Gifford KA, Price MJ, Horton JL, Jr., Wareing TA, Mourtada F. Optimization of deterministic transport parameters for the calculation of the dose distribution around a high dose-rate $^{192}$Ir brachytherapy source. Med Phys. 2008;35:2279-85.

# Chapter Nine

# Conclusions



## 9.1. SUMMARY

In this thesis, we addressed the main issues affecting the dose calculation accuracy for HDR $^{192}$Ir brachytherapy. BrachyGUI, an integrated software environment with treatment planning and dose evaluation capabilities, was developed for use in patient-specific dosimetric studies. The perturbation effects of a shielded endorectal applicator with iodine contrast solution were investigated using the GEANT4 MC code as well as ionization chamber and radiochromic film measurements. A CT-based MC dose calculation study was carried out for 40 endorectal treatment plans using PTRAN_CT. As well, we used the primary and scatter dose separation approach to evaluate tissue inhomogeneity effects and to examine how the lack of full photon backscatter affected the dose in the vicinity of tissue-air interfaces. Finally, we proposed a robust scatter correction technique and a fast analytical CT-based dose calculation algorithm, both of which were benchmarked against MC calculations.

### 9.1.1. *Development of BrachyGUI*

BrachyGUI, a MATLAB-based multi-purpose treatment planning tool, was developed and extensively used in this work. It can process DICOM-RT patient data and convert CT images to mass density and material data, streamlining the generation of PTRAN_CT input files for CT-based MC dose calculations. The dose calculation algorithms we proposed for HDR $^{192}$Ir brachytherapy were also integrated into BrachyGUI. Its dose evaluation and comparison tools are useful for both brachytherapy and external beam radiotherapy applications.

### 9.1.2. *Dosimetric study of an endorectal applicator*

We evaluated the dosimetric properties of an eight-channel silicone endorectal applicator for HDR-EBT treatment. Its central cavity allows for the insertion of an 8-mm-diameter shielding rod, which helps to spare the normal tissue contralateral to the target. GEANT4 calculations, as confirmed by ionization chamber measurements in a Lucite phantom, showed that the dose on the side opposite the source can be reduced by up to 85% for tungsten shielding, and 80% for lead. GEANT4 dose distributions around the shielded and unshielded applicators for two source configurations agreed with GAFCHROMIC EBT film measurements in water within experimental uncertainties. Also, the applicator can be inserted into an endocavitary balloon. When it is injected with undiluted contrast solution instead of water, the normal tissue dose may be reduced by an additional 8%. In this work, we validated a phase space source model for MC primary photon generation. The HDR source geometry does not need to be simulated when using a phase space source. We also demonstrated that the high spatial resolution and minimal energy dependence of EBT film make it a useful tool for $^{192}$Ir brachytherapy dosimetry.

### 9.1.3. *CT-based MC dose calculations for endorectal brachytherapy patients*

A retrospective MC dose calculation study was performed on 40 HDR-EBT patients treated with the endorectal applicator. We found that shielding reduced the target dose coverage by 3% on average, since the target was partially shielded in some patient plans. Also, accurate applicator localization is important, as ±2.5 mm longitudinal and ±15° rotational shifts in the dwell positions reduced the target dose by 3–4%. Tissue inhomogeneity effects were found to be small, except for the local differences of the order of 20% in cortical bone at low doses. Our results justify using an applicator-based dose superposition method for treatment planning, whose efficiency is about the same as that of TG-43. On the other hand, it is not yet feasible to calculate a CT-based HDR $^{192}$Ir treatment plan within a few minutes on a single computer with the MC method, as opposed to the cases with $^{103}$Pd or $^{125}$I sources [1, 2]. Nevertheless, the integrated software system developed in this work simplifies patient-specific dose calculations and will also be of interest for brachytherapy with lower-energy sources.

### 9.1.4. *Proposed dose calculation approach for HDR $^{192}$Ir brachytherapy*

It is well established that the scatter environment has an important influence on the dose in brachytherapy. However, the TG-43 formalism cannot account for the reduced photon backscatter near the skin. We developed a robust scatter correction technique that scales the scatter dose by a MC-derived factor based upon the distances between the dwell position, the body contour, and the point of interest. It was validated for multicatheter breast brachytherapy in which the doses to the target and the skin for 18 patients agreed with MC calculations within 1%. The algorithm takes 50% longer to run than TG-43, and works well provided the effects of internal inhomogeneities are minimal.

We developed a correction-based analytical method for CT-based HDR $^{192}$Ir dose calculations, partly based upon the previous work of Anagnostopoulos et al. [3]. In our method, the primary and scatter dose rates are first calculated assuming the source is in an infinite water phantom. The effects of high-Z shielding, if they are present, are also accounted for in this step using precalculated MC dose distributions. Next, we perform ray tracing to correct for low- or medium-*Z* inhomogeneity effects analytically. Lastly, our scatter correction technique is used to correct for the absence of full scatter conditions in the patient body. The algorithm was validated by PTRAN_CT calculations on phantom and patient geometries. We found that the effects of lateral scatter near regions of markedly higher or lower densities cannot be estimated correctly, and yet this limitation is unlikely to affect the target dose because the primary dose predominates in the near-source region. While the analytical method took 3.6 times longer to run than TG-43, it is a major improvement over TG-43 and is still sufficiently fast for use in clinical settings.

9.1.5. *Adequacy of contemporary TG-43-based treatment planning*

Our work confirmed previous investigations [4, 5] that tissue inhomogeneity effects for $^{192}$Ir brachytherapy are small in general. Because of the predominance of Compton scattering, the dose is relatively independent of tissue-composition variations. The water-based TG-43 formalism is therefore sufficiently accurate for target dose estimation, even when it is surrounded by the lungs or bone since the scatter contribution is small in the vicinity of the dwell positions. Its accuracy is most affected when contrast solution or high-Z shielding is present, or when the treatment site is near tissue-air interfaces where the backscatter radiation is reduced.

## 9.2. OUTLOOK AND FUTURE WORK

The analytical dose calculation method proposed by us is specific for $^{192}$Ir brachytherapy. It assumes that the scatter-to-primary dose ratio in the patient geometry can be estimated by density scaling. It also assumes that the energy spectrum of the scattered photons will not be greatly altered by tissue inhomogeneities. These two assumptions, while generally valid for $^{192}$Ir photons, break down at lower energies due to the increased importance of photoelectric effect. Therefore, we anticipate that accurate patient-specific treatment planning for low- and intermediate-energy sources will be done using more sophisticated algorithms such as the collapsed cone superposition, discrete ordinates, or MC methods, as discussed in Chapter 3.

Because of the high efficiency of our analytical method, it is feasible to apply it for anatomy-based treatment planning optimization. It may be incorporated in algorithms such as IPSA [6], a commercially available simulated annealing inverse planning technique that currently uses TG-43 for dose computation. On the other hand, it is important to derive the correct tissue material from CT Hounsfield units for patient-specific dose calculations. This can be done more accurately using dual-energy CT imaging [7, 8]. When shielding is present, metal artefact correction algorithms [9] will be useful as well. Finally, it will be of interest to incorporate deformable image registration capabilities in BrachyGUI to study the dosimetric effects of organ deformations introduced by the applicator insertion process for different treatment fractions [10].

## 9.3. REFERENCES


1. Chibani O, Williamson JF. MCPI: a sub-minute Monte Carlo dose calculation engine for prostate implants. Med Phys. 2005;32:3688-98.

2. Thomson RM, Taylor RE, Rogers DW. Monte Carlo dosimetry for $^{125}$I and $^{103}$Pd eye plaque brachytherapy. Med Phys. 2008;35:5530-43.

3. Anagnostopoulos G, Baltas D, Karaiskos P, Pantelis E, Papagiannis P, Sakelliou L. An analytical dosimetry model as a step towards accounting for inhomogeneities and bounded geometries in $^{192}$Ir brachytherapy treatment planning. Phys Med Biol. 2003;48:1625-47.

4. Meigooni AS, Nath R. Tissue inhomogeneity correction for brachytherapy sources in a heterogeneous phantom with cylindrical symmetry. Med Phys. 1992;19:401-7.

5. Melhus CS, Rivard MJ. Approaches to calculating AAPM TG-43 brachytherapy dosimetry parameters for $^{137}$Cs, $^{125}$I, $^{192}$Ir, $^{103}$Pd, and $^{169}$Yb sources. Med Phys. 2006;33:1729-37.

6. Lessard E, Pouliot J. Inverse planning anatomy-based dose optimization for HDR-brachytherapy of the prostate using fast simulated annealing algorithm and dedicated objective function. Med Phys. 2001;28:773-9.

7. Bazalova M, Carrier JF, Beaulieu L, Verhaegen F. Tissue segmentation in Monte Carlo treatment planning: a simulation study using dual-energy CT images. Radiother Oncol. 2008;86:93-8.

8. Johnson TR, Krauss B, Sedlmair M, Grasruck M, Bruder H, Morhard D, et al. Material differentiation by dual energy CT: initial experience. Eur Radiol. 2007;17:1510-7.

9. Bazalova M, Beaulieu L, Palefsky S, Verhaegen F. Correction of CT artifacts and its influence on Monte Carlo dose calculations. Med Phys. 2007;34:2119-32.

10. Christensen GE, Carlson B, Chao KS, Yin P, Grigsby PW, Nguyen K, et al. Image-based dose planning of intracavitary brachytherapy: registration of serial-imaging studies using deformable anatomic templates. Int J Radiat Oncol Biol Phys. 2001;51:227-43.

# Appendix I

## List of Abbreviations and Symbols

| | |
|---|---|
| AAPM | American Association of Physicists in Medicine |
| Bq | becquerel, unit of activity (1 Bq = 1 $s^{-1}$) |
| CPE | charged particle equilibrium |
| CT | computed tomography |
| CTV | clinical target volume |
| CN | conformation number |
| DHI | dose homogeneity index |
| DICOM | Digital Imaging and Communications in Medicine |
| $D_m$ | absorbed dose to medium |
| $D_n$ | minimum dose received by $n$% of the structure |
| $D_{ref}$ | prescribed or reference dose |
| DVH | dose-volume histogram |
| $D_w$ | absorbed dose to water |
| EI | external volume index |
| $F(r,\theta)$ | anisotropy function |
| $f_{scat}$ | scatter correction factor |

| | |
|---|---|
| g(*r*) | radial dose function |
| Gy | gray, unit of absorbed dose (1 Gy = 1 J $kg^{-1}$) |
| HDR | high dose rate |
| HDR-EBT | high-dose-rate endorectal brachytherapy |
| HU | Hounsfield Unit |
| HVL | Half value layer |
| ICRU | International Commission on Radiation Units and Measurements |
| IPSA | inverse planning simulated annealing |
| kerma | kinetic energy released per unit mass |
| $\Lambda$ | dose-rate constant |
| LDR | low dose rate |
| LET | linear energy transfer |
| MC | Monte Carlo |
| MDR | medium dose rate |
| netOD | net optical density |
| OAR | organ at risk |
| OER | oxygen enhancement ratio |
| PHSP | phase space |
| POI | point of interest |
| PDR | pulsed dose rate |
| PTV | planning target volume |

| | |
|---|---|
| RBE | relative biological effectiveness |
| SC | scatter correction |
| SDS | single-dwell superposition |
| $S_K$ | air-kerma strength |
| SPR | scatter-to-primary dose ratio |
| terma | total energy released per unit mass |
| TCP | tumor control probability |
| TG | Task Group |
| TLD | thermoluminescent dosimeter |
| TLE | track length estimator |
| $\mu/\rho$ | mass attenuation coefficient |
| $\mu_{en}/\rho$ | mass energy absorption coefficient |
| U | unit of air-kerma strength (1 U = 1 μGy $m^{-2}$ $h^{-1}$ or 1 cGy $cm^2$ $h^{-1}$) |
| ULDR | ultra-low dose rate |
| $V_n$ | volume of the structure receiving at least $n$% of the prescribed dose |
| $Z$ | atomic number |

# Bibliography


Afsharpour H, D'Amours M, Coté B, Carrier JF, Verhaegen F, Beaulieu L. A Monte Carlo study on the effect of seed design on the interseed attenuation in permanent prostate implants. Med Phys. 2008;35:3671-81.

Agostinelli S, Allison J, Amako K, Apostolakis J, Araujo H, Arce P, et al. GEANT4-a simulation toolkit. Nucl Instrum Methods Phys Res A. 2003;506:250-303.

Ahnesjö A. Collapsed cone convolution of radiant energy for photon dose calculation in heterogeneous media. Med Phys. 1989;16:577-92.

Ahnesjö A, Andreo P, Brahme A. Calculation and application of point spread functions for treatment planning with high energy photon beams. Acta Oncol. 1987;26:49-56.

Aird E. Sources in brachytherapy. In: Joslin CAF, Flynn A, Hall EJ, editors. Principles and practice of brachytherapy: using afterloading systems. London: Arnold; 2001. p. 3-10.

Alterovitz R, Lessard E, Pouliot J, Hsu IC, O'Brien JF, Goldberg K. Optimization of HDR brachytherapy dose distributions using linear programming with penalty costs. Med Phys. 2006;33:4012-9.

Altschuler MD, Sontag MR, Bloch P. Rapid three-dimensional treatment planning: I. ray-tracing approach to primary component dose calculations. Phys Med Biol. 1987;32:543-56.

American Association of Physicists in Medicine. Specification of brachytherapy source strength. New York: American Institute of physics.1987. Report No.: 21.

Anagnostopoulos G, Baltas D, Karaiskos P, Pantelis E, Papagiannis P, Sakelliou L. An analytical dosimetry model as a step towards accounting for inhomogeneities and bounded geometries in $^{192}$Ir brachytherapy treatment planning. Phys Med Biol. 2003;48:1625-47.

Anagnostopoulos G, Baltas D, Pantelis E, Papagiannis P, Sakelliou L. The effect of patient inhomogeneities in oesophageal $^{192}$Ir HDR brachytherapy: a Monte Carlo and analytical dosimetry study. Phys Med Biol. 2004;49:2675-85.

Anderson LL. Physical optimization of afterloading techniques. Strahlentherapie. 1985;161:264-9.

Angelopoulos A, Baras P, Sakelliou L, Karaiskos P, Sandilos P. Monte Carlo dosimetry of a new $^{192}$Ir high dose rate brachytherapy source. Med Phys. 2000;27:2521-7.

Angelopoulos A, Perris A, Sakellariou K, Sakelliou L, Sarigiannis K, Zarris G. Accurate Monte Carlo calculations of the combined attenuation and build-up factors, for energies (20-1500 keV) and distances (0-10 cm) relevant in brachytherapy. Phys Med Biol. 1991;36:763-78.

Armpilia CI, Dale RG, Coles IP, Jones B, Antipas V. The determination of radiobiologically optimized half-lives for radionuclides used in permanent brachytherapy implants. Int J Radiat Oncol Biol Phys. 2003;55:378-85.

Aronowitz JN. Buried emanation: the development of seeds for permanent implantation. Brachytherapy. 2002;1:167-78.

Arslan NC, Geard CR, Hall EJ. Low dose-rate effects of cesium-137 and iodine-125 on cell survival, cell progression, and chromosomal alterations. Am J Clin Oncol. 1986;9:521-6.

Aubry JF, Pouliot J, Beaulieu L. Correction of megavoltage cone-beam CT images for dose calculation in the head and neck region. Med Phys. 2008;35:900-7.

Bahena JH, Martinez A, Yan D, Mele E, Edmunson G, Brown D, et al. Spatial reproducibility of the ring and tandem high-dose rate cervix applicator. Int J Radiat Oncol Biol Phys. 1998;41:13-9.

Ballester F, Granero D, Pérez-Calatayud J, Melhus CS, Rivard MJ. Evaluation of high-energy brachytherapy source electronic disequilibrium and dose from emitted electrons. Med Phys. 2009;36:4250-6.

Baltas D, Karaiskos P, Papagiannis P, Sakelliou L, Loeffler E, Zamboglou N. Beta versus gamma dosimetry close to Ir-192 brachytherapy sources. Med Phys. 2001;28:1875-82.

Baltas D, Kolotas C, Geramani K, Mould RF, Ioannidis G, Kekchidi M, et al. A conformal index (COIN) to evaluate implant quality and dose specification in brachytherapy. Int J Radiat Oncol Biol Phys. 1998;40:515-24.

Baltas D, Sakelliou L, Zamboglou N. The early history of brachytherapy physics. The physics of modern brachytherapy for oncology. Boca Raton: Taylor & Francis; 2007. p. 1-14.

Baltas D, Sakelliou L, Zamboglou N. Production and construction of sealed sources. The physics of modern brachytherapy for oncology. Boca Raton: Taylor & Francis; 2007. p. 185-204.

Baltas D, Sakelliou L, Zamboglou N. Interaction properties of photons and electrons. The physics of modern brachytherapy for oncology. Boca Raton: Taylor & Francis; 2007. p. 87-140.

Barrow HG, Tenenbaum JM, Bolles RC, Wolf HC. Parametric correspondence and chamfer matching: Two new techniques for image matching. 5th International Joint Conference on Artificial Intelligence. Cambridge, MA: Cambridge University; 1977. p. 659-63.

Batten GW. The M. D. Anderson method for the computation of isodose curves around interstitial and intracavitary radiation sources. II. Mathematical and computational aspects. Am J Roentgenol Radium Ther Nucl Med. 1968;102:673-6.

Battermann JJ. Dose rates of the future. In: Mould RF, Battermann JJ, Martinez AA, Speiser BL, editors. Brachytherapy from radium to optimization. Veenendaal: Nucletron International; 1994. p. 385-91.

Bazalova M, Beaulieu L, Palefsky S, Verhaegen F. Correction of CT artifacts and its influence on Monte Carlo dose calculations. Med Phys. 2007;34:2119-32.

Bazalova M, Carrier JF, Beaulieu L, Verhaegen F. Tissue segmentation in Monte Carlo treatment planning: a simulation study using dual-energy CT images. Radiother Oncol. 2008;86:93-8.

Beatty J, Biggs PJ, Gall K, Okunieff P, Pardo FS, Harte KJ, et al. A new miniature x-ray device for interstitial radiosurgery: dosimetry. Med Phys. 1996;23:53-62.

Berger MJ. Energy deposition in water by photons from point isotropic sources. J Nucl Med. 1968:Suppl 1:17-25.

XCOM: photon cross section database (version 1.4) [database on the Internet]. National Institute of Standards and Technology, Gaithersburg, MD. 2009 [cited Apr 28, 2009]. Available from: http://physics.nist.gov/PhysRefData/Xcom/Text/XCOM.html.

Bidmead M, Ingham D. Brachytherapy treatment planning. In: Mayles P, Nahum AE, Rosenwald J-C, editors. Handbook of radiotherapy physics: theory and practice. New York: Taylor & Francis; 2007. p. 1141-80.

Bidmead M, Jones CH. Afterloading equipment for brachytherapy. In: Mayles P, Nahum AE, Rosenwald J-C, editors. Handbook of radiotherapy physics: theory and practice. New York: Taylor & Francis; 2007. p. 1117-29.

Blake P. Clinical introduction to brachytherapy. In: Mayles P, Nahum AE, Rosenwald J-C, editors. Handbook of radiotherapy physics: theory and practice. New York: Taylor & Francis; 2007. p. 1093-9.

Blasko JC, Grimm PD, Sylvester JE, Badiozamani KR, Hoak D, Cavanagh W. Palladium-103 brachytherapy for prostate carcinoma. Int J Radiat Oncol Biol Phys. 2000;46:839-50.

Borg J, Rogers DW. Spectra and air-kerma strength for encapsulated $^{192}$Ir sources. Med Phys. 1999;26:2441-4.

Borgefors G. Hierarchical chamfer matching - a parametric edge matching algorithm. IEEE Transactions on Pattern Analysis and Machine Intelligence. 1988;10:849-65.

Brahme A. Dosimetric precision requirements in radiation therapy. Acta Radiol Oncol. 1984;23:379-91.

Brant WE. Diagnostic imaging methods. In: Brant WE, Helms CA, editors. Fundamentals of diagnostic radiology. 3rd ed. Philadelphia: Lippincott, Williams & Wilkins; 2007. p. 3-26.

Brenner DJ, Hall EJ. Conditions for the equivalence of continuous to pulsed low dose rate brachytherapy. Int J Radiat Oncol Biol Phys. 1991;20:181-90. In: Battermann JJ. Dose rates of the future. In: Mould RF, Battermann JJ, Martinez AA, Speiser BL, editors. Brachytherapy from radium to optimization. Veenendaal: Nucletron International; 1994. p. 385-91.

Brucer M. Brachytherapy. Am J Roentgenol Radium Ther Nucl Med. 1958;79:1080-90.

Büermann L, Kramer HM, Schrader H, Selbach HJ. Activity determination of $^{192}$Ir solid sources by ionization chamber measurements using calculated corrections for self-absorption. Nucl Instrum Methods Phys Res A. 1994;339:369-76.

Burmeister J, Kota C, Maughan RL. Measured microdosimetric spectra and therapeutic potential of boron neutron capture enhancement of $^{252}$Cf brachytherapy. Radiat Res. 2005;164:312-8.

Butson MJ, Cheung T, Yu PK. Weak energy dependence of EBT gafchromic film dose response in the 50 kVp-10 MVp X-ray range. Appl Radiat Isot. 2006;64:60-2.

Cammà C, Giunta M, Fiorica F, Pagliaro L, Craxì A, Cottone M. Preoperative radiotherapy for resectable rectal cancer: A meta-analysis. JAMA. 2000;284:1008-15.

Campbell JM, Wong CO, Muzik O, Marples B, Joiner M, Burmeister J. Early dose response to yttrium-90 microsphere treatment of metastatic liver cancer by a patient-specific method using single photon emission computed tomography and positron emission tomography. Int J Radiat Oncol Biol Phys. 2009;74:313-20.

Canadian Cancer Society's Steering Committee. Canadian Cancer Statistics 2009. Toronto, ON: Canadian Cancer Society; 2009.

Carlsson AK, Ahnesjo A. Point kernels and superposition methods for scatter dose calculations in brachytherapy. Phys Med Biol. 2000;45:357-82.

Carlsson ÅK, Ahnesjö A. The collapsed cone superposition algorithm applied to scatter dose calculations in brachytherapy. Med Phys. 2000;27:2320-32.

Carlsson Tedgren Å, Ahnesjö A. Optimization of the computational efficiency of a 3D, collapsed cone dose calculation algorithm for brachytherapy. Med Phys. 2008;35:1611-8.

Carlsson Tedgren ÅK. Development of dose calculation methods for brachytherapy treatment planning [dissertation]. Stockholm: Stockholm University; 2003.

Carlsson Tedgren ÅK, Ahnesjö A. Accounting for high Z shields in brachytherapy using collapsed cone superposition for scatter dose calculation. Med Phys. 2003;30:2206-17.

Carrier JF, Beaulieu L, Therriault-Proulx F, Roy R. Impact of interseed attenuation and tissue composition for permanent prostate implants. Med Phys. 2006;33:595-604.

Carrier JF, D'Amours M, Verhaegen F, Reniers B, Martin AG, Vigneault E, et al. Postimplant dosimetry using a Monte Carlo dose calculation engine: a new clinical standard. Int J Radiat Oncol Biol Phys. 2007;68:1190-8.

Chang JN, Suh TS, Park SY, Cho KH, Kim S. A dual-energy technique for enhanced localization accuracy in intracavitary brachytherapy. Med Phys. 2005;32:376-9.

Cheng CW, Mitra R, Li XA, Das IJ. Dose perturbations due to contrast medium and air in MammoSite treatment: an experimental and Monte Carlo study. Med Phys. 2005;32:2279-87.

Chetty IJ, Curran B, Cygler JE, DeMarco JJ, Ezzell G, Faddegon BA, et al. Report of the AAPM Task Group No. 105: issues associated with clinical implementation of Monte Carlo-based photon and electron external beam treatment planning. Med Phys. 2007;34:4818-53.

Chibani O. Electron depth dose distributions in water, iron and lead: the GEPTS system. Nucl Instrum Methods Phys Res B. 1995;101:357-78.

Chibani O, Li XA. IVBTMC, a Monte Carlo dose calculation tool for intravascular brachytherapy. Med Phys. 2003;30:44-51.

Chibani O, Williamson JF. MCPI: a sub-minute Monte Carlo dose calculation engine for prostate implants. Med Phys. 2005;32:3688-98.

Chibani O, Williamson JF, Todor D. Dosimetric effects of seed anisotropy and interseed attenuation for $^{103}$Pd and $^{125}$I prostate implants. Med Phys. 2005;32:2557-66.

Chiu-Tsao ST, Schaart DR, Soares CG, Nath R. Dose calculation formalisms and consensus dosimetry parameters for intravascular brachytherapy dosimetry: recommendations of the AAPM Therapy Physics Committee Task Group No. 149. Med Phys. 2007;34:4126-57.

Chow JC, Leung MK. Treatment planning for a small animal using Monte Carlo simulation. Med Phys. 2007;34:4810-7.

Christensen GE, Carlson B, Chao KS, Yin P, Grigsby PW, Nguyen K, et al. Image-based dose planning of intracavitary brachytherapy: registration of serial-imaging studies using deformable anatomic templates. Int J Radiat Oncol Biol Phys. 2001;51:227-43.

Colorectal Cancer Collaborative Group. Adjuvant radiotherapy for rectal cancer: a systematic overview of 8,507 patients from 22 randomised trials. Lancet. 2001;358:1291-304.

Crum WR, Hartkens T, Hill DL. Non-rigid image registration: theory and practice. Br J Radiol. 2004;77 Spec No 2:S140-53.

Cullen DE, Hubbell JH, Kissel L. EPDL97: The Evaluated Photon Data Library, '97 Version. Livermore, CA: Lawrence Livermore National Laboratory1997. Report No.: UCRL-50400, Rev. 5.

Dale RG. Radiobiology of brachytherapy. In: Mayles P, Nahum AE, Rosenwald J-C, editors. Handbook of radiotherapy physics: theory and practice. New York: Taylor & Francis; 2007. p. 1181-91.

Dale RG, Deehan C. Brachytherapy. In: Dale RG, Jones B, editors. Radiobiological modelling in radiation oncology. London: British Institute of Radiology; 2007. p. 113-37.

Daskalov GM, Baker RS, Rogers DW, Williamson JF. Dosimetric modeling of the microselectron high-dose rate $^{192}$Ir source by the multigroup discrete ordinates method. Med Phys. 2000;27:2307-19.

Daskalov GM, Kirov AS, Williamson JF. Analytical approach to heterogeneity correction factor calculation for brachytherapy. Med Phys. 1998;25:722-35.

Daskalov GM, Loffler E, Williamson JF. Monte Carlo-aided dosimetry of a new high dose-rate brachytherapy source. Med Phys. 1998;25:2200-8.

Datta NR, Kumar S, Das KJ, Pandey CM, Halder S, Ayyagari S. Variations of intracavitary applicator geometry during multiple HDR brachytherapy insertions in carcinoma cervix and its influence on reporting as per ICRU report 38. Radiother Oncol. 2001;60:15-24.

Deasy JO, Blanco AI, Clark VH. CERR: a computational environment for radiotherapy research. Med Phys. 2003;30:979-85.

DeMarco JJ, Smathers JB, Burnison CM, Ncube QK, Solberg TD. CT-based dosimetry calculations for $^{125}$I prostate implants. Int J Radiat Oncol Biol Phys. 1999;45:1347-53.

Devic S, Seuntjens J, Sham E, Podgorsak EB, Schmidtlein CR, Kirov AS, et al. Precise radiochromic film dosimetry using a flat-bed document scanner. Med Phys. 2005;32:2245-53.

Devic S, Vuong T, Moftah B. Advantages of inflatable multichannel endorectal applicator in the neo-adjuvant treatment of patients with locally advanced rectal cancer with HDR brachytherapy. J Appl Clin Med Phys. 2005 Spring;6(2):44-9.

Devic S, Vuong T, Moftah B, Evans M, Podgorsak EB, Poon E, et al. Image-guided high dose rate endorectal brachytherapy. Med Phys. 2007;34:4451-8.

Dickler A. Xoft Axxent electronic brachytherapy: a new device for delivering brachytherapy to the breast. Nat Clin Pract Oncol. 2009;6:138-42.

Dickler A, Ivanov O, Francescatti D. Intraoperative radiation therapy in the treatment of early-stage breast cancer utilizing xoft axxent electronic brachytherapy. World J Surg Oncol. 2009;7:24.

Dickler A, Kirk MC, Coon A, Bernard D, Zusag T, Rotmensch J, et al. A dosimetric comparison of Xoft Axxent Electronic Brachytherapy and iridium-192 high-dose-rate brachytherapy in the treatment of endometrial cancer. Brachytherapy. 2008;7:351-4.

Dickler A, Kirk MC, Seif N, Griem K, Dowlatshahi K, Francescatti D, et al. A dosimetric comparison of MammoSite high-dose-rate brachytherapy and Xoft Axxent electronic brachytherapy. Brachytherapy. 2007;6:164-8.

Diffey BL, Klevenhagen SC. An experimental and calculated dose distribution in water around CDC K-type caesium-137 sources. Phys Med Biol. 1975;20:446-54.

Ding GX, Duggan DM, Coffey CW, Shokrani P, Cygler JE. First macro Monte Carlo based commercial dose calculation module for electron beam treatment planning-new issues for clinical consideration. Phys Med Biol. 2006;51:2781-99.

Dinsmore M, Harte KJ, Sliski AP, Smith DO, Nomikos PM, Dalterio MJ, et al. A new miniature x-ray source for interstitial radiosurgery: device description. Med Phys. 1996;23:45-52.

Dogan N, Siebers JV, Keall PJ. Clinical comparison of head and neck and prostate IMRT plans using absorbed dose to medium and absorbed dose to water. Phys Med Biol. 2006;51:4967-80.

Douglas RM, Beatty J, Gall K, Valenzuela RF, Biggs P, Okunieff P, et al. Dosimetric results from a feasibility study of a novel radiosurgical source for irradiation of intracranial metastases. Int J Radiat Oncol Biol Phys. 1996;36:443-50.

Duchemin B, Coursol N. Reevaluation de '$^{192}$Ir, Technical Note LPRI/93/018. France: DAMRI, CEA; 1993. In: Borg J, Rogers DW. Spectra and air-kerma strength for encapsulated $^{192}$Ir sources. Med Phys. 1999;26:2441-4. .

Duncan R. Radium: Its Local Application as a Therapeutic Agent-with Case Reports. Cal State J Med. 1917 Oct;15(10):406-12.

Dutreix J, Tubiana M, Pierquin B. The hazy dawn of brachytherapy. Radiother Oncol. 1998;49:223-32.

Edmundson GK. Volume optimisation: an American viewpoint. In: Mould RF, Battermann JJ, Martinez AA, Speiser BL, editors. Brachytherapy from radium to optimization. Veenendaal: Nucletron International; 1994. p. 314-8.

Edmundson GK, Vicini FA, Chen PY, Mitchell C, Martinez AA. Dosimetric characteristics of the MammoSite RTS, a new breast brachytherapy applicator. Int J Radiat Oncol Biol Phys. 2002;52:1132-9.

Ellett WH. Specific absorbed fractions for photon point sources within a scattering medium. Phys Med Biol. 1969;14:615-26.

Ellis F. History of brachytherapy. In: Williamson JF, Thomadsen BR, Nath R, editors. Brachytherapy physics. Madison, WI: Medical Physics Pub.; 1995. p. 1-6.

Emami B, Lyman J, Brown A, Coia L, Goitein M, Munzenrider JE, et al. Tolerance of normal tissue to therapeutic irradiation. Int J Radiat Oncol Biol Phys. 1991;21:109-22.

Endo M, Tsunoo T, Nakamori N, Yoshida K. Effect of scattered radiation on image noise in cone beam CT. Med Phys. 2001;28:469-74.

Ezzell GA, Luthmann RW. Clinical implementation of dwell time optimization techniques for single stepping-source remote applicators. In: Williamson JF, Thomadsen BR, Nath R, editors. Brachytherapy physics. Madison, WI: Medical Physics Pub.; 1995. p. 617-39.

Fragoso M, Seco J, Nahum AE, Verhaegen F. Incorporation of a combinatorial geometry package and improved scoring capabilities in the EGSnrc Monte Carlo Code system. Med Phys. 2003;30:1076-85.

Furstoss C, Reniers B, Bertrand MJ, Poon E, Carrier JF, Keller BM, et al. Monte Carlo study of LDR seed dosimetry with an application in a clinical brachytherapy breast implant. Med Phys. 2009;36:1848-58.

Furstoss C, Reniers B, Poon E, D'Amours M, Carrier JF, Beaulieu L, et al. Monte Carlo iodine brachytherapy dosimetry: study for a clinical application. J Phys Conf Ser. 2008;102:012011.

Gardner JK, Siebers JV, Kawrakow I. Comparison of two methods to compute the absorbed dose to water for photon beams. Phys Med Biol. 2007;52:N439-47.

Gauwerky F. Short time afterloading curietherapy of gynecological carcinomas: technique and problems [in German]. Strahlentherapie. 1977;153:793-801. In: Williamson JF. Brachytherapy technology and physics practice since 1950: a half-century of progress. Phys Med Biol. 2006;51:R303-25.

Gaze MN. The current status of targeted radiotherapy in clinical practice. Phys Med Biol. 1996;41:1895-903.

GEANT4 Collaboration. Physics Reference Manual 2006. Available from: http://geant4.web.cern.ch/geant4/.

Gerard JP, Chapet O, Nemoz C, Hartweig J, Romestaing P, Coquard R, et al. Improved sphincter preservation in low rectal cancer with high-dose preoperative radiotherapy: the lyon R96-02 randomized trial. J Clin Oncol. 2004;22:2404-9.

Gifford KA, Horton JL, Wareing TA, Failla G, Mourtada F. Comparison of a finite-element multigroup discrete-ordinates code with Monte Carlo for radiotherapy calculations. Phys Med Biol. 2006;51:2253-65.

Gifford KA, Price MJ, Horton JL, Jr., Wareing TA, Mourtada F. Optimization of deterministic transport parameters for the calculation of the dose distribution around a high dose-rate $^{192}$Ir brachytherapy source. Med Phys. 2008;35:2279-85.

Gilchrist TC. A case of dermatitis due to the X rays. Bull Johns Hopkins Hosp. 1897;8:17-22. In: Mould RF. Priority for radium therapy of benign conditions and cancer. Curr Oncol. 2007 Jun;14(3):118-22.

Glasgow GP. Brachytherapy. In: Van Dyk J, editor. The modern technology of radiation oncology: a compendium for medical physicists and radiation oncologists. Madison, WI: Medical Physics Pub.; 1999. p. 695-752.

Glasgow GP, Dillman LT. Specific gamma-ray constant and exposure rate constant of $^{192}$Ir. Med Phys. 1979;6:49-52.

Goodwin PN, Quimby EH, Morgan RH. Dosage with radioactive materials. Physical foundations of radiology. 4th ed. ed. New York; London: Harper & Row; 1970. p. 241-84.

Granero D, Perez-Calatayud J, Ballester F. Technical note: Dosimetric study of a new Co-60 source used in brachytherapy. Med Phys. 2007;34:3485-8.

Granero D, Perez-Calatayud J, Pujades-Claumarchirant MC, Ballester F, Melhus CS, Rivard MJ. Equivalent phantom sizes and shapes for brachytherapy dosimetric studies of $^{192}$Ir and $^{137}$Cs. Med Phys. 2008;35:4872-7.

Guedea F, Ellison T, Venselaar J, Borras JM, Hoskin P, Poetter R, et al. Overview of brachytherapy resources in Europe: a survey of patterns of care study for brachytherapy in Europe. Radiother Oncol. 2007;82:50-4.

Gutman G, Sozontov E, Strumban E, Yin FF, Lee SW, Kim JH. A novel needle-based miniature x-ray generating system. Phys Med Biol. 2004;49:4677-88.

Gutman G, Strumban E, Sozontov E, Jenrow K. X-ray scalpel - a new device for targeted x-ray brachytherapy and stereotactic radiosurgery. Phys Med Biol. 2007;52:1757-70.

Haie-Meder C, Pötter R, Van Limbergen E, Briot E, De Brabandere M, Dimopoulos J, et al. Recommendations from Gynaecological (GYN) GEC-ESTRO Working Group (I): concepts and terms in 3D image based 3D treatment planning in cervix cancer brachytherapy with emphasis on MRI assessment of GTV and CTV. Radiother Oncol. 2005 Mar;74:235-45.

Hall EJ, Giaccia AJ. Repair of radiation damage and the dose-rate effect. Radiobiology for the radiologist. 6th ed. Philadelphia: Lippincott Williams & Wilkins; 2006. p. 60-84.

Han P, Hu KS, Shankar RA, Harrison LB. Head and neck brachytherapy. In: Hoskins WJ, Perez CA, Young RC, Barakat RR, Markman M, Randall ME, editors. Principles and practice of gynecologic oncology. 4th ed. Philadelphia: Lippincott Williams & Wilkins; 2005. p. 49-92.

Hartmann Siantar CL, Walling RS, Daly TP, Faddegon B, Albright N, Bergstrom P, et al. Description and dosimetric verification of the PEREGRINE Monte Carlo dose calculation system for photon beams incident on a water phantom. Med Phys. 2001;28:1322-37.

Hedtjärn H, Carlsson GA, Williamson JF. Accelerated Monte Carlo based dose calculations for brachytherapy planning using correlated sampling. Phys Med Biol. 2002;47:351-76.

Hellebust TP, Dale E, Skjønsberg A, Olsen DR. Inter fraction variations in rectum and bladder volumes and dose distributions during high dose rate brachytherapy treatment of the uterine cervix investigated by repetitive CT-examinations. Radiother Oncol. 2001;60:273-80.

Hendricks JS, McKinney GW, Waters LS, Hughes HG. MCNPX user's manual, version 2.4.0. Los Alamos, NM: Los Alamos National Laboratory 2002.

Henschke UK, Hilaris BS, Mahan GD. Afterloading in interstitial and intracavitary radiation therapy. Am J Roentgenol Radium Ther Nucl Med. 1963;90:386-95.

Henschke UK, Hilaris BS, Mahan GD. Remote afterloading with intracavitary applicators. Radiology. 1964;83:344-5.

Henschke UK, Hilaris BS, Mahan GD. Intracavitary radiation therapy of cancer of the uterine cervix by remote afterloading with cycling sources. Am J Roentgenol Radium Ther Nucl Med. 1966;96:45-51.

Heyman J. The technique in the treatment of cancer uteri at Radiumhemmet. Acta Radiol. 1929;10:49-64.

Heyman J. The so-called Stockholm method and the results of treatment of uterine cancer at the Radiumhemmet. Acta Radiol. 1935;16:129-48.

Hill DL, Hawkes DJ, Crossman JE, Gleeson MJ, Cox TC, Bracey EE, et al. Registration of MR and CT images for skull base surgery using point-like anatomical features. Br J Radiol. 1991;64:1030-5.

Holt RW, Thomadsen BR, Orton CG. Point/Counterpoint. Miniature x-ray tubes will ultimately displace Ir-192 as the radiation sources of choice for high dose rate brachytherapy. Med Phys. 2008;35:815-7.

Hope CS, Laurie J, Orr JS, Walters JH. The computation of dose distribution in cervix radium treatment. Phys Med Biol. 1964;16:344-57.

Horwitz H, Kereiakes JG, Bahr GK, Cuxton SE, Barrett CM. An after-loading system utilizing Cesium 137 for the treatment of carcinoma of the cervix. Am J Roentgenol Radium Ther Nucl Med. 1964;91:176-91.

Hubbell JH, Seltzer SM. Tables of x-ray mass attenuation coefficients and mass energy-absorption coefficients 1 keV to 20 MeV for elements Z=1 to 92 and 48 additional substances of dosimetric interest. Gaithersburg, MD: National Institute of Standards and Technology 1995. Report No.: NISTIR 5632.

International Commission on Radiation Units and Measurements. Radiation quantities and units. Washington, DC: ICRU; 1980.

International Commission on Radiation Units and Measurements. Dose and volume specification for reporting intracavitary therapy in gynecology. Bethesda, MD: ICRU; 1985.

International Commission on Radiation Units and Measurements. Tissue substitutes in radiation dosimetry and measurement. Bethesda, MD: ICRU; 1989.

International Commission on Radiation Units and Measurements. Photon, electron, proton and neutron interaction data for body tissues. Bethesda, MD: ICRU; 1992.

International Commission on Radiation Units and Measurements. Prescribing, recording, and reporting photon beam therapy. Bethesda, MD: ICRU; 1993.

International Commission on Radiation Units and Measurements. Dose and volume specification for reporting interstitial therapy. Bethesda, MD: ICRU; 1997.

International Commission on Radiation Units and Measurements. Fundamental quantities and units for ionizing radiation. Bethesda, MD: ICRU; 1998.

Interstitial Collaborative Working Group. Interstitial brachytherapy: physical, biological, and clinical considerations. Anderson LL, Nath R, Weaver KA, editors. New York: Raven Press; 1990.

Jacobs F, Sundermann E, De Sutter B, Christiaens M, Lemahieu I. A fast algorithm to calculate the exact radiological path through a pixel or voxel space. J Comp Inf Technol. 1998;6:89-94.

Jaffray DA, Siewerdsen JH, Wong JW, Martinez AA. Flat-panel cone-beam computed tomography for image-guided radiation therapy. Int J Radiat Oncol Biol Phys. 2002;53:1337-49.

Janeway HH. Radium therapy in cancer at the Memorial Hospital, New York (First report: 1915-1916). New York: Paul B. Hoeber1917.

Johns HE, Cunningham JR. The fundamentals of nuclear physics. The physics of radiology. 4th ed. Springfield, IL: Charles C. Thomas; 1983. p. 71-101.

Johnson TR, Krauss B, Sedlmair M, Grasruck M, Bruder H, Morhard D, et al. Material differentiation by dual energy CT: initial experience. Eur Radiol. 2007;17:1510-7.

Joliot F, Curie I. Artificial production of a new kind of radio-element. Nature. 1934;133:201-2.

Jones CH. Calibration and quality assurance of brachytherapy sources. In: Mayles P, Nahum AE, Rosenwald J-C, editors. Handbook of radiotherapy physics: theory and practice. New York: Taylor & Francis; 2007. p. 1101-15.

Jozsef G, Streeter OE, Astrahan MA. The use of linear programming in optimization of HDR implant dose distributions. Med Phys. 2003;30:751-60.

Kapiteijn E, Marijnen CA, Nagtegaal ID, Putter H, Steup WH, Wiggers T, et al. Preoperative radiotherapy combined with total mesorectal excision for resectable rectal cancer. N Engl J Med. 2001;345:638-46.

Karaiskos P, Angelopoulos A, Baras P, Rozaki-Mavrouli H, Sandilos P, Vlachos L, et al. Dose rate calculations around $^{192}$Ir brachytherapy sources using a Sievert integration model. Phys Med Biol. 2000 Feb;45:383-98.

Karaiskos P, Angelopoulos A, Baras P, Sakelliou L, Sandilos P, Dardoufas K, et al. A Monte Carlo investigation of the dosimetric characteristics of the VariSource $^{192}$Ir high dose rate brachytherapy source. Med Phys. 1999;26:1498-502.

Karaiskos P, Angelopoulos A, Sakelliou L, Sandilos P, Antypas C, Vlachos L, et al. Monte Carlo and TLD dosimetry of an $^{192}$Ir high dose-rate brachytherapy source. Med Phys. 1998;25:1975-84.

Karaiskos P, Papagiannis P, Angelopoulos A, Sakelliou L, Baltas D, Sandilos P, et al. Dosimetry of $^{192}$Ir wires for LDR interstitial brachytherapy following the AAPM TG-43 dosimetric formalism. Med Phys. 2001;28:156-66.

Kassas B, Mourtada F, Horton JL, Lane RG. Contrast effects on dosimetry of a partial breast irradiation system. Med Phys. 2004;31:1976-9.

Kawrakow I. Accurate condensed history Monte Carlo simulation of electron transport. I. EGSnrc, the new EGS4 version. Med Phys. 2000;27:485-98.

Kawrakow I. VMC++, electron and photon Monte Carlo calculations optimized for radiation treatment planning. In: Kling A, Barao F, Nakagawa M, Tavora L, Vaz P, editors. Advanced Monte Carlo for Radiation Physics, Particle Transport Simulation and Applications; Lisbon. Berlin: Springer; 2001. p. 229-36.

Kawrakow I, Fippel M. Investigation of variance reduction techniques for Monte Carlo photon dose calculation using XVMC. Phys Med Biol. 2000;45:2163-83.

Kelley JR, Cuttino LW, Vicini FA, Arthur DW. Breast brachytherapy. In: Halperin EC, Perez CA, Brady LW, editors. Perez and Brady's principles and practice of radiation oncology. 5th ed. Philadelphia: Wolters Kluwer Health/Lippincott Williams & Wilkins; 2008. p. 115-35.

Kendall RL, Gifford KA, Kirsner SM. The impact of peak-kilovoltage settings on heterogeneity-corrected photon-beam treatment plans. Radiother Oncol. 2006;81:206-8.

Khan FM. Brachytherapy. The physics of radiation therapy. 3rd ed. Philadelphia; London: Lippincott Williams & Wilkins; 2003. p. 357-400.

Kirisits C, Siebert FA, Baltas D, De Brabandere M, Hellebust TP, Berger D, et al. Accuracy of volume and DVH parameters determined with different brachytherapy treatment planning systems. Radiother Oncol. 2007;84:290-7.

Kirk MC, Hsi WC, Chu JC, Niu H, Hu Z, Bernard D, et al. Dose perturbation induced by radiographic contrast inside brachytherapy balloon applicators. Med Phys. 2004;31:1219-24.

Kirov AS, Williamson JF. Two-dimensional scatter integration method for brachytherapy dose calculations in 3D geometry. Phys Med Biol. 1997;42:2119-35.

Kirov AS, Williamson JF, Meigooni AS, Zhu Y. Measurement and calculation of heterogeneity correction factors for an Ir-192 high dose-rate brachytherapy source behind tungsten alloy and steel shields. Med Phys. 1996;23:911-9.

Klein O, Nishina Y. The scattering of light by free electrons according to Dirac's new relativistic dynamics. Nature. 1928;122:398-9.

Kocher DC. Radioactive decay data tables: a handbook of decay data for application to radiation dosimetry and radiological assessments. Oak Ridge, TN: Technical Information Center, U.S. Dept. of Energy; 1981.

Kraus-Tiefenbacher U, Steil V, Bauer L, Melchert F, Wenz F. A novel mobile device for intraoperative radiotherapy (IORT). Onkologie. 2003;26:596-8.

Krempien RC, Daeuber S, Hensley FW, Wannenmacher M, Harms W. Image fusion of CT and MRI data enables improved target volume definition in 3D-brachytherapy treatment planning. Brachytherapy. 2003;2:164-71.

Lahanas M, Baltas D, Giannouli S. Global convergence analysis of fast multiobjective gradient-based dose optimization algorithms for high-dose-rate brachytherapy. Phys Med Biol. 2003;48:599-617.

Lahanas M, Baltas D, Zamboglou N. A hybrid evolutionary algorithm for multi-objective anatomy-based dose optimization in high-dose-rate brachytherapy. Phys Med Biol. 2003;48:399-415.

Le Y, Chibani O, Todor D, Siebers I, Williamson J. An integrated CT-based Monte Carlo dose-evaluation system for brachytherapy and its application to permanent prostate implant postprocedure dosimetric analysis. Med Phys. 2005;32:2068.

Lee HR, Pankuch M, Chu JC, Spokas JJ. Evaluation and characterization of parallel plate microchamber's functionalities in small beam dosimetry. Med Phys. 2002;29:2489-96.

Lessard E, Pouliot J. Inverse planning anatomy-based dose optimization for HDR-brachytherapy of the prostate using fast simulated annealing algorithm and dedicated objective function. Med Phys. 2001;28:773-9.

Li Z, Das RK, DeWerd LA, Ibbott GS, Meigooni AS, Pérez-Calatayud J, et al. Dosimetric prerequisites for routine clinical use of photon emitting brachytherapy sources with average energy higher than 50 keV. Med Phys. 2007;34:37-40.

Li Z, Williamson JF. Volume-based geometric modeling for radiation transport calculations. Med Phys. 1992;19:667-77.

Ling CC. Permanent implants using Au-198, Pd-103 and I-125: radiobiological considerations based on the linear quadratic model. Int J Radiat Oncol Biol Phys. 1992;23:81-7.

Ling CC, Li WX, Anderson LL. The relative biological effectiveness of I-125 and Pd-103. Int J Radiat Oncol Biol Phys. 1995;32:373-8.

Ling CC, Roy JN. Radiobiological aspects of brachytherapy. In: Williamson JF, Thomadsen BR, Nath R, editors. Brachytherapy physics. Madison, WI: Medical Physics Pub.; 1995. p. 39-69.

Ling CC, Spiro IJ, Mitchell J, Stickler R. The variation of OER with dose rate. Int J Radiat Oncol Biol Phys. 1985;11:1367-73.

Liu D, Poon E, Bazalova M, Reniers B, Evans M, Rusch T, et al. Spectroscopic characterization of a novel electronic brachytherapy system. Phys Med Biol. 2008;53:61-75.

Liu HH, Keall P. $D_m$ rather than $D_w$ should be used in Monte Carlo treatment planning. Med Phys. 2002;29:922-3.

Lulu BA, Bjärngard BE. Batho's correction factor combined with scatter summation. Med Phys. 1982;9:372-7.

Lux I, Koblinger L. Monte Carlo particle transport methods: neutron and photon calculations. Boca Raton, FL: CRC Press; 1991.

Luxton G, Jozsef G. Radial dose distribution, dose to water and dose rate constant for monoenergetic photon point sources from 10 keV to 2 MeV:EGS4 Monte Carlo model calculation. Med Phys. 1999;26:2531-8.

Lymperopoulou G, Pantelis E, Papagiannis P, Rozaki-Mavrouli H, Sakelliou L, Baltas D, et al. A Monte Carlo dosimetry study of vaginal $^{192}$Ir brachytherapy applications with a shielded cylindrical applicator set. Med Phys. 2004;31:3080-6.

Lymperopoulou G, Papagiannis P, Angelopoulos A, Karaiskos P, Georgiou E, Baltas D. A dosimetric comparison of $^{169}$Yb and $^{192}$Ir for HDR brachytherapy of the breast, accounting for the effect of finite patient dimensions and tissue inhomogeneities. Med Phys. 2006;33:4583-9.

Ma CM, Li JS, Pawlicki T, Jiang SB, Deng J, Lee MC, et al. A Monte Carlo dose calculation tool for radiotherapy treatment planning. Phys Med Biol. 2002;47:1671-89.

Mackie TR, Scrimger JW, Battista JJ. A convolution method of calculating dose for 15-MV x rays. Med Phys. 1985;12:188-96.

Mangold CA, Rijnders A, Georg D, Van Limbergen E, Pötter R, Huyskens D. Quality control in interstitial brachytherapy of the breast using pulsed dose rate: treatment planning and dose delivery with an Ir-192 afterloading system. Radiother Oncol. 2001;58:43-51.

Markman J, Williamson JF, Dempsey JF, Low DA. On the validity of the superposition principle in dose calculations for intracavitary implants with shielded vaginal colpostats. Med Phys. 2001;28:147-55.

Martin RC, Laxson RR, Miller JH, Wierzbicki JG, Rivard MJ, Marsh DL. Development of high-activity $^{252}$Cf sources for neutron brachytherapy. Appl Radiat Isot. 1997;48:1567-70.

Maruyama Y, van Nagell JR, Yoneda J, Donaldson ES, Gallion HH, Powell D, et al. A review of californium-252 neutron brachytherapy for cervical cancer. Cancer. 1991;68:1189-97.

Mauceri T, Biggs P, Beatty J, Flynn D. Scatter and attenuation measurements at distances greater than 10 cm from an $^{192}$Ir source. Med Phys. 1999;26:97-9.

Mayles P, Rosenwald J-C. Therapy with unsealed sources. In: Mayles P, Nahum AE, Rosenwald J-C, editors. Handbook of radiotherapy physics: theory and practice. New York: Taylor & Francis; 2007. p. 1203.

MCNP-a general Monte Carlo N-particle transport code. Version 4A. Briesmeister JF, editor. Los Alamos, NM: Los Alamos National Laboratory 1993.

Medich DC, Tries MA, Munro JJ, 2nd. Monte Carlo characterization of an ytterbium-169 high dose rate brachytherapy source with analysis of statistical uncertainty. Med Phys. 2006;33:163-72.

Meertens H, Borger J, Steggerda M, Blom A. Evaluation and optimisation of interstitial brachytherapy dose distributions. In: Mould RF, Battermann JJ, Martinez AA, Speiser BL, editors. Brachytherapy from radium to optimization. Veenendaal: Nucletron International; 1994. p. 300-6.

Meertens H, van der Laarse R. Screens in ovoids of a Selectron cervix applicator. Radiother Oncol. 1985;3:69-80.

Meigooni AS, Meli JA, Nath R. Interseed effects on dose for $^{125}$I brachytherapy implants. Med Phys. 1992;19:385-90.

Meigooni AS, Nath R. Tissue inhomogeneity correction for brachytherapy sources in a heterogeneous phantom with cylindrical symmetry. Med Phys. 1992;19:401-7.

Meigooni AS, Zhu Y, Williamson JF, Myerson RJ, Teague S, Loffler E, et al. Design and dosimetric characteristics of a high dose rate remotely afterloaded endocavitary applicator system. Int J Radiat Oncol Biol Phys. 1996;34:1153-63.

Meisberger LL, Keller RJ, Shalek RJ. The effective attenuation in water of the gamma rays of gold 198, iridium 192, cesium 137, radium 226, and cobalt 60. Radiology. 1968;90:953-7.

Melchert C, Kohr P, Schmidt R. Calculation of dose decrease in a finite phantom of a $^{192}$Ir point source. Med Phys. 2007;34:3943-50.

Melhus CS, Rivard MJ. Approaches to calculating AAPM TG-43 brachytherapy dosimetry parameters for $^{137}$Cs, $^{125}$I, $^{192}$Ir, $^{103}$Pd, and $^{169}$Yb sources. Med Phys. 2006;33:1729-37.

Meli JA, Meigooni AS, Nath R. On the choice of phantom material for the dosimetry of $^{192}$Ir sources. Int J Radiat Oncol Biol Phys. 1988;14:587-94.

Meredith WJ, Paterson JRK. Radium dosage; the Manchester system. 2d ed. Edinburgh, London: Livingstone; 1967.

Milickovic N, Giannouli S, Baltas D, Lahanas M, Kolotas C, Zamboglou N, et al. Catheter autoreconstruction in computed tomography based brachytherapy treatment planning. Med Phys. 2000;27:1047-57.

Mohan R, Chui C, Lidofsky L. Differential pencil beam dose computation model for photons. Med Phys. 1986;13:64-73.

Montemaggi P, Guerrieri P, Federico M, Mortellaro G. Clinical applications of brachytherapy: low-dose-rate and pulse-dose-rate. In: Halperin EC, Perez CA, Brady LW, editors. Perez and Brady's principles and practice of radiation oncology. 5th ed. ed. Philadelphia: Wolters Kluwer Health/Lippincott Williams & Wilkins; 2008. p. 476-539.

Mould RF. A century of x-rays and radioactivity in medicine: with emphasis on photographic records of the early years. Bristol; Philadelphia: Institute of Physics Pub.; 1993.

Mould RF. Radium brachytherapy: historical review. In: Mould RF, Battermann JJ, Martinez AA, Speiser BL, editors. Brachytherapy from radium to optimization. Veenendaal: Nucletron International; 1994. p. 1-8.

Mould RF. Priority for radium therapy of benign conditions and cancer. Curr Oncol. 2007 Jun;14(3):118-22.

Mould RF, Litten FS, Bruggmoser G, Aronowitz JN. Proposals for radium therapy in 1903. Nowotwory J Oncol. 2007;57:136e-8e.

Muench PJ, Nath R. Dose distributions produced by shielded applicators using $^{241}$Am for intracavitary irradiation of tumors in the vagina. Med Phys. 1992;19:1299-306.

Murphy MK, Piper RK, Greenwood LR, Mitch MG, Lamperti PJ, Seltzer SM, et al. Evaluation of the new cesium-131 seed for use in low-energy x-ray brachytherapy. Med Phys. 2004;31:1529-38.

Nag S, Owen JB, Farnan N, Pajak TF, Martinez A, Porter A, et al. Survey of brachytherapy practice in the United States: a report of the Clinical Research Committee of the American Endocurietherapy Society. Int J Radiat Oncol Biol Phys. 1995;31:103-7.

Nag S, Scruggs GR. Clinical aspects and applications of high-dose-rate brachytherapy. In: Halperin EC, Perez CA, Brady LW, editors. Perez and Brady's principles and practice of radiation oncology. 5th ed. Philadelphia: Wolters Kluwer Health/Lippincott Williams & Wilkins; 2008. p. 560-82.

Nath R. Physical properties and clinical uses of brachytherapy radionuclides. In: Williamson JF, Thomadsen BR, Nath R, editors. Brachytherapy physics. Madison, WI: Medical Physics Pub.; 1995. p. 7-37.

Nath R, Anderson LL, Luxton G, Weaver KA, Williamson JF, Meigooni AS. Dosimetry of interstitial brachytherapy sources: recommendations of the AAPM Radiation Therapy Committee Task Group No. 43. American Association of Physicists in Medicine. Med Phys. 1995;22:209-34.

Nath R, Anderson LL, Meli JA, Olch AJ, Stitt JA, Williamson JF. Code of practice for brachytherapy physics: report of the AAPM Radiation Therapy Committee Task Group No. 56. Med Phys. 1997;24:1557-98.

Nath R, Meigooni AS, Meli JA. Dosimetry on transverse axes of $^{125}$I and $^{192}$Ir interstitial brachytherapy sources. Med Phys. 1990;17:1032-40.

National Council on Radiation Protection and Measurements. Specification of gamma-ray brachytherapy sources. NCRP Report No. 41. Washington, DC: Government Printing Office; 1974.

National Council on Radiation Protection and Measurements. A Handbook of radioactivity measurements procedures with nuclear data for some biomedically important radionuclides, reevaluated between August 1983 and April 1984. Bethesda, MD: National Council on Radiation Protection and Measurements; 1985. Available from: http://www.knovel.com/knovel2/Toc.jsp?BookID=1623.

Nuclear data from NuDat 2.0, a web-based database maintained by the National Nuclear Data Center [database on the Internet]. Brookhaven National Laboratory, Upton, NY 2004. Available from: http://www.nndc.bnl.gov/nudat2.

Nelder JA, Mead R. A simplex method for function minimization. Comp J. 1965;7:308-13.

Nelson WR, Hirayama H, Rogers DWO. The EGS4 code system. Stanford: Stanford Linear Accelerator Center 1985. Report No.: SLAC-265.

O'Connell D, Howard N, Joslin CA, Ramsey NW, Liversage WE. A new remotely controlled unit for the treatment of uterine carcinoma. Lancet. 1965;2:570-1.

Oh M, Wang Z, Malhotra HK, Jaggernauth W, Podgorsak MB. Impact of surface curvature on dose delivery in intraoperative high-dose-rate brachytherapy. Med Dosim. 2009;34:63-74.

Oh S, Scott J, Shin DH, Suh TS, Kim S. Measurements of dose discrepancies due to inhomogeneities and radiographic contrast in balloon catheter brachytherapy. Med Phys. 2009;36:3945-54.

Palcic B, Skarsgard LD. Reduced oxygen enhancement ratio at low doses of ionizing radiation. Radiat Res. 1984;100:328-39.

Pantelis E, Baltas D, Dardoufas K, Karaiskos P, Papagiannis P, Rosaki-Mavrouli H, et al. On the dosimetric accuracy of a Sievert integration model in the proximity of $^{192}$Ir HDR sources. Int J Radiat Oncol Biol Phys. 2002;53:1071-84.

Pantelis E, Papagiannis P, Anagnostopoulos G, Baltas D, Karaiskos P, Sandilos P, et al. Evaluation of a TG-43 compliant analytical dosimetry model in clinical $^{192}$Ir HDR brachytherapy treatment planning and assessment of the significance of source position and catheter reconstruction uncertainties. Phys Med Biol. 2004;49:55-67.

Pantelis E, Papagiannis P, Karaiskos P, Angelopoulos A, Anagnostopoulos G, Baltas D, et al. The effect of finite patient dimensions and tissue inhomogeneities on dosimetry planning of $^{192}$Ir HDR breast brachytherapy: a Monte Carlo dose verification study. Int J Radiat Oncol Biol Phys. 2005;61:1596-602.

Papagiannis P, Angelopoulos A, Pantelis E, Sakelliou L, Baltas D, Karaiskos P, et al. Dosimetry comparison of $^{192}$Ir sources. Med Phys. 2002;29:2239-46.

Papagiannis P, Karaiskos P, Georgiou E, Baltas D, Lymperopoulou G, Pantelis E, et al. On the use of high dose rate $^{192}$Ir and $^{169}$Yb sources with the MammoSite radiation therapy system. Med Phys. 2007;34:3614-9.

Papanikolaou N, Battista JJ, Boyer AL, Kappas C, Klein E, Mackie TR, et al. Tissue inhomogeneity corrections for megavoltage photon beams. Madison, WI: American Association of Physicists in Medicine 2004. Report No.: 85.

Parsai EI, Zhang Z, Feldmeier JJ. A quantitative three-dimensional dose attenuation analysis around Fletcher-Suit-Delclos due to stainless steel tube for high-dose-rate brachytherapy by Monte Carlo calculations. Brachytherapy. 2009;8:318-23.

Paterson R, Parker HM. A dosage system for gamma-ray therapy. Br J Radiol. 1934;7:592-632.

Paterson R, Parker HM. A dosage system for interstitial radium therapy. Br J Radiol. 1938;11:252-66, 313-40.

Perez CA, Purdy JA, Li Z, Hall EJ. Biologic and physical aspects of radiation oncology. In: Hoskins WJ, Perez CA, Young RC, Barakat RR, Markman M, Randall ME,

editors. Principles and practice of gynecologic oncology. 4th ed. Philadelphia: Lippincott Williams & Wilkins; 2005. p. 375-459.

Pérez-Calatayud J, Granero D, Ballester F. Phantom size in brachytherapy source dosimetric studies. Med Phys. 2004;31:2075-81.

Perkins ST, Cullen DE, Chen MH, Hubbell JH, Rathkopf J, Scofield J. Tables and graphs of atomic subshell and relaxation data derived from the LLNL evaluated Atomic Data Library (EADL), Z=1–100. Livermore, CA: Lawrence Livermore National Laboratory 1991. Report No.: UCRL-50400.

Pierquin B, Dutreix A, Paine CH, Chassagne D, Marinello G, Ash D. The Paris system in interstitial radiation therapy. Acta Radiol Oncol Radiat Phys Biol. 1978;17:33-48.

Podgoršak EB. Treatment machines for external beam radiotherapy. In: Podgoršak EB, editor. Radiation oncology physics : a handbook for teachers and students. Vienna: International Atomic Energy Agency; 2005. p. 123-60.

Podgoršak EB. Basic radiation physics. In: Podgoršak EB, editor. Radiation oncology physics : a handbook for teachers and students. Vienna: International Atomic Energy Agency; 2005. p. 1-43.

Podgoršak EB. External photon beams: physical aspects. In: Podgoršak EB, editor. Radiation oncology physics: a handbook for teachers and students. Vienna: International Atomic Energy Agency; 2005. p. 161-217.

Poon E, Al-Halabi H, Reniers B, Verhaegen F. Effects of shielded ovoids in HDR $^{192}$Ir cervical brachytherapy: a Monte Carlo study using cone-Beam CT images. Med Phys. 2009;36:2773.

Poon E, Le Y, Williamson JF, Verhaegen F. BrachyGUI: an adjunct to an accelerated Monte Carlo photon transport code for patient-specific brachytherapy dose calculations and analysis. J Phys Conf Ser. 2008;102:012018.

Poon E, Reniers B, Devic S, Vuong T, Verhaegen F. Dosimetric characterization of a novel intracavitary mold applicator for $^{192}$Ir high dose rate endorectal brachytherapy treatment. Med Phys. 2006;33:4515-26.

Poon E, Seuntjens J, Verhaegen F. Consistency test of the electron transport algorithm in the GEANT4 Monte Carlo code. Phys Med Biol. 2005;50:681-94.

Poon E, Verhaegen F. Accuracy of the photon and electron physics in GEANT4 for radiotherapy applications. Med Phys. 2005;32:1696-711.

Poon E, Verhaegen F. Development of a scatter correction technique and its application to HDR $^{192}$Ir multicatheter breast brachytherapy. Med Phys. 2009;36:3703-13.

Poon E, Verhaegen F. A CT-based analytical dose calculation method for HDR $^{192}$Ir brachytherapy. Med Phys. 2009;36:3982-94.

Poon E, Williamson JF, Vuong T, Verhaegen F. Patient-specific Monte Carlo dose calculations for high-dose-rate endorectal brachytherapy with shielded intracavitary applicator. Int J Radiat Oncol Biol Phys. 2008;72:1259-66.

Potish RA, Gerbi BJ. Role of point A in the era of computerized dosimetry. Radiology. 1986;158:827-31.

Pouliot J, Tremblay D, Roy J, Filice S. Optimization of permanent $^{125}$I prostate implants using fast simulated annealing. Int J Radiat Oncol Biol Phys. 1996;36:711-20.

Prasad SC, Bassano DA, Kubsad SS. Buildup factors and dose around a $^{137}$Cs source in the presence of inhomogeneities. Med Phys. 1983;10:705-8.

Press WH, Flannery BP, Teukolsky SA, Vetterling WM. Numerical recipes in C : the art of scientific computing. Cambridge: Cambridge University Press; 1988.

Prestidge BR, Bice WS, Jurkovic I, Walker E, Marianne S, Sadeghi A. Cesium-131 permanent prostate brachytherapy: an initial report. Int J Radiat Oncol Biol Phys. 2005;63:S336-S7.

Price M. The imaging and dosimetric capabilities of a CT/MR-suitable, anatomically adaptive, shielded intracavitary brachytherapy applicator for the treatment of cervical cancer [dissertation]. Houston (TX): University of Texas; 2008.

Quimby EH, Castro V. The calculation of dosage in interstitial radium therapy. Am J Roentgenol Radium Ther Nucl Med. 1953;70:739-49.

Radiation Safety Information Computational Center. HUGO-VI: Photon Interaction Data in ENDF/B-VI Format. Oak Ridge, TN Oak Ridge National Laboratory; 1989.

Ragde H, Blasko JC, Grimm PD, Kenny GM, Sylvester JE, Hoak DC, et al. Interstitial iodine-125 radiation without adjuvant therapy in the treatment of clinically localized prostate carcinoma. Cancer. 1997;80:442-53.

Raina S, Avadhani JS, Oh M, Malhotra HK, Jaggernauth W, Kuettel MR, et al. Quantifying IOHDR brachytherapy underdosage resulting from an incomplete scatter environment. Int J Radiat Oncol Biol Phys. 2005;61:1582-6.

Regaud C. Radium therapy of cancer at the Radium Institute of Paris. Am J Roentgenol. 1929;21:1.

Reniers B, Liu D, Rusch T, Verhaegen F. Calculation of relative biological effectiveness of a low-energy electronic brachytherapy source. Phys Med Biol. 2008;53:7125-35.

Rief H. Generalized Monte Carlo perturbation algorithms for correlated sampling and a second-order Taylor series approach. Ann Nucl Ener. 1984;11:455-76.

Rivard MJ, Coursey BM, DeWerd LA, Hanson WF, Huq MS, Ibbott GS, et al. Update of AAPM Task Group No. 43 Report: A revised AAPM protocol for brachytherapy dose calculations. Med Phys. 2004;31:633-74.

Rivard MJ, Davis SD, DeWerd LA, Rusch TW, Axelrod S. Calculated and measured brachytherapy dosimetry parameters in water for the Xoft Axxent X-Ray Source: an electronic brachytherapy source. Med Phys. 2006;33:4020-32.

Rivard MJ, Melhus CS, Granero D, Perez-Calatayud J, Ballester F. An approach to using conventional brachytherapy software for clinical treatment planning of complex, Monte Carlo-based brachytherapy dose distributions. Med Phys. 2009;36:1968-75.

Rivard MJ, Venselaar JLM, Beaulieu L. The evolution of brachytherapy treatment planning. Med Phys. 2009;36:2136-53.

Rogers DWO, Bielajew AF. Monte Carlo techniques of electron and photon transport for radiation dosimetry. In: Kase KR, Bjärngard BE, Attix FH, editors. The dosimetry of ionizing radiation. New York: Academic; 1990. p. 427-539.

Ron E. Ionizing radiation and cancer risk: evidence from epidemiology. Radiat Res. 1998;150:S30-41.

Rownd J. Applicator design and dose distributions. In: Thomadsen B, Rivard MJ, Butler WM, editors. Brachytherapy physics. 2nd ed. Madison, WI.: Medical Physics Pub.; 2005. p. 797-804.

Russell KR, Ahnesjo A. Dose calculation in brachytherapy for a $^{192}$Ir source using a primary and scatter dose separation technique. Phys Med Biol. 1996;41:1007-24.

Russell KR, Carlsson Tedgren ÅK, Ahnesjö A. Brachytherapy source characterization for improved dose calculations using primary and scatter dose separation. Med Phys. 2005;32:2739-52.

Sakelliou L, Sakellariou K, Sarigiannis K, Angelopoulos A, Perris A, Zarris G. Dose rate distributions around $^{60}$Co, $^{137}$Cs, $^{198}$Au, $^{192}$Ir, $^{241}$Am, $^{125}$I (models 6702 and 6711) brachytherapy sources and the nuclide $^{99}$Tcm. Phys Med Biol. 1992;37:1859-72.

Samuel EC. Radium therapy. South Med J. 1917;10:490-4.

Sarkar A, Santiago RJ, Smith R, Kassaee A. Comparison of manual vs. automated multimodality (CT-MRI) image registration for brain tumors. Med Dosim. 2005;30:20-4.

Sauer R, Becker H, Hohenberger W, Rodel C, Wittekind C, Fietkau R, et al. Preoperative versus postoperative chemoradiotherapy for rectal cancer. N Engl J Med. 2004;351:1731-40.

Schoeppel SL, Fraass BA, Hopkins MP, La Vigne ML, Lichter AS, McShan DL, et al. A CT-compatible version of the Fletcher system intracavitary applicator: clinical application and 3-dimensional treatment planning. Int J Radiat Oncol Biol Phys. 1989;17:1103-9.

Sempau J, Wilderman SJ, Bielajew AF. DPM, a fast, accurate Monte Carlo code optimized for photon and electron radiotherapy treatment planning dose calculations. Phys Med Biol. 2000;45:2263-91.

Serago CF, Houdek PV, Pisciotta V, Schwade JG, Abitbol AA, Lewin AA, et al. Scattering effects on the dosimetry of iridium-192. Med Phys. 1991;18:1266-70.

Shalek RJ, Stovall M. The M. D. Anderson method for the computation of isodose curves around interstitial and intracavitary radiation sources. I. Dose from linear sources. Am J Roentgenol Radium Ther Nucl Med. 1968;102:662-72.

Sharpe MB, Battista JJ. Dose calculations using convolution and superposition principles: the orientation of dose spread kernels in divergent x-ray beams. Med Phys. 1993;20:1685-94.

Siddon RL. Fast calculation of the exact radiological path for a three-dimensional CT array. Med Phys. 1985;12:252-5.

Siebers JV, Keall PJ, Nahum AE, Mohan R. Converting absorbed dose to medium to absorbed dose to water for Monte Carlo based photon beam dose calculations. Phys Med Biol. 2000;45:983-95.

Sievert RM. Die intensitätsverteilung der primären γ-strahlung in der nähe medizinischer radiumpräparate. Acta Radiol. 1921;1:89-128.

Sloboda RS, Wang R. Combined experimental and Monte Carlo verification of $^{137}$Cs brachytherapy plans for vaginal applicators. Phys Med Biol. 1998;43:3495-507.

Smithers DW. The therapeutic use of radioactive isotopes: lecture delivered at the Royal College of Surgeons of England on 9th May 1958. Ann R Coll Surg Engl. 1958;23:238-47.

Steel G. Radiobiology of tumors. In: Mayles P, Nahum AE, Rosenwald J-C, editors. Handbook of radiotherapy physics: theory and practice. New York: Taylor & Francis; 2007. p. 127-48.

Sternick EB, Todor DA, Orton CG. Point/Counterpoint. Intensity modulated electronic brachytherapy will soon become the brachytherapy treatment of choice for

irregularly shaped tumor cavities or those closely bounded by critical structures. Med Phys. 2009;36:681-3.

Stevens LG. Injurious effects on the skin. Br Med J. 1896;1:998.

Stevenson WC. Preliminary clinical report on a new and economical method of radium therapy by means of emanation needles. Br Med J. 1914;2:9-10.

Stewart AJ, Jones B. Radiobiologic concepts for brachytherapy. In: Devlin PM, editor. Brachytherapy: applications and techniques. Philadelphia: Lippincott Williams & Wilkins; 2007. p. 1-19.

Stock RG, Stone NN, Tabert A, Iannuzzi C, DeWyngaert JK. A dose-response study for I-125 prostate implants. Int J Radiat Oncol Biol Phys. 1998;41:101-8.

Stovall M, Shalek RJ. The M. D. Anderson method for the computation of isodose curves around interstitial and intracavitary radiation sources. III. Roentgenograms for input data and relation of isodose calculations to the Paterson-Parker system. Am J Roentgenol Radium Ther Nucl Med. 1968;102:677-87.

Stovall M, Shalek RJ. A review of computer techniques for dosimetry of interstitial and intracavitary radiotherapy. Comput Programs Biomed. 1972;2:125-36.

Strebel H. Vorschläge zur Radiumtherapie [Proposals for radiumtherapy]. Dtsch Med Z. 1903;24:1145-6. In: Mould RF, Litten FS, Bruggmoser G, Aronowitz JN. Proposals for radium therapy in 1903. Nowotwory J Oncol. 2007;57:136e-8e.

Suntharalingam N, Podgorsak EB, Tölli H. Brachytherapy: physical and clinical aspects. In: Podgorsak EB, editor. Radiation oncology physics: a handbook for teachers and students. Vienna: International Atomic Energy Agency; 2005. p. 451-84.

Swedish Rectal Cancer Trial. Improved survival with preoperative radiotherapy in resectable rectal cancer. N Engl J Med. 1997;336:980-7.

Taylor RE, Rogers DW. An EGSnrc Monte Carlo-calculated database of TG-43 parameters. Med Phys. 2008;35:4228-41.

Taylor RE, Yegin G, Rogers DW. Benchmarking BrachyBose: voxel based EGSnrc Monte Carlo calculations of TG-43 dosimetry parameters. Med Phys. 2007;34:445-57.

Taylor RPE, Rogers DWO. EGSnrc Monte Carlo calculated dosimetry parameters for $^{192}$Ir and $^{169}$Yb brachytherapy sources. Med Phys. 2008;35:4933-44.

Thomadsen B, Das R. The physics and dosimetry of high-dose-rate brachytherapy. In: Halperin EC, Perez CA, Brady LW, editors. Perez and Brady's principles and practice of radiation oncology. 5th ed. Philadelphia: Wolters Kluwer Health/Lippincott Williams & Wilkins; 2008. p. 540-59.

Thomadsen BR, Williamson JF, Rivard MJ, Meigooni AS. Anniversary paper: past and current issues, and trends in brachytherapy physics. Med Phys. 2008;35:4708-23.

Thomson RM, Taylor RE, Rogers DW. Monte Carlo dosimetry for $^{125}$I and $^{103}$Pd eye plaque brachytherapy. Med Phys. 2008;35:5530-43.

Tobias JS, Vaidya JS, Keshtgar M, D'Souza DP, Baum M. Reducing radiotherapy dose in early breast cancer: the concept of conformal intraoperative brachytherapy. Br J Radiol. 2004;77:279-84.

Tod M, Meredith WJ. Treatment of cancer of the cervix uteri, a revised Manchester method. Br J Radiol. 1953;26:252-7.

Tod MC, Meredith WJ. A dosage system for use in the treatment of cancer of the uterine cervix. Br J Radiol. 1938;11:809-24.

Trott NG. Radionuclides in brachytherapy: radium and after. Br J Radiol Suppl. 1987;21:1-54. In: Aird E. Sources in brachytherapy. In: Joslin CAF, Flynn A, Hall EJ, editors. Principles and practice of brachytherapy: using afterloading systems. London: Arnold; 2001. p. 3-10.

Vaidya JS. Partial breast irradiation using targeted intraoperative radiotherapy (Targit). Nat Clin Pract Oncol. 2007;4:384-5.

Vaidya JS, Baum M, Tobias JS, D'Souza DP, Naidu SV, Morgan S, et al. Targeted intra-operative radiotherapy (Targit): an innovative method of treatment for early breast cancer. Ann Oncol. 2001;12:1075-80.

Vaidya JS, Baum M, Tobias JS, Morgan S, D'Souza D. The novel technique of delivering targeted intraoperative radiotherapy (Targit) for early breast cancer. Eur J Surg Oncol. 2002;28:447-54.

Vaidya JS, Tobias JS, Baum M, Keshtgar M, Joseph D, Wenz F, et al. Intraoperative radiotherapy for breast cancer. Lancet Oncol. 2004;5:165-73.

Valicenti RK, Kirov AS, Meigooni AS, Mishra V, Das RK, Williamson JF. Experimental validation of Monte Carlo dose calculations about a high-intensity Ir-192 source for pulsed dose-rate brachytherapy. Med Phys. 1995;22:821-9.

van der Laarse R, Meertens H. An algorithm for ovoid shielding of a cervix applicator. In: Cunningham JR, Ragan D, Van Dyk J, editors. 8th International Conference on the Use of Computers in Radiation Therapy; July 9-12, 1984; Toronto, Canada. Los Angeles, CA: IEEE Computer Society; 1984. p. 364-9.

van Herk M, de Munck JC, Lebesque JV, Muller S, Rasch C, Touw A. Automatic registration of pelvic computed tomography data and magnetic resonance scans including a full circle method for quantitative accuracy evaluation. Med Phys. 1998(10):2054-67.

van Herk M, Kooy HM. Automatic three-dimensional correlation of CT-CT, CT-MRI, and CT-SPECT using chamfer matching. Med Phys. 1994;21:1163-78.

Vanderstraeten B, Chin PW, Fix M, Leal A, Mora G, Reynaert N, et al. Conversion of CT numbers into tissue parameters for Monte Carlo dose calculations: a multi-centre study. Phys Med Biol. 2007;52:539-62.

van't Riet A, Mak AC, Moerland MA, Elders LH, van der Zee W. A conformation number to quantify the degree of conformality in brachytherapy and external beam irradiation: application to the prostate. Int J Radiat Oncol Biol Phys. 1997;37:731-6.

Vassiliev ON, Wareing TA, Davis IM, McGhee J, Barnett D, Horton JL, et al. Feasibility of a multigroup deterministic solution method for three-dimensional radiotherapy dose calculations. Int J Radiat Oncol Biol Phys. 2008;72:220-7.

Verellen D, De Neve W, Van den Heuvel F, Storme G, Coen V, Coghe M. On the determination of the effective transmission factor for stainless steel ovoid shielding segments and estimation of their shielding efficacy for the clinical situation. Med Phys. 1994;21:1677-84.

Verhaegen F, Devic S. Sensitivity study for CT image use in Monte Carlo treatment planning. Phys Med Biol. 2005;50:937-46.

Viswanathan AN, Dimopoulos J, Kirisits C, Berger D, Potter R. Computed tomography versus magnetic resonance imaging-based contouring in cervical cancer brachytherapy: results of a prospective trial and preliminary guidelines for standardized contours. Int J Radiat Oncol Biol Phys. 2007;68:491-8.

Vuong T, Belliveau PJ, Michel RP, Moftah BA, Parent J, Trudel JL, et al. Conformal preoperative endorectal brachytherapy treatment for locally advanced rectal cancer: early results of a phase I/II study. Dis Colon Rectum. 2002;45:1486-95.

Vuong T, Devic S, Moftah B, Evans M, Podgorsak EB. High-dose-rate endorectal brachytherapy in the treatment of locally advanced rectal carcinoma: technical aspects. Brachytherapy. 2005;4:230-5.

Vuong T, Devic S, Podgorsak E. High dose rate endorectal brachytherapy as a neoadjuvant treatment for patients with resectable rectal cancer. Clin Oncol. 2007;19:701-5.

Walstam R. Remotely-controlled afterloading radiotherapy apparatus (a preliminary report). Phys Med Biol. 1962;7:225-8.

Walters B, Kawrakow I, Rogers DW. DOSXYZnrc Users Manual. Ottawa: National Research Council Canada 2009. Report No.: NRCC Report PIRS-794revB.

Wang R, Li XA. Dose characterization in the near-source region for two high dose rate brachytherapy sources. Med Phys. 2002;29:1678-86.

Wang R, Sloboda RS. EGS4 dosimetry calculations for cylindrically symmetric brachytherapy sources. Med Phys. 1996;23:1459-65.

Wang R, Sloboda RS. Influence of source geometry and materials on the transverse axis dosimetry of $^{192}$Ir brachytherapy sources. Phys Med Biol. 1998;43:37-48.

Wang R, Sloboda RS. Brachytherapy scatter dose calculation in heterogeneous media: I. a microbeam ray-tracing method for the single-scatter contribution. Phys Med Biol. 2007;52:5619-36.

Wang R, Sloboda RS. Brachytherapy scatter dose calculation in heterogeneous media: II. empirical formulation for the multiple-scatter contribution. Phys Med Biol. 2007;52:5637-54.

Wang Y, Lewis D, Poon E, Verhaegen F, Podgorsak E, Devic S. Sensitivity of document scanners used for radiochromic film dosimetry. Med Phys. 2006;33:2135.

Watanabe Y, Roy JN, Harrington PJ, Anderson LL. Three-dimensional lookup tables for Henschke applicator cervix treatment by HDR $^{192}$IR remote afterloading. Int J Radiat Oncol Biol Phys. 1998;41:1201-7.

Waterman FM, Holcomb DE. Dose distributions produced by a shielded vaginal cylinder using a high-activity iridium-192 source. Med Phys. 1994;21:101-6.

Weeks KJ. Monte Carlo dose calculations for a new ovoid shield system for carcinoma of the uterine cervix. Med Phys. 1998;25:2288-92.

Wendling M, Zijp LJ, McDermott LN, Smit EJ, Sonke JJ, Mijnheer BJ, et al. A fast algorithm for gamma evaluation in 3D. Med Phys. 2007;34:1647-54.

Williamson JF. The accuracy of the line and point source approximations in Ir-192 dosimetry. Int J Radiat Oncol Biol Phys. 1986;12:409-14.

Williamson JF. Monte Carlo evaluation of kerma at a point for photon transport problems. Med Phys. 1987;14:567-76.

Williamson JF. Radiation transport calculations in treatment planning. Comput Med Imaging Graph. 1989;13:251-68.

Williamson JF. Dose calculations about shielded gynecological colpostats. Int J Radiat Oncol Biol Phys. 1990;19:167-78.

Williamson JF. Comparison of measured and calculated dose rates in water near I-125 and Ir-192 seeds. Med Phys. 1991;18:776-86.

Williamson JF. The Sievert integral revisited: evaluation and extension to $^{125}$I, $^{169}$Yb, and $^{192}$Ir brachytherapy sources. Int J Radiat Oncol Biol Phys. 1996;36:1239-50.

Williamson JF. Semiempirical dose-calculation models in brachytherapy. In: Thomadsen B, Rivard MJ, Butler WM, editors. Brachytherapy physics. 2nd ed. Madison, WI.: Medical Physics Pub.; 2005. p. 201-32.

Williamson JF. Brachytherapy technology and physics practice since 1950: a half-century of progress. Phys Med Biol. 2006;51:R303-25.

Williamson JF, Baker RS, Li ZF. A convolution algorithm for brachytherapy dose computations in heterogeneous geometries. Med Phys. 1991;18:1256-65.

Williamson JF, Brenner DJ. Physics and biology of brachytherapy. In: Halperin EC, Perez CA, Brady LW, editors. Perez and Brady's principles and practice of radiation oncology. 5th ed. Philadelphia: Wolters Kluwer Health/Lippincott Williams & Wilkins; 2008. p. 423-75.

Williamson JF, Deibel FC, Morin RL. The significance of electron binding corrections in Monte Carlo photon transport calculations. Phys Med Biol. 1984;29:1063-73.

Williamson JF, Li Z. Monte Carlo aided dosimetry of the microselectron pulsed and high dose-rate $^{192}$Ir sources. Med Phys. 1995;22:809-19.

Williamson JF, Li Z, Wong JW. One-dimensional scatter-subtraction method for brachytherapy dose calculation near bounded heterogeneities. Med Phys. 1993;20:233-44.

Williamson JF, Perera H, Li Z, Lutz WR. Comparison of calculated and measured heterogeneity correction factors for $^{125}$I, $^{137}$Cs, and $^{192}$Ir brachytherapy sources near localized heterogeneities. Med Phys. 1993;20:209-22.

Wu A, Ulin K, Sternick ES. A dose homogeneity index for evaluating $^{192}$Ir interstitial breast implants. Med Phys. 1988;15:104-7.

Yan X, Poon E, Reniers B, Vuong T, Verhaegen F. Comparison of dose calculation algorithms for colorectal cancer brachytherapy treatment with a shielded applicator. Med Phys. 2008;35:4824-30.

Ye SJ, Brezovich IA, Shen S, Duan J, Popple RA, Pareek PN. Attenuation of intracavitary applicators in $^{192}$Ir-HDR brachytherapy. Med Phys. 2004;31:2097-106.

Ye SJ, Brezovich IA, Shen S, Kim S. Dose errors due to inhomogeneities in balloon catheter brachytherapy for breast cancer. Int J Radiat Oncol Biol Phys. 2004;60:672-7.

Young ME, Batho HF. Dose tables for linear radium sources calculated by an electronic computer. Br J Radiol. 1964;37:38-44.

Zelefsky MJ, Kuban DA, Levy LB, Potters L, Beyer DC, Blasko JC, et al. Multi-institutional analysis of long-term outcome for stages T1-T2 prostate cancer treated with permanent seed implantation. Int J Radiat Oncol Biol Phys. 2007;67:327-33.

Zhou C, Inanc F. Integral-transport-based deterministic brachytherapy dose calculations. Phys Med Biol. 2003;48:73-93.

Zwahlen D, Jezioranski J, Chan P, Haider MA, Cho YB, Yeung I, et al. Magnetic resonance imaging-guided intracavitary brachytherapy for cancer of the cervix. Int J Radiat Oncol Biol Phys. 2009;74:1157-64.